STUDY OF ORDERING AND LOCAL ATOMIC ENVIRONMENTS IN IRON-BASED MAGNETOSTRICTIVE ALLOYS

by

Chai Ren

A dissertation submitted to the faculty of
The University of Utah
in partial fulfillment of the requirements for the degree of

Doctor of Philosophy

Department of Metallurgical Engineering

The University of Utah

August 2012

The University of Utah Graduate School

STATEMENT OF DISSERTATION APPROVAL

The dissertation of **Chai Ren**

has been approved by the following supervisory committee members:

Sivaraman Guruswamy	, Chair	**4/23/2012** Date Approved
Zhigang Zak Fang	, Member	**4/23/2012** Date Approved
Michael L. Free	, Member	**4/23/2012** Date Approved
Michael S. Moats	, Member	**4/23/2012** Date Approved
Andrey Rogachev	, Member	**4/23/2012** Date Approved

and by **Jan D. Miller** , Chair of the Department of **Metallurgical Engineering**

and by Charles A. Wight, Dean of The Graduate School.

ABSTRACT

The α-phases of Fe-Ga and Fe-W alloys show large low field magnetostriction and the observed magnetostrictive behavior is sensitive to the solute content and thermal history. In order to improve understanding of magnetostriction, the first part of this work examines the influence of W substitution for Ga in Fe-Ga alloys and a more detailed examination of Fe-W alloys. The variation of magnetostriction coefficient λ_{100} with W substitution for Ga in various Fe-x at.% Ga alloys was examined.

Fe-12.5 at.% Ga-2.5 at.% W, Fe-15 at.% Ga-2.5 at.% W and Fe-17.5 at.% Ga-2.5 at.% W single crystals were prepared by vertical Bridgman technique and annealed in the α-phase region followed by rapid water quenching. Increase of the Ga content in Fe-x at.% Ga-2.5 at.% W increased λ_{100} magnetostriction values up to 307 x 10^{-6} for 15 at.% Ga and further increase in Ga content decreased the magnetostriction value. Comparing the magnetostriction of Fe-Ga-W alloys to those of Fe-Ga alloys, the substitution of W for Ga caused more than a 7% drop in magnetostriction. The magnetostriction coefficients λ_{111} were also measured using of [220]- or [211]-oriented single crystals of Fe-12.5 at.% Ga-2.5 at.% W, Fe-3 at.% W, Fe-6 at.% W and Fe-7.5 at.% W alloys. The magnetostriction increases as the W content increased from 3 at.% to 7.5 at.% W.

In the second part, the B2 and DO_3 types of ordering were examined in annealed and quenched magnetostrictive Fe-27.5 at.% Ga single crystal and the presence of both B2 and DO_3 ordered domains is demonstrated. The relative amounts of B2 phase

domains increased with increasing depth up to about 100 um depth. After that, the volume ratio of B2 and DO_3 domains showed little variation beyond this depth.

In the third part, the extended x-ray fluorescence spectroscopy (EXAFS) studies of local atomic environment of Fe-27.5 at.% Ga, Fe-20 at.% Ga and Fe-15 at.% Ga single crystals were carried out. The study focused on the first and second nearest neighbors. The results obtained in the examination of Ga-Ga first nearest neighbor bond distance show a large positive increase after long-term annealing and the value of this positive strain increases as the Ga content increases. As the change of magnetostriction value with the changes in Ga content or thermal history follows the same tendency, it suggests a correlation between local lattice distortions to the material's magnetostrictive behavior.

TABLE OF CONTENTS

ABSTRACT……... iii

LIST OF TABLES…….. viii

LIST OF FIGURES…… x

ACKNOWLEDGEMENTS…… xvii

1. INTRODUCTION…… 1

2. BACKGROUND……. 5

2.1 Magnetism……... 5
2.1.1 Magnetic Field…….. 5
2.1.2 Magnetic Moment……. 7
2.1.3 Magnetization……... 8
2.1.4 Magnetization Curve and Hysteresis Loop……... 8
2.1.5 Magnetic Anisotropy in Cubic Crystals…… 11
2.1.6 Origin of Magnetic Properties…….. 12
2.1.7 Magnetic Behaviors…….. 12
2.1.7.1 Diamagnetism……... 12
2.1.7.2 Paramagnetism…….. 13
2.1.7.3 Ferromagnetism…… 13
2.1.7.4 Antiferromagnetism…….. 16
2.1.7.5 Ferrimagnetism……. 16
2.2 Magnetostriction……. 17
2.2.1 Volume Magnetostriction and Joule Magnetostriction……. 17
2.2.2 Saturation Magnetostriction in Cubic Crystals……. 18
2.2.3 Physical Origin of Magnetostriction……. 22
2.2.4 Previous Works on Fe-based Magnetostrictive Alloys……. 22
2.2.4.1 Dy, Tb and Terfenol Alloys…….. 22
2.2.4.2 Fe-Al Alloys……. 25
2.2.4.3 Fe-Ga Alloys……. 26
2.2.4.4 Fe-W Alloys…….. 30
2.3 Extended X-ray Absorption Fine Structure (EXAFS) ……... 33
2.3.1 Introduction of EXAFS……. 33
2.3.2 EXAFS History……. 33

2.3.3 Synchrotron Radiation for EXAFS……... 35
2.3.4 Basic Physics of EXAFS…….. 36
2.3.5 EXAFS Equation…….. 37
2.3.6 Previous EXAFS Studies on Fe-Ga Alloys…….. 40

3. OBJECTIVES AND METHOLOGY……... 42

4. EXPERIMENTAL WORK…….. 45

4.1 Magnetic and Magnetostriction Study of Single Crystals…….. 45
4.1.1 Alloy Preparation and Vacuum Arc Melting…… 45
4.1.2 Directional Casting……... 46
4.1.3 Directional Growth……... 46
4.1.4 Single Crystal Orientation and Preparation…….. 48
4.1.5 Magnetostriction Measurement……..... 50
4.1.6 Heat Treatment……. 51
4.1.7 Magnetization Measurement……. 51
4.2 Extended X-ray Absorption Fine Structure Study of Fe-based Alloys... 53
4.2.1 Beamline Setup and Data Collection…… 53
4.2.2 Data Processing……..... 55
4.2.3 Data Analysis…… 56

5. RESULTS AND DISCUSSION……... 59

5.1 Magnetostriction and Magnetization Studies of Fe-Ga-W Alloys……. 59
5.1.1 XRD Analysis of Single Crystals……. 59
5.1.2 Magnetostriction Measurement of $(3/2)\lambda_{100}$ Coefficient…….. 63
5.1.3 Magnetostriction Measurement of $(3/2)\lambda_{111}$ Coefficient…….. 74
5.1.4 Saturation Magnetization Measurement……... 76
5.1.5 TEM Study of Fe-Ga-W Alloy……. 81
5.2 Magnetostriction Study of Fe-W alloys…….. 85
5.2.1 XRD Analysis and Single Crystal Characterization……. 85
5.2.2 Magnetostriction Measurement of $(3/2)\lambda_{111}$ Coefficient…….. 89
5.3 X-ray Diffraction Studies of Ordering in Quenched Single Crystal of Fe-27.5 at.%Ga……... 102
5.3.1 Theta-2 Theta Scans of (100) Face……... 104
5.3.2 Theta-2Theta Scans of (111) Face…… 107
5.4 EXAFS Studies of Local Atomic Environment of Fe-x at.% Ga Single Crystals……... 113
5.4.1 Sample Condition ……..…….. 113
5.4.2 EXAFS Data Processing and Analysis……. 113
5.4.2.1 Data Processing Using Athena® Software……... 115
5.4.2.2 Data Modeling Using Artemis® Software……... 121
5.4.3 Results of Fe-Ga Alloy First Nearest Neighbor Analysis …… 127
5.4.3.1 Artemis Results of Fe-27.5 at.% Ga Single Crystals… 127
5.4.3.2 Artemis Results of Fe-20 at.% Ga Single Crystals…... 138
5.4.3.3 Artemis Results of Fe-15 at.% Ga Single Crystals…... 141

5.4.3.4 Data Analysis of the First Nearest Neighbor Atomic Environment for Fe-Ga Alloy System…….. 146
5.4.4 Results of Fe-Ga Alloy Second Nearest Neighbor Analysis ... 151
5.4.4.1 Artemis Results of Fe-27.5 at.% Ga Single Crystal….. 151
5.4.4.2 Artemis Results of Fe-20 at.% Ga Single Crystal……. 163
5.4.4.3 Artemis Results of Fe-15 at.% Ga Single Crystal……. 171
5.4.4.4 Data Analysis of Second Nearest Neighbor Atomic environment for Fe-Ga Alloy System……... 178

6. CONCLUSION……. 180

APPENDICES

A. X-RAY DIFFRACTION PATTERNS OF IRON-BASED ALLOYS…….. 182

B. HYSTERESIS CURVES OF IRON-GALLIUM-TUNGSTEN…… 198

REFERENCES……... 201

LIST OF TABLES

Table		Page
2.1	Equilibrium phases and related crystal structures of iron-gallium alloy……..	29
2.2	Equilibrium phases and related crystal structures of iron-tungsten alloy……..	32
5.1	Magnetostriction coefficient $(3/2)\lambda_{100}$ values for [001]-oriented Fe-Ga-W alloy single crystals in the as-grown condition……..	68
5.2	Magnetostriction coefficient $(3/2)\lambda_{100}$ values obtained for [001]-oriented Fe-Ga-W alloy single crystals in the annealed condition…...	72
5.3	Magnetization values obtained for various Fe- at.% Ga- 2.5 at.% W alloys…….	79
5.4	List of disc shaped Fe-X at.% W single crystals and their corresponding orientation…….	90
5.5	Magnetostriction coefficient $(3/2)\lambda_{111}$ values obtained for [220] or [211]-oriented Fe-W alloy single crystals at as-grown condition…….	96
5.6	Heat treatment conditions for Fe-X at.% W single alloy crystals…….	97
5.7	Magnetostriction coefficient $(3/2)\lambda_{111}$ values obtained for [220] or [211]-oriented Fe-W alloy single crystals in the annealed condition...	101
5.8	Sample compositions and thermal histories for all of the single crystals used for EXAFS measurements……...	114
5.9	Lattice position, coordination number and distance from core atom of 1^{st} to 6^{th} nearest neighbors in a typical BCC crystal structure……..	122
5.10	First nearest neighbor analysis results of Fe-27.5 at.% Ga single crystal as-grown (DG) sample Fe K-edge and Ga K-edge scan……....	132

5.11 First nearest neighbor analysis results of Fe-27.5 at.% Ga single crystal long-term annealed (LTA) sample Fe K-edge and Ga K-edge scan……... 134

5.12 First nearest neighbor analysis results of Fe-27.5 at.% Ga single crystal ordering (ORD) sample Fe K-edge and Ga K-edge scan…….. 137

5.13 First nearest neighbor analysis results of Fe-20 at.% Ga single crystal as-grown (DG) sample Fe K-edge and Ga K-edge scan……... 140

5.14 First nearest neighbor analysis results of Fe-20 at.% Ga single crystal long-term annealed (LTA) sample Fe K-edge and Ga K-edge scan……... 143

5.15 First nearest neighbor analysis results of Fe-15 at.% Ga single crystal as-grown (DG) sample Fe K-edge and Ga K-edge scan……... 146

5.16 First nearest neighbor analysis results of Fe-15 at.% Ga single crystal long-term annealed (LTA) sample Fe K-edge and Ga K-edge scan……... 148

5.17 Change of lattice strain of Ga-Ga first nearest neighbor bond and λ_{100} magnetostriction coefficient value before and after long time annealing of Fe-Ga single crystals…… 150

5.18 Results of Fe-27.5 at.% Ga as-grown (DG) single crystal second nearest neighbor analysis…….. 153

5.19 Results of Fe-27.5 at.% Ga long-term annealed (LTA) single crystal second nearest neighbor analysis…….. 157

5.20 Results of Fe-27.5 at.% Ga ordered (ORD) single crystal second nearest neighbor analysis…….. 161

5.21 Results of Fe-20 at.% Ga as-grown (DG) single crystal second nearest neighbor analysis…….. 165

5.22 Results of Fe-20 at.% Ga long-term annealed (LTA) single crystal second nearest neighbor analysis…….. 169

5.23 Results of Fe-15 at.% Ga as-grown (DG) single crystal second nearest neighbor analysis……. 173

5.24 Results of Fe-15 at.% Ga long-term annealed (LTA) single crystal second nearest neighbor analysis…….. 176

LIST OF FIGURES

Figure		Page
2.1	Schematic illustrations of magnetization curves and hysteresis loops. (a) Magnetization versus applied magnetic field curve. (b) Induction versus applied magnetic field curve …….	10
2.2	A Schematic illustration of domains in a ferromagnetic material and magnetization process with an applied magnetic field…….	15
2.3	A Schematic of the volume magnetostriction and Joule magnetostriction……	19
2.4	Mechanism of Magnetostriction (Adapted from Reference [1])……..	23
2.5	Phase diagram of binary iron-gallium alloy…….	28
2.6	Phase diagram of binary iron-tungsten alloy (Adapted from Reference [47])…….	31
2.7	Typical x-ray absorption spectrum for the K-edge of Fe-Ga alloy…..	34
2.8	A Schematic of the interaction between local atoms and photoelectron waves…….	38
4.1	A Schematic of the directional casting experimental setup……..	47
4.2	A Schematic of directional growth experimental setup……	49
4.3	A Schematic of experimental setup for both λ_{100} and λ_{100} magnetostriction measurements……	52
4.4	Beamline setup for fluorescence mode EXAFS measurements……...	54
5.1	Theta- 2 theta x-ray diffraction scan on the first cut face of DG rod of the Fe-12.5 at.% Ga-2.5 at.% W single crystal……	60
5.2	Theta- 2 theta x-ray diffraction scan on the (200) face of the [001]-oriented Fe-12.5 at.% Ga-2.5 at.% W single crystal…….	61

5.3 Rocking curve x-ray diffraction scan on the (200) face of the [001]-oriented Fe-12.5 at.% Ga-2.5 at.% W single crystal……. 62

5.4 Magnetostrictive strain value versus applied magnetic field curves for the [001]-oriented Fe-12.5 at.% Ga-2.5 at.% W single crystal in the as-grown condition, with applied magnetic field (a) parallel and (b) perpendicular to the [001] direction……...……. 64

5.5 Magnetostrictive strain value versus applied magnetic field curves for the [001]-oriented Fe-15 at.% Ga-2.5 at.% W single crystal in the as-grown condition, with applied magnetic field (a) parallel and (b) perpendicular to the [001] direction……..…… 65

5.6 Magnetostrictive strain value versus applied magnetic field curves for the [001]-oriented Fe-17.5 at.% Ga-2.5 at.% W single crystal in the as-grown condition, with applied magnetic field (a) parallel and (b) perpendicular to the [001] direction……...……. 66

5.7 Magnetostrictive strain value versus applied magnetic field curves for the [001]-oriented Fe-12.5 at.% Ga-2.5 at.% W single crystal in the annealed condition, with applied magnetic field (a) parallel and (b) perpendicular to the [001] direction……...……. 69

5.8 Magnetostrictive strain value versus applied magnetic field curves for the [001]-oriented Fe-15 at.% Ga-2.5 at.% W single crystal in the annealed condition, with applied magnetic field (a) parallel and (b) perpendicular to the [001] direction……..…… 70

5.9 Magnetostrictive strain value versus applied magnetic field curves for the [001]-oriented Fe-17.5 at.% Ga-2.5 at.% W single crystal in the annealed condition, with applied magnetic field (a) parallel and (b) perpendicular to the [001] direction……...……. 71

5.10 Magnetostriction coefficients $(3/2)\lambda_{100}$ value vs. solute content in Fe plots of Fe-x at.% Ga-2.5 at.% W and Fe-x at.% Ga alloy single crystals…….. 73

5.11 Magnetostrictive strain value versus applied magnetic field curves obtained for the [220]-oriented Fe-12.5 at.% Ga-2.5 at.% W single crystal at as-grown condition, with applied magnetic field (a) parallel and (b) perpendicular to the [111] direction……. 75

5.12 Magnetostrictive strain value versus applied magnetic field curves obtained for the [220]-oriented Fe-12.5 at.% Ga-2.5 at.% W single crystal at annealed condition, with applied magnetic field (a) parallel and (b) perpendicular to the [111] direction…… 77

5.13 Hysteresis curve of Fe-12.5 at.% Ga-2.5 at.% W alloy as directional cast sample…… 78

5.14 Magnetization value versus solute content for various Fe-x at.% Ga-2.5 at.% W alloys…….. 80

5.15 Bright-field TEM image of annealed Fe-17.5 at.% Ga-2.5 at.% W alloy single crystal. …….. 82

5.16 Diffraction pattern of annealed Fe-17.5 at.% Ga-2.5 at.% W alloy single crystal corresponding to the image shown in Figure 5.17…….. 83

5.17 Lorentz image of annealed Fe-17.5 at.% Ga-2.5 at.% W alloy single crystal on the [001]-oriented face……. 84

5.18 Theta- 2 theta x-ray diffraction scan on the first cut face of DG rod of the Fe-3 at.% W single crystal…….. 86

5.19 Theta- 2 theta x-ray diffraction scan on the (220) face of the [220]-oriented Fe-3 at.% W single crystal…….. 87

5.20 Rocking curve x-ray diffraction scan on the (220) face of the [220]-oriented Fe-3 at.% W single crystal…….. 88

5.21 Magnetostrictive strain value versus applied magnetic field curves obtained for the [220]-oriented Fe-3 at.% W single crystal at as-grown condition, with applied magnetic field (a) parallel and (b) perpendicular to the [111] direction…….. 91

5.22 Magnetostrictive strain value versus applied magnetic field curves obtained for the [211]-oriented Fe-6 at.% W single crystal at annealed condition, with applied magnetic field (a) parallel and (b) perpendicular to the [111] direction……..…… 93

5.23 Magnetostrictive strain value versus applied magnetic field curves obtained for the [220]-oriented Fe-7.5 at.% W single crystal at annealed condition, with applied magnetic field (a) parallel and (b) perpendicular to the [111] direction……..…… 94

5.24 Magnetostrictive strain value versus applied magnetic field curves obtained for the [220]-oriented Fe-3 at.% W single crystal at annealed condition, with applied magnetic field (a) parallel and (b) perpendicular to the [111] direction……..…… 98

5.25 Magnetostrictive strain value versus applied magnetic field curves obtained for the [211]-oriented Fe-6 at.% W single crystal at annealed condition, with applied magnetic field (a) parallel and (b) perpendicular to the [111] direction..…… 99

5.26 Magnetostrictive strain value versus applied magnetic field curves obtained for the [220]-oriented Fe-7.56 at.% W single crystal at annealed condition, with applied magnetic field (a) parallel and (b) perpendicular to the [111] direction……..…… 100

5.27 Magnetostriction coefficient values versus atomic W content of Fe-W alloy single crystals (Blue line: $(3/2)\lambda_{100}$ magnetostriction coefficient values. Green line: $(3/2)\lambda_{111}$ magnetostriction coefficient values.)…….. 103

5.28 Theta-2 theta XRD pattern from the (100) face of a [001]-oriented Fe-27.5 at.% Ga single crystal. ……..... 105

5.29 Theta-2 theta XRD pattern from the (100) face of a [001]-oriented Fe-27.5 at.% Ga single crystal ……. 106

5.30 Theta- 2 Theta x-ray diffraction scan pattern obtained from the (111) sample face of the [111]-oriented Fe-27.5 at.% Ga single crystal after polishing off to a depth of 3μm from the surface…….. 108

5.31 Theta- 2 Theta x-ray diffraction scan pattern over a 2 Theta range of 25°-28° obtained from the (111) sample face of the [111]-oriented Fe-27.5 at.% Ga single crystal after removal of material by polishing to various depths from the surface…… 111

5.32 XRD (110) scan patterns of (222) peak with various depths from the (111) surface of the [111]-oriented Fe-27.5 at.% Ga single crystal in 2 Theta range of 53°-57°……... 112

5.33 X-ray absorption spectra obtained from EXAFS measurement before and after normalize……... 116

5.34 Example of same EXAFS spectra in E, k, R and q- space……... 118

5.35 Example of EXAFS spectra for the same sample before and after merge…… 119

5.36 Example of EXAFS spectra before and after self absorption……... 120

5.37 (a) Example of single scattering path of photoelectron in BCC structure. (b) Example of multiple scattering path of photoelectron in BCC structure……... 125

5.38 Plots of χ for Fe K-edge and Ga K-edge scans of Fe-27.5 at.% Ga as-grown (DG) single crystal first nearest neighbor analysis in R space. (Blue: Experimental Data; Red: Fit Data)……..... 128

5.39 Plots of χ for Fe K-edge and Ga K-edge scans of Fe-27.5 at.% Ga as-grown (DG) single crystal first nearest neighbor analysis in k space. (Blue: Experimental Data; Red: Fit Data)…… 129

5.40 Plots of χ for Fe K-edge and Ga K-edge scans of Fe-27.5 at.% Ga as-grown (DG) single crystal first nearest neighbor analysis in q space. (Blue: Experimental Data; Red: Fit Data)…… 130

5.41 Plots of χ for Fe K-edge and Ga K-edge scans of Fe-27.5 at.% Ga long-term annealed (LTA) single crystal first nearest neighbor analysis in R space. (Blue: Experimental Data; Red: Fit Data)…….... 133

5.42 Plots of χ for Fe K-edge and Ga K-edge scans of Fe-27.5 at.% Ga ordering (ORD) single crystal first nearest neighbor analysis in R space. (Blue: Experimental Data; Red: Fit Data)……. 136

5.43 Plots of χ for Fe K-edge and Ga K-edge scans of Fe-20 at.% Ga as-grown (DG) single crystal first nearest neighbor analysis in R space. (Blue: Experimental Data; Red: Fit Data)…… 139

5.44 Plots of χ for Fe K-edge and Ga K-edge scans of Fe-20 at.% Ga long-term annealed (LTA) single crystal first nearest neighbor analysis in R space. (Blue: Experimental Data; Red: Fit Data)…… 142

5.45 Plots of χ for Fe K-edge and Ga K-edge scans of Fe-15 at.% Ga as-grown (DG) single crystal first nearest neighbor analysis in R space. (Blue: Experimental Data; Red: Fit Data)……. …….. 145

5.46 Plots of χ for Fe K-edge and Ga K-edge scans of Fe-15 at.% Ga long-term annealed (LTA) single crystal first nearest neighbor analysis in R space. (Blue: Experimental Data; Red: Fit Data)…… 147

5.47 Plots of χ for Fe K-edge and Ga K-edge scans of Fe-27.5 at.% Ga as-grown (DG) single crystal second nearest neighbor analysis result in R space. (Blue: Experimental Data; Red: Fit Data)…….. 152

5.48 Plots of χ for Fe K-edge and Ga K-edge scans of Fe-27.5 at.% Ga long-term annealed (LTA) single crystal second nearest neighbor analysis result in R space. (Blue: Experimental Data; Red: Fit Data)…….. 156

5.49 Plots of χ for Fe K-edge and Ga K-edge scans of Fe-27.5 at.% Ga ordered (ORD) single crystal second nearest neighbor analysis result in R space. (Blue: Experimental Data; Red: Fit Data)…….. 160

5.50 Plots of χ for Fe K-edge and Ga K-edge scans of Fe-20 at.% Ga as-grown (DG) single crystal second nearest neighbor analysis result in R space. (Blue: Experimental Data; Red: Fit Data)…….. 164

5.51 Plots of χ for Fe K-edge and Ga K-edge scans of Fe-20 at.% Ga long-term annealed (LTA) single crystal second nearest neighbor analysis result in R space. (Blue: Experimental Data; Red: Fit Data)…….. 168

5.52 Plots of χ for Fe K-edge and Ga K-edge scans of Fe-15 at.% Ga as-grown (DG) single crystal second nearest neighbor analysis result in R space. (Blue: Experimental Data; Red: Fit Data)…….. 172

5.53 Plots of χ for Fe K-edge and Ga K-edge scans of Fe-15 at.% Ga long-term annealed (LTA) single crystal second nearest neighbor analysis result in R space. (Blue: Experimental Data; Red: Fit Data)…….. 175

A.1 Theta- 2 theta x-ray diffraction scan on the first cut face of DG rod of the Fe-15 at.% Ga-2.5 at.% W single crystal……... 183

A.2 Theta- 2 theta x-ray diffraction scan on the (200) face of the [001]-oriented Fe-15 at.% Ga-2.5 at.% W single crystal…… 184

A.3 Rocking curve x-ray diffraction scan on the (200) face of the [001]-oriented Fe-15 at.% Ga-2.5 at.% W single crystal…… 185

A.4 Theta- 2 theta x-ray diffraction scan on the first cut face of DG rod of the Fe-17.5 at.% Ga-2.5 at.% W single crystal…… 186

A.5 Theta- 2 theta x-ray diffraction scan on the (200) face of the [001]-oriented Fe-17.5 at.% Ga-2.5 at.% W single crystal……. 187

A.6 Rocking curve x-ray diffraction scan on the (200) face of the [001]-oriented Fe-15 at.% Ga-2.5 at.% W single crystal…… 188

A.7 Theta- 2 theta x-ray diffraction scan on the first cut face of DG rod of the Fe-12.5 at.% Ga-2.5 at.% W single crystal…… 189

A.8 Theta- 2 theta x-ray diffraction scan on the (220) face of the [220]-oriented Fe-12.5 at.% Ga-2.5 at.% W single crystal……. 190

A.9 Rocking curve x-ray diffraction scan on the (220) face of the [220]-oriented Fe-12.5 at.% Ga-2.5 at.% W single crystal……. 191

A.10 Theta- 2 theta x-ray diffraction scan on the first cut face of DG rod of the Fe-6 at.% W single crystal…….. 192

A.11 Theta- 2 theta x-ray diffraction scan on the (211) face of the [211]-oriented Fe-6 at.% W single crystal…….. 193

A.12 Rocking curve x-ray diffraction scan on the (211) face of the [211]-oriented Fe-6 at.% W single crystal…….. 194

A.13 Theta- 2 theta x-ray diffraction scan on the first cut face of DG rod of the Fe-7.5 at.% W single crystal……... 195

A.14 Theta- 2 theta x-ray diffraction scan on the (220) face of the [220]-oriented Fe-7.5 at.% W single crystal……... 196

A.15 Rocking curve x-ray diffraction scan on the (220) face of the [220]-oriented Fe-7.5 at.% W single crystal……... 197

B.1 Hysteresis curve of Fe-15 at.% Ga-2.5 at.% W alloy as directional cast sample…… 199

B.2 Hysteresis curve of Fe-17.5 at.% Ga-2.5 at.% W alloy as directional cast sample…… 200

ACKNOWLEDGEMENTS

I would like to express my sincere thanks to my advisor, Professor Sivaraman Guruswamy, for his guidance and financial support throughout my PhD life. I thank him for providing me the opportunity to work as a graduate research assistant in his group and explore this exciting metallurgical engineering field. Because of his expertise, I could deepen my understanding of magnetostriction and finish my dissertation work. My grateful thanks to my supervisory committee, Professor Zhigang Zak Fang, Professor Michael L. Free, Professor Michael S. Moats and Professor Andrey Rogachev, for their time and suggestions.

I would like to thank my colleagues, Dr. Gavin J. Garside, Biswadeep Saha and Meenakshisundaram Ramanathan, for their help and assistance. I also would like to thank Mrs. Karen Haynes, Mrs. Kay Argyle and Mrs. Evelyn Wells for their cooperation.

Support of this work by the National Science Foundation through the award DMR-0854166 and the Advanced Photon Source, Argonne National Laboratory is gratefully acknowledged. The use of the Advanced Photon Source was supported by the U. S. Department of Energy, Office of Science, Office of Basic Energy Sciences, under Contract No. DE-AC02-06CH11357. Critical help of Dr. Daniel Haskel and beamline scientists, Dr. Trudy Bolin and Dr. Nadia Leyarovska, at Argonne National Laboratory in the Extended X-ray Absorption Fine Structure experiment and analysis are gratefully acknowledged. Transmission Electron Microscopy study was done in the Electron

Microscopy Center at Argonne National Laboratory operated by the University of Chicago under U.S. Department of Energy Contract No. DEAC02_06CH17357.

Finally, my deepest gratitude to my parents, Professor Limin Chai and Mrs. Caiping Ren, for their love and encouragement throughout my life. I realize that their accomplishment of bringing me up from an idiotic kid was much more difficult than what I have done for my PhD.

CHAPTER 1

INTRODUCTION

Magnetostrictive behavior refers to the exhibition of reversible strains and changes in the elastic properties of a material on the application of magnetic field, or the reciprocal effect of changes in the magnetic properties with the application of stress [1]. The materials with this kind of behavior are called magnetostrictive materials. There are two parts of magnetostriction, the isotropic part and the anisotropic part. The anisotropic part, which is also called Joule magnetostriction, is a behavior where change in linear dimension occurs on the application of magnetic field. This Joule magnetostriction was discovered by an English physicist, James Prescott Joule, who observed an increase in the length of an iron rod on applying magnetic field.

Generally, all of the magnetic materials have some level of magnetostrictive response. The first material with giant magnetostrictive strains was discovered in the 1960s. It was a (Dy, Tb) rare-earth alloy which shows about 10,000 x 10^{-6} magnetostrictive strain in the basal planes at cryogenic temperature of -123˚C [2]. But this alloy has not been widely used because of the requirement of a large saturation field and low working temperature. Further research in rare-earth-based alloys resulted in the discovery of $Tb_{0.27}Dy_{0.73}Fe_2$ (Tefenol-D) alloy with 1600 to 2400 x 10^{-6} room temperature magnetostrictive strain at an applied magnetic field of less than 2 kOe [3]. However, the high cost of rare-earth elements, relatively large saturation field and poor

mechanical properties limited this alloy's application. Fe-based alloys without rare-earth additions were considered as good candidates in the development of magnetostrictive materials with low cost and good mechanical properties. Fe-Al alloys showed an appreciable magnetostrictive strain as high as 140 x 10^{-6} in the [001] direction at a solute content of about 15 at.% to 20 at.% combined with other advantages like low saturation field, good mechanical strength and large ductility [4-7].

The large increase in the Joule magnetostriction value due to the addition of Ga to Fe was observed in the late 1990s by Guruswamy et al. [8-10]. This new type of alloy provided a λ_{100} magnetostriction coefficient value as high as 379 x 10^{-6} in Fe-20 at.% Ga single crystal which is several times larger than other Fe-based alloys [11]. The ductile α-Fe phase provides a large strength as well as good ductility. Compared to the expensive rare-earth elements Tb and Dy, the relatively cheaper Fe and Ga used for this alloy decrease the cost. Less difficulty in material production expands the application areas of Fe-Ga alloys. Extensive research has been carried out on Fe-Ga alloys in the last ten years, including the following: the study about effect of Ga composition on the magnetostrictive behavior of Fe-Ga alloy polycrystalline and single crystal samples [8-14]; the study about the effect of ordering on the magnetostrictive behavior of Fe-Ga alloys [10,11,15]; and the study about the substitution of Ga with other elements on the magnetostrictive behavior of Fe-Ga alloys [16]. The recent research by Thuanboon and Garside et al. showed that additions of W or Mo to Fe also result in a large enhancement of magnetostriction [11,17,18].

In Fe-Ga alloys, Ga atoms have relatively larger atomic size compared to the Fe atoms. It can be expected that by substituting Fe with Ga, large local distortion and strain

will be introduced into the α-Fe lattice matrix. Heat treatment will change the phase and type of ordering in Fe-Ga alloys and this affects the alloy's magnetostrictive behavior [10,11,15]. It has been suggested that the local atomic environment is a key factor that influences the material's magnetostriction.

Extended x-ray absorption fine structure (EXAFS) spectroscopy is a powerful tool for studying the local structure at atomic and molecular scale [19,20,21]. The earlier research on EXAFS of Fe-27.5 at.% Ga alloy single crystals by Garside [22] shows that the Ga-Ga first nearest neighbor pairs with large bond distance in the Fe-27.5 at.% Ga alloy crystal lattice may affect its magnetostrictive behavior. However, improvements in the analysis are required and analyses on Fe-Ga alloys with various Ga contents are also needed to obtain a better understanding of the local atomic environment of Fe-Ga alloys.

The major objectives of this research work are: (i) to study the changes in magnetostrictive coefficient λ_{100} by W substitution for Ga in various Fe-x at.% Ga alloys (Fe-12.5 at.% Ga-2.5 at.% W, Fe-15 at.% Ga-2.5 at.% W and Fe-17.5 at.% Ga-2.5 at.% W) and various heat treatment conditions (directionally grown and annealed) of Fe-Ga alloy single crystals; (ii) to study the changes in magnetostrictive coefficient λ_{111} with various compositions of W (3 at.%, 6 at.% and 7.5 at.%) and various heat treatment conditions (directionally grown and annealed); (iii) to study the presence of B2 and DO_3 ordered domains in annealed and water quenched Fe-27.5 at.% Ga alloy single crystals and the variation in their distribution as a function of depth from the surface to understand the influence of sample size and thermal history on the nature of short-range and long-range ordering; (iv) to study the local atomic environment of Fe-Ga alloys by using EXAFS analysis with an improved structure model, better data accuracy, extended

modeling range and multiple samples with different alloy composition and thermal histories.

CHAPTER 2

BACKGROUND

2.1 Magnetism

2.1.1 Magnetic Field

All magnets have a pair of unlike poles located at the opposite geometric ends from where the magnetic force appears to originate. Magnets have the behavior that unlike poles attract and like poles repel each other. The attractive or repulsive force between the magnetic poles is called the magnetic force and the force between two poles is described by the following equation:

$$F = k\frac{p_1 p_2}{d^2} \qquad 2.1$$

where F is the magnetic force, k is a proportional constant, p_1 and p_2 are the strengths of poles and d is the distance between the two interacting poles. In the cgs-emu system, the unit of pole strength is defined based on this equation. By assuming k equal to 1, one unit pole exerts a force of 1 dyne to another unit pole at a distance of 1cm. This equation can also be expressed in another form:

$$F = kpH \qquad 2.2$$

where the H is called the field intensity of the magnetic field generated by one of the poles. The unit of field intensity is oersted (Oe) which is defined by the field that exerts a 1 dyne force on a unit pole. The magnetic field can also be represented by “the lines of force” and 1 Oe field is considered to have one line of force per cm^2.

The magnetic field is also produced by an electrical charge motion. In the most general case of a current flow inside a straight wire, a magnetic field will be generated with a magnitude given by

$$H = \frac{2i}{10r} Oe \qquad 2.3$$

where i is the current in amperes and r is the distance from the wire in cm. The magnetic field is circular around the wire in a plane perpendicular to the wire axis and the direction can be determined by the right-hand law. If the wire is not straight but in a solenoid shape, the magnetic field will be generated along the solenoid axis with a magnitude at the midpoint given by

$$H = \frac{4\pi ni}{10L} Oe \qquad 2.4$$

where i is the current, n is the number of turns and L is the length of the solenoid.

If a ferromagnetic material is placed inside the solenoid, the material will become magnetized by the magnetic field H. The degree to which a material gets magnetized is called magnetization M. In this case, the actual magnitude of magnetic field is a combination of magnetic field H generated by flowing current and $4\pi M$ introduced by the ferromagnetic material. These combined lines of force are called the magnetic flux. The

total number of lines of magnetic flux per unit area is called the induction B which is described by the equation

$$B = H + 4\pi M \tag{2.5}$$

The induction B is usually measured by the unit gauss (G) which is lines or maxwells per cm^2.

2.1.2 Magnetic Moment

If a magnet with poles of strength p spaced apart a distance l is placed at angle θ in a uniform field H, a torque will act on the magnet and turn it parallel to the field direction. By assuming the field intensity H = 1 Oe and θ = 90°, the moment can be given by

$$m = pl \tag{2.6}$$

where m is defined as the magnetic moment of the magnet. It is an important parameter in the calculation of the potential energy E_p of a magnet in a magnetic field. The potential energy E_p is given by

$$dE_p = 2(pH\sin\theta)(\frac{l}{2})d\theta = mH\sin\theta d\theta \tag{2.7}$$

$$E_p = \int_{90°}^{\theta} mH\sin\theta d\theta = -mH\sin\theta \tag{2.8}$$

In the cgs system, the potential energy E_p is in ergs and the unit of magnetic moment is erg/oersted, which is an electromagnetic unit of magnetic moment simply called emu.

2.1.3 Magnetization

As discussed earlier, magnetic material will be magnetized if it is placed in a magnetic field. The degree to which the material gets magnetized is called intensity of magnetization or simply magnetization M. The magnetization M can be described by

$$M = \frac{m}{v} \tag{2.9}$$

$$M = \frac{pl}{v} = \frac{p}{A} \tag{2.10}$$

where m is the magnetic moment, v is the volume and A is the cross section of the magnet. In the cgs system, the unit of this magnetization is erg/oersted·cm^3 or simply emu/cm^3. This magnetization can also be defined for a unit mass rather than unit volume, and in this case, it is called a specific magnetization which is given by

$$\sigma = \frac{m}{w} = \frac{M}{\rho} \tag{2.11}$$

where w is the total mass of magnet and ρ is the density of magnetic material.

2.1.4 Magnetization Curve and Hysteresis Loop

A ferromagnetic or ferrimagnetic material's magnetic property is arising from a lot of small magnetic moments. These magnetic moments are introduced by the orbital

motion and spin motion of the electrons in the atoms. The small regions in which all the magnetic moments are aligned in the same direction in a ferromagnetic material are called domains. The interfaces that separate domains with different spontaneous magnetization directions are called domain walls. As discussed earlier, after placing a magnetic material initially in an unmagnetized state in a field, the magnetization process will start inside the material. This magnetization process involves both domain wall motion and domain rotation. If the applied magnetic field is large enough, both of these magnetization processes will drive the magnet to reach its saturation. The curve used to describe the magnetization M or induction B versus applied magnetic field H change during the magnetization process is called the magnetization curve. By applying magnetic field in two opposite directions, the magnetization curve will show a loop shape which is called the hysteresis loop, as shown in Figure 2.1.

In Figure 2.1, the initial magnetization curve is the dashed lines from the origin to saturation in the first quadrant. Magnetization becomes constant after reaching the saturation value and the induction continues to increase with H. M_s is the maximum magnetization that a material can reach and is called saturation magnetization. M_r is the residual magnetization in the absence of applied magnetic field and is called remanence or remanent magnetization. Hc_i is the reverse field required to reach zero magnetization and is called the coercive field. In the induction hysteresis loop, B_s is the saturation induction, B_r is the remanent induction and the H_c is the coercive field for the induction hysteresis loop.

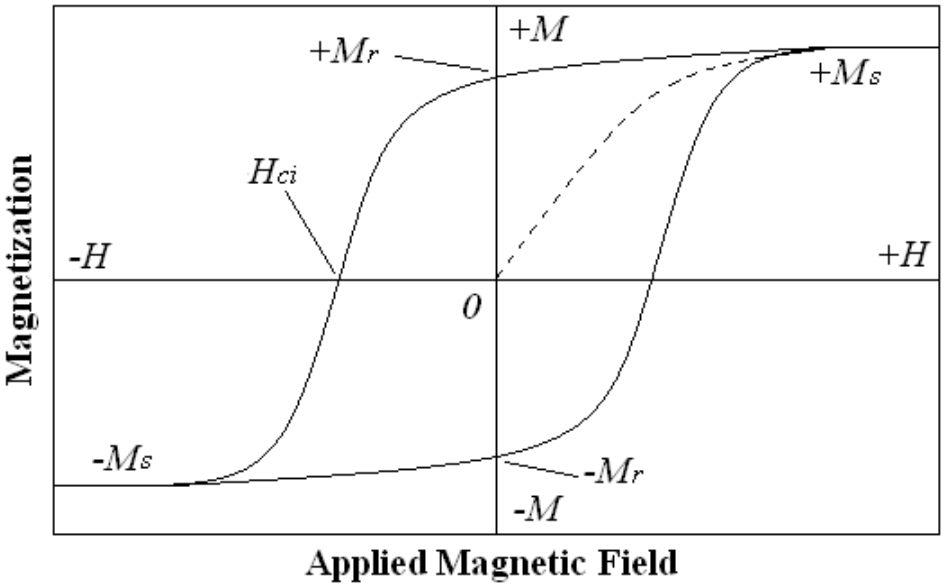

(a)

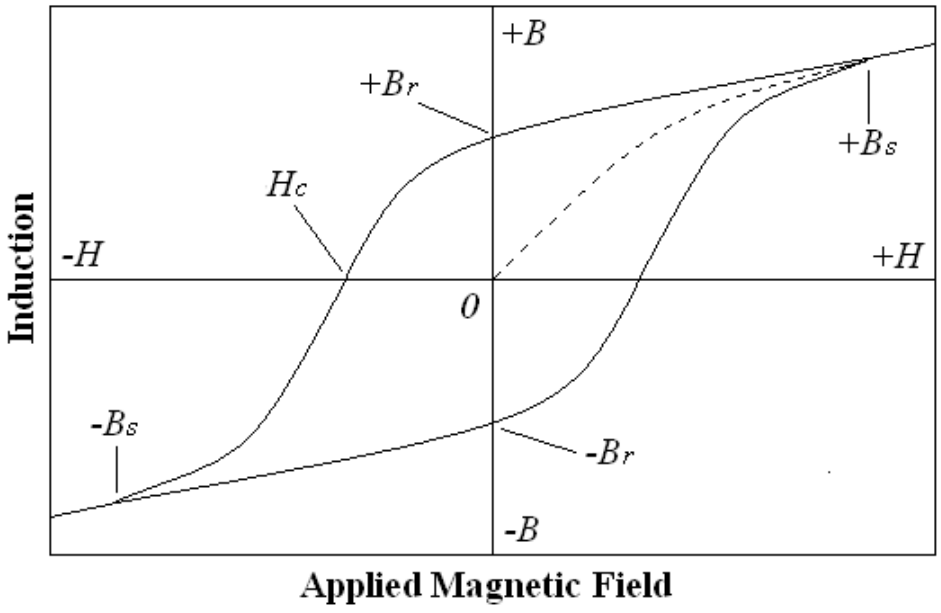

(b)

Figure 2.1 Schematic illustrations of magnetization curves and hysteresis loops. (a) Magnetization versus applied magnetic field curve. (b) Induction versus applied magnetic field curve.

2.1.5 Magnetic Anisotropy in Cubic Crystals

The magnetic properties' dependence on the measurement direction is called magnetic anisotropy. This factor strongly affects the shape of the magnetization curve and hysteresis loop. For iron single crystal with a body centered cubic structure, the saturation magnetization can be achieved with relatively low magnetic field along the <100> crystallographic direction. If the field is applied in the <110> or <111> directions, much larger H values will be required to achieve the saturation magnetization. In this case, the <100> direction is called the easy direction of magnetization.

As discussed earlier, magnetization involves two processes, the domain rotation and domain wall motion. The domain wall motion process requires less energy than the domain rotation and is more preferred at a low magnetic field.

In a demagnetized BCC iron magnet, the natural spontaneous magnetization directions of domains are in the <100> crystallographic directions. The magnetization process to obtain saturation magnetization in the <100> directions will require more domain wall motion and less domain rotation. Compared to the <100> directions, a large amount of domain rotation process will be required to obtain saturation magnetization in the <110> directions. As a result less energy is required for magnetization saturation in the <100> direction than for saturation in the <110> direction.

The energy provided by the magnetic field which is used to work against the anisotropy force to turn the magnetization vector away from the easy direction is called crystal anisotropy energy E [23, 24]. The magnitude of this energy is given by

$$E = K_0 + K_1(\alpha_1^2\alpha_2^2 + \alpha_2^3\alpha_3^2 + \alpha_3^2\alpha_1^2) + K_2(\alpha_1^2\alpha_2^2\alpha_3^2) + \cdots \qquad 2.12$$

where α_1, α_2 and α_3 are the direction cosines of Ms relative to crystal axes and K_0, K_1 and K_2 are the anisotropy constants for a specific material at a specific temperature. For BCC iron, the values of anisotropy energies vary as $E_{100}<E_{110}<E_{111}$.

2.1.6 Origin of Magnetic Properties

As described earlier, the magnetic properties of a material mainly arise from the orbital motion and spin motion of the electrons in the atoms. For the orbital motion, the negatively charged electron rotates around a nucleus and this can be considered as a current loop which introduces a small magnetic moment along the axis of rotation. For the spin motion, each electron is spinning around a certain axis and forms a small spin magnetic moment along either the up or down direction. Thus, if the sum of the orbital motion magnetic moments and spin motion magnetic moments of all the electrons in an atom does not cancel out to zero, the atom will have a net magnetic moment and can be considered as a tiny magnet [1, 25]. Magnetic material is a collection of these tiny magnets. The magnetic moment of a substance is the sum of magnetic moment vectors of all the tiny magnets inside the material. If the cancellation of orbital motion magnetic moments and spin motion magnetic moments are complete in all the atoms, the material is referred to as a diamagnetic material. If the cancellation is incomplete, the material can be paramagnetic, ferromagnetic, antiferromagnetic or ferrimagnetic material.

2.1.7 Magnetic Behaviors

2.1.7.1 Diamagnetism

The origin of diamagnetism is the effect of applied magnetic field on the orbital motion of electrons inside the material. For each electron orbit of an atom, the applied magnetic field will slightly reduce the effective current of the orbit, therefore forming a

magnetic moment in the opposite direction of the applied field [1]. By summing up all the magnetic moments of the orbital electrons in the material, a diamagnetic material will have a small negative magnetic susceptibility on the order of 10^{-5} [26]. Based on the natural interaction between electrons and magnetic field, this diamagnetism is not permanent and will be present in all materials. However, because the magnetic susceptibility of diamagnetism is so small, it is only possible to observe this behavior when all other types of magnetism are totally absent.

2.1.7.2 Paramagnetism

For the atoms or molecules of paramagnetic materials, the spin and orbital moments of electrons do not fully cancel out. Each of these atoms or molecules will have a magnetic moment. In the case of ideal paramagnetic behavior, no mutual interaction occurs between these magnetic moments. Without an external applied magnetic field, all the magnetic moments are oriented randomly and cancel out each other. When a magnetic field is applied, the magnetic field tends to align all the magnetic moments along the field direction while the thermal agitation tends to keep the moments in random directions [1]. The combined effect of magnetic field and thermal agitation causes a partial alignment of the magnetic moments and creates a relatively small but positive susceptibility (about 10^{-5} to 10^{-2}) [26].

2.1.7.3 Ferromagnetism

Ferromagnetic materials exhibit a large net moment for each atom and large net magnetization even in the absence of an external magnetic field. As in paramagnetic material, magnetic moments originating from the spin and orbit moments of the electrons of the atoms or molecules of ferromagnetic materials have not fully cancelled out. Above

Curie temperature because the thermal agitation is so high, the directions of magnetic moments are fully random and ferromagnetic material behaves the same as a paramagnetic material. Below the Curie temperature, ferromagnetic behavior is observed where the positive exchange interactions between net spin magnetic moments manifest as a large internal molecular field which aligns all the moments in a preferred direction. In general, the ferromagnetic material is divided into a lot of small regions in which magnetic moments are aligned in the same direction by the internal molecular field and reach the saturation even without the absence of an externally applied field. Each of these small regions inside the material is called a domain. In the demagnetized state of a ferromagnetic material, directions of magnetization in different domains are arranged in such a way that they cancel out each other. Applied magnetic field leads to domain wall movement or domain rotation which tries to align the magnetizations of all the domains along the field direction and cause a large net magnetization. If the applied field is large enough, all the domains will be aligned in the same direction and the material reaches its saturation magnetization. Figure 2.2 shows a schematic illustration of domains in a ferromagnetic material and the magnetization process with the application of magnetic field. The magnetic susceptibility of ferromagnetic materials can be as high as 10^6. Most well known ferromagnetic materials are Fe, Ni and Co alloys. These also include the $Nd_2Fe_{14}B$ permanent magnets, Fe-Si soft magnetic materials, and the Fe-Ga and Fe-W giant magnetostrictive alloys studied in this work.

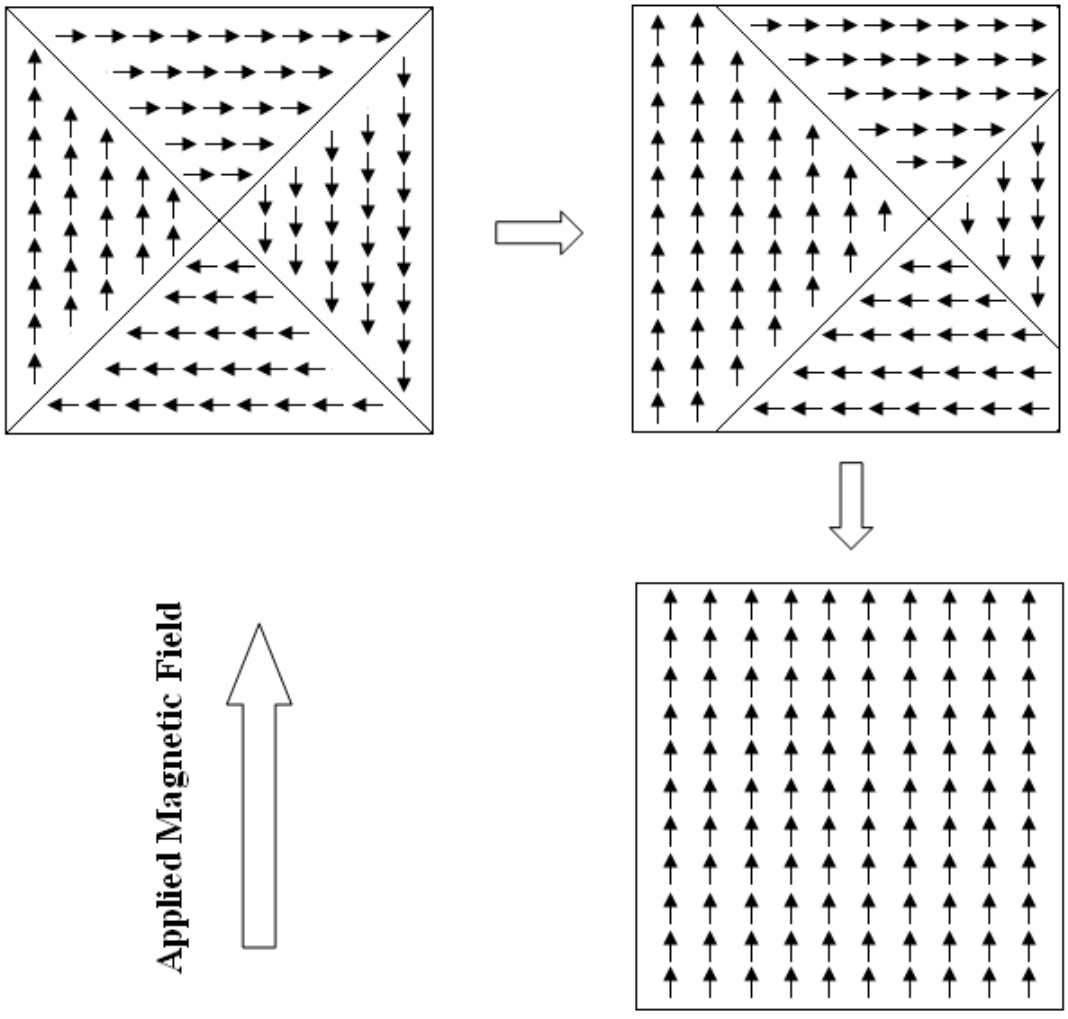

Figure 2.2 A schematic illustration of domains in a ferromagnetic material and magnetization process with an applied magnetic field.

2.1.7.4 Antiferromagnetism

A large internal molecular field also occurs in antiferromagnetic materials. However, compared to ferromagnetic materials, this internal molecular field of antiferromagnetic materials introduces a negative exchange interaction between neighboring atoms or molecules and negative exchange interaction leads to the arrangement of adjacent magnetic moments in an antiparallel alignment [27]. In the antiparallel alignment, all the magnetic moments of atoms or ions are divided into two groups with the same magnetization. Within each group, the magnetic moments are aligned in the same direction just like ferromagnetic materials. However, the two groups of aligned magnetic moments are arranged in the exactly opposite direction. In this way, the magnetizations of two groups of moments cancel out and result in a very small positive susceptibility for the antiferromagnetic material. The susceptibility of antiferromagnetic materials varies with temperature. At high temperature, antiferromagntic material behaves the same as a paramagnetic material. As the temperature decreases, the susceptibility increases and reaches the maximum point at a critical temperature called Néel temperature T_N. Below Néel temperature, the antiparallel alignment of magnetic moments occurs. The most common antiferromagnetic materials are metal oxides, for example, MnO, CuO and NiO.

2.1.7.5 Ferrimagnetism

Ferrimagnetic material has similar magnetic moment arrangement as in antiferromagnetic materials. The magnetic moments were divided into two groups with each group aligned in the antiparallel direction. The difference for ferrimagnetic material is that the two moment groups do not have the same magnetization. This difference

results in a net magnetization in the antiparallel aligned magnetic moments and self-saturated domains inside the material. Ferrimagnetic material also exhibits magnetic saturation and hysteresis and its susceptibility can be as high as some ferromagnetic materials. The most famous ferrimagnetic material is $FeO \cdot Fe_2O_3$ which is one of the most important permanent magnetic materials in magnetic applications.

2.2 Magnetostriction

2.2.1 Volume Magnetostriction and Joule Magnetostriction

The behavior of exhibiting reversible strains with applied magnetic field or reciprocal effect of changes in magnetic properties with application of stress is called magnetostriction. There are two aspects to magnetostriction, the isotropic part and the anisotropic part. The isotropic part shows a change of volume on the application of magnetic field which can be expressed by

$$\varepsilon = \frac{\Delta v}{v} = e_{xx} + e_{yy} + e_{zz} \qquad 2.12$$

where ε is the isotropic magnetostriction strain and e_{xx}, e_{yy}, e_{zz} are the strain tensor components along different directions. This isotropic magnetostriction is also called volume magnetostriction or forced magnetostriction. Its value is only of the order of 10^{-10} per oersted which is very small and generally causes no effect on the material's behaviors.

The anisotropic part of magnetostriction, which is also called Joule magnetostriction, shows a change in linear dimension with an applied magnetic field. The Joule magnetostriction is described by the equation

$$\lambda = \frac{\Delta l}{l} \qquad 2.13$$

In this equation, the fractional change of length $\Delta l/l$ is the magnetically introduced strain defined with a special symbol λ. The value of λ at magnetic saturation is called saturation magnetostriction λ_s which is commonly used to define the material's magnetostrictive behavior. This magnetostriction occurs in all kinds of magnetic materials but the magnitude is typically on the order of 10^{-5} which is relatively small. Figure 2.3 shows a schematic of the volume magnetostriction and Joule magnetostriction.

2.2.2 Saturation Magnetostriction in Cubic Crystals

In the general case, the magnetostriction λ can be expressed in terms of strain tensor components ε_{ij} and directional cosines βi (or βj) of the angle between the directions of relative change of length and crystallographic axes [28]

$$\lambda = \varepsilon_{xx}\beta_1^2 + \varepsilon_{yy}\beta_2^2 + \varepsilon_{zz}\beta_3^2 + \varepsilon_{yz}\beta_2\beta_3 + \varepsilon_{zx}\beta_3\beta_1 + \varepsilon_{xy}\beta_1\beta_2 \qquad 2.14$$

For a cubic single crystal, the achieved saturation magnetostriction strain tensor components from the demagnetized state can be expressed by

$$\varepsilon_{xx} = (h_0 - \frac{1}{3}h_1 - \frac{1}{3}h_4) + h_4\alpha_1^2 + h_4\alpha_1^2 + (h_3 + \frac{2}{3}h_4)(\alpha_1^2\alpha_2^2 + \alpha_2^2\alpha_3^2 + \alpha_3^2\alpha_1^2) + \cdots,$$

$$\varepsilon_{yy} = (h_0 - \frac{1}{3}h_1 - \frac{1}{3}h_4) + h_1\alpha_2^2 + h_4\alpha_2^2 + (h_3 + \frac{2}{3}h_4)(\alpha_1^2\alpha_2^2 + \alpha_2^2\alpha_3^2 + \alpha_3^2\alpha_1^2) + \cdots, \qquad 2.15$$

$$\varepsilon_{zz} = (h_0 - \frac{1}{3}h_1 - \frac{1}{3}h_4) + h_1\alpha_3^2 + h_4\alpha_3^2 + (h_3 + \frac{2}{3}h_4)(\alpha_1^2\alpha_2^2 + \alpha_2^2\alpha_3^2 + \alpha_3^2\alpha_1^2) + \cdots,$$

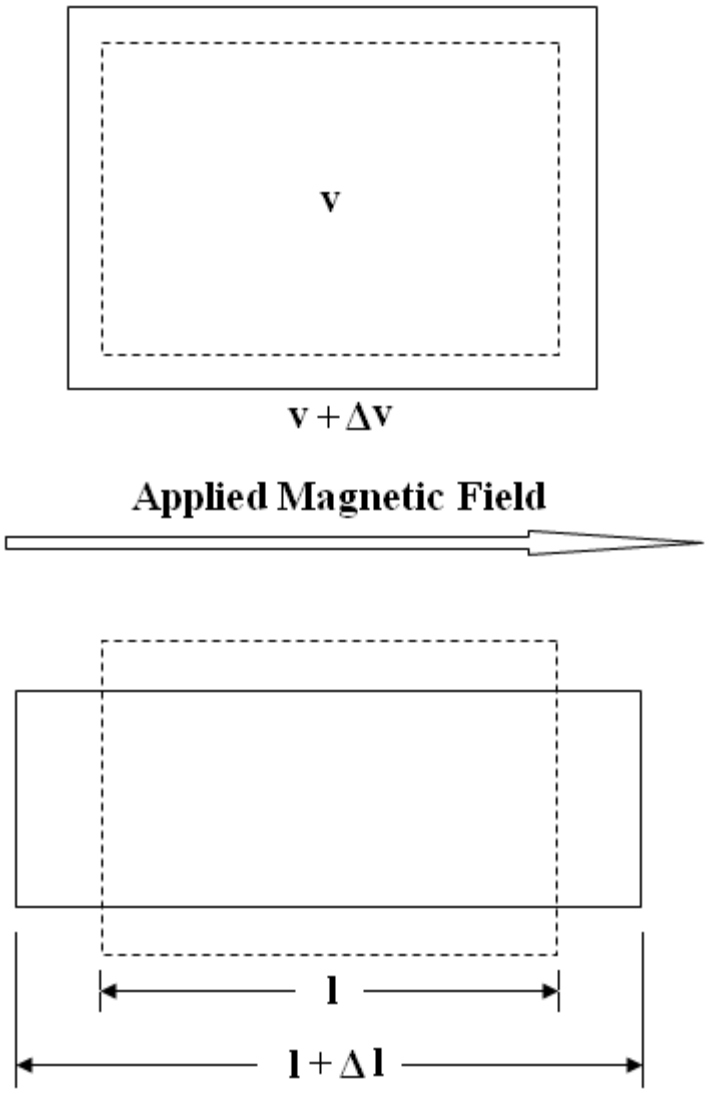

Figure 2.3. A schematic of the volume magnetostriction and Joule magnetostriction

$$\varepsilon_{xy} = 2h_2\alpha_1\alpha_2 + 2h_5\alpha_1\alpha_2\alpha_3^2 + \cdots,$$

$$\varepsilon_{yz} = 2h_2\alpha_2\alpha_3 + 2h_5\alpha_1^2\alpha_2\alpha_3 + \cdots,$$

$$\varepsilon_{zx} = 2h_2\alpha_3\alpha_1 + 2h_5\alpha_1\alpha_2^2\alpha_3 + \cdots$$

where α_i are the direction cosines of the angle between magnetization direction and crystallographic axes, and h_i are the constants related to the material's magnetostrictive behavior. Substituting the strain tensor component equations in the earlier magnetostriction λ equation, the saturation magnetostriction λ_{si} can be expressed by

$$\begin{aligned}\lambda_{si} = {} & h_0 + h_1(\alpha_1^2\beta_2^2 + \alpha_2^2\beta_2^2 + \alpha_3^2\beta_3^2 - \frac{1}{3}) \\ & + 2h_2(\alpha_1\alpha_2\beta_1\beta_2 + \alpha_2\alpha_3\beta_2\beta_3 + \alpha_3\alpha_1\beta_3\beta_1) \\ & + h_3(\alpha_1^2\alpha_2^2 + \alpha_2^2\alpha_3^2 + \alpha_3^2\alpha_1^2) \\ & + h_4[\alpha_1^4\beta_1^2 + \alpha_2^4\beta_2^2 + \alpha_3^4\beta_3^2 + \frac{2}{3}(\alpha_1^2\alpha_2^2 + \alpha_2^2\alpha_3^2 + \alpha_3^2\alpha_1^2) - \frac{1}{3}] \\ & + 2h_5(\alpha_1\alpha_2\alpha_3^2\beta_1\beta_2 + \alpha_1^2\alpha_2\alpha_3\beta_2\beta_3 + \alpha_1\alpha_2^2\alpha_3\beta_1\beta_3) + \cdots\end{aligned} \qquad 2.16$$

One could neglect the h_3, h_4 and h_5 components due to their smaller values from the equation. Constant h_0 refers to anomalous thermal expansion around the Curie temperature and this can also be ignored from the equation. The saturation magnetostriction equation can then be simplified to

$$\lambda_{si} = h_1(\alpha_1^2\beta_1^2 + \alpha_2^2\beta_2^2 + \alpha_3^2\beta_3^2 - \frac{1}{3}) + 2h_2(\alpha_1\alpha_2\beta_1\beta_2 + \alpha_2\alpha_3\beta_2\beta_3 + \alpha_3\alpha_1\beta_3\beta_1) \qquad 2.17$$

$h_1 = \frac{3}{2}\lambda_{100}$ and $h_2 = \frac{3}{2}\lambda_{111}$ where the λ_{100} and λ_{111} are the saturation magnetostriction values of cubic single crystal measured along the <100> and <111> crystallographic directions, respectively. Equation 2.17 becomes

$$\lambda_{si} = \frac{3}{2}\lambda_{100}(\alpha_1^2\beta_1^2 + \alpha_2^2\beta_2^2 + \alpha_3^2\beta_3^4 - \frac{1}{3}) + 3\lambda_{111}(\alpha_1\alpha_2\beta_1\beta_2 + \alpha_2\alpha_3\beta_2\beta_3 + \alpha_3\alpha_1\beta_3\beta_1) \quad 2.18$$

λ_{100} and λ_{111} are also called magnetostriction coefficients of a particular crystal.

For measuring this λ_{si} strain, the ideal demagnetization state is required. However, in the real situation, this requirement can be avoided by measuring the saturation magnetization of λ_{100} and λ_{111} in the referred directions as the crystal is rotated from one orientation to another. For example, the λ_{100} measurements in this work were done by measuring the strain along the [100] direction on an [001]-oriented single crystal by applying magnetic field parallel and perpendicular to the [100] direction. The $\lambda_{parallel}$ and $\lambda_{perpendicular}$ are referred to as the strain measured with parallel applied magnetic field and perpendicular magnetic field, respectively. The λ_{100} value can be calculated based on the equation

$$\frac{3}{2}\lambda_{100} = \lambda_{parallel} - \lambda_{perpendicular} \quad 2.19$$

A similar idea was applied for λ_{111} measurement also. For λ_{111} measurements, the $[1\bar{1}2]$-oriented single crystal disc was prepared and magnetostrictive strain measurements were performed along the $[\bar{1}11]$ direction (a) with magnetic field applied in the $[\bar{1}11]$ direction for $\lambda_{parallel}$ strain measurement and (b) with magnetic field along the [220] direction for $\lambda_{perpendicular}$ strain measurement. Alternatively, a [220]-oriented single crystal disc was prepared and the magnetostrictive strain measurements were performed along the $[\bar{1}11]$ direction (a) with magnetic field applied along the $[\bar{1}11]$ direction for

$\lambda_{parallel}$ strain measurement and (b) with magnetic field along the $[1\bar{1}2]$ direction for $\lambda_{perpendicular}$ strain measurement. The λ_{111} value can be calculated by using the equation

$$\frac{3}{2}\lambda_{111} = \lambda_{parallel} - \lambda_{perpendicular} \qquad 2.20$$

2.2.3 Physical Origin of Magnetostriction

The physical origin of magnetostriction arises from the spin-orbit coupling. After applying an external field, the spins of electrons in an atom will trend to reorient along the field direction, but the orbit is strongly coupled with the lattice which resists the tendency for the rotation of the spin axis. The combined effect of spin and orbit result in a distortion of the electron cloud around the nucleus. Above the Curie temperature, the strong thermal agitation causes complete randomization of the magnetic moments of the atoms and the material behaves as a paramagnetic material. As the temperature drops below T_c, the effect of spontaneous magnetization will rotate the spins towards the easy direction of the crystal, resulting in a change in interatomic distances (Figure 2.4). Therefore, a small strain $\Delta L'/L$ would be introduced into the crystal lattice. If an external magnetic field is applied to the material, all the electron clouds would rotate parallel to the field direction and create a magnetostrictive strain $\Delta L/L$.

2.2.4 Previous Studies on Fe-based Magnetostrictive Alloys

2.2.4.1 Dy, Tb and Terfenol Alloys

Large magnetostriction was observed in single crystals of pure rare-earth elements Dy and Tb in the 1960s [2, 29]. The Dy single crystal has a large basal plane magnetostriction of 8700 x 10^{-6} at an applied magnetic field of 13.5 kOe [29]. The Tb

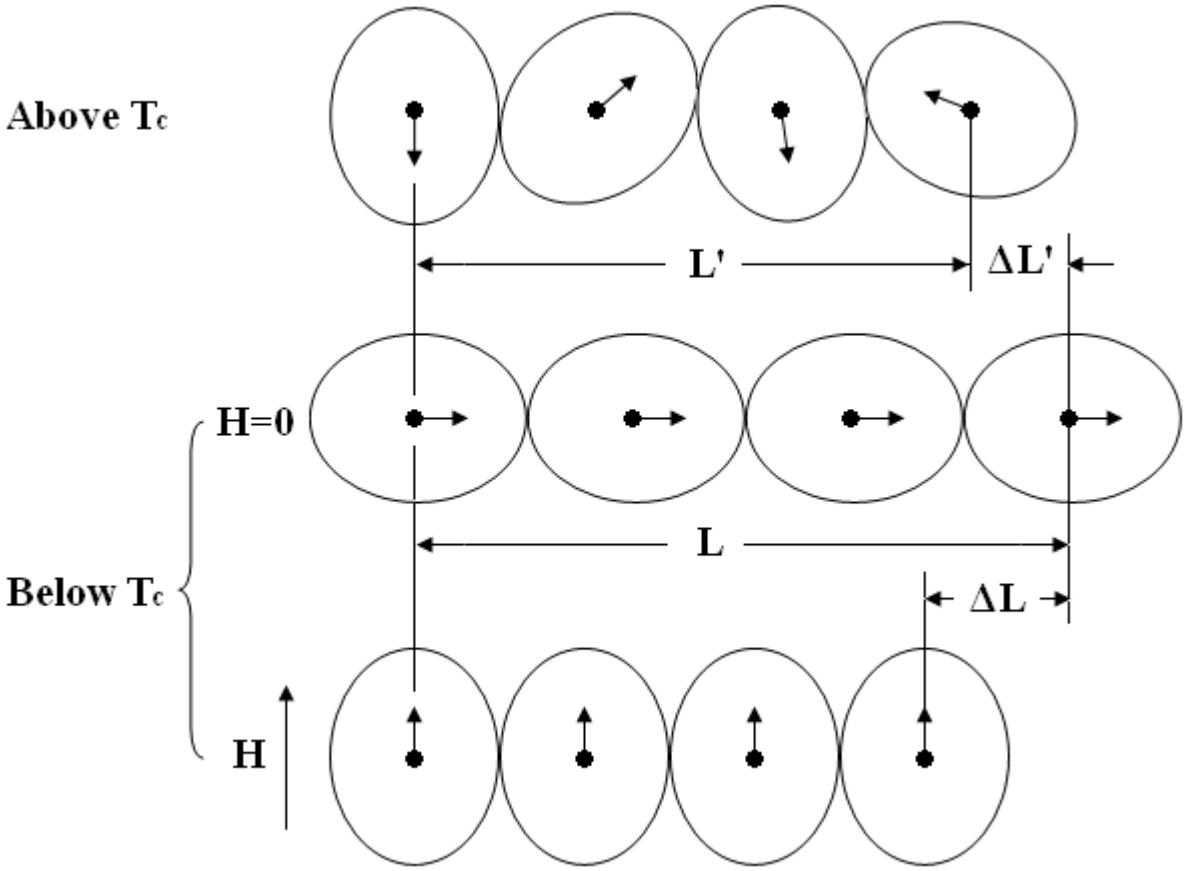

Figure 2.4 Mechanism of magnetostriction (Adapted from Reference [1])

single crystal has a similar basal plane magnetostriction of 8800 x 10^{-6} at an applied field of 16.3 kOe [2]. Although these rare-earth elements exhibit large magnetostriction, there are several disadvantages that limited their applications. First, the applied magnetic field required for obtaining the saturation magnetostriction is relatively high. Second, the Curie temperatures for both Dy and Tb are very low: -184˚C for Dy and -53˚C for Tb [30]. Third, the rare-earth elements Tb and Dy are relatively expensive compared to most of the other elements.

In order to overcome the limitation of low Curie temperature, extensive work has been done on Fe-rare-earth magnetostrictive alloys. Polycrystalline $DyFe_2$ and $TbFe_2$ alloys with magnetostriction of 650 x 10^{-6} and 2630 x 10^{-6} and Curie temperatures of 362˚C and 431˚C, respectively, were developed [31]. For a single crystal $TbFe_2$ alloy, magnetostriction can be as high as 3690 x 10^{-6} along the [111] crystallographic direction at room temperature. However, an extremely large applied magnetic field up to 25kOe is required to obtain the saturation magnetostriction due to the strong magnetization and magnetostrictive anisotropy of this alloy.

Partial substitution of Tb with Dy can decrease the crystal anisotropy and the $Tb_{0.27}Dy_{0.73}Fe_2$ alloy, also called Terfenol-D, was developed based on this idea. At room temperature, the saturation magnetostriction along the [111] crystallographic direction of the Terfenol-D rods grown using the Czochralski crystal growth technique is about 2460 x 10^{-6} and the required applied magnetic field is less than 2 kOe [31]. Although the magnetostrictive behavior of this alloy is very desirable, its brittle mechanical behavior and relatively high cost limited its applications.

2.2.4.2 Fe-Al Alloys

The first magnetostrictive behavior study of Fe-Al alloys was done at the end of the 1950s, and magnetostrictive value along the [001] crystallographic direction as high as 140 x 10^{-6} was obtained for the Al content between 15 at.% and 20 at.% with an applied magnetic field of 10 kOe [4, 5]. The magnetostriction value of Fe-Al is only about 2% of the value for Dy or Tb single crystals which were developed at almost the same time, but good mechanical properties and low cost [6, 7] of Fe-Al alloys make them a valuable candidate for sensor or actuator applications.

From the Fe-Al binary phase diagram [32], one can see that Al dissolves up to about 20 at.% in α-Fe and forms a disordered A2 terminal solid solution phase. As the Al content increases to more than 21 at.%, an ordered Fe_3Al phase with DO_3 crystal structure will form. An XRD study demonstrated that the structure in a high Al content Fe-Al alloy consists of Fe_3Al phase regions completely surrounded by FeAl ordered phase fields [33]. Another study on Fe-14 at.% Al and Fe-23 at.% Al single crystals was done by J. E. Epperson and J. E. Spruiell [34, 35]. The combined presence of B2 and DO_3 phases in an A2 matrix was demonstrated for high Al content Fe-Al alloys with proper heat treatments [34]. The other part of their work shows short-range ordering that tends toward the DO_3 type and the ordered structure is more fully developed in the more concentrated alloy [35]. Later studies in 1979 and 1984 proved that the presence of these second phases decreases the magnetostriction of Fe-Al alloy to about 75 x 10^{-6} along the [001] direction and 45 x 10^{-6} along the [110] direction for Fe-21 at.% Al alloy with an applied magnetic field of about 3 kOe [36, 37].

2.2.4.3 Fe-Ga Alloys

An Fe-Ga alloy with large low field magnetostriction property was first discovered by Guruswamy et al. [8]. Large Joule magnetostriction as high as 379 x 10^{-6} single crystal has been observed for Fe-20 at.% Ga [11]. With their other attractive properties like large mechanical strength, good ductility and relatively low cost, the Fe-Ga alloys are of natural interest in the recent search for giant magnetostrictive materials.

Extensive research has been carried out to study the effect of Ga content and thermal history on the magnetostriction of Fe-Ga alloy. Guruswamy et al. [10,11] showed that the $(3/2)\lambda_{100}$ magnetostriction coefficient of Fe-Ga alloy increased with the increase of Ga content up to 379 x 10^{-6} for Fe-20 at.% Ga and further increase in Ga content drops the magnetostriction to 340 x 10^{-6} for Fe-27.5 at.% Ga due to the formation of a second phase. For all Fe-Ga alloys with various Ga content, long-term annealing heat treatment in the α-phase region trends to cause a large increase in magnetostriction. Similar research was done by Clark et al. [13, 14]. In their result, the $(3/2)\lambda_{100}$ magnetostriction coefficient of furnace cooled alloy was increased to a value of about 300 x 10^{-6} for Fe-17 at.% Ga and then drops to about 250 x 10^{-6} for Fe-24 at.% Ga. For the 800°C annealed and water quenched samples, this $(3/2)\lambda_{100}$ value increased up to 330 x 10^{-6} for Fe-19.5 at.% Ga alloy and further increase in Ga content decreased this property.

It was considered that the effect of thermal history on Fe-Ga alloy's magnetostriction was caused by structural changes. The stable phases that can form on cooling A2 phase alloys from high temperature are B2, DO_3, L12 and DO_{19}, according to Figure 2.5 of the Fe-Ga phase diagram given by Okomoto [38]. While L12 and DO_{19} structures have been obtained by long-term annealing in the corresponding phase stability

region given by the equilibrium phase diagram (Table 2.1), the formation of these phases is kinetically very slow and can be suppressed even under relatively slow cooling rates. In Fe-Ga alloys, rapid quenching extends the single-phase A2 to higher Ga concentrations up to 21.1 at.% [39]. A short-range ordering in the Fe-Ga alloy with Ga content of 13-18 at.% has been suggested without a detailed discussion of the x-ray data [39]. An examination of diffuse scattering peaks in the θ-2θ scan of [100] and [111]-oriented $Fe_{81.6}Ga_{18.4}$ single crystals slow-cooled from the A2 phase region suggests short-range ordering with DO_3 character in $Fe_{81.6}Ga_{18.4}$ alloy [40]. Qing et al. report that slow-cooled alloys with Ga contents in the range of 22.5 to 28 at.% contain a single phase with DO_3 structure [39]. Quenched Fe–25 at.% Ga and Fe–29.9 at.% Ga alloys show a phase mixture of A2, B2 and DO_3 [41]. DO_{19} or $L1_2$ type ordered structure decreases the magnetostriction value to zero or very small negative values [10]. Based on these observations, a detailed analysis of phase formation and local atomic environment is required to extend the understanding of magnetostriction in Fe-Ga alloys.

Study of ternary alloy systems by partial substitutions of Ga with elements Be, Al, Sn, Si and Ge have been done using single crystal or polycrystalline samples [42-44]. Be or Al substitution of Ga in the [100] textured polycrystalline Fe-Ga alloys does not significantly reduce the magnetostriction [42]. Substitution of Ga with Sn, Si and Ge results in a decrease of magnetostriction in the polycrystalline and single crystal Fe-Ga alloys [43-44].

By applying an optimal compressive stress, the saturation magnetostriction can generally reach a maximum value which is larger than the unloaded condition. For the Fe-19 at.% Ga alloy, the saturation magnetostriction increases from 230×10^{-6} in the

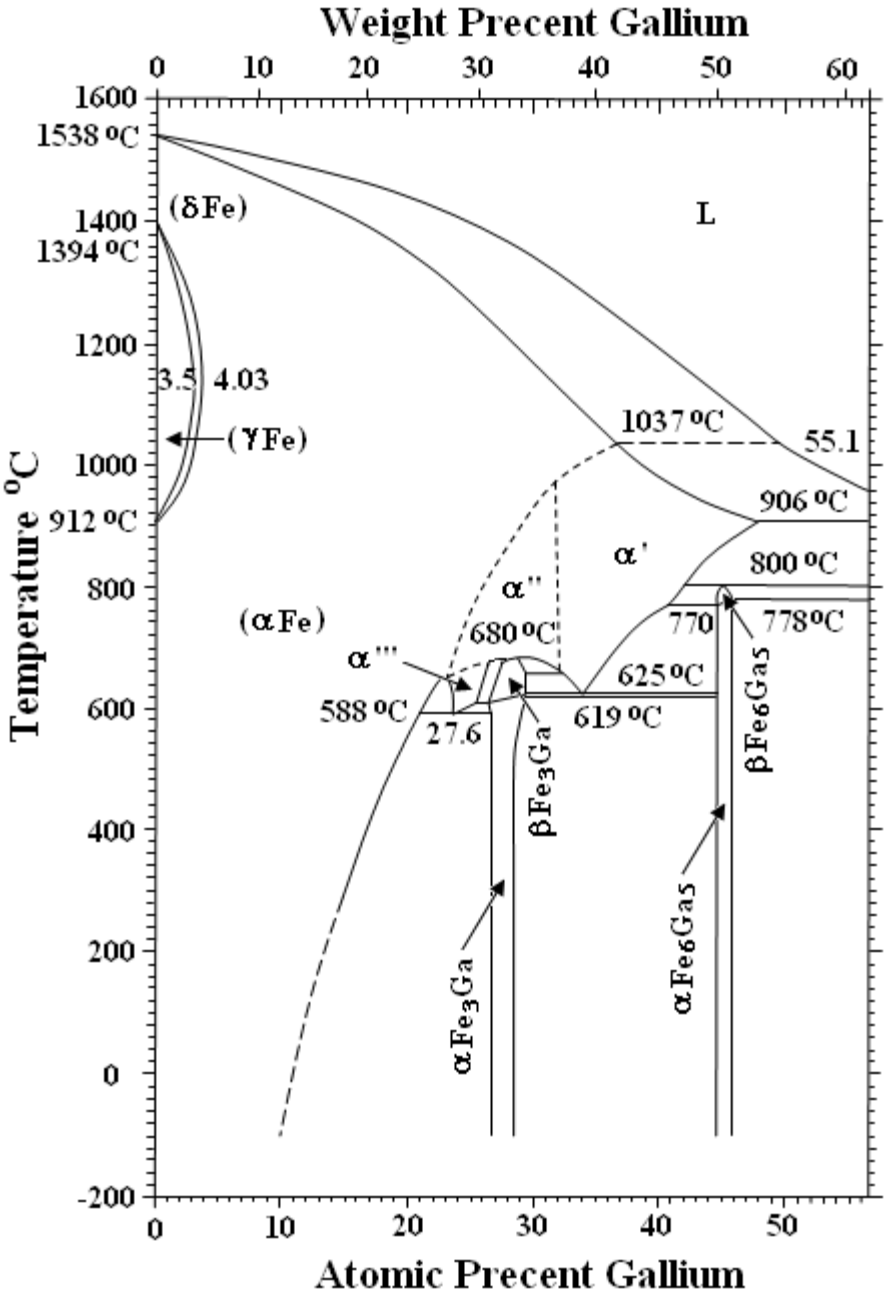

Figure 2.5 Phase diagram of binary iron-gallium alloy [38].

Table 2.1 Equilibrium phases and related crystal structures of iron-gallium alloy [38]

Phase	Composition, wt% Ga	Pearson symbol	Space group
(γFe)	0 to 3.5	*cF4*	$Fm\bar{3}m$
(αFe)	0 to 41	*cI2*	$Im\bar{3}m$
α'	36.5 to 53.0	*cP2*	$Pm\bar{3}m$
α"	26.9 to 37.1	*cF16*	$Fm\bar{3}m$
α"'	26.9 to 30.4	*cF16*	$Fm\bar{3}m$
βFe_3Ga	30.5 to 33.8	*hP8*	$P6_3/mmc$
αFe_3Ga	30.7 to 34.0	*cP4*	$Pm\bar{3}m$
βFe_6Ga_5	50.0 to 51.0	*hR26*	$R\bar{3}m$
αFe_6Ga_5	50.0 to 51.0	*mC44*	*C2/m*

unloaded condition to about 290 x 10^{-6} at 80 MPa [45]. This result is consistent with the general trend. But as the Ga content increases to 24.7 and 29 at.%, the saturation magnetostriction decreases as the applied stress increases [45, 46]. This effect was suggested to be caused by the complex elastic interaction of different phases formed at high alloy compositions but no detailed examination has been done yet.

2.2.4.4 Fe-W Alloys

Compared to Fe-Ga alloys, a very limited amount of work has been done on the Fe-W alloys. Figure 2.6 shows the Fe-W phase diagram and the crystal structures of the stable phases in different conditions are shown in Table 2.2 [47]. Thuanboon et al. prepared single crystal samples of Fe-4.4 at.% W and Fe-10 at.% W to examine the magnetostriction values of these alloys in the as-grown and annealed conditions [11,17,18]. Garside extended this work with the measurements of $(3/2)\lambda_{100}$ magnetostriction coefficients of Fe-3 at.%W, Fe-6 at.%W and Fe-7.5 at.%W single crystals [22]. Their work showed a general trend of increase in magnetostriction as the W content increases. For each percentage increase in solute content, Fe-W alloys provide a larger increase of magnetostriction compared to Fe-Ga alloys. However, the solid solubility limit for W in Fe without forming a second phase is relatively low compared to Fe-Ga alloys and this limits the maximum magnetostriction observed in these alloys. In order to get the saturation magnetostriction λ_{si} value for a Fe-W alloy system, measurements of λ_{111} magnetostriction coefficients are required. A study of changes in magnetostriction by W substitution for Ga in various Fe-x at.% Ga alloys was also needed.

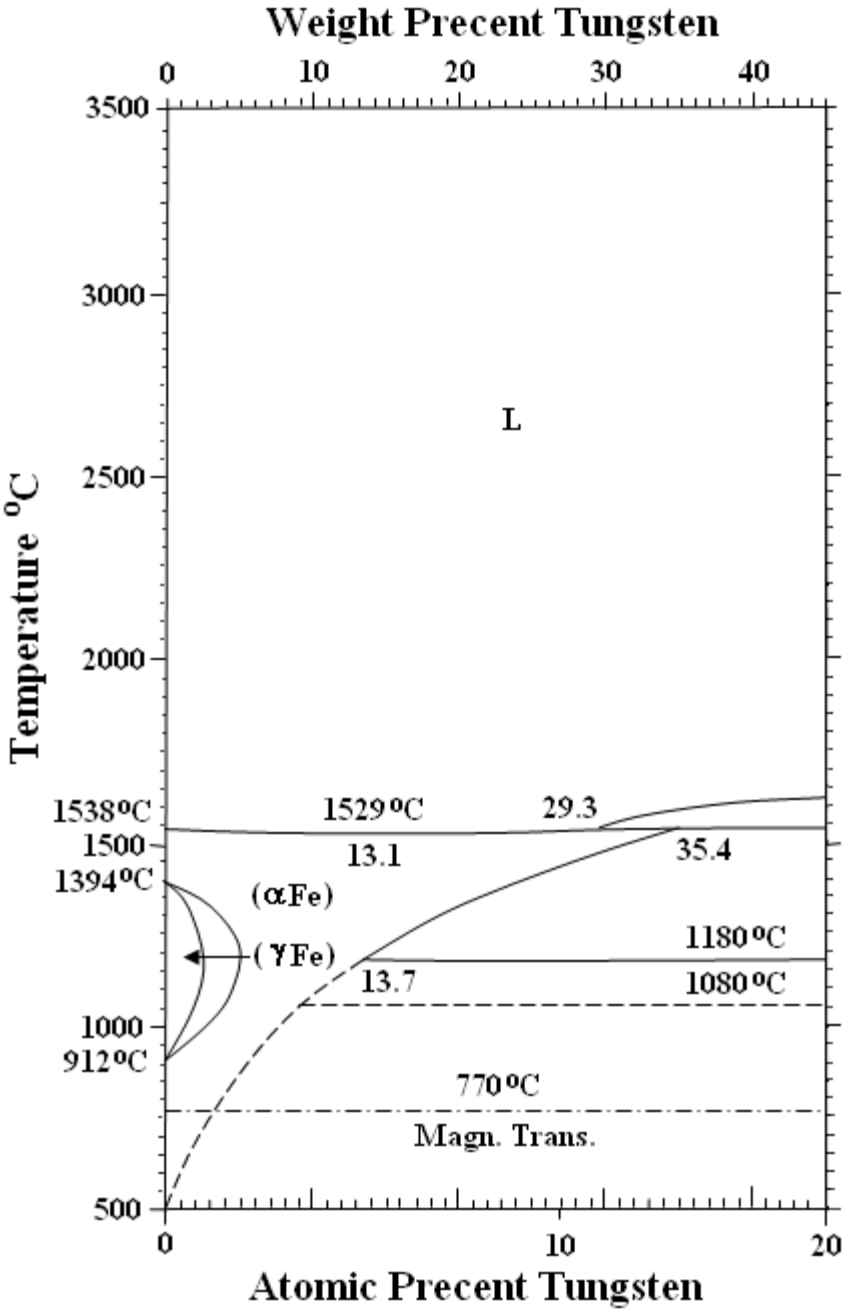

Figure 2.6 Phase diagram of binary iron-tungsten alloy (Adapted from [47]).

Table 2.2 Equilibrium phases and related crystal structures of iron-tungsten alloy [47]

Phase	Composition, wt% W	Pearson symbol	Space group
(γFe)	0	*cF4*	$Fm\bar{3}m$
(αFe)	0	*cI2*	$Im\bar{3}m$
Fe_7W_6 (μ)	~70.5	*hR13*	$R\bar{3}m$
FeW (δ)	~77.2	*Orthorhombic*	$P2_12_12_1$
Metastable phase			
Fe_2W (λ)	62.2	*hP12*	$P6_3/mmc$

2.3 Extended X-ray Absorption Fine Structure (EXAFS)

2.3.1 Introduction of EXAFS

Extended x-ray absorption fine structure (EXAFS) is part of the x-ray absorption fine structure (XAFS) spectroscopy and it is a unique tool for studying the atomic and molecular scale local structure around the selected elements inside a material [19]. There are two main regions contained in typical x-ray absorption spectra, the x-ray absorption near edge structure (XANES) and extended x-ray absorption fine structure (EXAFS). A typical x-ray absorption spectrum obtained from this work is shown in Figure 2.7. In the figure, the x-axis is the energy of the x-ray photon and the y axis is the x-ray absorption coefficient measured during the experiment. The first region which is within about 50eV of the absorption edge is referred to as the XANES region; the second region somewhat past the absorption edge and extending to about 1000 eV is the EXAFS region which is the focus of this work. There are several unique features of EXAFS. First, it is a technique focusing on the local atomic environment and long-range order is not required. Second, each element inside a material can be studied separately as the x-ray energy can be tuned for the specific absorption edge of each element. Third, EXAFS has a relatively smaller resolution compare to a lot of other techniques used in the similar area.

2.3.2 EXAFS History

The first observation of the x-ray absorption edge was done by Maurice de Broglie in 1913 on the K-edge of Ag and Br in the photographic emulsion [48]. About 7 years after that, the first experimental detection of the extended x-ray absorption fine structure was done by Fricke for the K-edge of elements Mg, Fe and Cr [49] and by Hertz for the L-edges of Cs to Nd [50]. In 1931, Hanawalt carried out the first EXAFS study

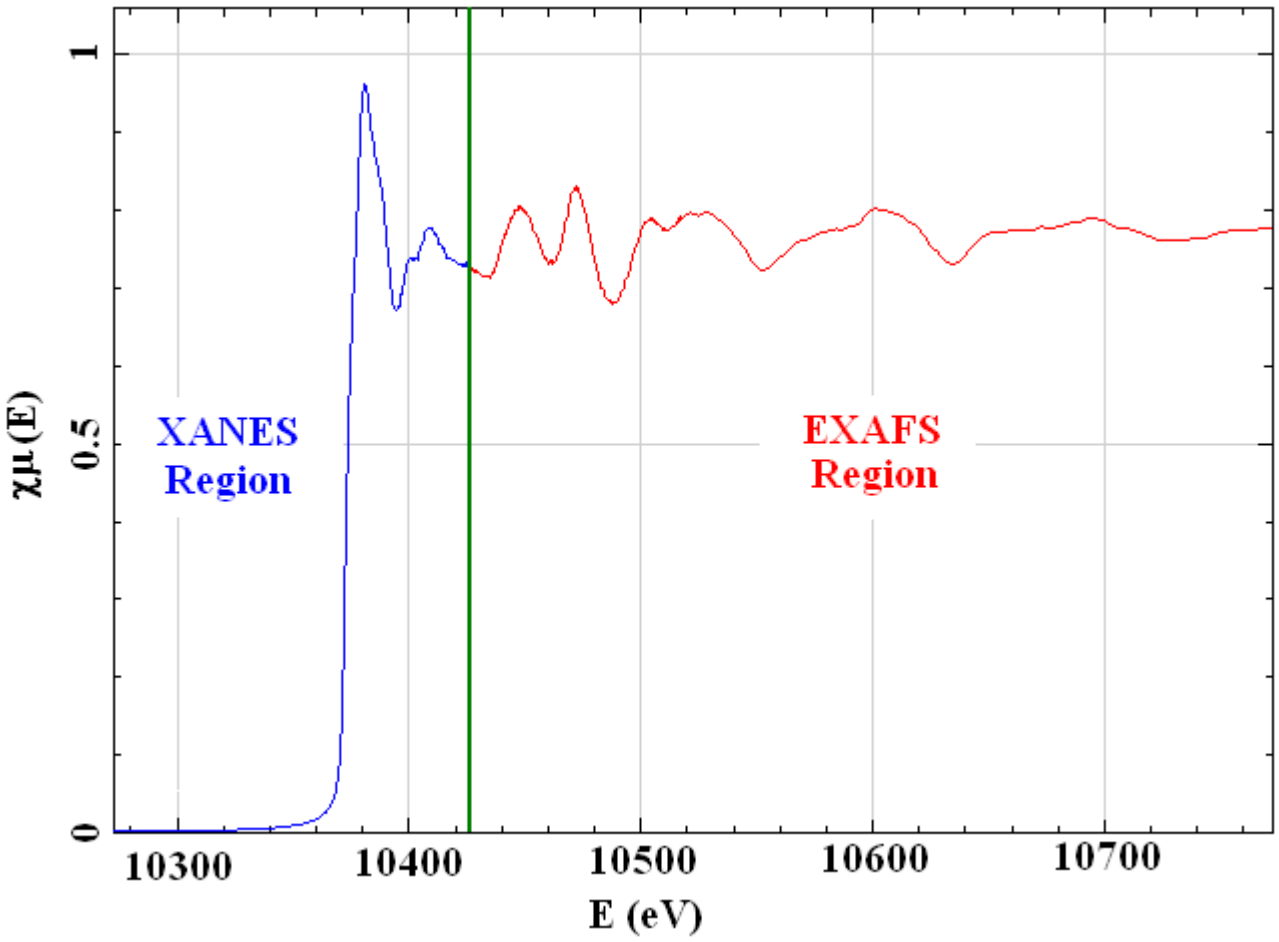

Figure 2.7 Typical x-ray absorption spectrum for the K-edge of Fe-Ga alloy

on the temperature dependence in EXAFS in gases [51]. In the same year, the first theory of EXAFS using quantum mechanics was accomplished by Kronig [52]. This has been called the long-range order (LRO) theory for EXAFS but later on, it was shown that there is a fundamental error in this theory. One year after that, Kronig developed another EXAFS short-range order (SRO) theory for molecules [53] which first considered the effect of backscattered photoelectrons from the surrounding atoms on the final state wave function. Kostarev worked on Kronig's SRO theory and proved it is also applicable to the condensed state matter [48]. In 1963, the Debye-Waller factor was introduced to EXAFS theory by Schmidt to account for the thermal vibrations and structural vibrations [48]. From 1965 to 1975, extensive work was done by Lytle, Stern and Sayers, including first determination of the nearest neighbor distance using EXAFS and development of Fourier transform analysis [54-57]. The use of synchrotron radiation for EXAFS study improves both the experimental speed and data quality which opened a new era in EXAFS research.

2.3.3 Synchrotron Radiation for EXAFS

Almost all of the modern EXAFS measurements were done by using the x-ray generated from a synchrotron. Typically, a synchrotron is built by evacuated pipes guided around a closed ring shape path of 100 to 1000 meter circumference by vertical magnetic fields [58]. The electrons generated by a hot cathode can be accelerated inside the ring to speeds close to the speed of light These high energy electrons emit high power electromagnetic radiation with more directional radiation pattern. The main benefit of using synchrotron radiation in EXAFS study is the high energy x-ray with more directional radiation pattern which makes its easier to employ x-ray optics [19]. A special

kind of monochromator designed for continuous energy scanning is used on the synchrotron beam line and the energy resolution of the typical x-ray beam used for EXAFS measurements can be as small as 1eV. This high energy and high resolution x-ray beam provides both faster scan speed and better data quality in EXAFS experiments.

2.3.4 Basic Physics of EXAFS

During an EXAFS measurement when the energy of the x-ray photon is large enough, a bound electron in one of the shells of an atom will be ejected as a photoelectron, leaving behind a core hole in the atom. The absorption edge corresponds to the energy of the x-ray photon just enough to free a bound electron. If the electron is from the most tightly bound n=1 shell, the edge is called a K-edge and if the electron is from the n=2 shell, the edge is called an L-edge. Quantum mechanically, the photoelectron generated in this way must be treated as a wave with a wavelength λ which is given by

$$\lambda = \frac{h}{p} \tag{2.20}$$

where p is the momentum of the photoelectron and h is Planck's constant. In the EXAFS, p is determined by the equation

$$\frac{p^2}{2m} = h\nu - E_0 \tag{2.21}$$

where m is the mass of the electron, ν is the frequency of the x-ray photon and E_0 is the binding energy of the electron.

When the outgoing photoelectron wave reaches the surrounding atoms, as shown in Figure 2.8, it will get scattered and the state of the photoelectron will be modified based on the nature of surrounding atoms. This modified photoelectron will be scattered by another surrounding atom or scattered back to the initial atom and forms a backscattered wave. Depending on the relative phase of the backscattered wave, it may work to add or subtract the outgoing wave from the center atom and enhance or reduce the total amplitude of the electron wave function. This modification of the photoelectron wave adjusts the probability of x-ray absorption. As the energy of the photon varies, its wavelength varies following the Equations 2.20 and 2.21. If at certain energy, the backscattered wave is in phase with the outgoing one, a peak will be present in the EXAFS spectra; and if the backscattered wave is out of phase with the outgoing one, a valley will occur. As a result, the distance between atoms can be determined by the analysis of the phase variation with the wavelength of the photoelectron, and the type of surrounding atom can be determined by analysis of the variation of backscattering strength as a function of the energy of photoelectrons [59].

2.3.5 EXAFS Equation

The basic idea of EXAFS modeling is to do evaluation and calculation by using the EXAFS equation for each scattering path. The parameters describing the local atomic structure can be obtained from the calculation result that fits best to the experimental EXAFS spectra. The equation used in this work is the classic EXAFS equation of Stern, Sayers and Lytle [60]

$$\chi(k) = \sum_j \frac{N_j S_0^2 f_j(k)}{kR_j^2} e^{-2R_j/\lambda(k)} e^{-2k^2\sigma_j^2} \sin[2kR_j + \delta_j(k)] \qquad 2.22$$

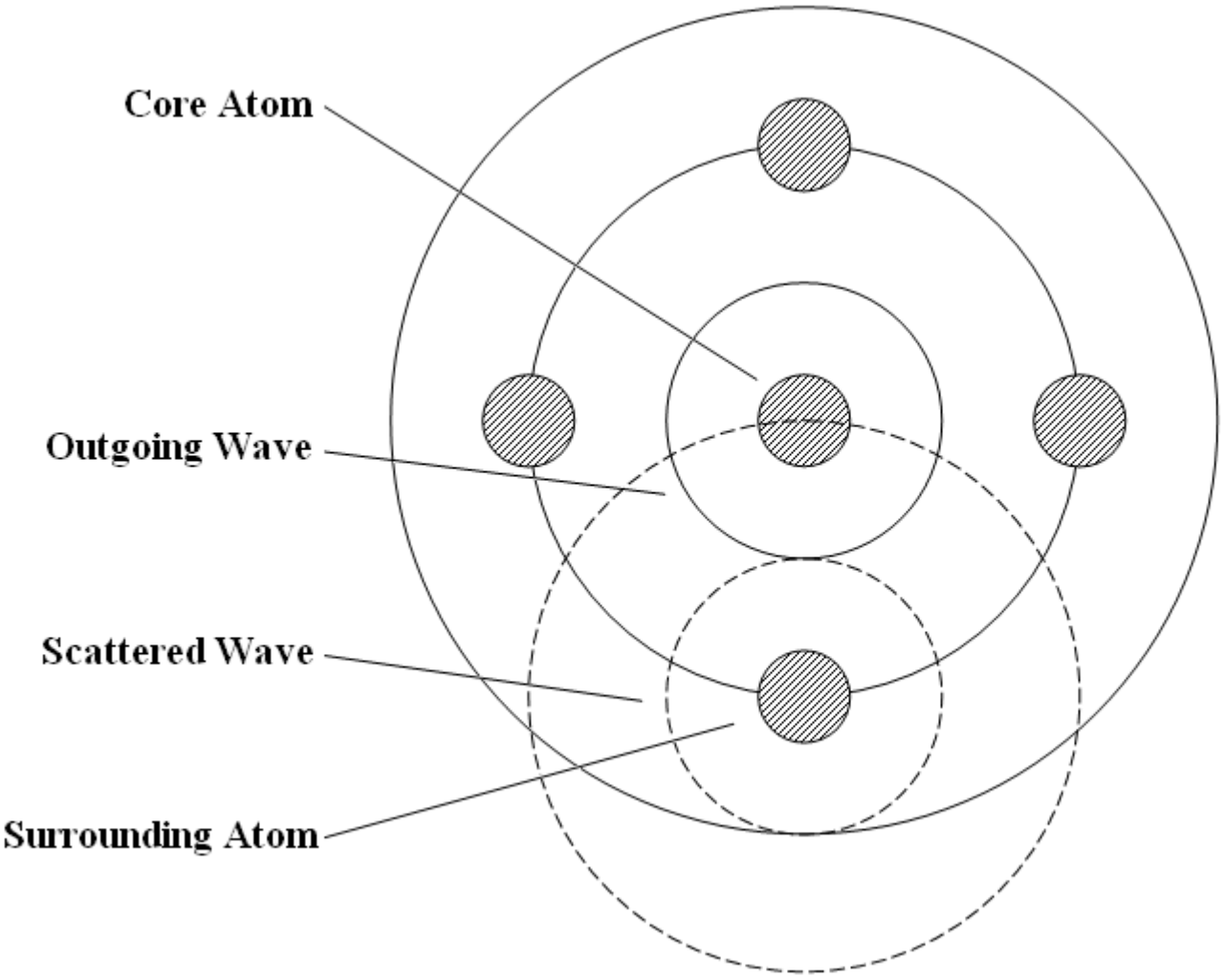

Figure 2.8 A schematic of the interaction between local atoms and photoelectron waves

where $k = \sqrt{2m(E - E_0)/\hbar^2}$ is the free photoelectron wave number, E refers to the photon energy and E_0 refers to the absorption threshold for core electron excitation, $S_0^2 N_j$ is the effective coordination number, $f_j(k)$ is the scattering amplitude, R_j is the distance to neighboring atoms, $\lambda(k)$ is the mean-free path that depends on the atomic number, σ_j^2 is the mean square variation of distances about the average R_j to atoms in the jth shell and $\delta_j(k)$ is the phase-shift that depends on atomic number.

In the classic EXAFS equation, $\chi(k)$ is the fractional change in the absorption coefficient $\mu(E)$ that is introduced by the presence of neighboring atoms. This correction factor is defined by

$$\chi = (\mu - \mu_0)/\mu_0 \qquad 2.23$$

where $\mu(E)$ is the total absorption coefficient and the $\mu_0(E)$ is the absorption coefficient for an isolated atom. In the EXAFS theory, the absorption coefficient can be describe by Fermi's Golden Rule as a transition between quantum states [61]

$$\mu(E) \sim \left| < i|\mathrm{H}|f > \right|^2 \qquad 2.24$$

where $\langle i|$ is the initial state that has a core level electron and a photon, H is the interaction and $|f\rangle$ is the final state that has a photoelectron, a hole in the core and no photon. The initial state is not affected by the neighboring atoms, but the final state is dependent on the photoelectron scattering events happening at the neighbor atoms.

The effective coordination number $S_0^2 N_j$ includes two parts; N_j is the coordination number of the j^{th} nearest neighbor shell and S_0^2 is the amplitude reduction

term which is due to the relaxation of all the other (N-1) electrons in the absorbing atom to the hole in core level. This amplitude term is generally described by

$$S_0^2 = \left| \left\langle \Phi_f^{N-1} \middle| \Phi_0^{N-1} \right\rangle \right|^2 \qquad 2.25$$

where the $\left|\Phi_0^{N-1}\right\rangle$ is the wave function state of the unexcited atom and $\left\langle\Phi_f^{N-1}\right|$ is the electron state relaxation of the other N-1 electrons in the excited atom.

In this EXAFS modeling work, specified variables have been defined for R_j, N_j, σ_j^2 and $\delta_j(k)$ and related data about the local atomic environment were obtained.

2.3.6 Previous EXAFS Studies on Fe-Ga Alloys

EXAFS has been considered as a powerful tool for the analysis of the local structure at atomic and molecular scale and a huge amount of research has been done on various kinds of materials. However, as a result of the difficulty in data analysis, there is only a very limited amount of work that has been done about the study of Fe-Ga alloy using EXAFS.

Pascarelli et al. show that inside a $Fe_{80}Ga_{20}$ melt-spun ribbon crystal structure, the first shell Fe-Ga bonds exhibit a +1% strain with respect to the first shell Fe-Fe bonds and the second shell Ga-Ga distance has a +4% strain in the <001> crystallographic direction with respect to the corresponding Fe-Fe distance [62]. Turtelli et al. have done a study on $Fe_{85}Ga_{15}$ melt-spun ribbon and found that there is about +1% strain on the first shell Fe-Ga bond and a +0.3% strain on the second Fe-Ga shell in the A2 structure with random substitution of Fe and Ga atoms [63]. Gao et al. studied the effect on the Fe-Fe and Fe-Ga bonds on adding boron to Fe-Ga thin films and showed that Fe-Fe/Ga bond

distances and the lattice parameters reduced as the boron content increased [64]. More recently, Garside analyzed the Ga-Ga bond distance in the Fe-27.5 at.% Ga single crystals with different thermal histories and showed a large increase in the Ga-Ga first nearest neighbor distance after long-term annealing treatment [22].

Because of the very limited amount of information about the local atomic environment of Fe-Ga alloy and the importance of this alloy in magnetostriction research, a detailed EXAFS analysis of Fe-Ga alloys of various solute contents and different thermal histories will be valuable for the future design and improvement of these Fe-Ga alloys.

CHAPTER 3

OBJECTIVES AND METHOLOGY

There are four main objectives for this work. The first objective is to study the changes in magnetostrictive coefficient λ_{100} by W substitution for Ga in various Fe-x at.% Ga alloys and various heat treatment conditions (directionally grown and annealed) for Fe-Ga alloy single crystals. The compositions of Fe-Ga-W single crystals used for this study are Fe-12.5 at.% Ga-2.5 at.% W, Fe-15 at.% Ga-2.5 at.% W and Fe-17.5 at.% Ga-2.5 at.% W alloys. Single crystals for each composition were grown by the vertical Bridgman technique. [001]-oriented single crystal samples were prepared by crystal orientation using XRD and polishing. Samples were annealed in the α-phase region to obtain more homogeneous structure. Values of $(3/2)\lambda_{100}$ magnetostriction coefficients were calculated based on the strain measurements using a strain gage along the <001> direction on the oriented crystals in both as-grown and annealed conditions. Saturation magnetization values were also measured using a VSM system on the as-cast samples.

The second objective is to study the changes in magnetostriction coefficient λ_{111} with W content and heat treatment conditions. Single crystals of Fe-3 at.% W, Fe-6 at.% W and Fe-7.5 at.% W were grown by the vertical Bridgman technique. [220] or [211]-oriented disc shaped single crystals with the <111> direction lying parallel to the disc faces were prepared, XRD was used to determine crystal orientation and this information was used in cutting and polishing. Samples were annealed in the α-Fe phase region.

Magnetostriction measurements along the <111> direction were done on all the crystals in both the as-grown and annealed conditions. Using the $(3/2)\lambda_{111}$ magnetostriction coefficients from this study coupled with earlier measurements of $(3/2)\lambda_{100}$ magnetostriction coefficients, λ_{si} for various crystallographic orientations can be calculated.

The third objective is to study the presence of B2 and DO_3 ordered domains in annealed and water quenched Fe-27.5 at.% Ga alloy single crystals and the variation in their distribution as a function of depth from the surface to understand the influence of sample size and thermal history on the nature of short-range and long-range ordering. Single crystal of Fe-27.5 at.% Ga alloy were grown using the vertical Bridgman technique and disc shaped [111]-oriented single crystals were prepared. Annealing in the α-phase region was performed on the crystal followed by rapid water quench. Theta- 2 theta XRD scans were performed as a function of depth by sequentially removing material through controlled polishing steps up to 200μm from the top surface. Volume ratio of B2 and DO_3 long-range ordered domains was calculated based on the XRD patterns for each depth. The temperature gradient formed at the surface of the sample during quenching was calculated.

The fourth objective is to study the local atomic environment of Fe-Ga alloys by using EXAFS analysis. Compared to the earlier analysis methods, the Fe and Ga K-edge scans have been fit simultaneously for all the ARTEMIS® projects. The error ranges of fit results have been decreased by adjusting the variables and applying restraints. Scattering factor differences of Fe and Ga atoms were considered during the building of the crystal model for FEFF calculation. EXAFS analysis of the first nearest neighbor

distances were done for three Fe-Ga single crystals with various alloy compositions (Fe-27.5 at.% Ga, Fe-20 at.% Ga and Fe-15 at.% Ga) and thermal histories (as-grown, long-term annealed and ordered). EXAFS analysis was extended to the second nearest neighbors, which will provide more detailed results about local lattice distortion and atom coordination numbers.

CHAPTER 4

EXPERIMENTAL WORK

4.1 Magnetic and Magnetostriction Study of Single Crystals

4.1.1 Alloy Preparation and Vacuum Arc Melting

The ingots of Fe-x at.% W and Fe-x at.% Ga-2.5 at.% W alloys were prepared from high purity elements using an Edmund Beuhler® high vacuum arc-melting system. By using a digital balance, each element of the alloys was weighed out carefully to control the error to less than 0.001 at.% from the desired alloy composition. For every alloy, 5 sets of material weighting about 25g each were prepared for arc-melting and directional casting. As Ga has a relative low melting temperature and lower boiling point than Fe, extra Ga (2% of the desired Ga content) was added to the alloy to minimize the effect of vaporization loss of Ga during arc melting.

The elemental mixtures were first loaded in the vacuum arc-melting system. Before melting, the chamber was evacuated using an Edwards® diffusion pump down to $<10^{-4}$ Torr and then backfilled with ultra-high purity (UHP) argon to about 0.7 atmosphere to minimize the oxygen and water molecules deposition on the sample and chamber surface. A small titanium piece was first melted to get any remaining oxygen or moisture inside the chamber. Arc-melting of alloy was started with a low power level, then the power was gradually increased to a higher level to melt and mix the elements

completely. The lowest power level has been used in order to minimize the amount of Ga loss during arc-melting. Each ingot was flipped over and remelted 4 to 6 times to ensure homogeneity before directional casting.

4.1.2 Directional Casting

Directional casting of alloy rods was carried out inside the arc-melting chamber. Each 25g ingot of Fe-x at.% W and Fe-x at.% Ga-2.5 at.% W alloys was loaded on a copper block with a thick 9.5 mm alumina sleeve insulating the 12.5mm diameter cylindrical cavity. After the complete melting of the ingot, the liquid metal was allowed to flow into the cylindrical cavity and touches the water-cooled surface at the bottom of the copper block. Solidification was initiated at the bottom side with water cooling, and progressed upward along the rod and finished within a few seconds. Due to the rapid one-dimensional heat extraction, columnar crystals formed in the preferred crystallographic orientation which will benefit the directional growth process. The metal oxidization was also minimized as most of the metal surface was covered by alumina sleeve or copper block during solidification. The cast rods which are about 9.4mm in diameter and 24mm in length are referred to as as-directionally-cast ingots. Figure 4.1 shows a schematic of the directional casting experimental setup.

4.1.3 Directional Growth

The setup for the directional growth processing consists of a MoS_2 resistance heated 2-zone furnace. The two heating zones in this furnace can be maintained at the same or different temperature and provide a temperature gradient along the tube direction. A good control of the heat transfer and movement speed of the liquid/solid

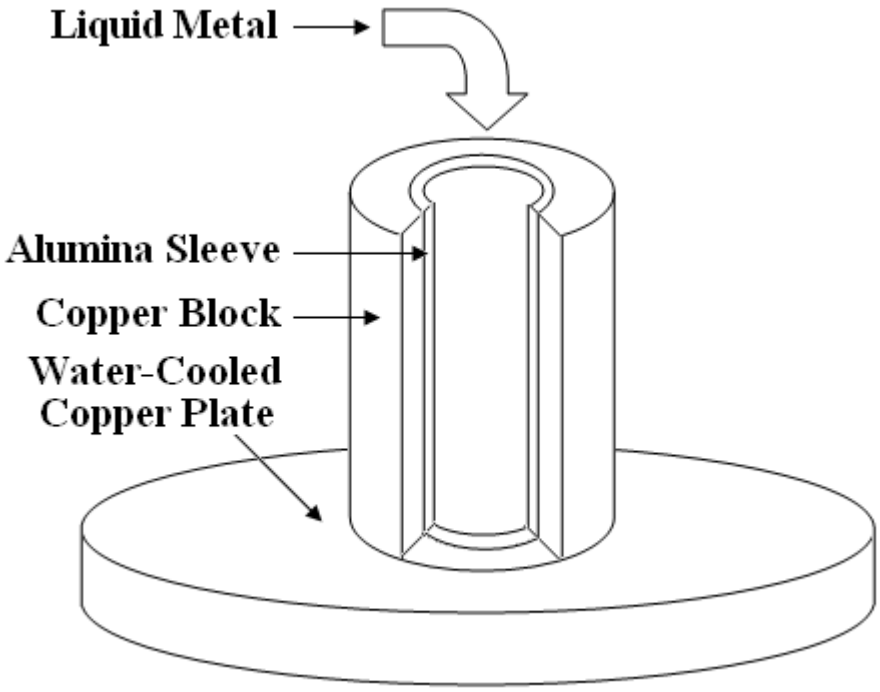

Figure 4.1 A schematic of the directional casting experimental setup.

interface can be obtained by using a stepper-motor to move the sample tube down the temperature gradient at a low speed. In this case, solidification and single crystal formation will start at the bottom of the alumina tube as the liquid metal moves down the temperature gradient.

The cast alloy rods were loaded inside a 12.5 mm in diameter and 76 mm long close-one-end alumina tube. The open end of the tube was connected to a mechanical pump and ultra-high purity (UHP) argon gas cylinder. The tube was set inside the furnace with the sample positioned at the maximum temperature region. Before the start of heating, the tube was evacuated and refilled with UHP argon several times to ensure removal of oxygen and a low rate argon flow was maintained during the directional growth. After 2 hours holding of the sample in the maximum temperature region to ensure the complete melting of alloys, the tube was moved down at a speed of 22.5 mm/h through the temperature gradient. The predefined temperatures used for the three single crystals were 1550 °C for Fe-17.5 at.% Ga-2.5 at.% W, 1560 °C for Fe-15 at.% Ga-2.5 at.% W and 1570 °C for Fe-12.5 at.% Ga-2.5 at.% W. Figure 4.2 shows a schematic of the directional growth experimental setup.

4.1.4 Single Crystal Orientation and Preparation

X-ray examination of the single crystal was performed using the Cu K_α radiation in a Siemens® D5000 x-ray diffractometer. The as-directionally grown (DG) rod may contain several single crystals, and a cut was done at the region with the largest crystal. The sample was polished and mounted flat on the XRD sample holder. A θ-2θ scan was performed on the sample face. In a θ-2θ scan, the sample is rotated perpendicular to the

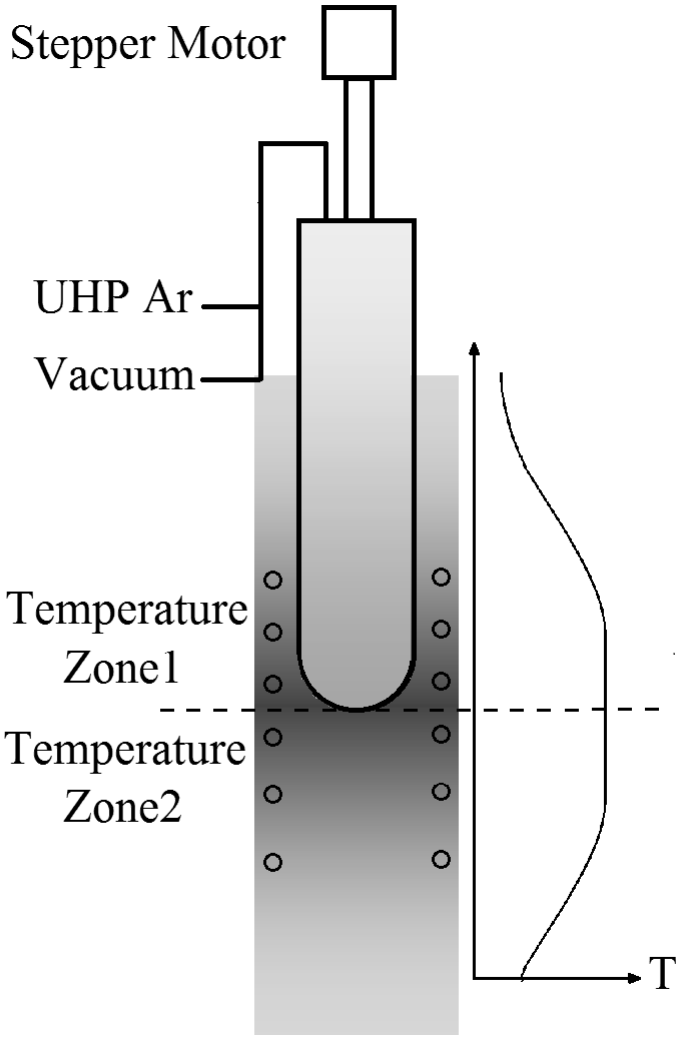

Figure 4.2 A schematic of the directional growth experimental setup.

phi axis and the detector is rotated at a rate that is double the sample speed. A θ-2θ scan pattern was obtained with a series of peaks corresponding to different planes of the Fe-based alloy's BCC structure. The value of $2\theta_{hkl}$ peaks in the 10˚ to 125˚ range of the θ-2θ scan pattern was obtained and these included (110), (200), (211), (220) and (310) peaks. These $2\theta_{hkl}$ values were used to perform rocking curve and phi scans to identify the crystal orientations.

The shape of the sample crystal for a magnetostriction coefficient $(3/2)\lambda_{100}$ measurement is a rectangular parallelepiped with all six faces oriented to within 1˚ off the [001] direction. For a magnetostriction coefficient $(3/2)\lambda_{111}$ measurement, the samples were disc-shaped single crystals with both faces oriented to within˚ 1 from the [220] direction or [211] direction. For the Fe-27.5 at.% Ga sample used in B2 and DO_3 phase analysis, about 2 mm thick plate samples oriented to within 0.25° from the [001] or [111] direction were prepared.

4.1.5 Magnetostriction Measurement

Strain gages were used to measure the magnetostriction coefficient values for the single crystal samples. For measuring the $(3/2)\lambda_{100}$ magnetostriction coefficient, the strain gage was mounted at the center of the longitudinal [100]-oriented face along the [001] direction and strain measurements were made with magnetic field parallel or perpendicular to the [001] direction. For measuring the $(3/2)\lambda_{111}$ magnetostriction coefficient, the strain gage was mounted at the center of the [220] or $[1\bar{1}2]$-oriented face along the $[\bar{1}11]$ direction and measurements were made with magnetic field parallel and

perpendicular to the $[\bar{1}11]$ direction. Figure 4.3 shows a schematic of the experimental setup for both λ_{100} and λ_{100} magnetostriction measurements. The full bridge technique was used with an active strain gage attached to the [001], [220] or $[1\bar{1}2]$-oriented sample face and three dummy gages attached to a Bi rod, which has a coefficient of thermal expansion similar to Fe. Magnetic field was applied using a magnetic field surrounding the sample. Magnetostriction and applied magnetic field signal was collected by the IOTECH® ADC 488/16A analog digital convertor and IOTECH® MUX 488/16SC signal conditioning multiplexer. A LabVIEW® program was used to acquire and plot the data of magnetostriction versus applied magnetic field. A zero field strain value was measured before applying the field and input into the program for zero correction

4.1.6 Heat Treatment

Single crystal samples were glass-sealed in quartz tubes with argon atmosphere to prevent oxidation during heat treatment. These crystals were heated up to a certain temperature, which is within the alpha phase region of Fe-based alloys, and annealed for 4 hours. This temperature was decided based on the relevant phase diagrams. A rapid water quench of these samples was performed after taking the sample out of the furnace so as to retain the alpha phase crystal structure at room temperature. A slight surface polish is required for removing the oxide layer formed during annealing. Parallel and perpendicular magnetostriction measurements were performed on the single crystals again.

4.1.7 Magnetization Measurement

Cubic shape samples, about 2mm x 2mm x 2mm in size, were cut from the

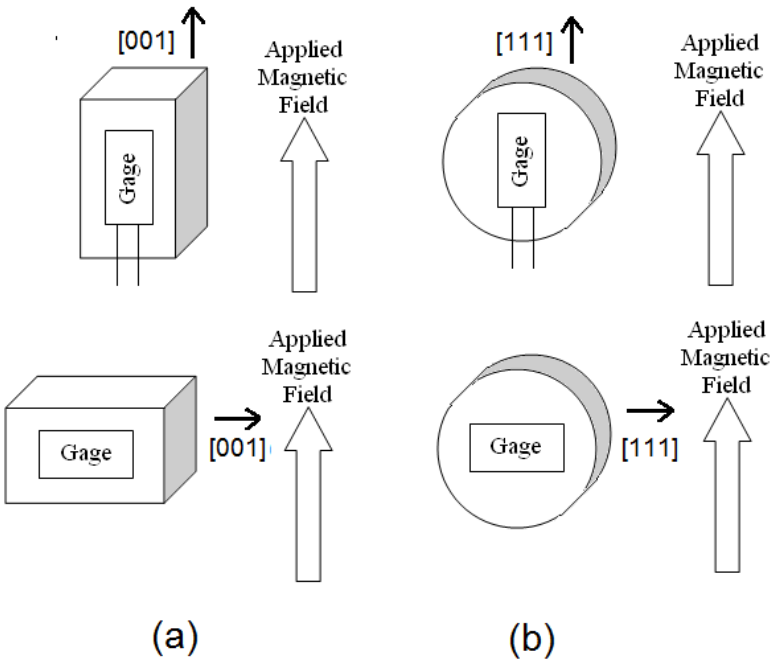

Figure 4.3 A schematic of experimental setup for both (a) λ_{100} and (b) λ_{111} magnetostriction measurements.

as-directionally-cast ingots of Fe-12.5 at.% Ga-2.5 at.% W, Fe-15 at.% Ga-2.5 at.% W and Fe-17.5 at.% Ga-2.5 at.% W alloys. Magnetic properties were determined using a LakeShore® Model 7307 vibrating sample magnetometer with a LakeShore® Model 735 VSM control electronics and a LakeShore® Model 450 Gaussmeter with maximum applied field of 10 kG at room temperature.

4.2 Extended X-ray Absorption Fine Structure Study of Fe-base Alloys

4.2.1 Beamline Setup and Data Collection

The extended x-ray absorption fine structure (EXAFS) data were obtained in earlier research. The x-ray used in the EXAFS measurement was split off from the synchrotron ring and sent down to the beamline station through a straight evacuated tube. After exiting the tube and before passing through the ion chamber, the x-ray beam was pointed downward by a Pd-coated flat mirror and focused by a Pd-coated torroidal mirror to a size of 0.8 x 1.2 mm. The sample was taped on the sample holder which was located 39 cm from the ion chamber and rotated 45̊ from the incoming beam . The detector used in this work is a Canberra 13-element Ge detector placed 19.3 cm from the sample holder at an angle of 90° from the incoming beam direction to minimize elastic scattering in the detector and reduce dead time. Figure 4.4 shows the beamline setup for EXAFS measurements. To decrease the dead time of measurement, the count rate has been limited to 100,000 counts/sec by placing aluminum foils in front of the detector. Each of these 30μm thick aluminum foils can reduce the count rate by half and based on the measurement, more than one foil may be used. As EXAFS measurement is sensitive to the sample surface condition, all of the single crystals were polished with 0.03μm diamond polish just before loading on the holder to ensure a flat surface and removal of

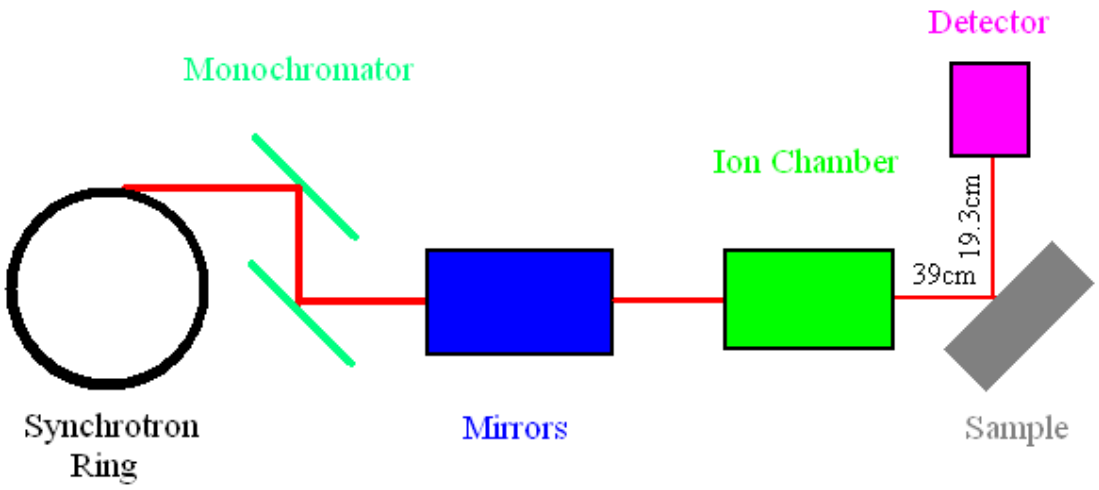

Figure 4.4 Beamline setup for fluorescence mode EXAFS measurements

any oxide layer. All the data were collected in the fluorescence mode. Fe scan was measured with fluorescence energy of Fe K-alpha at 6400eV for Fe K-edge absorption at 7112 eV. Ga scan was made with fluorescence energy of Ga K-alpha at 9250eV for Ga K-edge absorption at 10367eV. Each scan takes about 20 minutes and 5 to 7 scans were taken for each alloy single crystal.

4.2.2 Data Processing

All the scan data sets were processed using the ATHENA® software for the preparation of data analysis. ATHENA® is a graphical front for processing EXAFS data based on the IFEFFIT library written in the Perl programming language [65]. By using the ATHENA® software, the raw data obtained from EXAFS measurements were first converted to $\mu(E)$ spectra. All of the 5 to 7 scans of the same sample were then merged by calculating the average and standard deviation at each point in the $\mu(E)$ energy space to a single data set. Another important correction done on the scan data by ATHENA® is self-absorption correction. Self-absorption happens as the fluorescence photon generated may be re-absorbed before escaping the sample. For an ideal condition, it can be taken into data analysis consideration by applying the photoelectric part of the x-ray absorption coefficient. However, the mean absorption depth in the fluorescence mode EXAFS measurement is not a constant as the energy of incident photon E keeps changing. This leads to the changes in the probability of fluorescence photon re-absorbed by the sample and causes attenuation in the oscillatory structure of χ. The self-absorption correction amplified the EXAFS oscillations and improved the quality of the scan data.

4.2.3 Data Analysis

ARTEMIS® software was used for EXAFS data analysis in this work. ARTEMIS® is software included in the IFEFFIT software package with a graphical front for analysis of EXAFS data using the theoretical models based on the FEFF program [65]. The basic idea of ARTEMIS® is the FEFF's multiple-scattering path expansion. A series of possible scattering paths are defined by the user. For each scattering path, the EXAFS equation is evaluated and calculated by the FEFF program. The results of all the defined scattering paths are summed and fit to match with the experimental spectra [66].

To define the possible scattering paths, a specified kind of unit cell with atoms placed at the correct location is required for set up in the Atoms page of ARTEMIS®. For the Fe-based alloy single crystals studied in this work, the crystal structure is a simple Fe-based body centered cubic (BCC) structure with other element atoms substituted at various atomic sites. A core atom at position (0, 0, 0) is referred to as the absorbing atom and it may be defined as an iron or other alloy element atom based on the data set. The lattice parameters for different alloys were calculated using the XRD data and input to ARTEMIS® as one of the constants. Take Fe-x at.% Ga alloy for example. For the first nearest neighbor modeling, the type of atom at the first nearest neighbor position of the BCC structure (0.5, 0.5, 0.5) needs to be defined. The four types of atomic arrangement for the first nearest neighbors were Fe-Fe and Fe-Ga for Fe K-edge scans, and Ga-Fe and Ga-Ga for Ga K-edge scans. For the first nearest neighbor modeling, all the other atoms above the first nearest neighbor have been defined as the average value based on the alloy composition.

Second nearest neighbor modeling also uses the same data, but the atomic arrangement of scattering paths has been defined specifically up to second nearest neighbors or second scattering atoms. Beyond second nearest neighbor, random distribution of the solute atom is assumed. For a Fe-x at.% Ga alloy, the defined atomic arrangements include Fe-Fe-Fe, Fe-Fe-Ga, Fe-Ga-Fe and Fe-Ga-Ga for Fe K-edge scan data or Ga-Fe-Fe, Ga-Fe-Ga, Ga-Ga-Fe and Ga-Ga-Ga for Ga K-edge scan data. Then, ARTEMIS® software will calculate all the possible scattering paths based on the defined crystal structure and atomic arrangement. For each possible scattering path, a variable or constant of interatomic distance, coordination number of different type of atoms and the mean-square disorder of neighbor distance is required. In order to get a modeling result with physical meaning, some restraints need to be applied to the variables.

The ARTEMIS® projects used in this work were programmed based on the following ideas. For each alloy with specified thermal history, the Fe K-edge and Ga K-egde data sets were included in the same ARTEMIS® project which makes it possible to fit multiple data sets of the same sample simultaneously and provide very good data consistency. Each atomic arrangement was defined as an individual FEFF calculation. The scattering factor difference between Fe and Ga atoms was taken into consideration in the atom list of the FEFF calculation and also the variables of amplitude for scattering paths. A common restraint has been introduced to all the amplitude variables in one data set to ensure the coordination number of atoms will match with the alloy composition. Variables for interatomic distance and mean-square disorder of neighbor distance were defined individually for each FEFF calculation and the method of combination of these variables was defined specifically for each scattering path. A series of restraints were

introduced to the projects to ensure the variables will not exceed their physical limitations. By applying all of these ideas into the programming of ARTEMIS® projects, the freedom and constraints of the projects have been managed with a reasonable balance which increases the possibility of acquiring theoretically meaningful and relative high quality fit results.

Several parameters were used to identify the quality of the fit data generated by the ARTEMIS® program. A high quality fit should show a visible good match between the theoretical spectra generated by calculation and the experimental spectra obtained from measurement. The parameters of R-factor, Chi-square and reduced Chi-square are good references for the quality of spectra match. The E0 value correlated to the edge energy used in the experiment should not shift too much. The delE0 parameters which stand for the change of E0 value should be within the range of {-10, 10}. The amplitude parameters should be within {0.5, 1.2}. And the restrains introduced in the fit should not have a large value.

After successful program fits of the calculation result to the experimental spectra, the mean values and uncertainties of the variables for all the scattering paths up to sixth nearest neighbor can be obtained in the fit result. Depending on the number of atomic arrangements defined during the program setup, interatomic spacing and atomic coordination numbers up to the first or second nearest neighbors that are meaningful can be obtained. An understanding of the local atomic environment can be obtained based on analysis all of these results.

CHAPTER 5

RESULTS AND DISCUSSION

5.1 Magnetostriction and Magnetic Studies of Fe-Ga-W Alloys

5.1.1 XRD Analysis of Single Crystals

XRD analyses were done for all of the single crystals during sample preparation to obtain the crystal orientation information of each sample. Figure 5.1 shows the θ-2θ XRD scan of the Fe-12.5 at.% Ga-2.5 at.% W alloy sample after the first cut made on the DG rod. Several peaks were observed on the θ-2θ XRD scan pattern. Each peak corresponds to different crystal planes based on its 2θ value. As discussed in the experimental section, the single crystal was oriented based on the XRD data.

If the sample is carefully oriented, there will be diffraction only from the {h00} family of planes of a [001]-oriented single crystal. Figure 5.2 shows the θ-2θ scan made on the (100) face normal to the longitude axis of the Fe-12.5 at.% Ga-2.5 at.% W single crystal sample prepared for magnetostriction measurements and the 2θ value corresponding to (200) fundamental reflection is 64.20°. Figure 5.3 shows the rocking curve scan made on one of the [100]-oriented faces with the detector position fixed at the angular position $2\theta_{200}$= 64.20° and the sample rotated about the diffractometer axis. The angle between sample and x-ray source beam direction is denoted by ω. The maximum diffracted x-ray intensity from the (200) plane will occur when the sample position ω

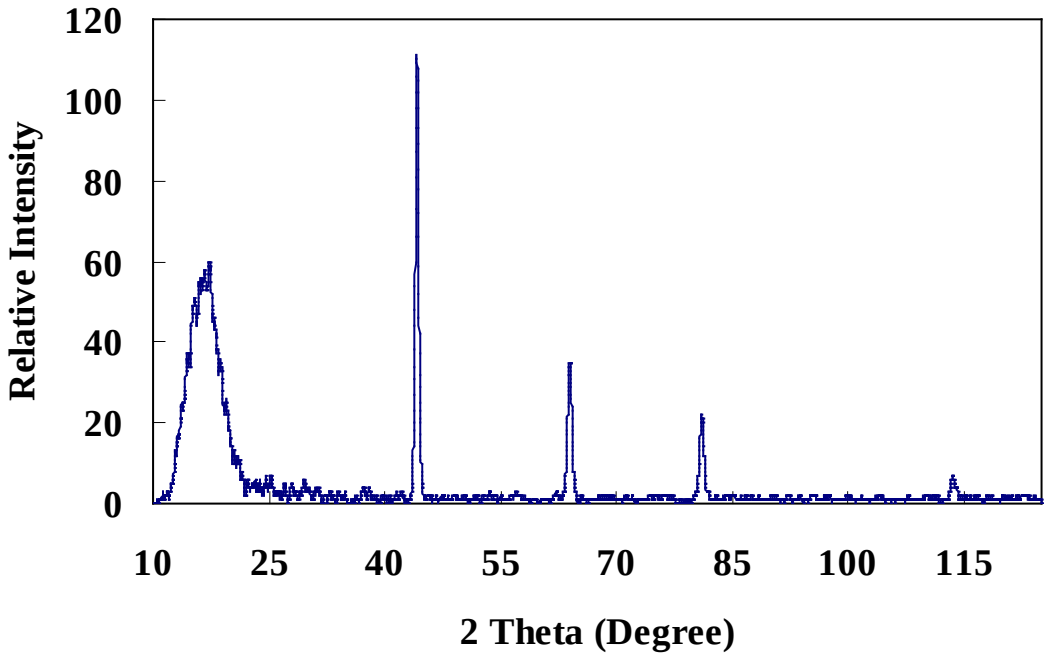

Figure 5.1 Theta- 2 theta x-ray diffraction scan on the first cut face of DG rod of the Fe-12.5 at.% Ga-2.5 at.% W single crystal.

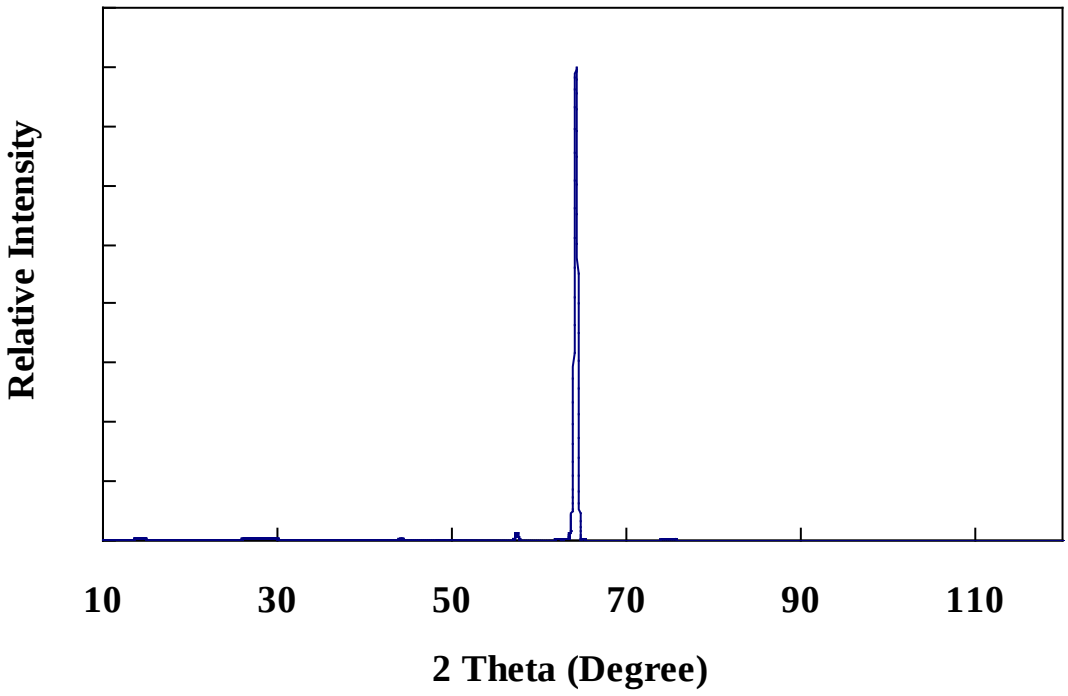

Figure 5.2 Theta- 2 theta x-ray diffraction scan on the (200) face of the [001]-oriented Fe-12.5 at.% Ga-2.5 at.% W single crystal.

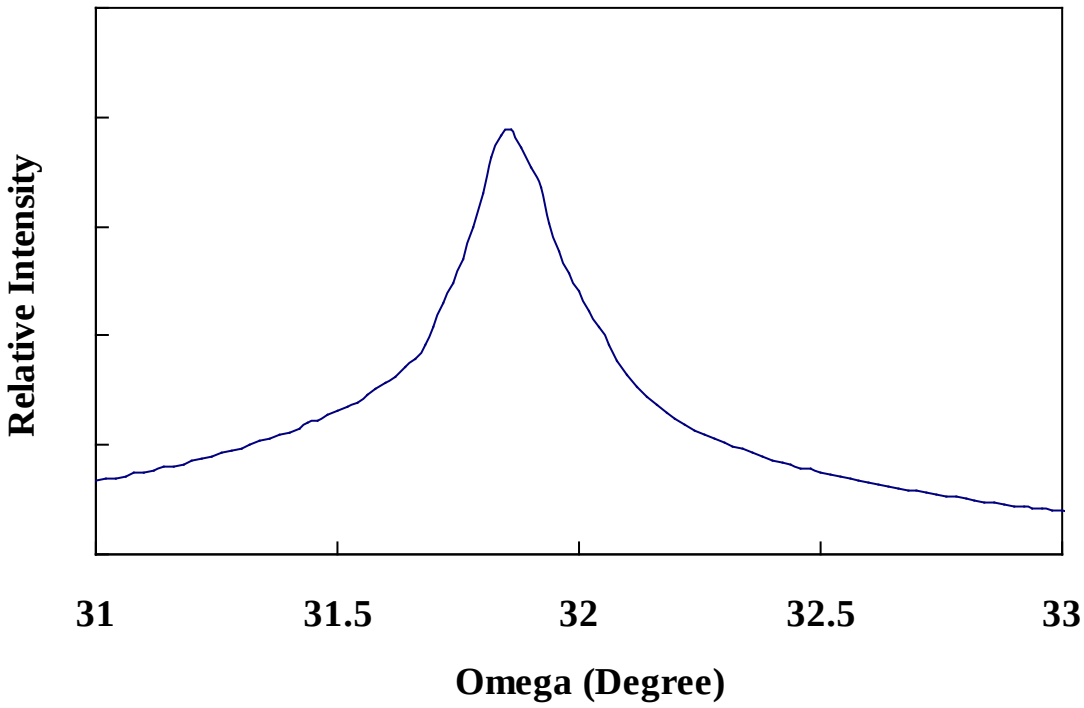

Figure 5.3 Rocking curve x-ray diffraction scan on the (200) face of the [001]-oriented Fe-12.5 at.% Ga-2.5 at.% W single crystal.

satisfies the Bragg condition and an intensity peak will be recorded on the rocking curve scan. The deviation of ω from the value corresponding to the half of the 2 θ_{hkl} value is the deviation of the sample face orientation from the desired crystal orientation. Figure 5.3 shows that the ω value at the peak position is 31.86° and therefore, the face is oriented within 0.25° from the [001] orientation. This single crystal orientation work was done on all the faces of Fe-12.5 at.% Ga-2.5 at.% W, Fe-15 at.% Ga-2.5 at.% W and Fe-17.5 at.% Ga-2.5 at.% W single crystals samples on which magnetostriction measurements were made.

5.1.2 Magnetostriction Measurement of $(3/2)\lambda_{100}$ Coefficient

The magnetostriction measurements were made along the [001] direction by applying the magnetic field parallel or perpendicular to this direction. The strain gages were mounted parallel to the [001] crystal axis and $\lambda_{parallel}$ was obtained by applying the magnetic field along the [001] crystallographic direction. The $\lambda_{perpendicular}$ magnetostriction strain values were obtained by applied magnetic field perpendicular to the [001] direction which will be the [010] direction. Figure 5.4 shows the magnetostriction strain value versus applied magnetic field curves for $\lambda_{parallel}$ and $\lambda_{perpendicular}$ measurements corresponding to the as-grown condition of the Fe-12.5 at.% Ga-2.5 at.% W single crystal. The magnetostriction coefficient $(3/2)\lambda_{100}$ of each alloy single crystal was calculated using the equation $(3/2)\lambda_{100} = \lambda_{parallel} - \lambda_{perpendicular}$. Similar measurements were also done for the [001]-oriented Fe-17.5 at.% Ga-2.5 at.% W and Fe-15 at.% Ga-2.5 at.% W single crystals and the magnetostrictive strain versus applied magnetic field curves from these measurements are shown in Figure 5.5 and Figure 5.6.

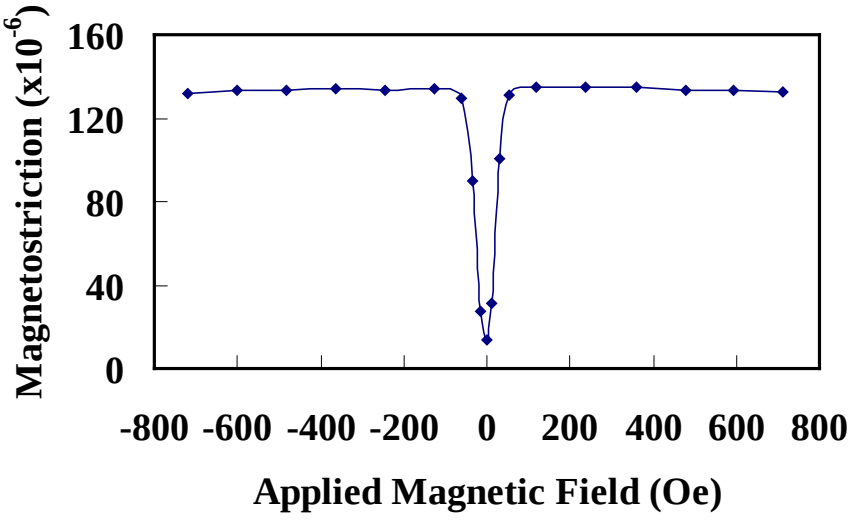

(a)

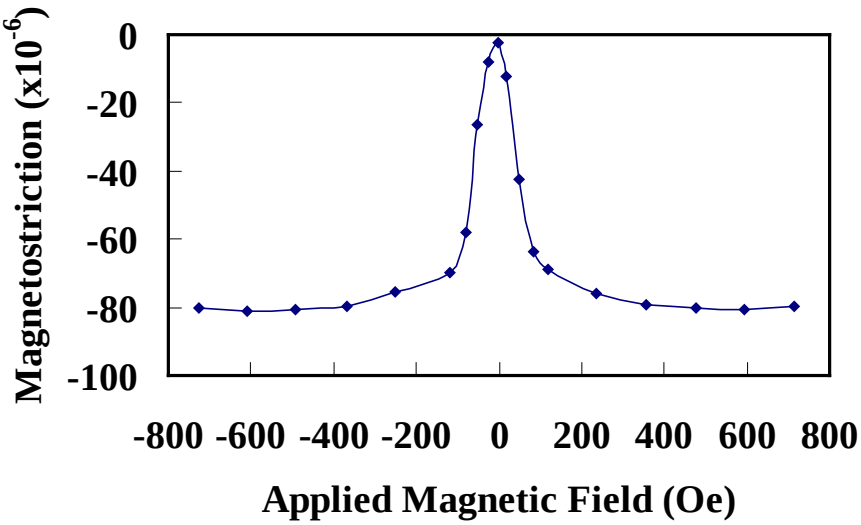

(b)

Figure 5.4 Magnetostrictive strain value versus applied magnetic field curves for the [001]-oriented Fe-12.5 at.% Ga-2.5 at.% W single crystal in the as-grown condition, with applied magnetic field (a) parallel and (b) perpendicular to the [001] direction.

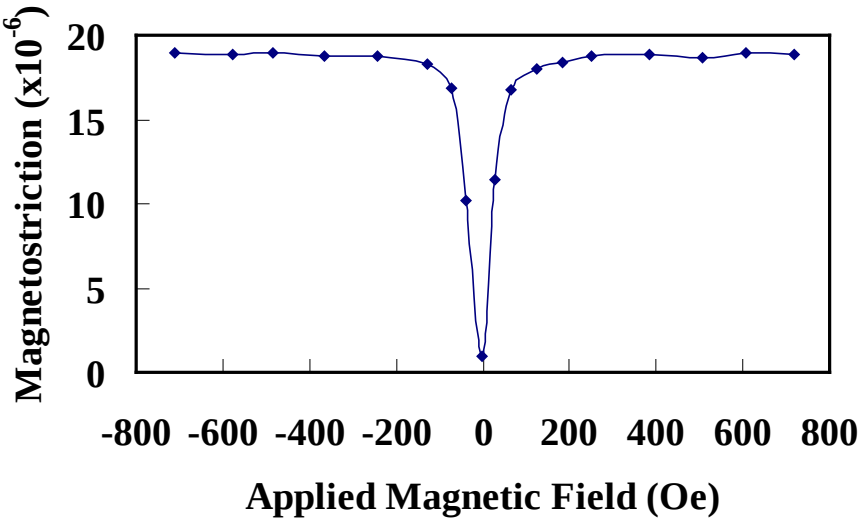

(a)

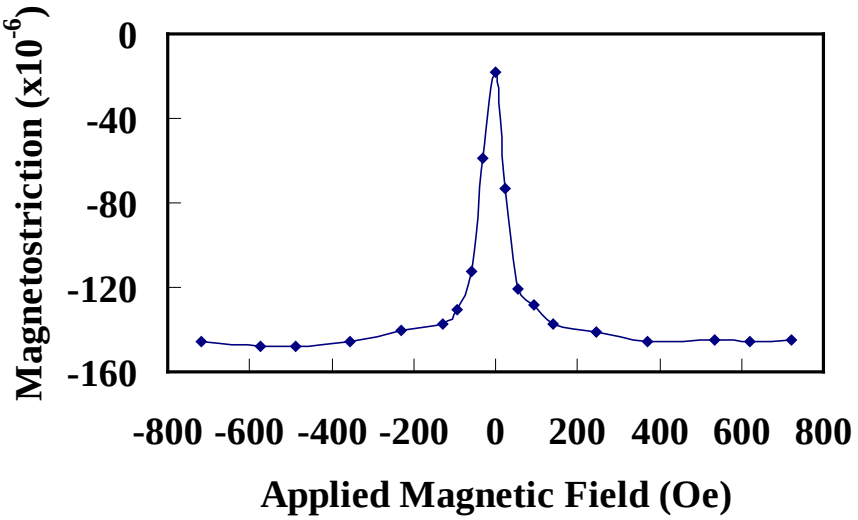

(b)

Figure 5.5 Magnetostrictive strain value versus applied magnetic field curves for the [001]-oriented Fe-15 at.% Ga-2.5 at.% W single crystal in the as-grown condition, with applied magnetic field (a) parallel and (b) perpendicular to the [001] direction.

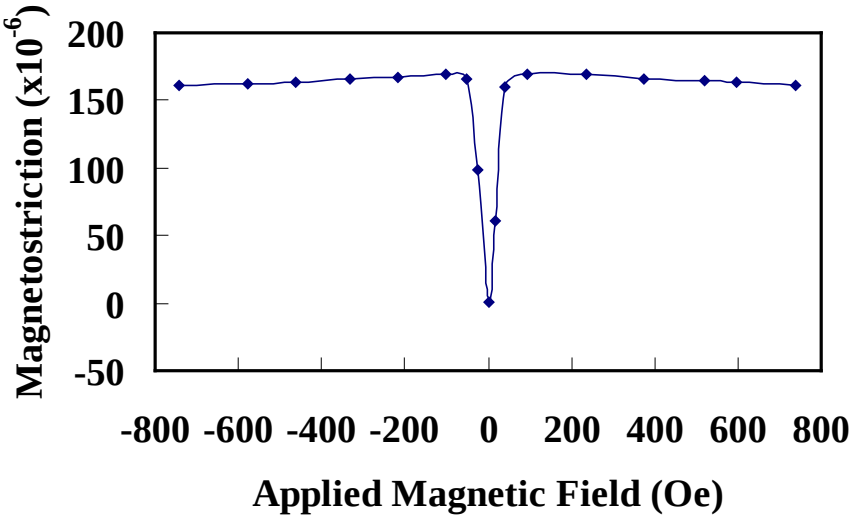

(a)

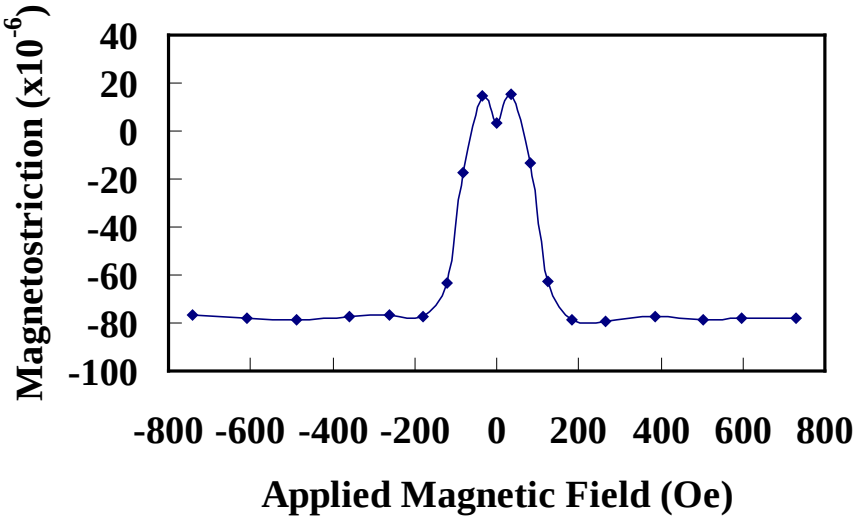

(b)

Figure 5.6 Magnetostrictive strain value versus applied magnetic field curves for the [001]-oriented Fe-17.5 at.% Ga-2.5 at.% W single crystal in the as-grown condition, with applied magnetic field (a) parallel and (b) perpendicular to the [001] direction.

Table 5.1 shows the magnetostriction coefficient $(3/2)\lambda_{100}$ values in the as-grown condition for [001]-oriented Fe-17.5 at.% Ga-2.5 at.% W, Fe-15 at.% Ga-2.5 at.% W and Fe-12.5 at.% Ga-2.5 at.% W single crystals.

After magnetostriction measurements in the as-grown condition, all of the Fe-Ga-W alloy single crystals were annealed at 1150°C for 4 hours followed by rapid water quenching to obtain the disordered α-phase at room temperature. Measurements of magnetostriction coefficient $(3/2)\lambda_{100}$ values were carried out on all of the samples after annealing. Figures 5.7, 5.8 and 5.9 show the magnetostrictive strain value versus applied magnetic field curves for $\lambda_{parallel}$ and $\lambda_{perpendicular}$ measurements in the annealed conditions of Fe-17.5 at.% Ga-2.5 at.% W, Fe-15 at.% Ga-2.5 at.% W and Fe-12.5 at.% Ga-2.5 at.% W single crystals. Table 5.2 shows the magnetostriction coefficient $(3/2)\lambda_{100}$ values in the annealed condition for [001]-oriented Fe-17.5 at.% Ga-2.5 at.% W, Fe-15 at.% Ga-2.5 at.% W and Fe-12.5 at.% Ga-2.5 at.% W single crystals.

Figure 5.10 shows a plot of magnetostriction coefficients $(3/2)\lambda_{100}$ value versus solute content in Fe, obtained from the data of Fe-Ga-W alloy single crystals from this work and Fe-Ga alloy single crystal data reported in earlier work [11]. As the Ga content increased by 2.5 at.% from Fe-12.5 at.% Ga-2.5 at.% W to Fe-15 at.% Ga-2.5 at.% W, the magnetostriction coefficient $(3/2)\lambda_{100}$ value in the annealed condition increased by about 67%. Further increase in Ga content by 2.5 at.% from Fe-15 at.% Ga-2.5 at.% W to Fe-17.5 at.% Ga-2.5 at.% W decreases the magnetostriction value by about 48%. Compared to the Fe-Ga alloy with similar solute content, W substitution results in at least a 7% decrease in the Fe-Ga alloy's magnetostriction coefficient $(3/2)\lambda_{100}$ value.

Table 5.1 Magnetostriction coefficient $(3/2)\lambda_{100}$ values for [001]-oriented Fe-Ga-W alloy single crystals in the as-grown condition.

Alloy Composition	Magnetostriction coefficient $(3/2)\lambda_{100}$ (x 10^{-6})
Fe-17.5 at.% Ga-2.5 at.% W	242
Fe-15 at.% Ga-2.5 at.% W	146
Fe-12.5 at.% Ga-2.5 at.% W	197

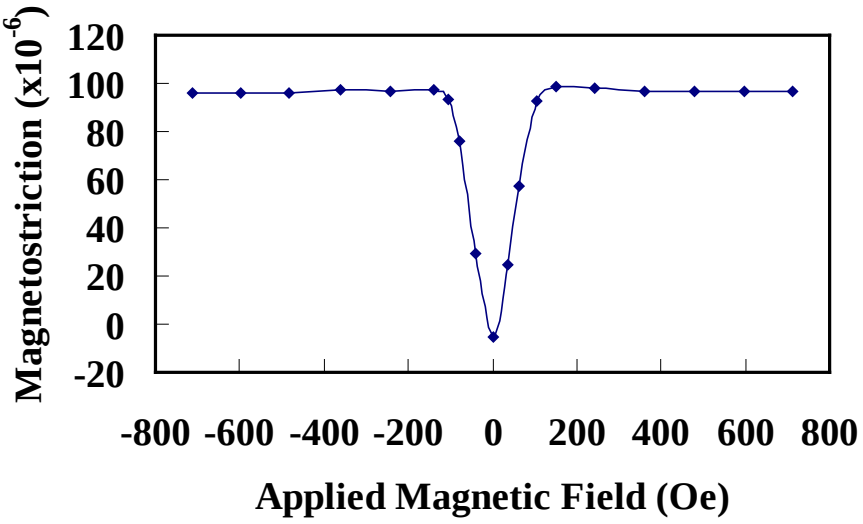

(a)

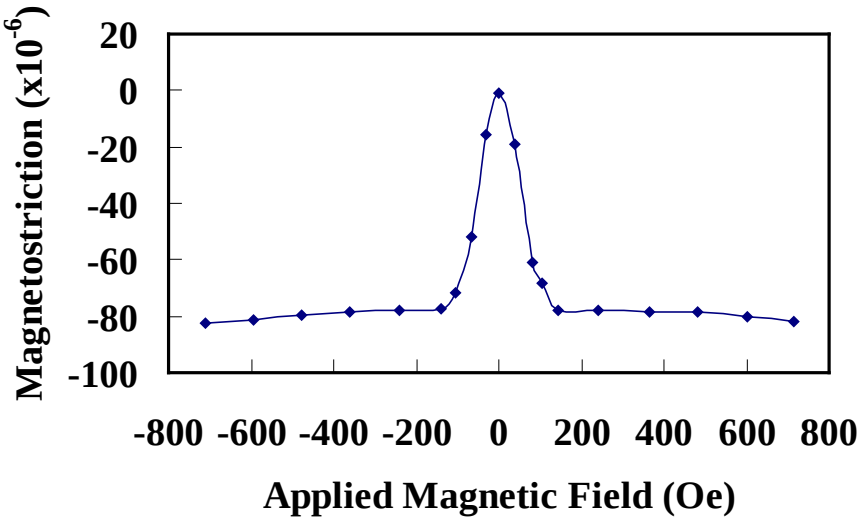

(b)

Figure 5.7 Magnetostrictive strain value versus applied magnetic field curves for the [001]-oriented Fe-12.5 at.% Ga-2.5 at.% W single crystal in the annealed condition, with applied magnetic field (a) parallel and (b) perpendicular to the [001] direction.

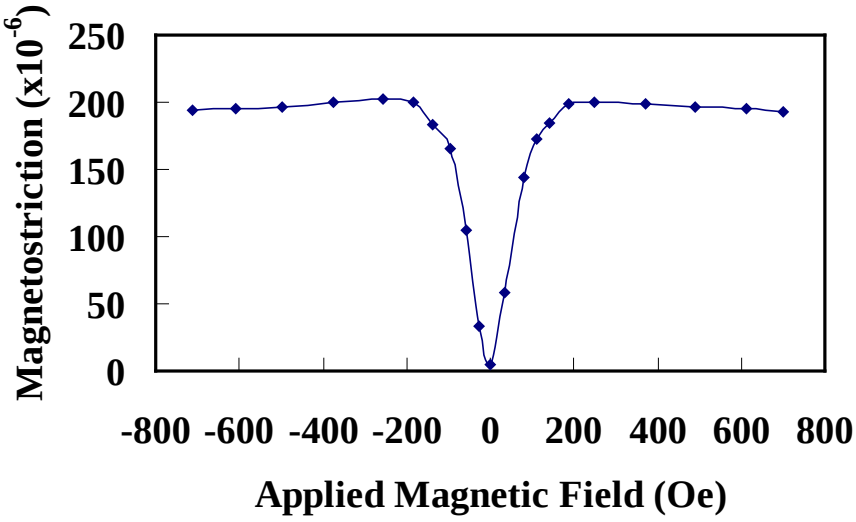

(a)

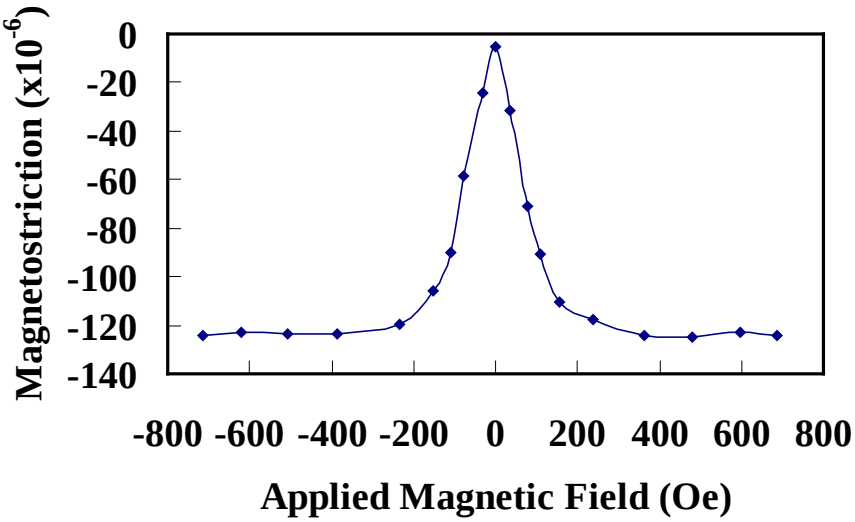

(b)

Figure 5.8 Magnetostrictive strain value versus applied magnetic field curves for the [001]-oriented Fe-15 at.% Ga-2.5 at.% W single crystal in the annealed condition, with applied magnetic field (a) parallel and (b) perpendicular to the [001] direction.

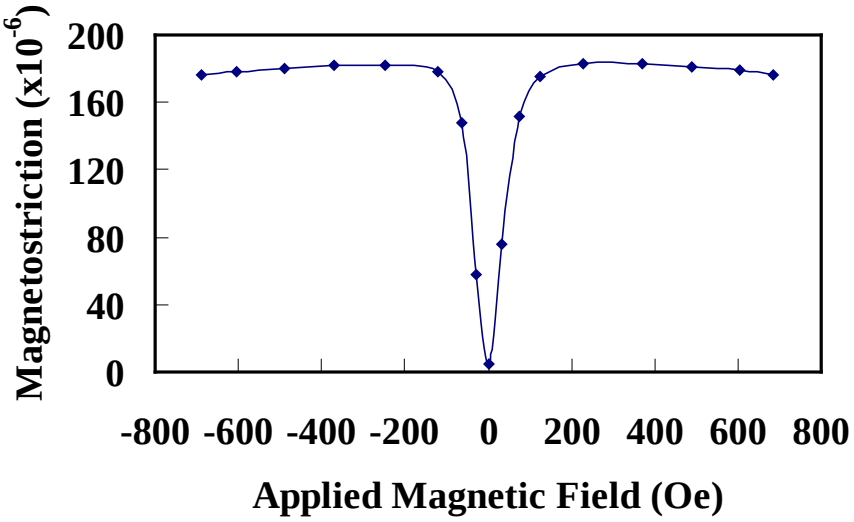

(a)

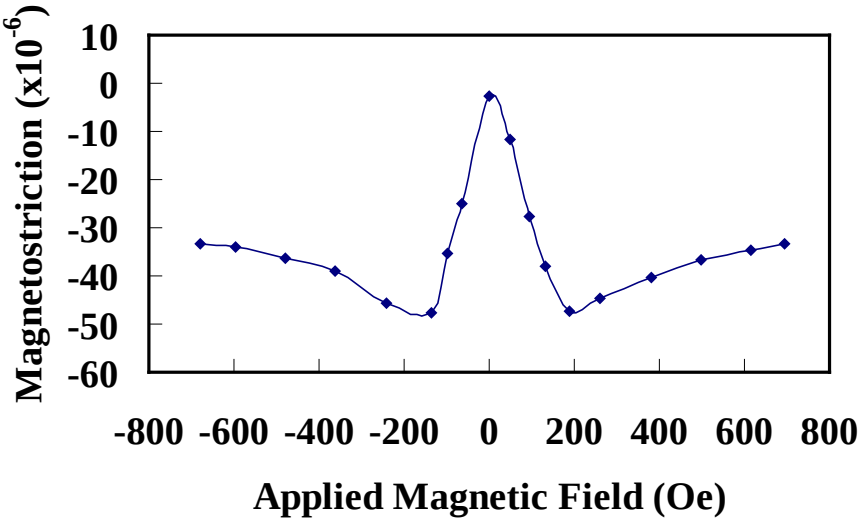

(b)

Figure 5.9 Magnetostrictive strain value versus applied magnetic field curves for the [001]-oriented Fe-17.5 at.% Ga-2.5 at.% W single crystal in the annealed condition, with applied magnetic field (a) parallel and (b) perpendicular to the [001] direction.

Table 5.2 Magnetostriction coefficient $(3/2)\lambda_{100}$ values obtained for [001]-oriented Fe-Ga-W alloy single crystals in the annealed condition.

Alloy Composition	Magnetostriction coefficients $(3/2)\lambda_{100}$ (x 10^{-6})
Fe-17.5 at.% Ga-2.5 at.% W	203
Fe-15 at.% Ga-2.5 at.% W	307
Fe-12.5 at.% Ga-2.5 at.% W	183

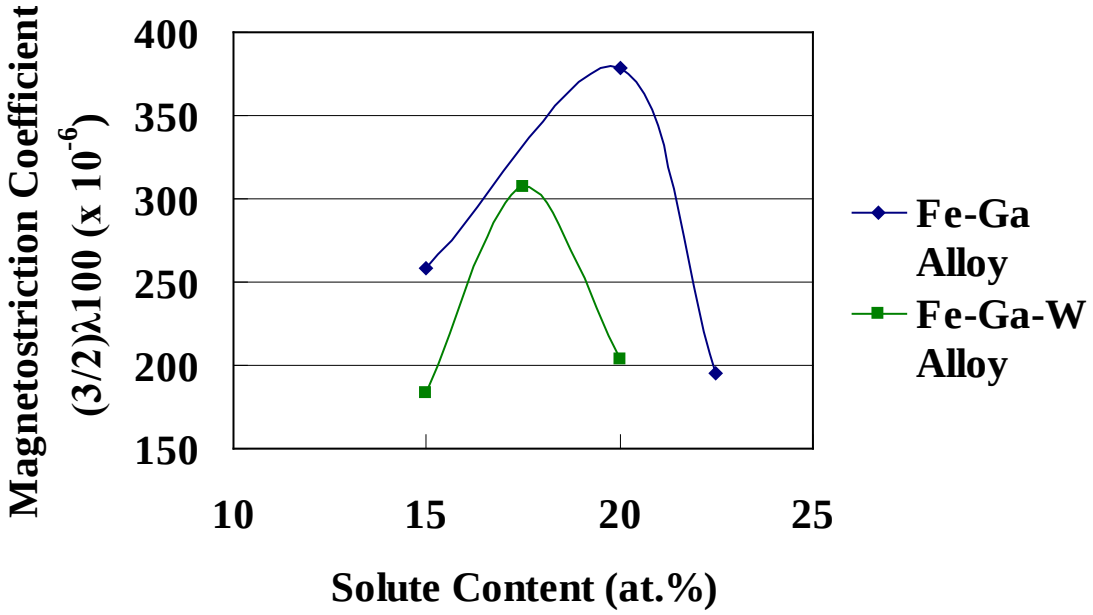

Figure 5.10 Magnetostriction coefficients $(3/2)\lambda_{100}$ value vs. solute content in Fe plots of Fe-x at.% Ga-2.5 at.% W and Fe-x at.% Ga alloy single crystals.

The substitution of W to various high Ga content Fe-x at.% Ga alloys can cause the formation of ordered intermetallic second phases in the alpha-Fe alloy terminal solid solution matrix phase. These second phases have different crystal structure and densities compared to the matrix α-phase with disordered BCC structure and can introduce internal strains across the lattice. The reduction in the magnetostriction by W substitution is most likely related to the expected formation of these second phases and the associated strains.

5.1.3 Magnetostriction Measurement of $(3/2)\lambda_{111}$ Coefficient

The magnetostriction measurements were made on the [220]-oriented Fe- 12.5 at.% Ga- 2.5at.% W alloy disc-shaped single crystal to obtain the $(3/2)\lambda_{111}$ magnetostriction coefficient. The strain gage was mounted at the center of the [220]-oriented face and parallel to the $[\bar{1}11]$ crystallographic direction. Magnetostriction strain values were obtained by applying magnetic field along the $[\bar{1}11]$ direction for $\lambda_{parallel}$ and along the $[1\bar{1}2]$ direction for $\lambda_{perpendicular}$ measurements. Figure 5.11 shows the magnetostriction strain value versus applied magnetic field curves of the as-grown Fe-12.5 at.% Ga- 2.5 at.% W alloy single crystal sample. The $\lambda_{parallel}$ value observed is about -10×10^{-6} and the $\lambda_{perpendicular}$ value is about 24×10^{-6}. Based on the calculation $(3/2)\lambda_{111} = \lambda_{parallel} - \lambda_{perpendicular}$, the $(3/2)\lambda_{111}$ value of Fe- 12.5 at.% Ga- 2.5 at.% W alloy was observed to be -34×10^{-6} for the as-grown condition.

After magnetostriction measurements in the as-grown condition, the [220]-oriented Fe- 12.5at.% Ga- 2.5at.% W single crystal was annealed at 1150°C for 4 hours followed by rapid water quenching. This heat treatment process minimizes the formation of second phases and provides a more homogeneous disordered α-phase. Measurements

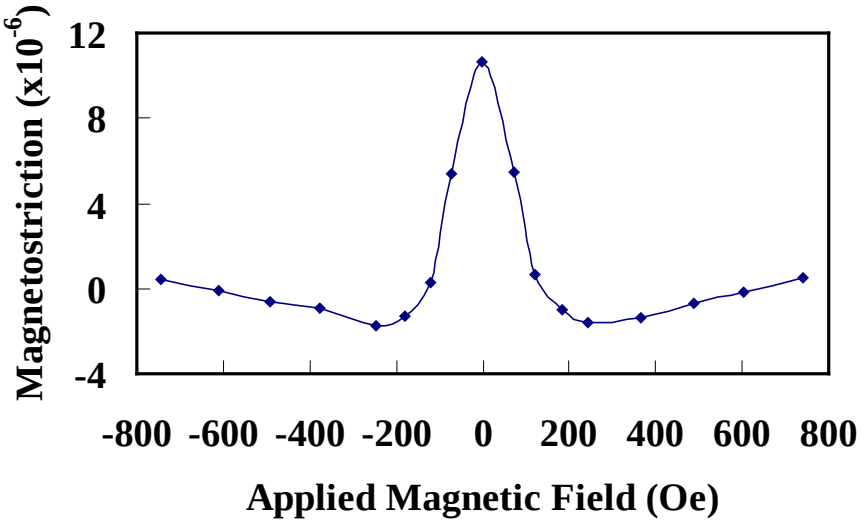

(a)

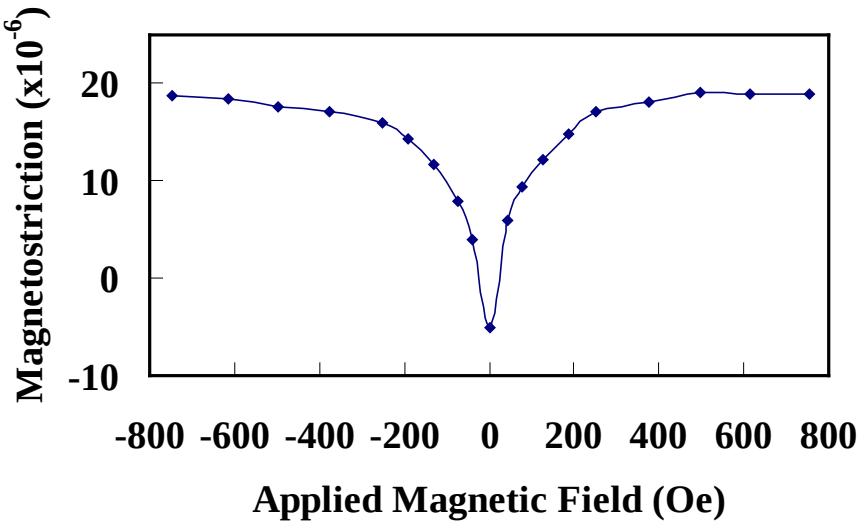

(b)

Figure 5.11 Magnetostrictive strain value versus applied magnetic field curves obtained for the [220]-oriented Fe-12.5 at.% Ga-2.5 at.% W single crystal at as-grown condition, with applied magnetic field (a) parallel and (b) perpendicular to the $[\bar{1}11]$ direction.

of magnetostriction coefficient $(3/2)\lambda_{111}$ values were carried out on this sample after annealing in the same configuration as for DG condition measurements. Figure 5.12 shows the magnetostriction strain value versus applied magnetic field curves for $\lambda_{parallel}$ and $\lambda_{perpendicular}$ measurements in the annealed condition of the Fe-12.5 at.% Ga-2.5 at.% W single crystal. In this condition, the $\lambda_{parallel}$ value is about -32×10^{-6} and the $\lambda_{perpendicular}$ value is about 15×10^{-6}. The $(3/2)\lambda_{111}$ magnetostriction coefficient value of annealed Fe-12.5 at.% Ga- 2.5 at.% W alloy was observed to be -47×10^{-6}. By using the Equation 2.18 discussed in the background section, the saturation magnetostriction λ_{si} of all the crystallographic directions for this alloy can be calculated from the $(3/2)\lambda_{100}$ and $(3/2)\lambda_{111}$ magnetostriction coefficients.

5.1.4 Saturation Magnetization Measurement

For saturation magnetization measurements, samples of Fe-12.5 at.% Ga-2.5 at.% W, Fe-15 at.% Ga-2.5 at.% W and Fe-17.5 at.% Ga-2.5 at.% W that were about 2 x 2 x 2 mm^3 in size were cut and prepared from the as-cast ingots as discussed in the experimental section. Hysteresis curves were obtained for all of the samples by applying magnetic fields up to 10 kG. Figure 5.13 shows the hysteresis curve of the Fe-12.5 at.% Ga-2.5 at.% W alloy. The hysteresis curves of Fe-15 at.% Ga-2.5 at.% W and Fe-17.5 at.% Ga-2.5 at.% W alloys are presented in Appendix B. The summary of the saturation magnetization for all of the Fe-Ga-W alloys is shown in Table 5.3. Figure 5.14 shows a plot of magnetization value versus solute content for the three Fe-x at.% Ga-2.5 at.% W alloys.

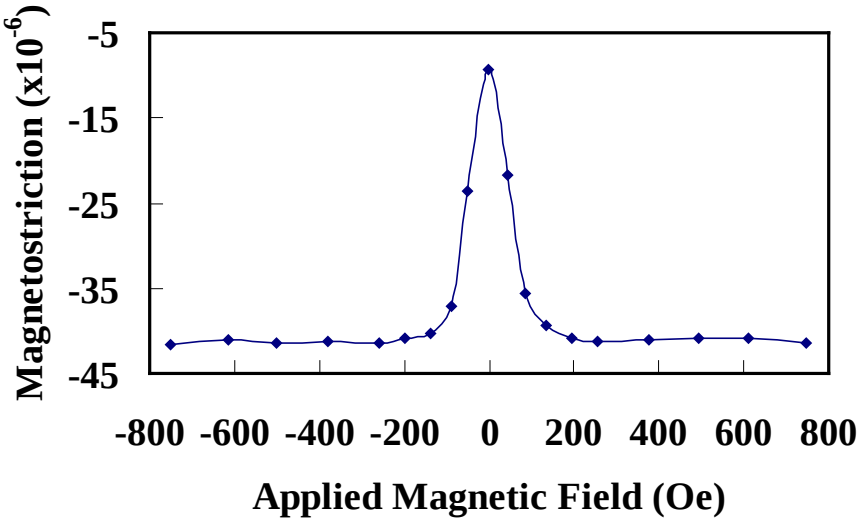

(a)

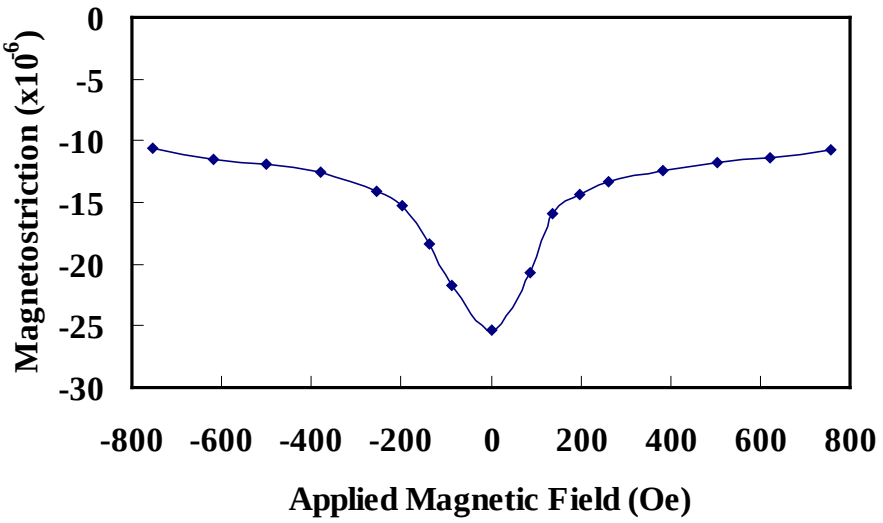

(b)

Figure 5.12 Magnetostrictive strain value versus applied magnetic field curves obtained for the [220]-oriented Fe-12.5 at.% Ga-2.5 at.% W single crystal at annealed condition, with applied magnetic field (a) parallel and (b) perpendicular to the $[\bar{1}11]$ direction.

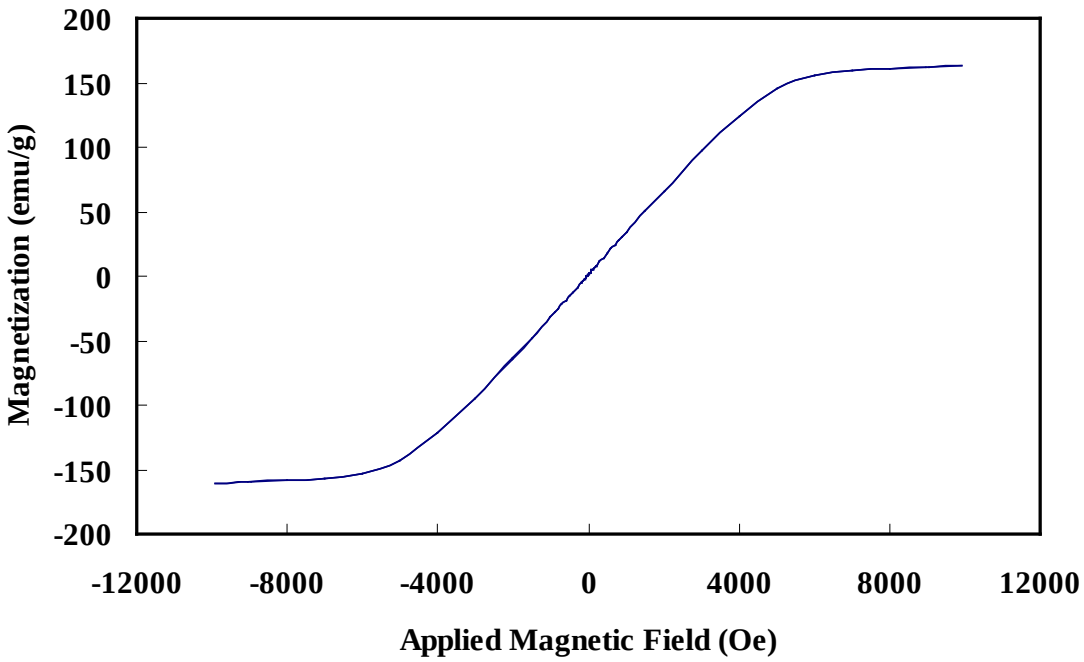

Figure 5.13 Hysteresis curve of Fe-12.5 at.% Ga-2.5 at.% W directionally cast alloy sample.

Table 5.3 Magnetization values obtained for various Fe- x at.% Ga- 2.5 at.% W alloys

Alloy Composition	Magnetization (emu/g)
Fe-12.5 at.% Ga-2.5 at.% W	164
Fe-15 at.% Ga-2.5 at.% W	159
Fe-17.5 at.% Ga-2.5 at.% W	140

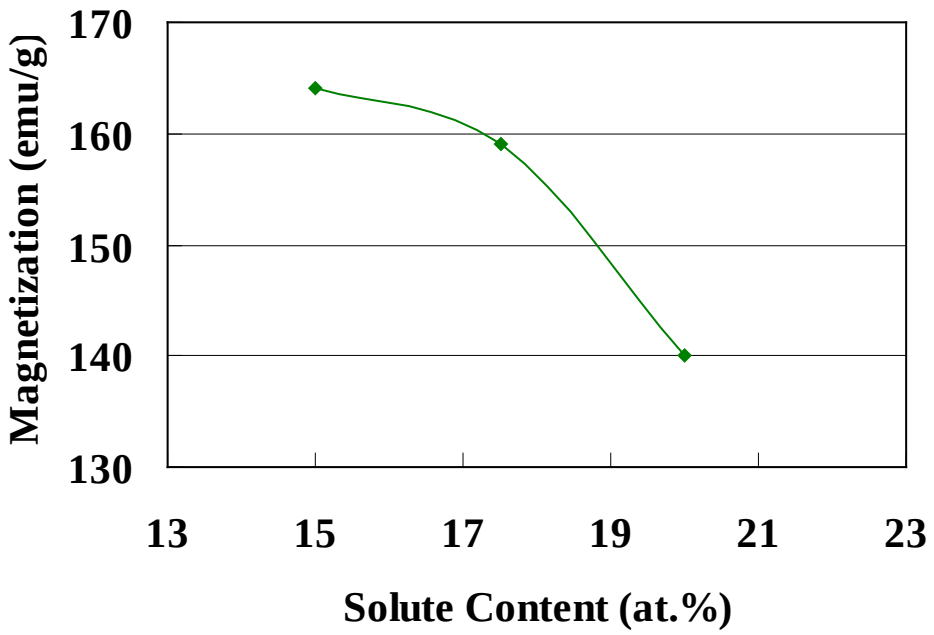

Figure 5.14 Magnetization value versus solute content for various Fe-x at.% Ga-2.5 at.% W alloys.

As the solute content increases, the magnetization of Fe-Ga-W alloys decreases rapidly. The drop in saturation magnetization after solute content increased to more than that of the Fe-15 at.% Ga-2.5 at.% W alloy is likely caused by the formation of intermetallic second phases. This result is consistent with the results of magnetostriction measurements.

5.1.5 TEM Study of Fe-Ga-W Alloy

The TEM sample of Fe-Ga-W alloy was prepared from the cut piece of the Fe-17.5 at.% Ga-2.5 at.% W alloy single crystal. The 3mm diameter sample disc was oriented in the [001] crystallographic direction and annealed at 1150°C for 4 hours to obtain similar structure as the magnetostriction measurement sample. Figure 5.15 shows a bright-field TEM image obtained from the annealed Fe-17.5 at.% Ga-2.5 at.% W sample and no significant second phase region can be observed. Based on the image, the second phases formed inside the Fe-Ga-W alloy after annealing must be small domains coherent with the main disordered α-Fe matrix. Figure 5.16 shows the [001] diffraction pattern which indicates the high quality of the single crystal and orientation. Figure 5.17 shows the Lorentz image obtained on the [001]-oriented single crystal face. Rod-shaped magnetic domains nicely aligned parallel to each other and along one crystallographic direction can be observed.

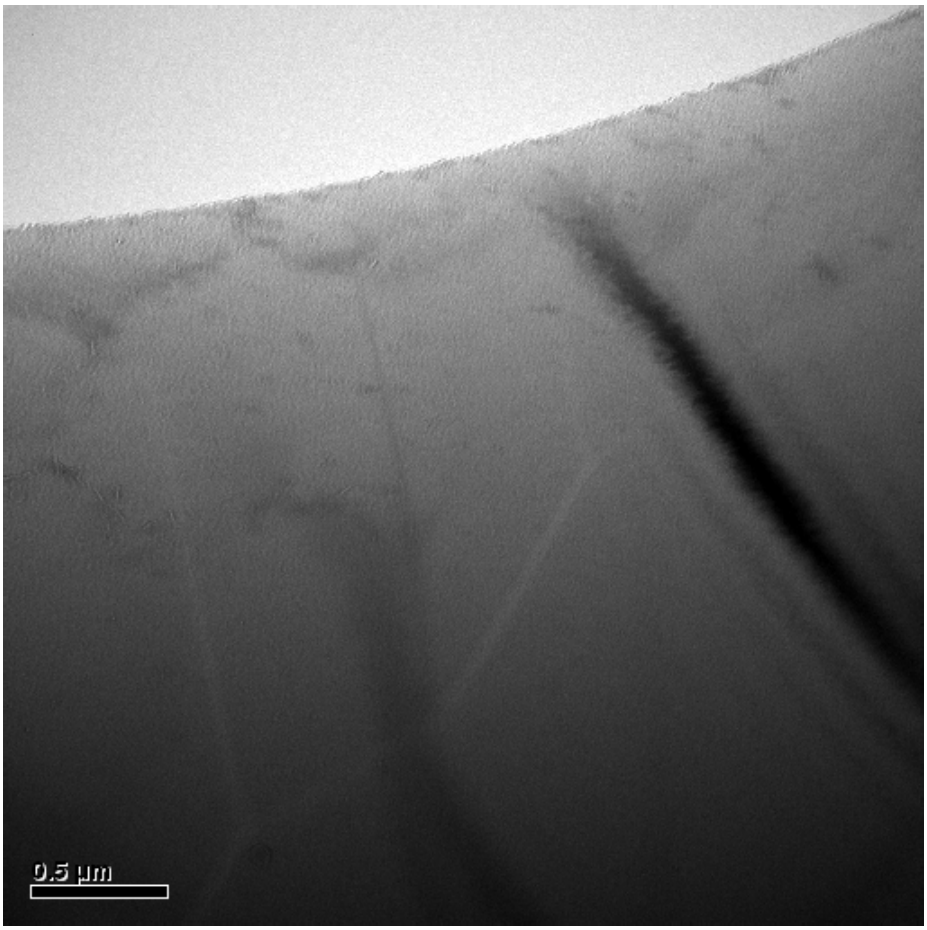

Figure 5.15 Bright-field TEM image of annealed Fe-17.5 at.% Ga-2.5 at.% W alloy single crystal.

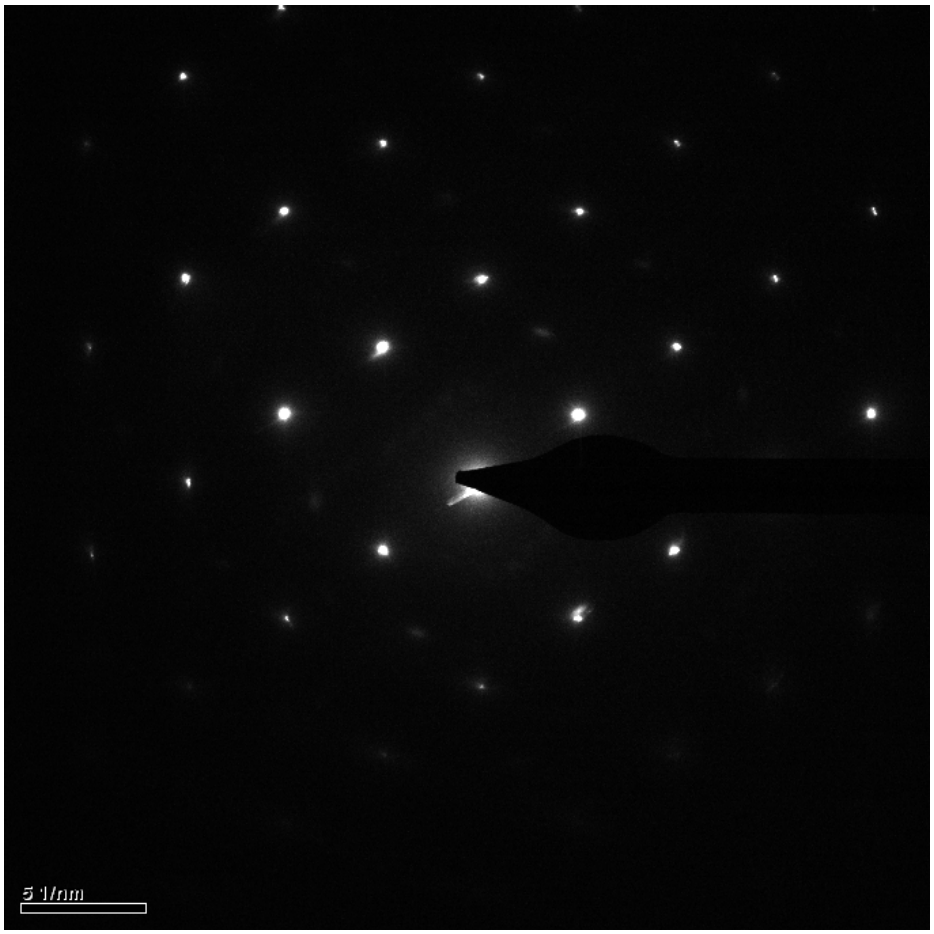

Figure 5.16 Diffraction pattern of annealed Fe-17.5 at.% Ga-2.5 at.% W alloy single crystal corresponding to the image shown in Figure 5.17.

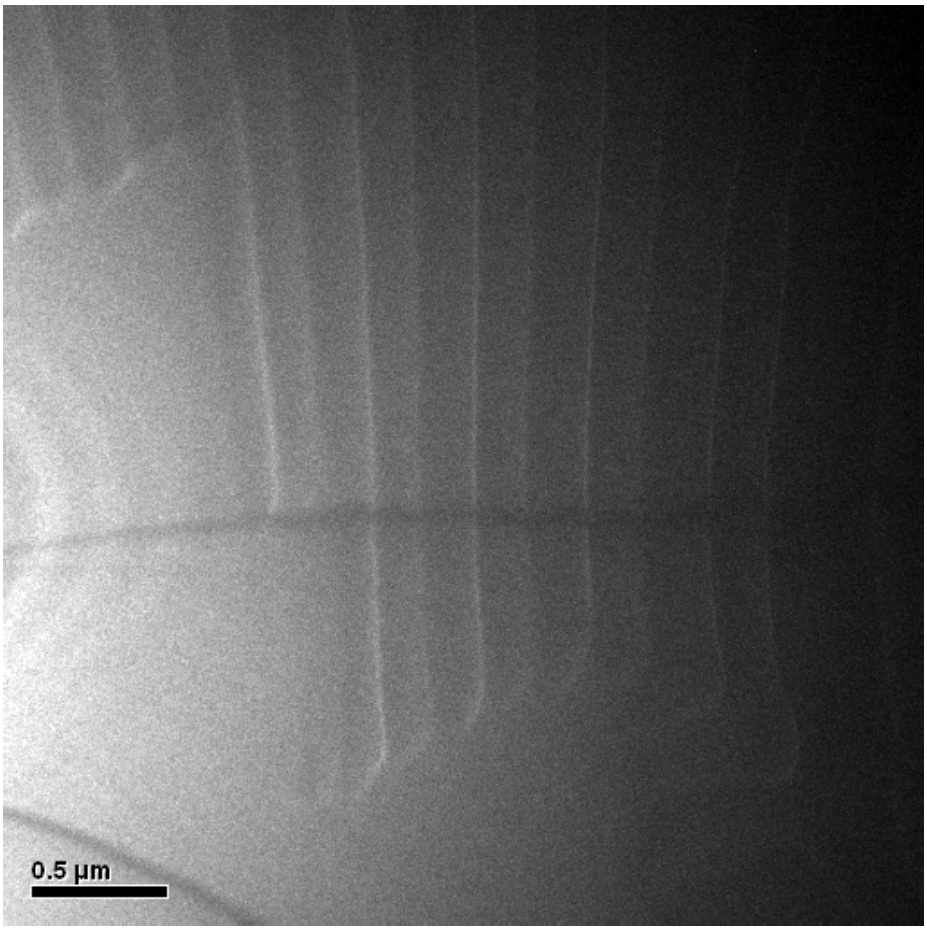

Figure 5.17 Lorentz image of annealed Fe-17.5 at.% Ga-2.5 at.% W alloy single crystal on the [001]-oriented face.

5.2 Magnetostriction Study of Fe-W alloys

5.2.1 XRD Analysis and Single Crystal Characterization

X-ray diffraction scans were made on all of the samples after large crystals were cut from a directionally grown ingot to obtain the crystal orientation data for each of the alloys. For an XRD θ-2θ scan pattern of an as-cut face, a set of peaks are observed. Each of these peaks corresponds to one of the crystal planes. Figure 5.18 shows the θ-2θ scan pattern of the as-cut face of the Fe-3 at.% W alloy DG ingot. As discussed in the experimental section, these $2\theta_{hkl}$ values are used in the single crystal characterization using rocking curve scans. In the rocking curve scans, the detector is fixed at the corresponding $2\theta_{hkl}$ value and the sample is rotated about the diffractometer axis. The position of the rocking curve peak provides the ω value of the cut face. The deviation of ω from the value corresponding to half of the 2 θ_{hkl} value is the deviation of the sample face orientation from the desired crystal orientation. Figure 5.19 shows the rocking curve scan of the [220]-oriented face of the Fe-3 at.% W single crystal. The ω value at the rocking curve peak position is 49.25°. As the θ_{220} value of this alloy is 49.17°, the face is already oriented within 0.1° off the desired [220] orientation. If the sample is perfectly oriented, there will be diffraction only from the (hh0) family of planes of a [220]-orientation single crystal. Figure 5.20 shows the θ-2θ scan made on the (220) face of the disc-shaped Fe-3 at.% W single crystal prepared for λ_{111} magnetostriction measurements. Only the 2θ peaks corresponding to the (110) fundamental reflection at 44.68° and (220) fundamental reflection at 98.58° appeared in the XRD pattern which proved the quality of crystal orientation work. Similarly this single crystal orientation work was also done on

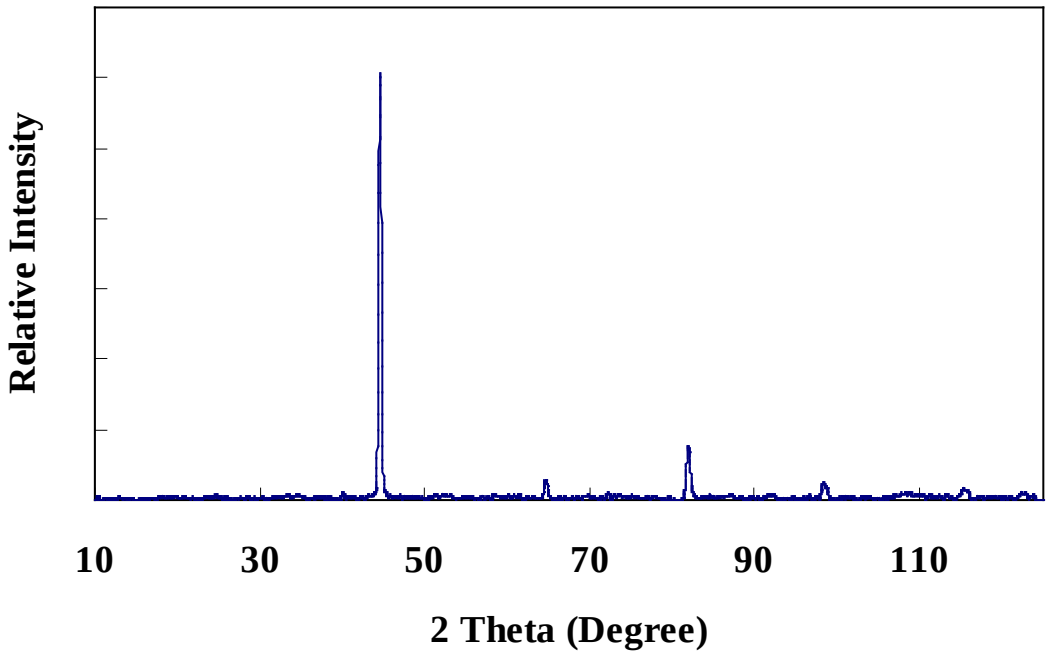

Figure 5.18 Theta- 2 theta x-ray diffraction scan on the first cut face of DG rod of the Fe-3 at.% W single crystal.

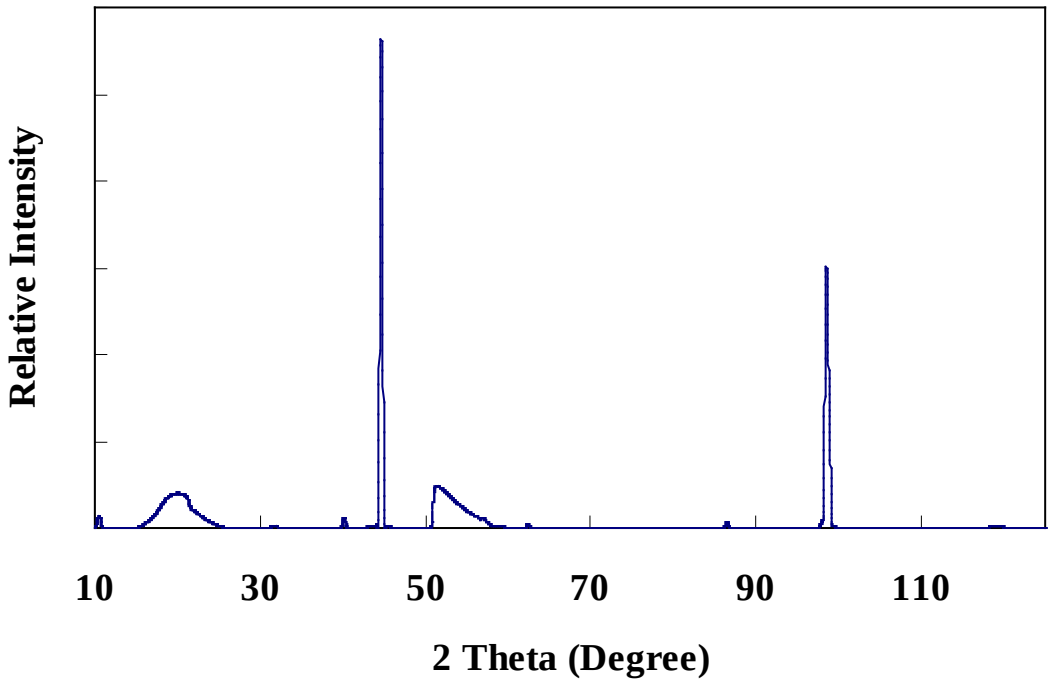

Figure 5.19 Theta- 2 theta x-ray diffraction scan on the (220) face of the [220]-oriented Fe-3 at.% W single crystal.

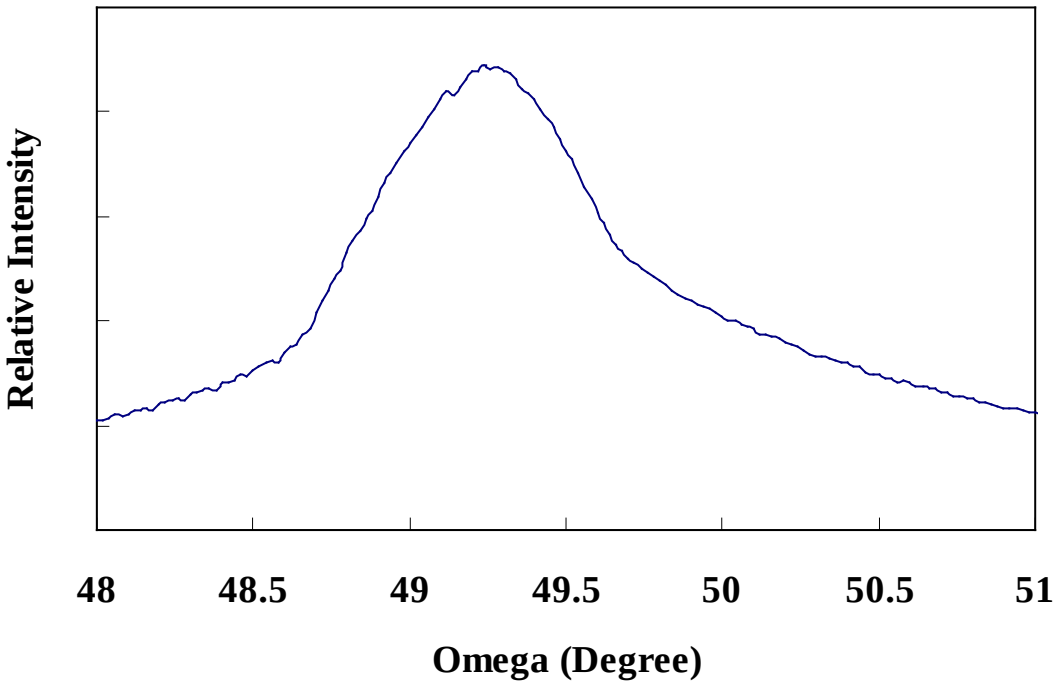

Figure 5.20 Rocking curve x-ray diffraction scan on the (220) face of the [220]-oriented Fe-3 at.% W single crystal.

the [220]-oriented Fe-7.5 at.% W and [211]-oriented Fe- 6 at.% W single crystals. The list of disc-shaped Fe-x at.% W single crystals and their corresponding orientation are shown in Table 5.4, and the related θ-2θ scans on the as-cut faces, rocking curve scan on oriented faces and θ-2θ scans on oriented faces are presented in Appendix A.

5.2.2 Measurement of Magnetostriction Coefficient $(3/2)\lambda_{111}$

Magnetostriction measurements were made at room temperature without any external load on the samples. The strain gages were mounted parallel to the $[\bar{1}11]$ crystallographic directions on the flat [220] or [211]-oriented disc faces. The $\lambda_{parallel}$ and $\lambda_{perepndicular}$ values were obtained by placing the sample's $[\bar{1}11]$ direction parallel or perpendicular to the magnetic field and measuring the saturation magnetostriction. As discussed in the experimental work section, the $(3/2)\lambda_{111}$ magnetostriction coefficient values can be calculated based on the equation $(3/2)\lambda_{100} = \lambda_{parallel} - \lambda_{perpendicular}$.

Figure 5.21 shows the magnetostrictive strain value versus applied magnetic field curves for $\lambda_{parallel}$ and $\lambda_{perpendicular}$ measurements corresponding to the as-grown condition of the [220]-oriented Fe- 3 at.% W disc-shaped single crystal. For this sample, the strain gage was mounted on the [220]-oriented face along the $[\bar{1}11]$ crystallographic direction. Figure 5.21(a) corresponds to the magnetostriction measurement by applying the magnetic field parallel to the $[\bar{1}11]$ direction to obtain the $\lambda_{parallel}$ value. The saturation magnetostriction strain under this condition was -14×10^{-6}. Figure 5.21(b) corresponds to the magnetostriction measurement by applying the magnetic field along the $[1\bar{1}2]$ crystallographic direction which is perpendicular to the $[\bar{1}11]$ direction on the [220] face.

Table 5.4 List of disc-shaped Fe-x at.% W single crystals and their corresponding orientations.

Alloy Composition	Disk Face Orientation	Strain Measurement Direction	Magnetic field direction for Parallel Measurement	Magnetic field direction for Perpendicular Measurement
Fe- 3at.% W	[220]	$[\bar{1}11]$	$[\bar{1}11]$	$[1\bar{1}2]$
Fe- 6at.% W	[211]	$[\bar{1}11]$	$[\bar{1}11]$	$[0\bar{2}2]$
Fe- 7.5at.% W	[220]	$[\bar{1}11]$	$[\bar{1}11]$	$[1\bar{1}2]$

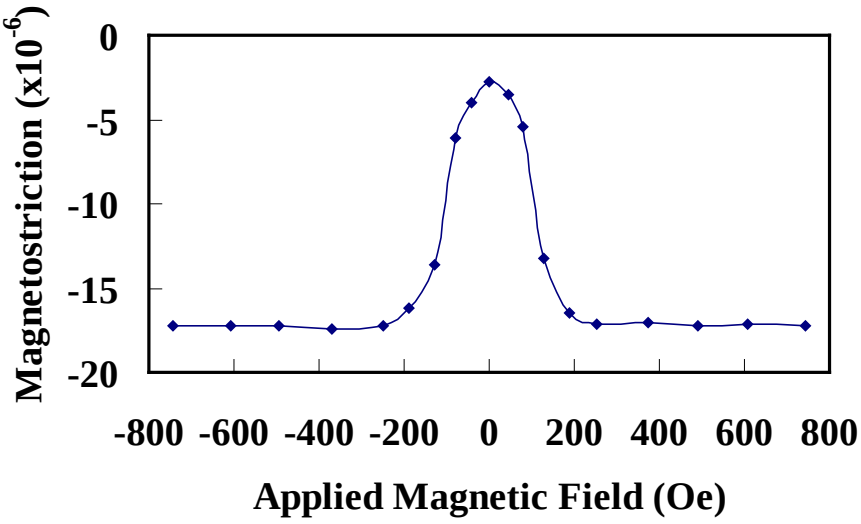

(a)

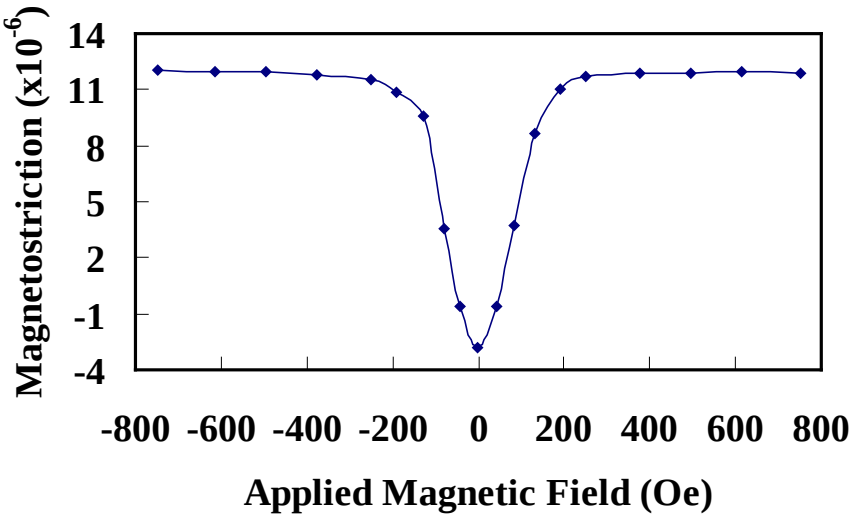

(b)

Figure 5.21 Magnetostrictive strain value versus applied magnetic field curves obtained for the [220]-oriented Fe-3 at.% W single crystal in the as-grown condition, with applied magnetic field (a) parallel and (b) perpendicular to the $[\bar{1}11]$ direction.

The saturation magnetostrictive strain under this condition was 15 x 10^{-6}. For the Fe- 3 at.% W DG alloy sample, the $(3/2)\lambda_{111}$ value was observed to be -29 x 10^{-6}.

Figure 5.22 shows the magnetostrictive strain value versus applied magnetic field curves for $\lambda_{parallel}$ and $\lambda_{perpendicular}$ measurements corresponding to the as-grown condition of the [211]-oriented Fe- 6 at.% W disc-shaped single crystal. For this sample, the strain gage was mounted on the [211]-oriented face along the $[\bar{1}11]$ crystallographic direction. Figure 5.22 (a) corresponds to the magnetostriction measurement by applying magnetic field parallel to the $[\bar{1}11]$ direction to obtain the $\lambda_{parallel}$ value. The saturation magnetostrictive strain under this condition was -14 x 10^{-6}. Figure 5.22 (b) corresponds to the magnetostriction measurement by applying magnetic field along $[0\bar{2}2]$ crystallographic direction, which is perpendicular to the $[\bar{1}11]$ direction on the [211] face. The saturation magnetostriction strain under this condition was 17 x 10^{-6}. For the Fe- 6 at.% W DG sample, the $(3/2)\lambda_{111}$ value was observed to be -31 x 10^{-6}.

Figure 5.23 shows the magnetostrictive strain value versus applied magnetic field curves for $\lambda_{parallel}$ and $\lambda_{perpendicular}$ measurements corresponding to the as-grown condition of the [220]-oriented Fe- 7.5 at.% W disc-shaped single crystal. For this sample, the strain gage was mounted on the [220]-oriented face along the $[\bar{1}11]$ crystallographic direction. Figure 5.23 (a) corresponds to the magnetostriction measurement by applying magnetic field parallel to the $[\bar{1}11]$ direction to obtain the $\lambda_{parallel}$ value. The saturation magnetostriction strain under this condition was -19 x 10^{-6}. Figure 5.23 (b) corresponds to the magnetostriction measurement by applying magnetic field along the $[1\bar{1}2]$ crystallographic direction, which is perpendicular to the $[\bar{1}11]$ direction on the [220]

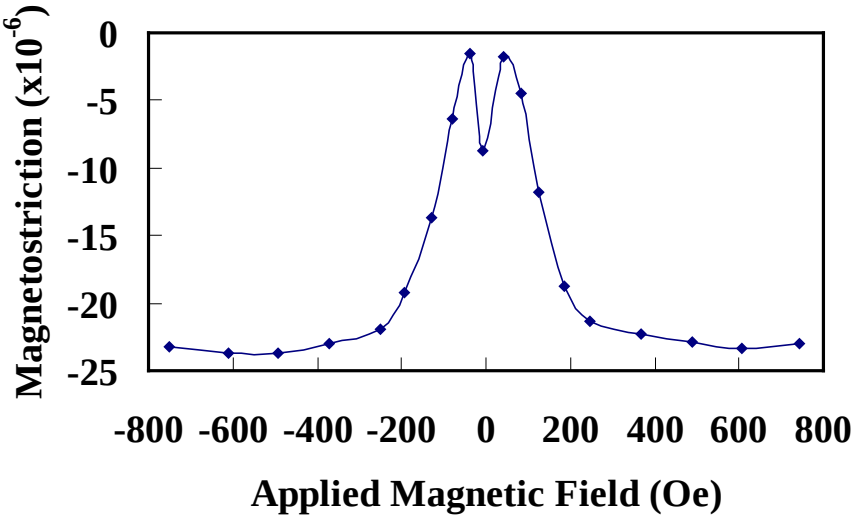

(a)

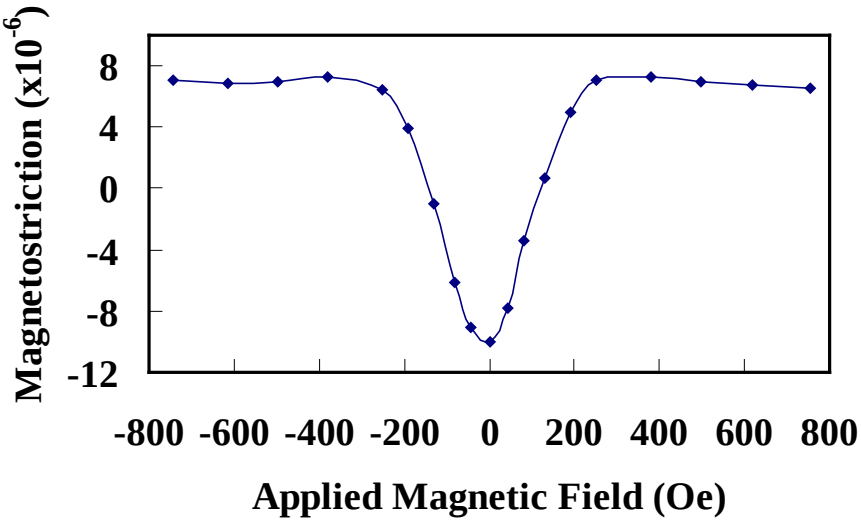

(b)

Figure 5.22 Magnetostrictive strain value versus applied magnetic field curves obtained for the [211]-oriented Fe-6 at.% W single crystal in the annealed condition, with applied magnetic field (a) parallel and (b) perpendicular to the $[\bar{1}11]$ direction.

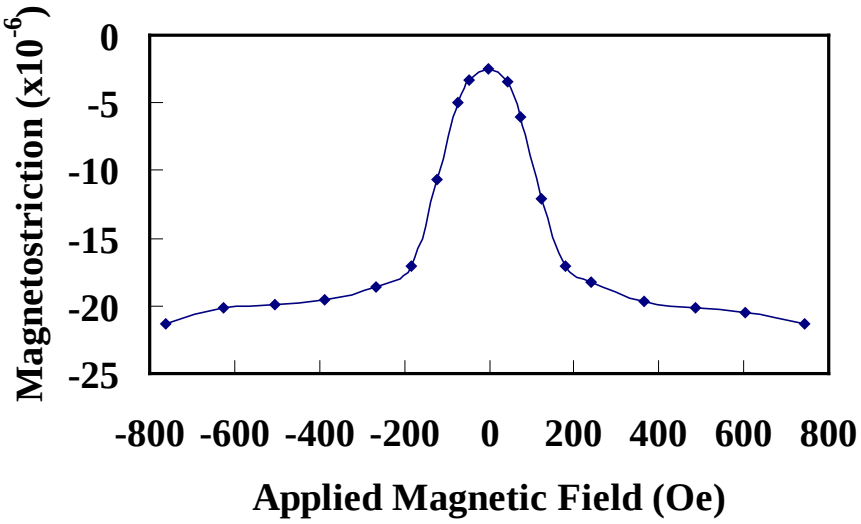

(a)

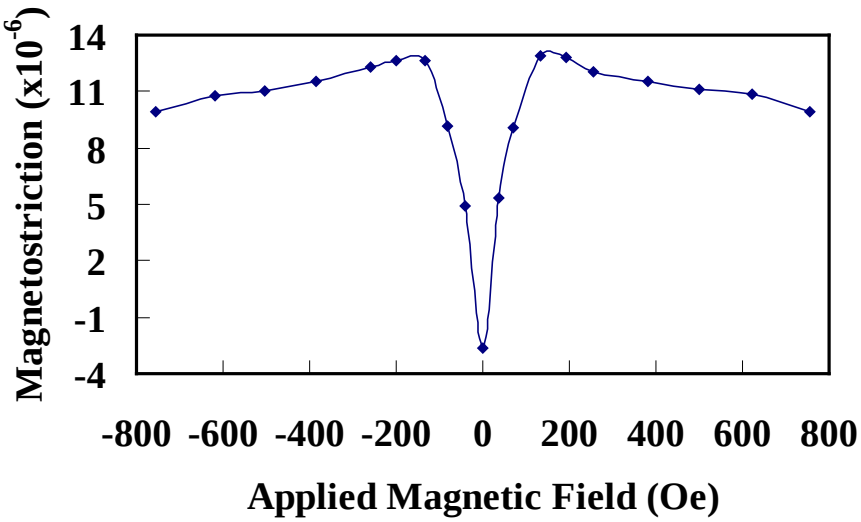

(b)

Figure 5.23 Magnetostrictive strain value versus applied magnetic field curves obtained for the [220]-oriented Fe-7.5 at.% W single crystal at annealed condition, with applied magnetic field (a) parallel and (b) perpendicular to the [111] direction.

face. The saturation magnetostriction strain under this condition was 13 x 10^{-6}. For the Fe- 7.5 at.% W DG alloy sample, the $(3/2)\lambda_{111}$ value was observed to be -32 x 10^{-6}.

Table 5.5 shows the summary of magnetostriction coefficient $(3/2)\lambda_{111}$ values in the as-grown condition for Fe- 3at.% W, Fe- 6at.% W and Fe- 7.5 at.% W alloy single crystals. There is a tendency for the increase of magnetostriction as the W content increased. Based on the Fe-W phase diagram [47], when Fe-W alloy is cooled slowly from the high temperature ordered second phase, Fe_7W_6 precipitate can form in the BCC disordered matrix. This second phase has different crystal structure and density compared to the disordered α-Fe matrix and its presence is the likely cause for the reduction of magnetostriction.

After magnetostriction measurements in the as-grown condition, all the Fe-W alloy single crystals were annealed in the α-phase region followed by rapid water quenching. The details of heat treatment conditions for various Fe-W alloys are shown in Table 5.6. This process minimizes the formation of the second phase and obtains a more homogeneous disordered α-phase matrix inside the crystal structure.

Measurements of magnetostriction coefficient $(3/2)\lambda_{111}$ values were carried out on all of the samples after this heat treatment process. The strain gages were mounted exactly in the same position as in the measurements in the DG condition and by applying the magnetic field parallel and perpendicular to the magnetostrictive strain measurement direction. $\lambda_{parallel}$ and $\lambda_{perepndicular}$ values were obtained from these measurements. Figures 5.24, 5.25 and 5.26 correspond to the magnetostrictive strain value versus applied magnetic field curves for $\lambda_{parallel}$ and $\lambda_{perpendicular}$ measurements of Fe-3 at.% W, Fe-6at.%W and Fe- 7.5at.% W disc-shaped annealed single crystals, respectively. Table 5.7

Table 5.5 Magnetostriction coefficient $(3/2)\lambda_{111}$ values obtained for [220] or [211]-oriented Fe-W alloy single crystals in the as-grown condition.

Alloy Composition	Magnetostriction coefficients $(3/2)\lambda_{111}$ (x 10^{-6})
Fe-3 at.% W	-29
Fe-6 at.% W	-31
Fe-7.5 at.% W	-32

Table 5.6 Heat treatment conditions for Fe-x at.% W single alloy crystals

Alloy Composition	Annealing Temperature (˚C)	Annealing Time (Hours)
Fe- 3 at.% W	1250	4
Fe- 6 at.% W	1420	4
Fe- 7.5 at.% W	1420	4

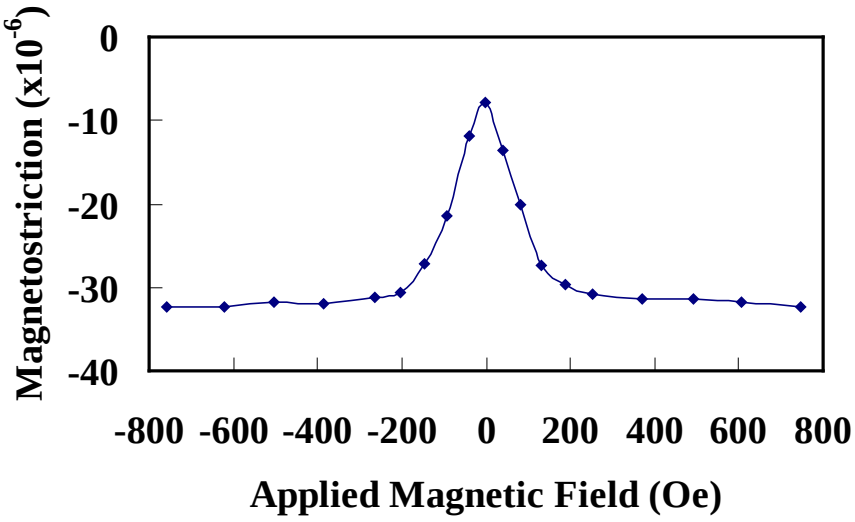

(a)

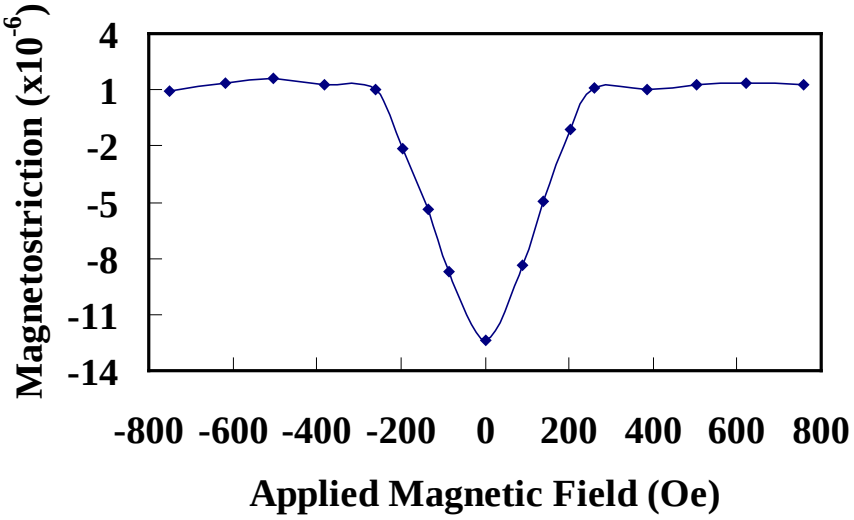

(b)

Figure 5.24 Magnetostrictive strain value versus applied magnetic field curves obtained for the [220]-oriented Fe-3 at.% W single crystal at annealed condition, with (a) applied magnetic field parallel and (b) perpendicular to the $[\bar{1}11]$ direction.

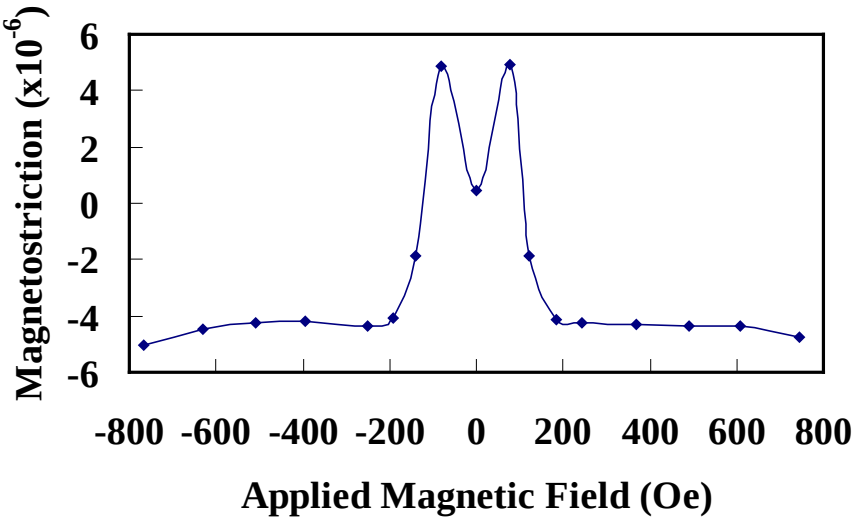

(a)

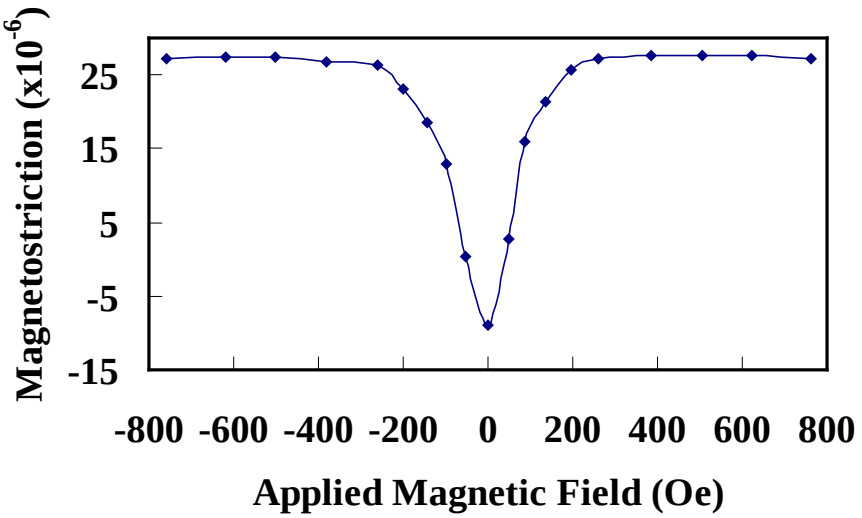

(b)

Figure 5.25 Magnetostrictive strain value versus applied magnetic field curves obtained for the [211]-oriented Fe-6 at.% W single crystal at annealed condition, with applied magnetic field (a) parallel and (b) perpendicular to the $[\bar{1}11]$ direction.

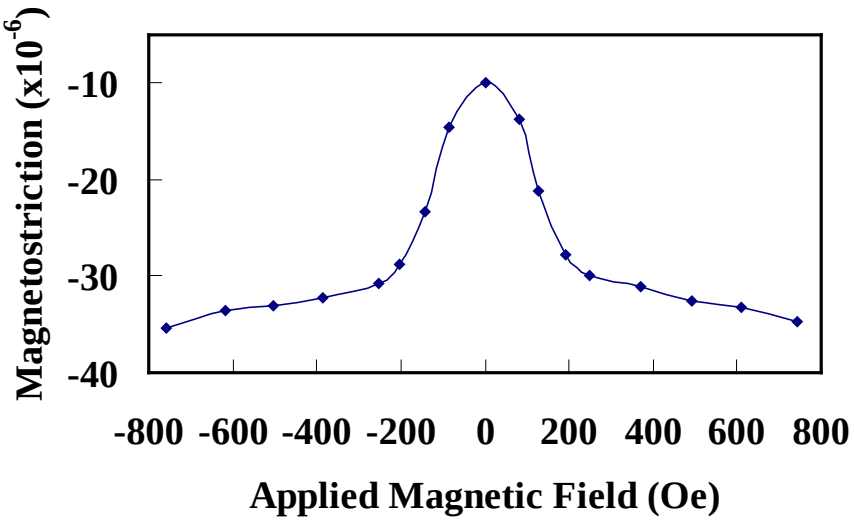

(a)

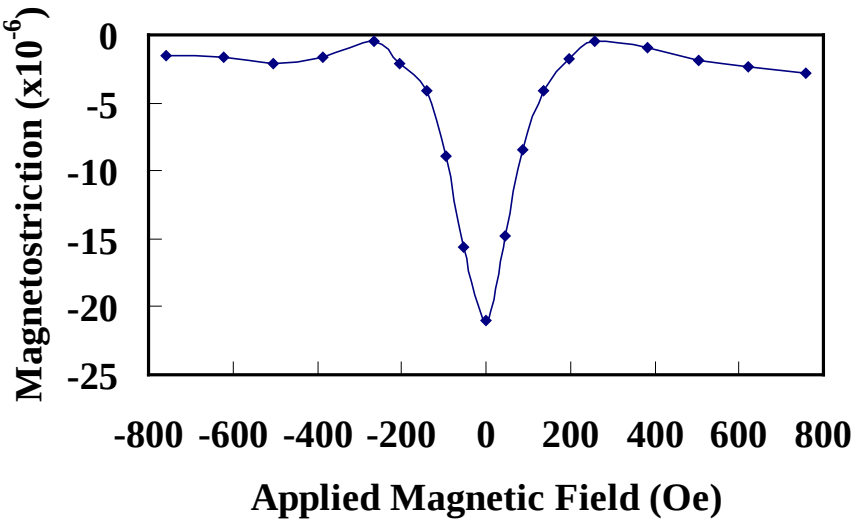

(b)

Figure 5.26 Magnetostrictive strain value versus applied magnetic field curves obtained for the [220]-oriented Fe-7.56 at.% W single crystal at annealed condition, with applied magnetic field (a) parallel and (b) perpendicular to the $[\bar{1}11]$ direction.

Table 5.7 Magnetostriction coefficient $(3/2)\lambda_{111}$ values obtained from [220] or [211]-oriented Fe-W alloy single crystals in the annealed condition.

Alloy Composition	Magnetostriction coefficients $(3/2)\lambda_{111}$ (x 10^{-6})
Fe-3 at.% W	-39
Fe-6 at.% W	-41
Fe-7.5 at.% W	-43

summarizes the magnetostriction measurement results and the $(3/2)\lambda_{111}$ magnetostriction coefficient values of Fe-W alloy single crystals. Compared with the DG measurement values, this heat treatment results in a 30 to 40% increase in the Fe-W alloy's $(3/2)\lambda_{111}$ magnetostriction coefficient value. Figure 5.27 shows the comparison of $(3/2)\lambda_{100}$ and $(3/2)\lambda_{111}$ magnetostriction coefficient values for Fe-X at.% W alloys in a magnetostriction versus W content plot. As the W content increased from Fe-3 at.% W to Fe-7.5 at.% W, the $(3/2)\lambda_{111}$ magnetostriction coefficient value in the annealed condition increased by about 13%. The $(3/2)\lambda_{111}$ values are about 30 to 50% of the $(3/2)\lambda_{100}$ values for the same alloy composition. As discussed in the background section, using these λ_{111} magnetostriction coefficients and the λ_{100} magnetostriction coefficients obtained from earlier research [22] in Equation 2.18, the saturation magnetostriction of Fe-W alloys can be calculated for along any crystallographic direction.

5.3 X-ray Diffraction Studies of Ordering in Quenched Single Crystals of Fe-27.5 at.% Ga

A single crystal of Fe-27.5 at.% Ga was cut from a DG ingot and a 2mm thick disc-shaped sample was prepared with both faces oriented within 0.25° from the [001] or [111] directions using the method discussed in the experimental work section. The sample was glass-sealed in a quartz tube in argon atmosphere and annealed at 1100°C in the α-Fe phase region for 2 hours. A rapid water quench was performed to retain the high temperature phase at room temperature and the expected crystal structure will be a mixture of A2, B2 and DO_3 phases. Theta- 2 theta XRD scans were performed along a random direction on the [001]-oriented face or along the [220] direction on the [111]-oriented face to obtain the desired scan patterns.

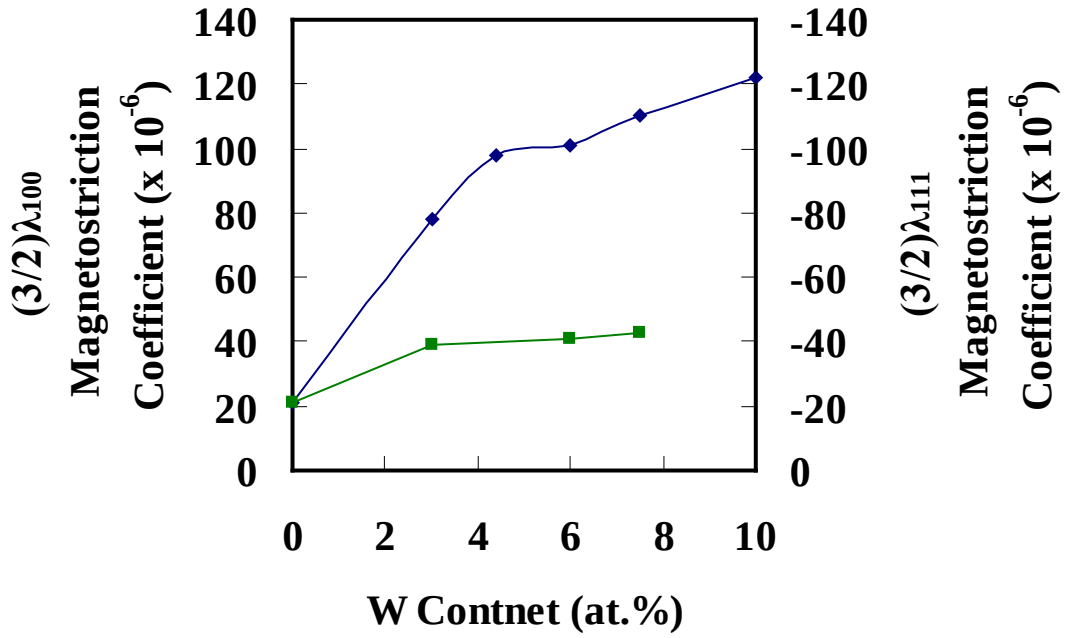

Figure 5.27 Magnetostriction coefficient values versus W content of Fe-W alloy single crystals (Blue line with solid diamond markers: $(3/2)\lambda_{100}$ magnetostriction coefficient values. Green line with solid square markers: $(3/2)\lambda_{111}$ magnetostriction coefficient values.)

5.3.1 Theta-2 Theta Scans of (100) Face

If the sample is carefully prepared and perfectly oriented, there will be diffraction only from (h00) family planes of [100]-oriented crystals. Figure 5.28 shows the θ-2θ scan made on the (001) face of the [001]-oriented Fe-27.5 at.% Ga single crystal. There is a peak with a large intensity at about 64.2° which corresponds to the (200) fundamental reflection. The low intensity peak shows up at about 31° on the top of a wide diffuse peak that corresponds to the superlattice reflection (100). Both the (100) and (200) peaks are narrow and sharp; the full width of the (200) peak at half the maximum intensity is less than 0.35° and for the (100) peak it is less than 0.27°. From the x-ray diffraction theory, the (200) reflection is present in the scan of the [001] oriented face when A2, DO_3 and/or B2 structures are present and the (100) superlattice peak is present when DO_3 and B2 phase regions are present. The wide diffuse peak at the bottom from 22° to 45° includes the combined effect of short-range ordering, thermal scattering and Compton scattering but with primary contribution arising from short-range ordering. To minimize the contribution from the K_β or $K_{\alpha 2}$ wavelength, the high resolution scan was also done on this [001] oriented sample. The high resolution XRD pattern of Figure 5.29 shows the superlattice reflections as well as the diffuse peak at about 31˚. The absolute intensity values and the FWHM are smaller as expected. From the relative peak intensities of these (100) superlattice peaks and the (200) peak, one could estimate the relative volume of the ordered domains. Based on Figure 5.28 and Figure 5.29, the crystal structure inside this Fe-27.5 at.% Ga single crystal will be dominantly a disordered A2 matrix with a small amount of B2 or DO_3 second phase regions in it.

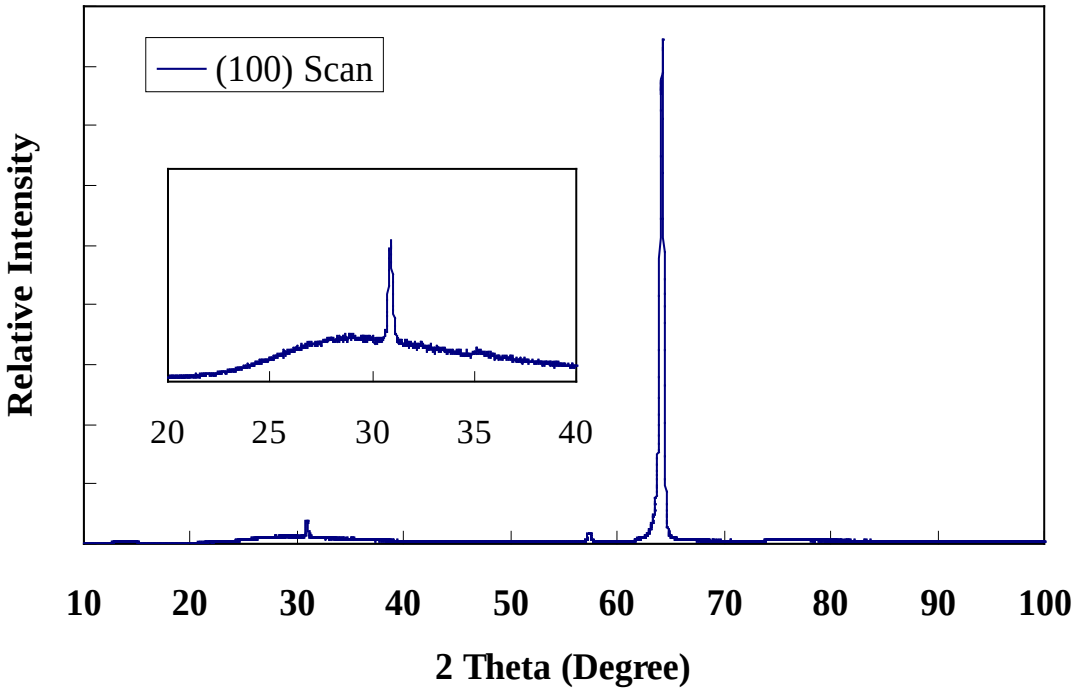

Figure 5.28 Theta-2 theta XRD pattern from the (100) face of a [001]-oriented Fe-27.5 at.% Ga single crystal.

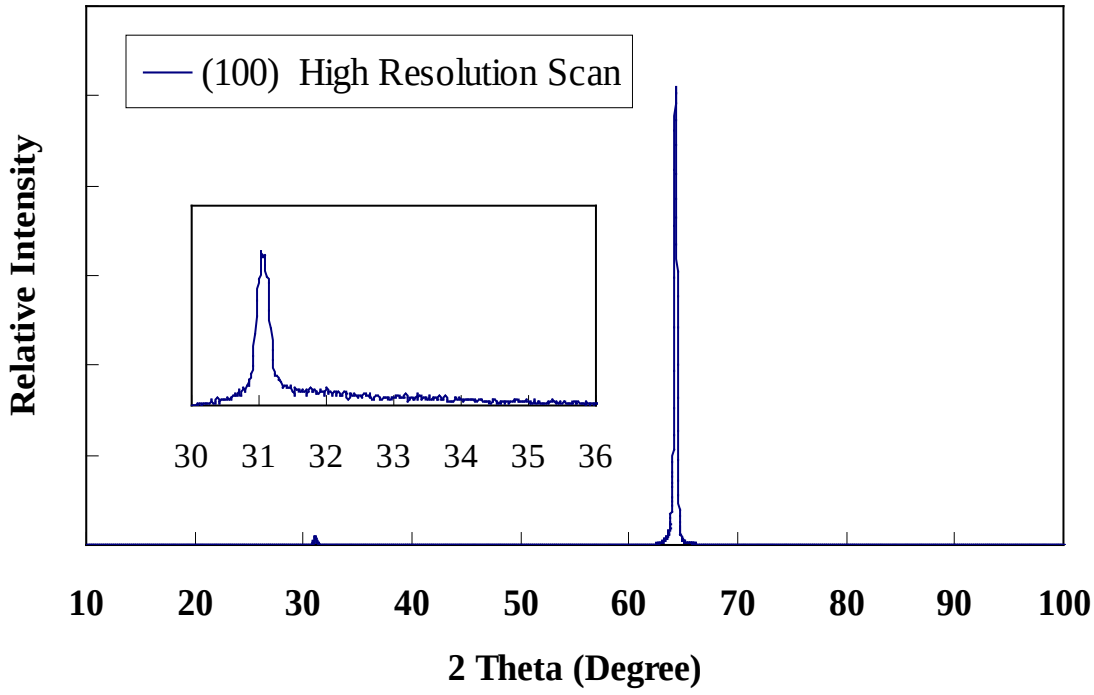

Figure 5.29 Theta-2 theta XRD pattern from the (100) face of a [001]-oriented Fe-27.5 at.% Ga single crystal.

5.3.2 Theta-2 Theta Scans of (111) Face

For θ-2θ scans on the (111) face of the Fe-27.5 at.% Ga alloy single crystal, only the diffraction signal from the (h h h) family of planes including (111), (222) and (333) will be present. In these peaks, B2 structure only contributes to the (222) peak, but DO_3 will contribute to all of the (111), (222) and (333) peaks. As there are significant effects of atom displacement on the intensity of the (333) peak, only the (111) and (222) peaks can be used to decide the nature of ordering and structure in the samples. The disordered A2 phase will not contribute to any of these peaks. Figure 5.30 shows the θ-2θ scan of the (111) face of the [111]-oriented Fe-27.5 at.% Ga single crystal which was scanned from the (110) direction to the $\left(\bar{1}\,\bar{1}\,0\right)$ direction. It can be seen that there are three main peaks. The first one at about 26.6° is the (111) diffraction peak. The second one at about 54.7° is the (222) diffraction peak. The third one at 87.1° is the (333) diffraction peak. The A2 structure is a BCC disordered structure which will not contribute to any of these three peaks. The B2 structure will only contribute to the (222) peak and DO_3 will contribute to all of the three peaks. So, by calculating the relative intensity of these diffraction peaks, an estimation of the volume ratio of B2 and DO_3 phases can be made. As shown in the XRD patterns, all of the three peaks have a narrow and sharp shape. The average full width of the (222) peak at half maximum intensity is less than 0.38°, and so the nature of B2 and DO_3 structures inside the crystal lattice should be long-rang ordered domains coherent with the disordered A2 matrix phase.

As a sample is heated to high temperature and then quenched by water or gas flow at room temperature, the atoms in the crystal lattice will lose their mobility rapidly as a result of the decreasing of temperature. Due to the rapidly reduced diffusional rates, the

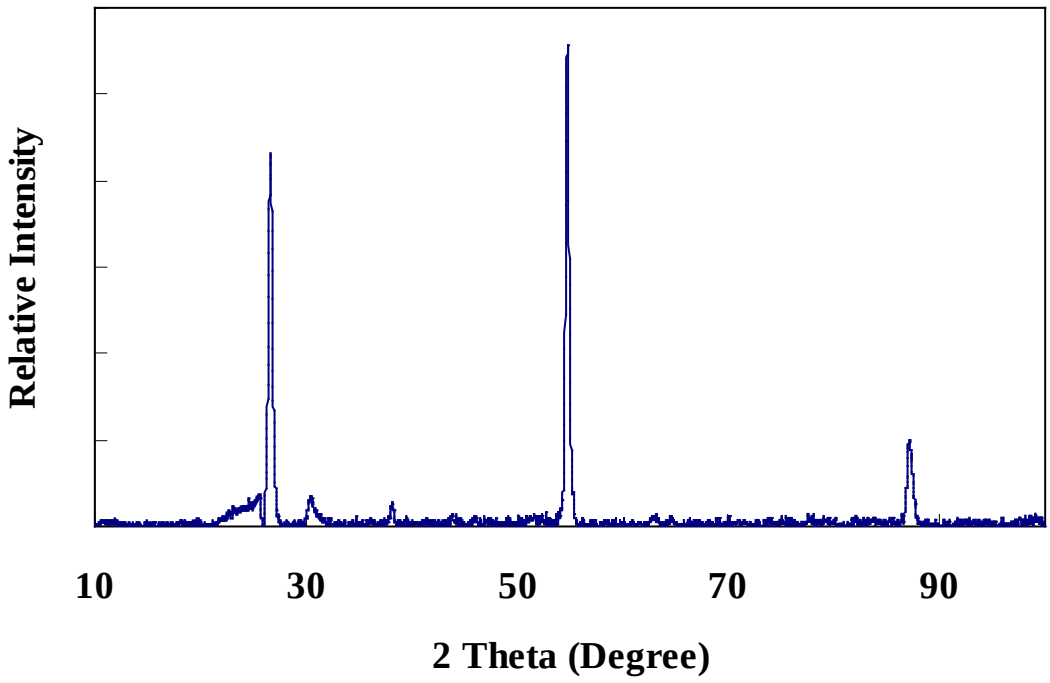

Figure 5.30 Theta-2 Theta x-ray diffraction pattern obtained from the (111) sample face of the [111]-oriented Fe-27.5 at.% Ga single crystal after polishing off to a depth of 3μm from the surface.

crystal structure of the high temperature phase of the sample can be quenched in. At an estimated heat transfer coefficient at the interface between Fe-alloys and water as large as 10^4-10^5 W/m^{2}K and an estimated thermal conductively of 80 W/mK for iron alloys, a steep internal temperature gradient will be formed as a function of depth from the surface to the center of the sample

$$\frac{T-T_f}{T_i-T_f}=2\sum_{n=1}^{\infty}\frac{\sin\lambda_n L}{\lambda_n L+\sin(\lambda_n L)\cos(\lambda_n L)}\exp(-\lambda_n^2\alpha t)\cos(\lambda_n x) \qquad 5.1$$

where T is the temperature at the location x from the center of the sample after time t, α is the ratio of x and semithickness L, T_i is the initial temperature and T_f is the gas flow temperature. λ_n are roots of calculation from the equation

$$\cot\lambda_n L=\frac{1}{(h/k)L}(\lambda_n L) \qquad 5.2$$

For the Fe-27.5 at.% Ga single crystal sample, the time for the temperature to drop from 1150℃ to the long-range ordered α'' phase region at 860℃ at the top surface is less than 0.05s. At 100 μm depth from the surface, this time will increase to about 0.08s. The time needed for this temperature drop at the center part, which is 1200 μm from the surface, will be more than 0.27s. Based on this calculation, there is a steep temperature gradient near the surface during water quenching and the temperature gradient is small at the interior region. As A2, B2 and DO_3 have the same Bravais lattice and the jump frequency of an atom at high temperature can be more than 10^{10} times/second, the 0.03s cooling time difference between the top surface and 100 μm

depth into the sample is significant enough to cause a differences in the ordering process at various depths from the surface region.

A magnified view of the diffraction patterns in the 2θ range of 25° to 28° and 53° to 57° for the [111]-oriented single crystal of Fe 27.5 at.% Ga at different depths from the top surface are shown in Figures 5.31 and 5.32. Figure 5.31 indicates the decrease in the relative intensity of the (111) peak in the XRD pattern with increasing depth from the surface to 200 μm below the original surface of the sample. Figure 5.32 indicates the increase of relative intensity of the (222) peak as the depth changes. As mentioned before, the percentages of the B2 and DO_3 phase in the structure can be calculated by comparing the relative intensities of (111) and (222) diffraction peaks. These XRD patterns suggest an increase in the percentage of the B2 phase as a function of depth in this high temperature heat treated and rapid water quenched Fe-Ga single crystal. Ignoring the effect of the disordered A2 matrix phase, at the surface, more than 70% of the ordered domains' volume has DO_3 structure, and at about 60 μm from the surface, this percentage drops to about 50%. As the depth increases to 100 μm, the percentage of DO_3 keeps dropping and the B2 phase volume increases to as much as 65%. But as the depth changes from 100 μm to 200 μm, no further change in the relative amounts of these two phases is seen. Compared to the internal temperature gradient data and XRD patterns, at the first 100 μm range of depth from the surface, there is a significant temperature gradient which can cause drastic difference in crystal structure formed during water quenching. However, the temperature gradient curve becomes more flat as the depth increases to more then 100 μm. It can be expected that a more homogeneous

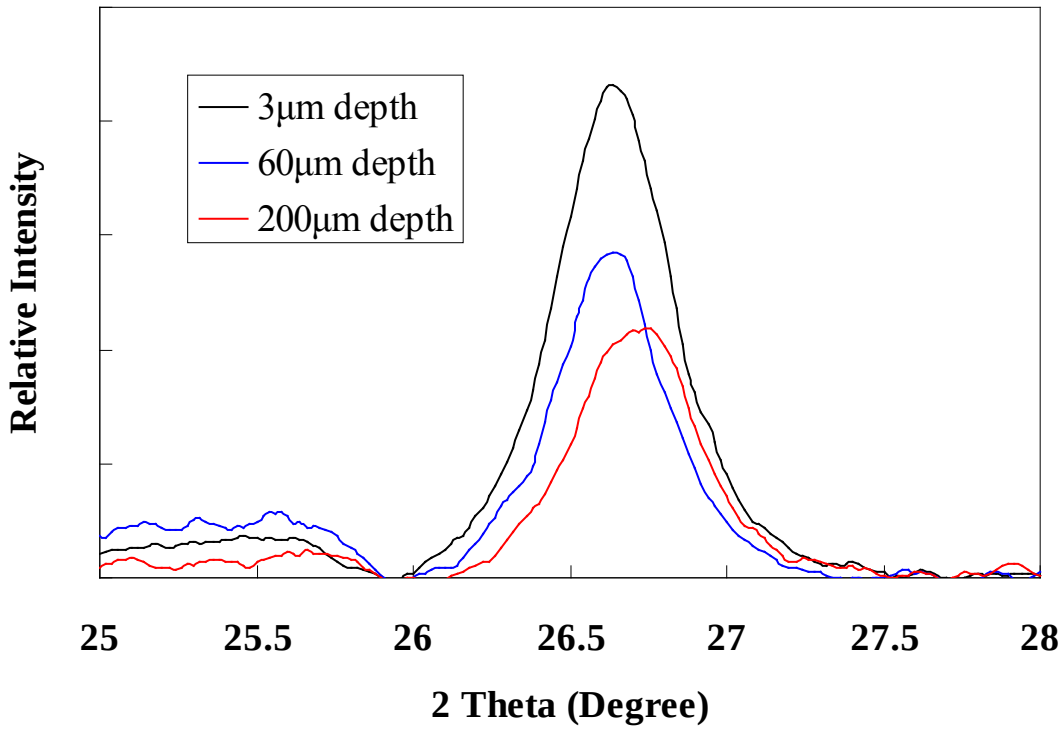

Figure 5.31 Theta-2 Theta x-ray diffraction pattern over a 2θ range of 25°-28° obtained from the (111) sample face of the [111]-oriented Fe-27.5 at.% Ga single crystal after the removal of material by polishing to various depths from the surface.

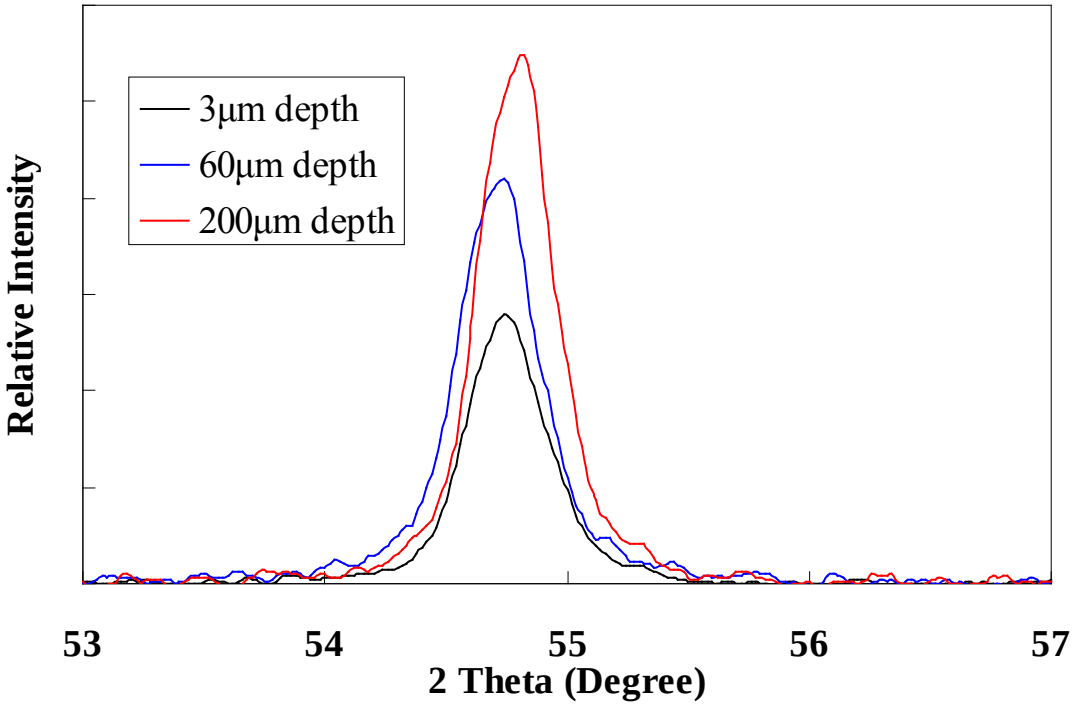

Figure 5.32 Theta-2 Theta XRD patterns showing the (222) peak obtained at various depths from the (111) surface of the [111]-oriented Fe-27.5 at.% Ga single crystal in the 2θ range of 53°-57°.

structure will be formed for this Fe-Ga alloy in most of the sample except the first 100μm depth from surface region.

5.4 EXAFS Studies of Local Atomic Environment of Fe-x at.% Ga Single Crystals

5.4.1 Sample Conditions

A total of 7 single crystal samples with three different alloy compositions (Fe-15 at.% Ga, Fe-20 at.% Ga and Fe- 27.5 at.% Ga) and three different thermal histories (As-grown, long-term annealed and ordering) were prepared for the EXAFS study. A list of the alloy compositions and related heat treatments are shown in Table 5.8. The method of single crystal growth preparation and annealing are the same as discussed in the earlier experimental section. EXAFS measurements were performed on the [001]-oriented face.

5.4.2 EXAFS Data Processing and Analysis

All of the EXAFS measurements used in this study were performed in Sector 12-BM of the Advanced Photon Source at Argonne National Laboratory. Seven Fe-Ga single crystals with three different alloy compositions and three different thermal histories were studied. As discussed in the background section, Fe-Ga alloy's magnetostriction behavior is very sensitive to the alloy composition and thermal history. The earlier research and also the other results sections in this thesis already showed that the effect of alloy composition and heat treatment is partly from the formation of coherent and incoherent second phases. The behavior of magnetostriction and second phase formation during heat treatment has already been studied for all of these seven Fe-Ga alloys. A detailed EXAFS study of the local atomic environment of these Fe-Ga alloys will be valuable as it will improve the understanding of the Fe-Ga alloy system as well as the origin of

Table 5.8 Sample compositions and thermal histories for all of the single crystals used for EXAFS measurements

Sample Name	Thermal History
Fe-27.5 at.% Ga single crystal DG sample	As-directional-grown condition
Fe-27.5 at.% Ga single crystal LTA sample	Long-term annealed at 1100˚C for 70 days
Fe-27.5 at.% Ga single crystal ORD sample	DO_3 ordering treatment at 1100˚C for 1 hour followed by 730˚C for 75 days
Fe-20 at.% Ga single crystal DG sample	As–directional-grown condition
Fe-20 at.% Ga single crystal LTA sample	Long-term annealed at 1250˚C for 70 days
Fe-15 at.% Ga single crystal DG sample	As–directional-grown condition
Fe-15 at.% Ga single crystal LTA sample	Long-term annealed at 1250˚C for 70 days

magnetostriction. The relation between local atomic strain and the alloy's magnetostrictive behavior at different alloy compositions and thermal histories will be an important contribution towards future magnetostrictive alloy design and development.

Athena® and Artemis® programs of the IFEFFIT software package were used for data processing and analysis in this work. A detailed description about the data processing and modeling method will be discussed in the following sections.

5.4.2.1 EXAFS Data Processing Using Athena® Software

The first step of EXAFS data processing using Athena® software is the data conversion between different spaces using basic calculation or Fourier transform. The scan data were input into the program and the x-ray absorption spectra were normalized by subtracting the pre-edge line from the entire spectra. Figure 5.33 shows an example of the x-ray absorption spectra obtained from EXAFS measurement before and after normalization. The normalized spectra were converted from the incident x-ray energy E space that was directly measured from experiments to the wave number k space using the following relationship,

$$k^2 = \frac{2m_e(E - E_0 + \Delta E_0)}{\hbar} \qquad 5.3$$

where k is the wave number, m_e is the electron mass, $(E\text{-}E_0)$ is the energy above edge, ΔE_0 is the energy shift and $\hbar$ is the Plank's constant.

Fourier transform was applied to the k-space plot based on the selected k-range and data were converted to an R-space plot which is normally used in the EXAFS modeling. Back Fourier transform was performed to convert the R-space plot which only

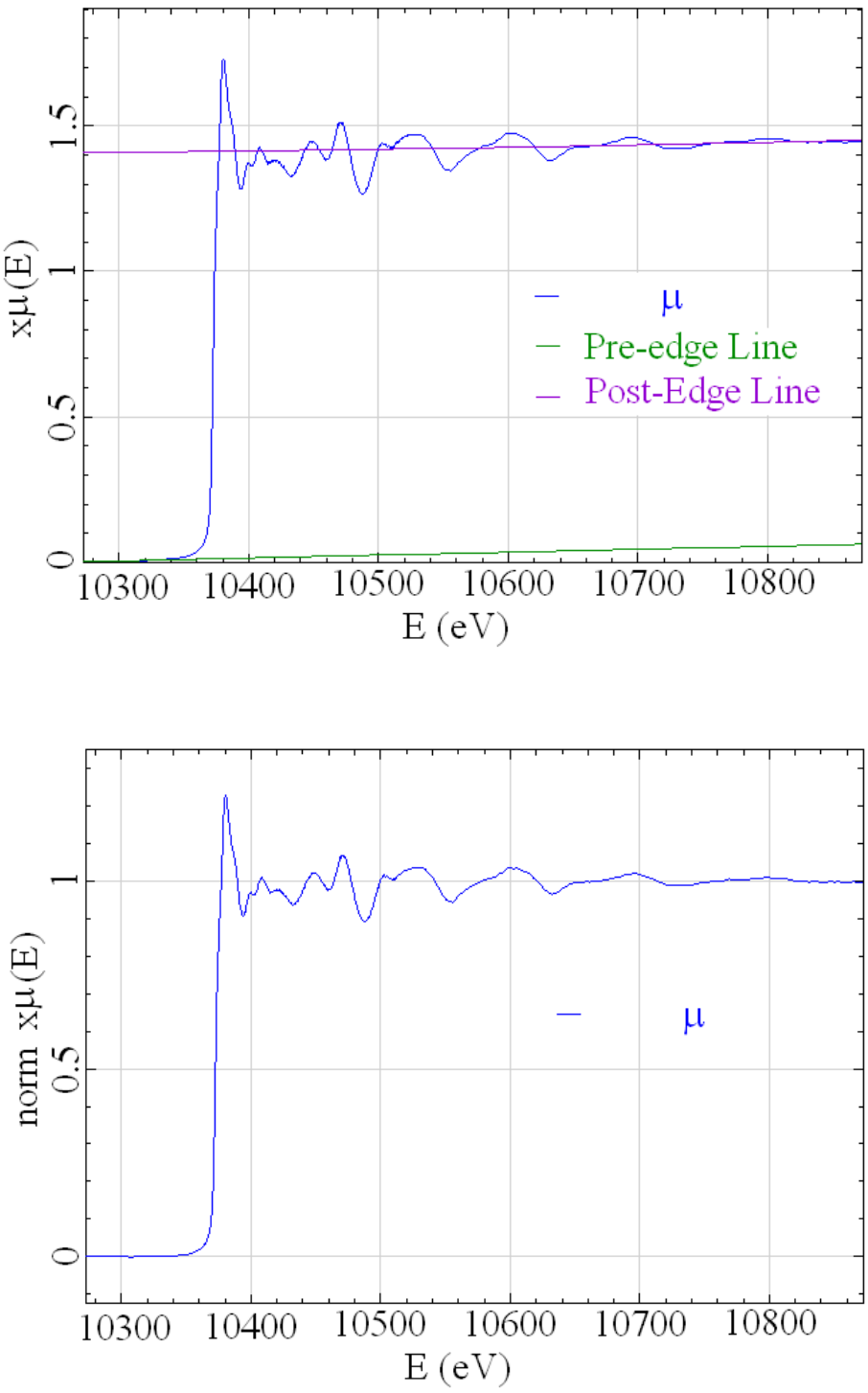

Figure 5.33 X-ray absorption spectra obtained from EXAFS measurement before and after normalization.

contains the information within R-range to another wave number q-space. By comparing the q-space data with the k-space data, the idea about the difference between processed data and the original EXAFS signal can be obtained. Figure 5.34 shows the example of the same EXAFS spectra in E, k, R and q- space.

For each single crystal sample, about 5 to 7 scans were taken during the EXAFS measurements. The second step of data processing will be calculating the average of the multiple scans to minimize the experiment noise. This step is called “Merge” in the Athena® software. During the merge process, the average values and standard deviations of each point in the EXAFS E-space were calculated based on the different sets of data of the same sample. The merged spectra were built based on the averaged points. Figure 5.35 shows the example of the EXAFS spectra for the same sample before and after merge.

As discussed in the experiment section, the self-absorption effect caused by the change of mean absorption depth during EXAFS could lead to a significant effect to the measurement results. The self-absorption correction was performed on all of the EXAFS data. By defining the experimental set up information, including alloy composition, incident and scattered beam angle in the EXAFS Troger algorithm, Athena® software is able to correct for the effect of self-absorption on the experimental data. This correction always amplified the EXAFS oscillations as the strong signal reduction was caused by self-absorption during a fluorescence mode EXAFS experiment. Figure 5.36 shows an example of the EXAFS spectra before and after self-absorption correction.

As a result of using oriented single crystal samples, high quality EXAFS data were obtained during the experiment and only limited correction is required on the raw

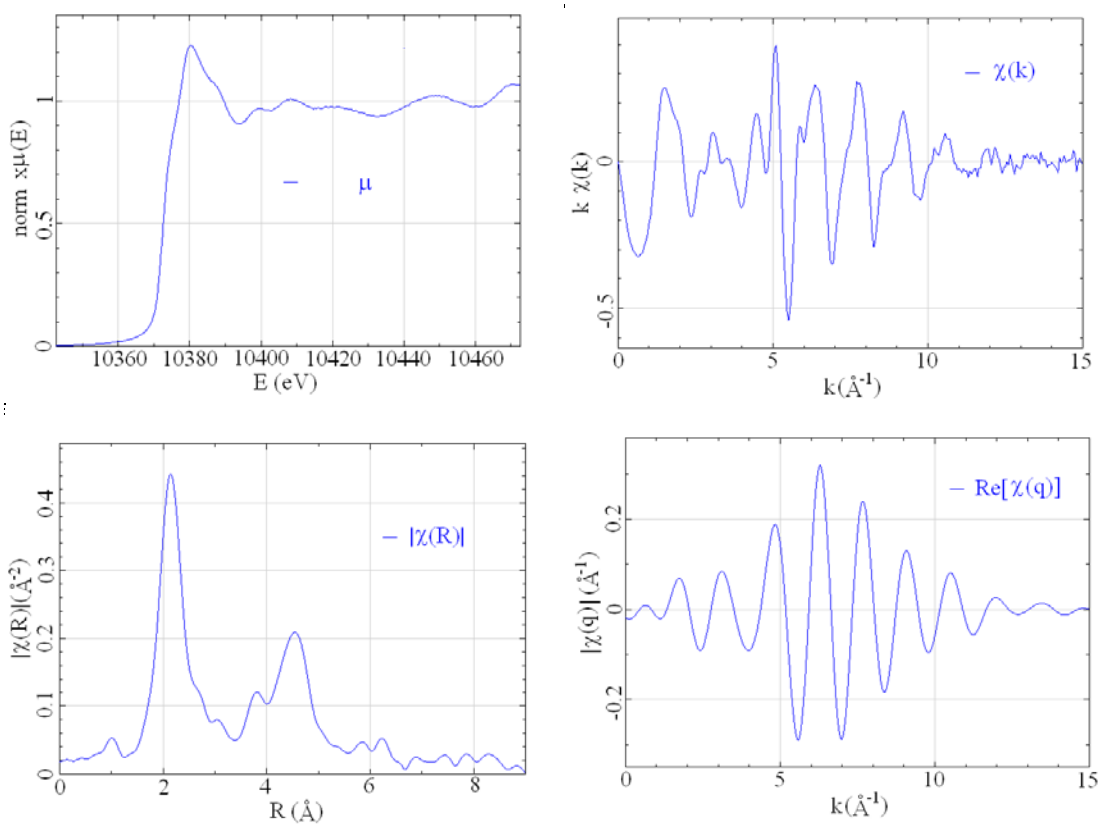

Figure 5.34 Example of same EXAFS spectra in E, k, R and q- space

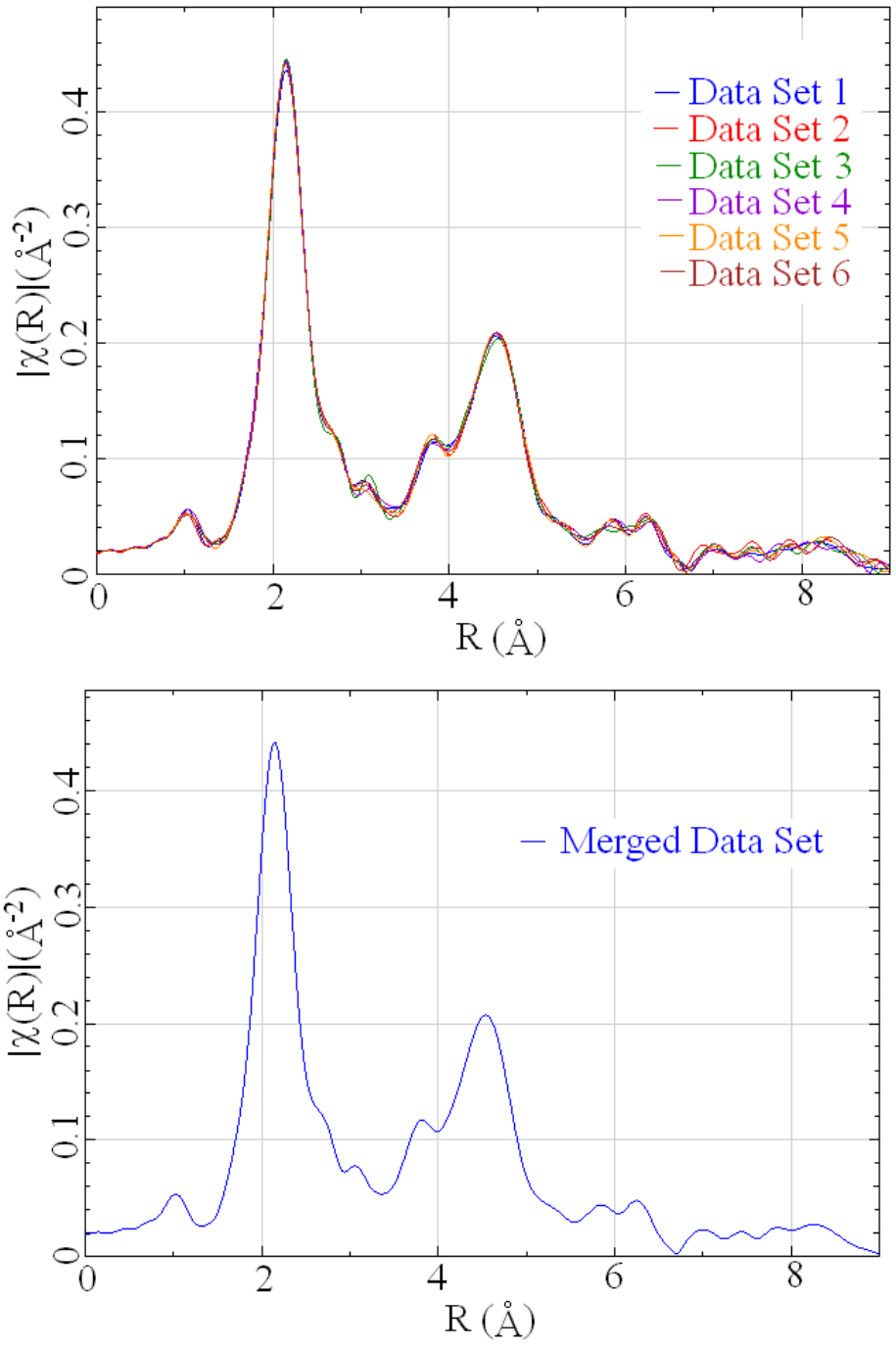

Figure 5.35 Example of EXAFS spectra for the same sample before and after merge.

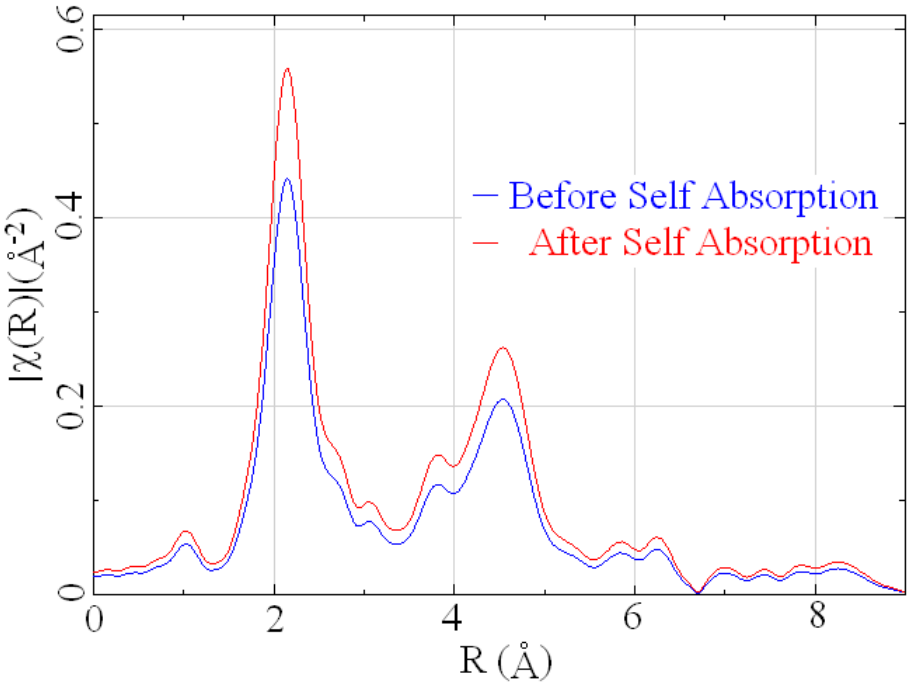

Figure 5.36 Example of EXAFS spectra before and after self-absorption correction.

data during data processing using Athena® software. This also improved the accuracy of modeling results.

5.4.2.2 EXAFS Data Analysis Using Artemis® Software

The processed EXAFS experimental data were imported into Artemis® software and are used as a reference spectrum during the modeling process. As discussed earlier in the experimental work section, Artemis® modeling is based on the FEFF's multiple-scattering path expansion. For each type of local atomic environment, a series of scattering paths need to be defined by the user. Evaluation of the EXAFS equation is done for each scattering path. The combined contribution of all the scattering paths provides a model of the EXAFS spectrum.

There are three main steps to define the scattering paths in Artemis® software. The first step is to define the local atomic arrangement near the core atom in an "atoms" page. In this step, the atoms at each nearest neighbor position included in the local atomic arrangement need to be defined by their element type and position inside the lattice. Table 5.9 shows the lattice position, coordination number and distance from the core atom of 1^{st} to 6^{th} nearest neighbors in a BCC crystal structure. For example, for a Fe K-edge scan, Fe will be defined as the core atom at position (0, 0, 0). After that, the first nearest neighbor position (0.5, 0.5, 0.5) may be occupied by either an Fe or Ga atom, and these two kinds of possibility will be considered in separate atoms pages. For the second nearest neighbor modeling, this definition will be extended to second nearest neighbor positions. Each of the atoms pages will lead to a separate FEFF list of scattering paths, so for the first nearest neighbor modeling, there will be 2 atoms pages for each scan and 4

Table 5.9 Lattice position, coordination number and distance from core atom of 1st to 6th nearest neighbors in a typical BCC crystal structure

No. of Nearest Neighbor	Position in Lattice	Coordination Number	Distance From Core Atom (a: lattice parameter)
1st Nearest Neighbor	(0.5, 0.5, 0.5)	8	0.866a
2nd Nearest Neighbor	(1, 0, 0)	6	a
3rd Nearest Neighbor	(1, 1, 0)	12	1.414a
4th Nearest Neighbor	(1.5, 0.5, 0.5)	24	1.658a
5th Nearest Neighbor	(1, 1, 1)	8	1.732a
6th Nearest Neighbor	(2, 0, 0)	6	2a

atoms page for each sample, including Fe-Fe, Fe-Ga, Ga-Fe and Ga-Ga. For the second nearest neighbor modeling, there will be Fe-Fe-Fe, Fe-Fe-Ga, Fe-Ga-Fe and Fe-Ga-Ga atoms pages for the Fe K-edge scan and Ga-Fe-Fe, Ga-Fe-Ga, Ga-Ga-Fe and Ga-Ga-Ga atoms pages for the Ga K-edge scan. After defining the nearest neighbor atoms, the type of space group was input to calculate the coordination numbers of each nearest neighbors. Cluster size determines the total number of atoms involved in the EXAFS modeling. The lattice parameters used in the "atoms" page calculation were obtained from the earlier XRD study of Fe-Ga alloys.

The second main step to define the scattering paths is defining the local atomic environment in the "feff.inp" page. After defining crystal structure and lattice parameters that describe the local atomic arrangement, the specific positions of all the atoms involved in the photoelectron scattering will be calculated and this information shows up as a list in the feff.inp page. This feff.inp page provides the user the ability to adjust the element type and exact positions for each specific atom. In this work, in order to minimize the number of variables so that it is less than the allowed number of variables for a given data set range, all the atoms in one nearest neighbor shell were specified. All the other atoms beyond the defined nearest neighbor shell were assumed to be randomly distributed. The list of atoms in the feff.inp page will be used to calculate the possible scattering paths for a photoelectron. The scattering factor of different elements will be considered during the calculation of scattering paths, and scattering paths with too small amplitudes will be ignored.

All the scattering paths with large enough amplitude are then selected for inclusion in the "FEFF calculation list" which is the third step in Artemis® modeling.

There are two kinds of scattering paths, the single scattering paths and the multiple scattering paths. Figure 5.37(a) shows an example of a single scattering path. After a photoelectron is excited from the core atom, it is scattered by one of the nearest neighbor atoms; for example, the 1^{st} nearest neighbor atom at position (0.5, 0.5, 0.5), then backscattered to the core atom. For a multiple scattering path, as shown in Figure 5.37(b), the photoelectron excited from the core atom is scattered by one of the nearest neighbor atoms and then scattered by one or several more nearest neighbor atoms before being backscattered to the core atom. In general, single scattering paths have larger amplitude than multiple scattering paths and provide a more significant contribution to the EXAFS spectra. For a multiple scattering path, its intensity will decrease as the scattering angle between two atoms in its scattering path increases. As a result, the multiple scattering paths with large scattering angle may provide very limited contribution to the modeling spectra but increase the complexity and error to the EXAFS modeling. In order to improve the modeling result, part of the multiple scattering paths needs to be excluded from the FEFF calculation list.

As discussed in the experiment section, several parameters need to be defined for each scattering path in the EXAFS modeling. The parameters defined for scattering paths in this modeling work include the effective coordination number S02, energy shift $delE_0$, change in distance of the scattering path delR and mean square variation of distances $sigma^2$. The effective coordination number S02 includes the coordination number of the nearest neighbor shell N_j which is determined by the crystal structure and the amplitude reduction term S_0^2 due to the relaxation of all the other electrons in the absorbing atom (core atom) to the hole in the core level. These two terms are completely correlated with

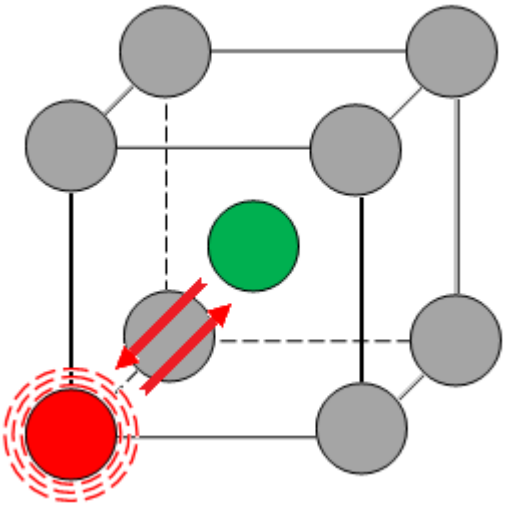

(a)

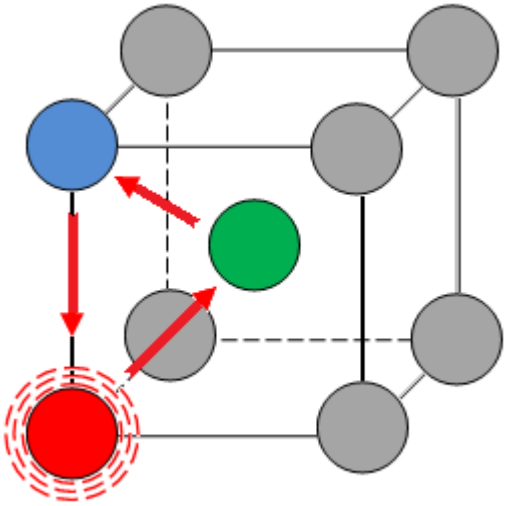

(b)

Figure 5.37 (a) Example of single scattering path of a photoelectron in a BCC crystal structure. (b) Example of a multiple scattering path of a photoelectron in a BCC crystal.

each other. In the first nearest modeling, this parameter was defined as a single variable "amp" for each FEFF calculation list and was correlated to the "amp" term to obtain the coordination number. In the second nearest neighbor modeling work, the S02 part is also defined as a single variable "amp" for each FEFF calculation list. The energy shift E0 is defined as a single variable for each scan as it will be a constant within the same scan data. For the delR parameter, the "reff", R effective distance determined by the atomic arrangement in the atoms page, was multiplied with the "scale" variables. The "scale" variables are the fractional change of the distance between the core atom to the nearest neighbor atoms; for example, the "scaleFeFeNN" means the fractional change of the distance from the core atom Fe to the second nearest neighbor atoms in a Fe-Fe type of atomic arrangement. For a single scattering path, only one "scale" variable is involved, and for a multiple scattering path, several "scale" variables may be involved based on the different legs of the scattering paths. The mean square variation of distances $sigma^2$ comes from a combined effect of two terms, the thermal vibrations represented by the Debye-Waller correction and the structural disorder represented by a series of "static" variables. For example, for a typical single scattering path, the $sigma^2$ parameter is defined as "debye(300,theta_GaFe)+static_GaFeNN", where debye(300, theta_GaFe) is the Debye-Waller correction at the measurement temperature of 300K and for the material with Debye temperature, "theta_GaFe", static_GaFeNN is the structural disorder variable for the distance from the core atom to the second nearest atoms in the Ga-Fe type atomic arrangement.

During the building of the EXAFS model using Artemis® software, all of these variables or constants need to be defined individually in a "Guess, Def, Set" page which

is used to manage the defined parameters. Restraints may be applied to the variables in order to keep the modeling result within a reasonable range. For both first and second nearest neighbor modeling work, restraint has been applied to the coordination number and amplitude reduction term to keep these values within a physically meaningful range. Different k-weights can be chosen during set up for the Artemis® fit. By using different k-weights for the fits, the Artemis® software will try to fit the modeling spectrum to a different portion of the experimental data; for example, the k-weight of 2 refers to an emphasis on the middle part of the spectrum and k-weight of 1 refers to an emphasis on the front part. If every parameter is defined correctly, a successful Artemis® fit will provide the user meaningful information about the atomic distance and coordination number about the local atomic environment.

5.4.3 Results of Fe-Ga Alloy First Nearest Neighbor Analysis

5.4.3.1 Artemis Results for Fe-27.5 at.% Ga Single Crystals

The best fit result for the Fe-27.5 at.% Ga single crystal DG sample was obtained by the fit of the data with k-weight 1 and 2 for both the Fe K-edge and Ga K-edge scans and excluding the third scattering path which is a combination of high angle scattering by the first and then second nearest neighbor atoms. The fit results of this Fe-27.5 at.% Ga DG sample for the Fe K-edge and Ga K-edge in R, k and q space are shown in Figures 5.38, 5.39 and 5.40.

As shown in these figures, the fit matches with the experimental spectra, and for the Ga K-edge scan which provides Ga-Ga bond distance, no large discrepancy is observed except for a small mismatch at about 3.2 Å in R space. This R value is already

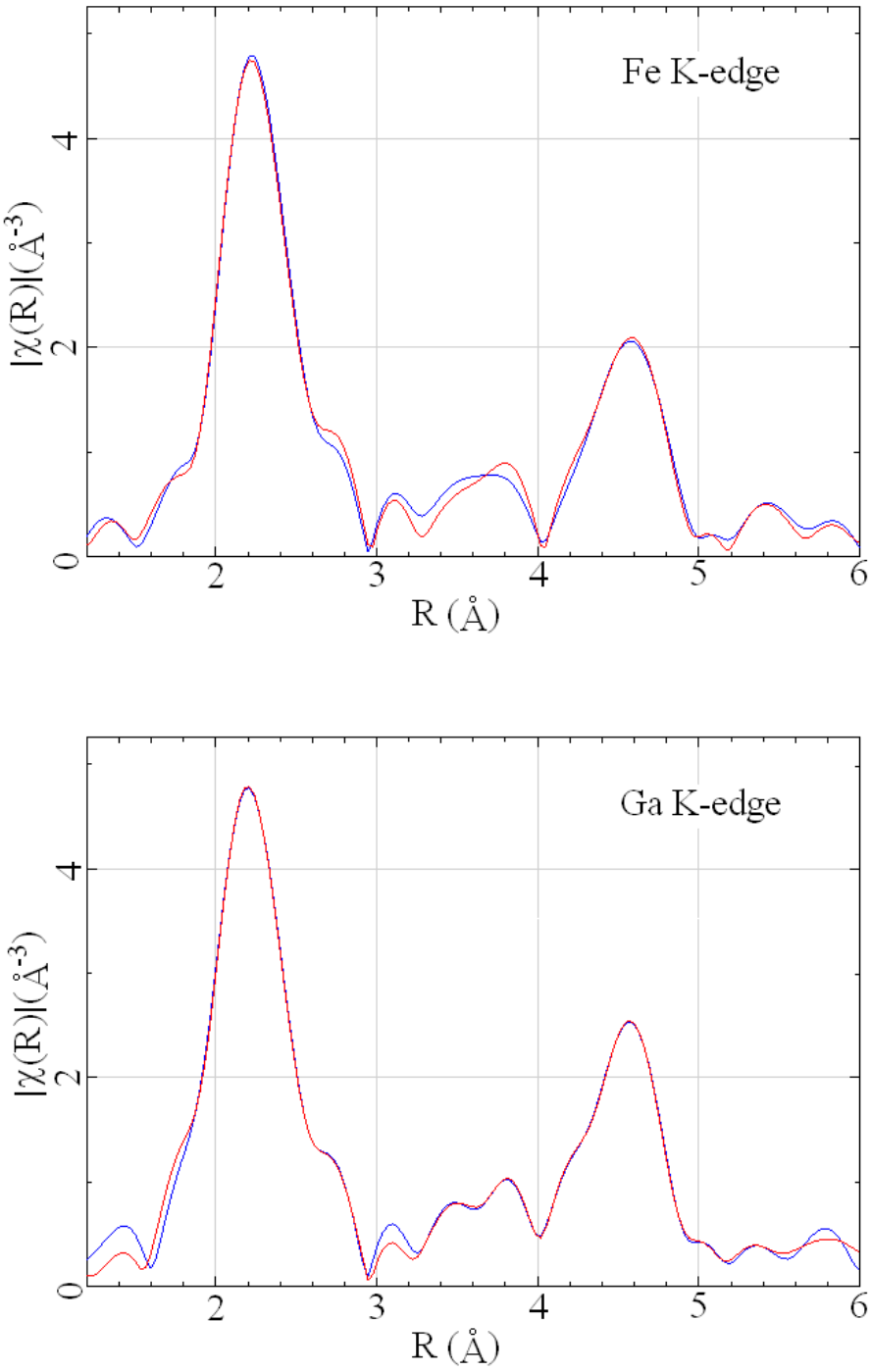

Figure 5.38 Plots of χ for Fe K-edge and Ga K-edge scans of Fe-27.5 at.% Ga as-grown (DG) single crystal first nearest neighbor analysis in R space. (Blue: Experimental Data; Red: Fit Data)

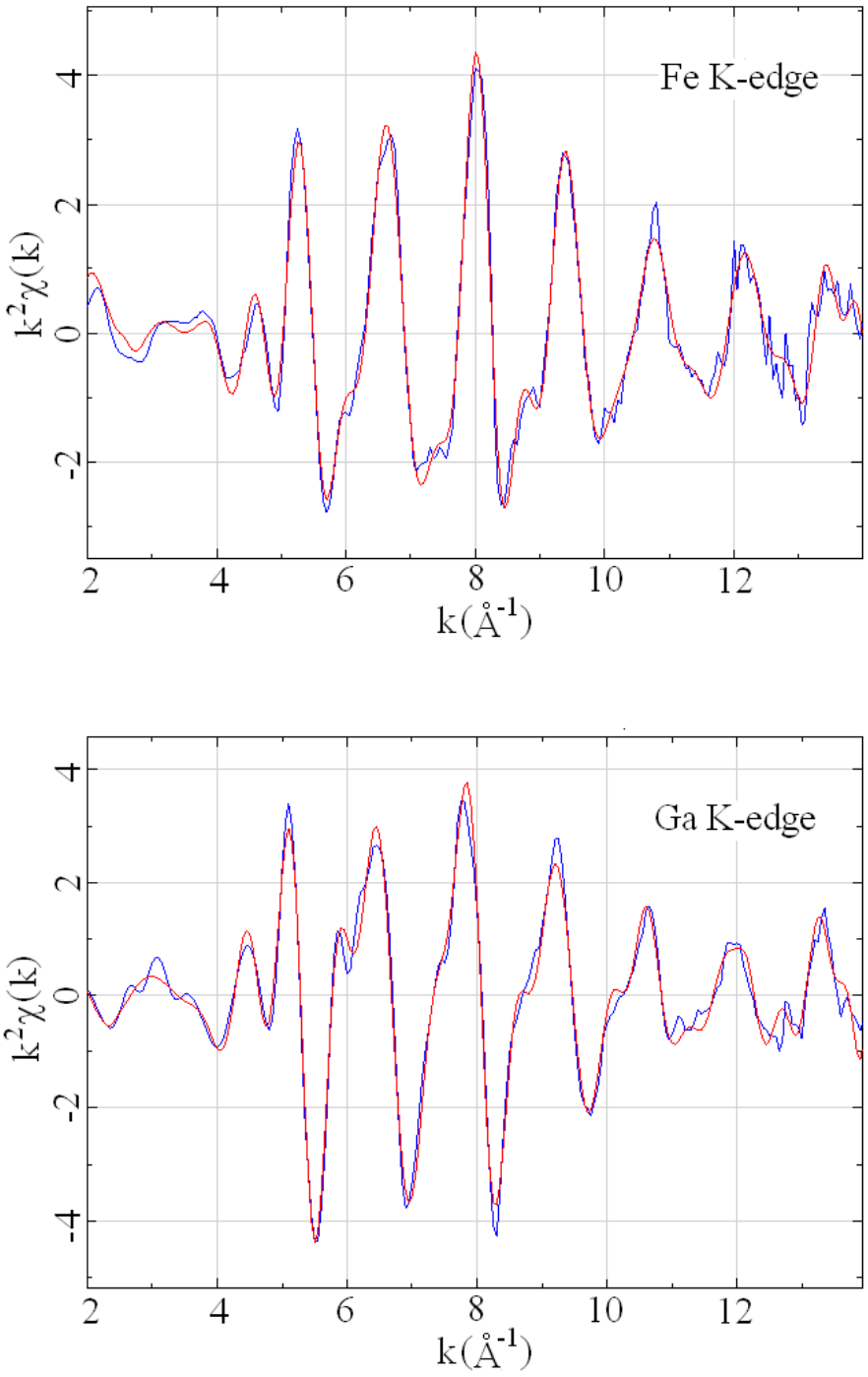

Figure 5.39 Plots of χ for Fe K-edge and Ga K-edge scans of Fe-27.5 at.% Ga as-grown (DG) single crystal first nearest neighbor analysis in k space. (Blue: Experimental Data; Red: Fit Data)

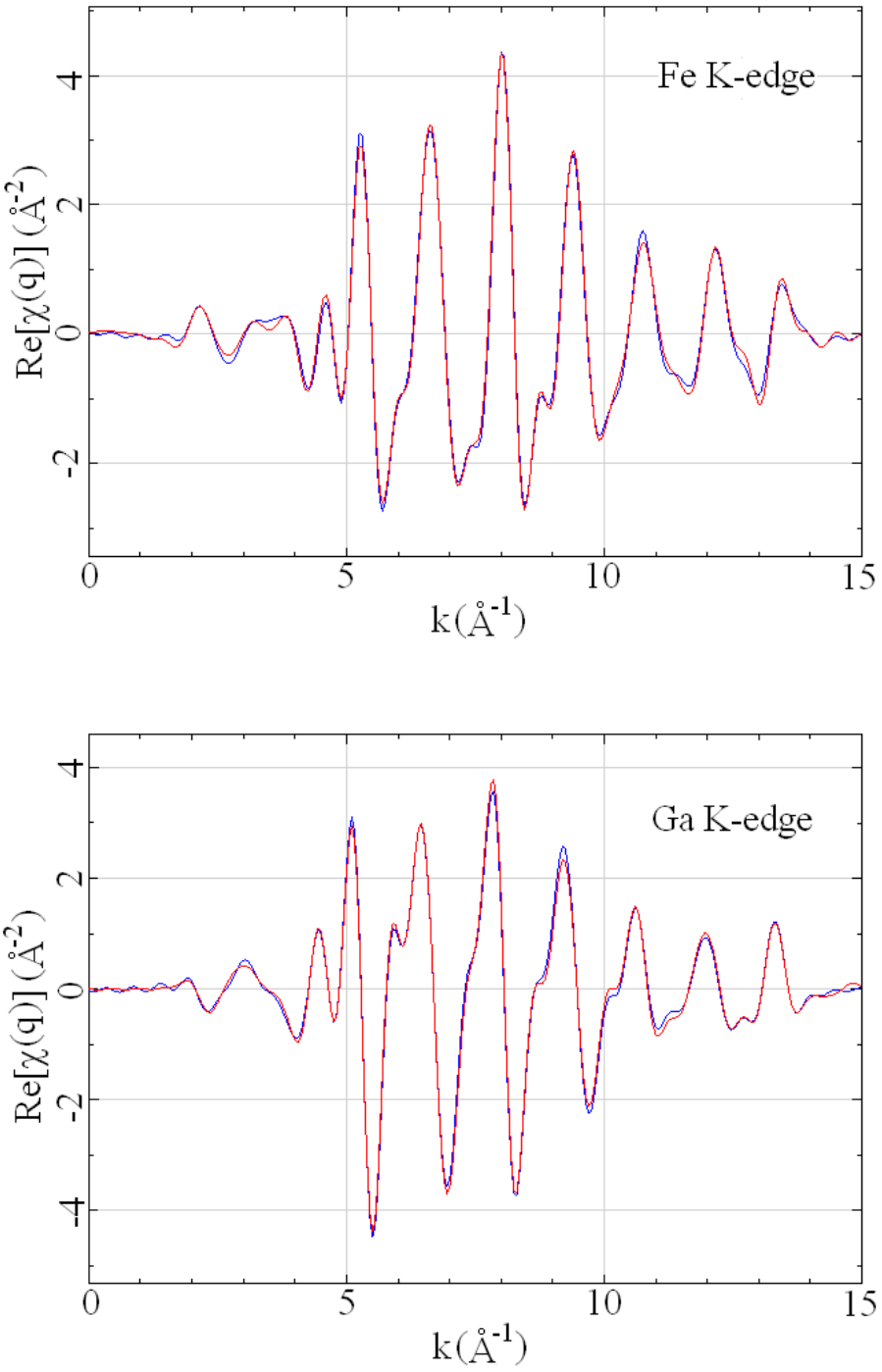

Figure 5.40 Plots of χ for Fe K-edge and Ga K-edge scans of Fe-27.5 at.% Ga as-grown (DG) single crystal first nearest neighbor analysis in q space. (Blue: Experimental Data; Red: Fit Data)

out of the second nearest neighbor range. The R-factor is 0.0031 which is far lower than the acceptable maximum R-factor value 0.02 for EXAFS modeling. All the other fits used in this work show similar or better quality as the one shown in Figures 5.38 to 5.40 and provide confidence on the EXAFS modeling results. The results about atomic spacing of first and second nearest neighbor, atomic spacing uncertainty, delE0 value of enot and amplitude are shown in Table 5.10.

In the A2 phase of the Fe-Ga alloys with a BCC crystal structure, the first nearest neighbors are always along the <111> direction and the second nearest neighbors are along one of the <100> directions. The average atomic spacing for the Fe-27.5 at.% Ga single crystal in the as-grown condition calculated based on Bragg's law from the x-ray diffraction patterns are 2.538 Å for the first nearest neighbor and 2.930 Å for the second nearest neighbor. Compared to the average values, the first nearest neighbor distance of Fe-Fe and Fe-Ga (or Ga-Fe) shows smaller values (2.5143 Å for Fe-Fe and 2.4664 Å for Fe-Ga or Ga-Fe). The Ga-Ga scattering path has a 2.5313 Å distance for the first nearest neighbor which is about the same as the average value.

A similar ARTEMIS® project with the same scattering paths and variables defined was programmed and fits were ran for the EXAFS data of long-term annealed (LTA) and ordered (ORD) Fe-27.5 at.% Ga samples . The best fit of the Fe-27.5 at.% Ga LTA sample was obtained using a k-weight of 1 for both Fe K-edge and Ga K-edge scans and excluding the third scattering path from all of the FEFF calculations. Figure 5.41 shows the fit result of this LTA sample with the Fe K-edge and Ga K-edge scan plotted in R space. The results acquired from this fit are shown in Table 5.11.

Table 5.10 First nearest neighbor analysis results of Fe-27.5 at.% Ga single crystal as-grown (DG) sample Fe K-edge and Ga K-edge scan.

Fe K-edge	
Fe-Fe Path 1st Nearest Neighbor Distance (Å)	2.5143 ± 0.0201
N Value of Fe-Fe Path 1st Nearest Neighbor	0.3649 ± 0.2832
Enot Value of Fe-Fe Path (eV)	6.4121
Fe-Ga Path 1st Nearest Neighbor Distance (Å)	2.4664 ± 0.0167
N Value of Fe-Ga Path1st Nearest Neighbor	0.6351 ± 0.2832
Enot Value of Fe-Ga Path (eV)	5.3097
Ga K-edge	
Ga-Ga Path 1st Nearest Neighbor Distance (Å)	2.5313 ± 0.0125
N Value of Ga-Ga Path 1st Nearest Neighbor	0.2217 ± 0.1239
Enot Value of Ga-Ga Path (eV)	1.2238
Ga-Fe Path 1st Nearest Neighbor Distance (Å)	2.4664 ± 0.0167
N Value of Ga-Fe Path1st Nearest Neighbor	0.7783 ± 0.1239
Enot Value of Ga-Fe Path (eV)	2.7618
R-factor for the Fit	0.0031
amp for the Fit	0.9

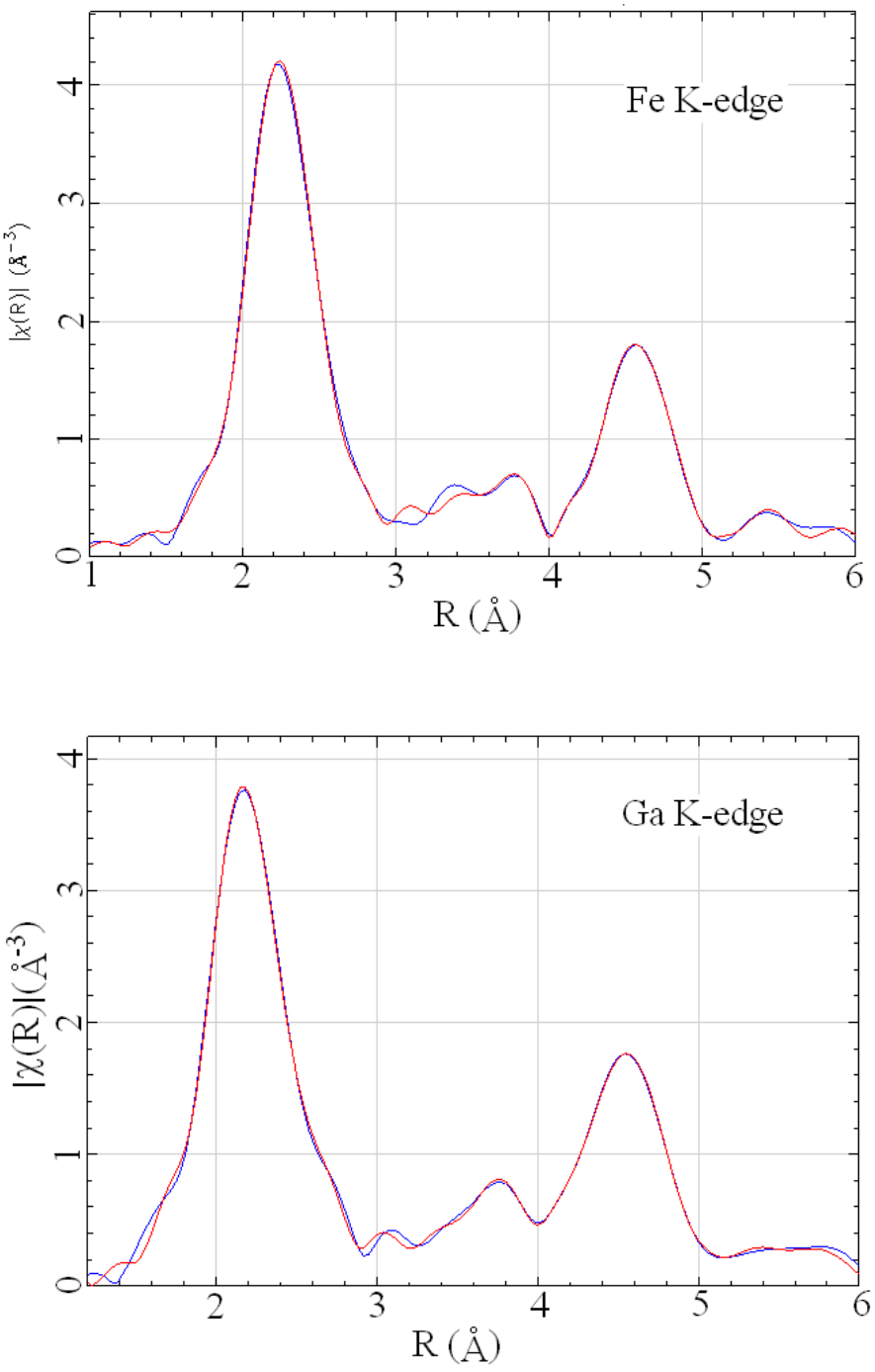

Figure 5.41 Plots of χ for Fe K-edge and Ga K-edge scans of Fe-27.5 at.% Ga long-term annealed (LTA) single crystal first nearest neighbor analysis in R space. (Blue: Experimental Data; Red: Fit Data)

Table 5.11 First nearest neighbor analysis results of Fe-27.5 at.% Ga single crystal long-term annealed (LTA) sample Fe K-edge and Ga K-edge scan.

Fe K-edge	
Fe-Fe Path 1st Nearest Neighbor Distance (Å)	2.4880 ± 0.0097
N Value of Fe-Fe Path 1st Nearest Neighbor	0.6312 ± 0.1741
Enot Value of Fe-Fe Path (eV)	3.9667
Fe-Ga Path 1st Nearest Neighbor Distance (Å)	2.4696 ± 0.0090
N Value of Fe-Ga Path 1st Nearest Neighbor	0.3688 ± 0.1741
Enot Value of Fe-Ga Path (eV)	-3.9678
Ga K-edge	
Ga-Ga Path 1st Nearest Neighbor Distance (Å)	2.8096 ± 0.0212
N Value of Ga-Ga Path 1st Nearest Neighbor	0.5691 ± 0.2000
Enot Value of Ga-Ga Path (eV)	-0.2500
Ga-Fe Path 1st Nearest Neighbor Distance (Å)	2.4696 ± 0.0090
N Value of Ga-Fe Path 1st Nearest Neighbor	0.4309 ± 0.2000
Enot Value of Ga-Fe Path (eV)	2.4237
R-factor for the Fit	0.0018
amp for the Fit	1.2819

Compared to the as-grown sample, there is an increase in the atomic spacing of the first nearest neighbor in the Ga-Ga path. The Fe-Ga or Ga-Fe atomic spacing has no significant change after long-term annealing, and the Fe-Fe path atomic spacing drops from 2.5143 Å for the DG sample to 2.4880 Å for the LTA sample. The first nearest neighbor Ga-Ga pair has a larger atomic spacing of 2.8096 Å which is close to the theoretical value for metallic Ga-Ga bond spacing in a pure Ga metal lattice.

The best fit for the ordered (ORD) Fe-27.5 at.% Ga single crystal sample data was obtained with a k-weight of 2 and 3 for both Fe K-edge and Ga K-edge scans with all of the scattering paths included in the calculation. Fit results of this ORD sample are shown in Figure 5.42 with Fe K-edge and Ga K-edge scans plotted in R space. The corresponding parameter values are shown in Table 5.12. For this ordered sample, the first nearest neighbor atomic spacing of Fe-Fe, Fe-Ga and Ga-Fe paths are almost the same as the long-term annealed sample. The first nearest neighbor atomic spacing of the Ga-Ga path shows a value similar to that of the as-grown sample.

The EXAFS analyses on the three Fe-27.5 at.% Ga single crystals show the effect of different thermal histories on the local atomic environment. It is seen from Tables 5.10 to 5.12 that the first nearest neighbor atomic spacing of Fe-Fe, Fe-Ga and Ge-Fe paths have nearly the same values. The atomic spacing difference between all the three samples with different thermal histories is less than 0.05 Å. However, the bond length for the Ga-Ga first nearest neighbor shows a 0.28 Å increase after the long-term annealing treatment of the as-grown sample. As a result, the Ga-Ga pair in the LTA crystal has a large bond length, which is 0.3 Å larger than the average first nearest neighbor bond length of 2.5097 Å obtained from x-ray diffraction measurement. However, all Fe-Fe and

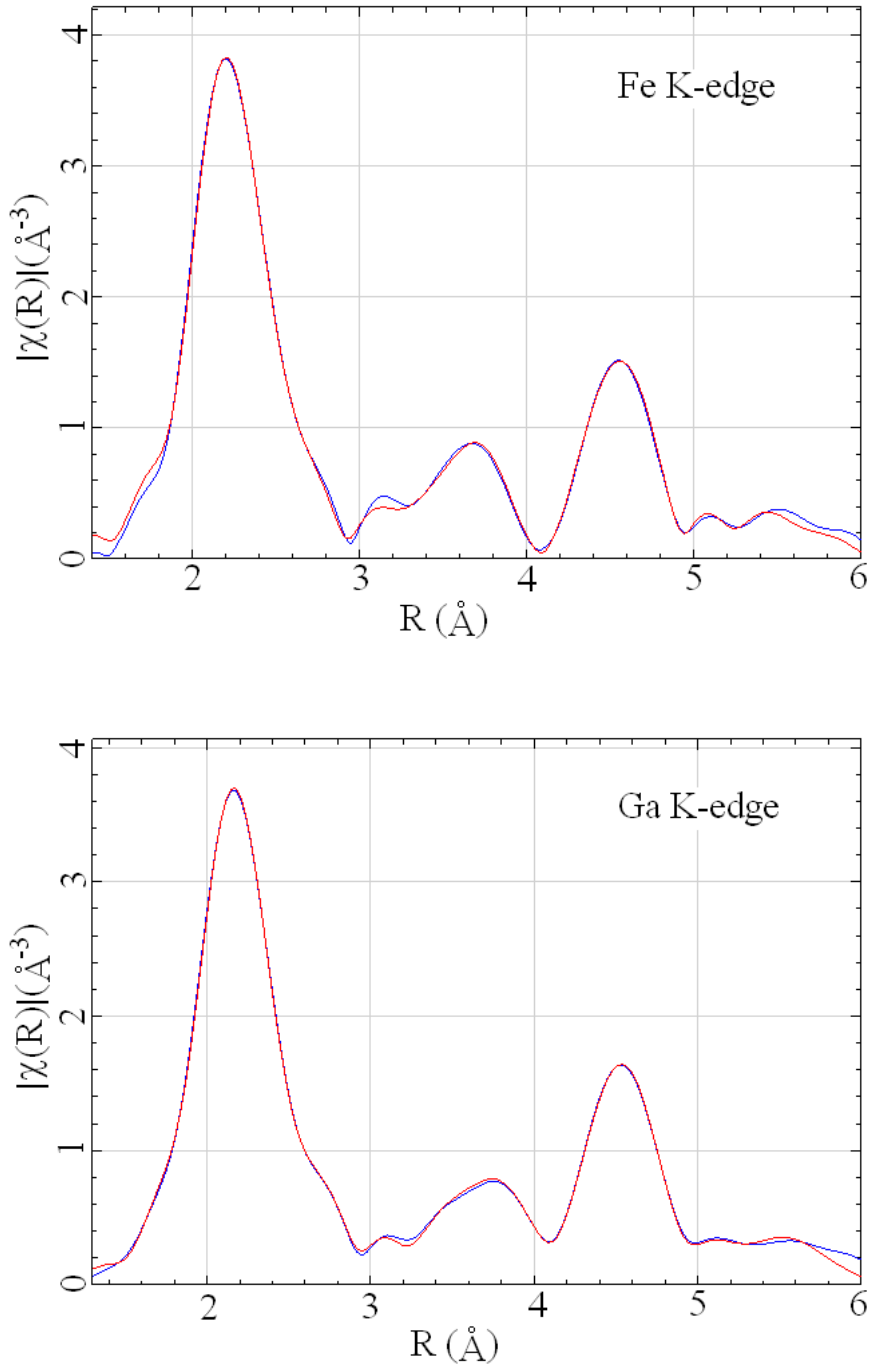

Figure 5.42 Plots of χ for Fe K-edge and Ga K-edge scans of Fe-27.5 at.% Ga ordering (ORD) single crystal first nearest neighbor analysis in R space. (Blue: Experimental Data; Red: Fit Data)

Table 5.12 First nearest neighbor analysis results of Fe-27.5 at.% Ga single crystal ordered sample Fe K-edge and Ga K-edge scan.

Fe K-edge	
Fe-Fe Path 1st Nearest Neighbor Distance(Å)	2.4832 ± 0.0097
N Value of Fe-Fe Path 1st Nearest Neighbor	0.5636 ± 0.1650
Enot Value of Fe-Fe Path (eV)	2.4485
Fe-Ga Path 1st Nearest Neighbor Distance(Å)	2.4832 ± 0.0358
N Value of Fe-Ga Path1st Nearest Neighbor	0.4364 ± 0.1650
Enot Value of Fe-Ga Path (eV)	-6.4474
Ga K-edge	
Ga-Ga Path 1st Nearest Neighbor Distance(Å)	2.4964 ± 0.0727
N Value of Ga-Ga Path 1st Nearest Neighbor	0.2238 ± 0.1671
Enot Value of Ga-Ga Path (eV)	-2.3115
Ga-Fe Path 1st Nearest Neighbor Distance(Å)	2.4832 ± 0.0358
N Value of Ga-Fe Path1st Nearest Neighbor	0.7762 ± 0.1671
Enot Value of Ga-Fe Path (eV)	4.6904
R-facor for the Fit	0.000045
amp for the Fit	1.1353

Ga-Fe bond lengths are shortened relative to the values calculated from the lattice parameter values and compensate for the strain placed in the lattice by the Ga-Ga nearest-neighbor bond. This observation indicates a large local distortion in the lattice. The results suggest the larger magnetostriction value for long-term annealed alloys ($(3/2)\lambda_{100}$ of 340 x 10^{-6} for the LTA sample compared to 193 x 10^{-6} for the DG sample) is related to the increase in the average Ga-Ga first nearest neighbor bond distance in the alloy.

In order to observe if a similar trend exists in other Fe-Ga alloys, EXAFS analysis of the first nearest neighbor atomic environment was also done for Fe-20 at.% Ga and Fe-15 at.% Ga alloy single crystals in their as-grown and long-term annealed conditions.

5.4.3.2 Artemis Results of Fe-20 at.% Ga Single Crystals

The best fit result for the Fe-20 at.% Ga alloy single crystal as-grown (DG) sample was obtained using a k-weight of 2 for both Fe K-edge and Ga K-edge scans and excluding the third scattering paths for all the FEFF calculations. The fit results for the Fe-20 at.% Ga as-grown sample is plotted in R space for both Fe K-edge and Ga K-edge scans and shown in Figure 5.43. The details of data obtained from the fit are presented in Table 5.13.

The fits for Fe-20 at.% Ga single crystals shows good quality as in the Fe-27.5 at.% Ga alloys. The R-factor for this fit is 0.000166, almost a hundred times smaller than the generally accepted limit. The consistency of the good quality of EXAFS fits shows that the modeling method applied in this work is more improved than in Garside's work [22]. The average atomic spacing of the first nearest neighbor calculated from x-ray diffraction analysis for this alloy is 2.5253 Å. As shown in Table 5.13, the Ga-Ga bond has a relatively larger value compare to the Fe-Fe or Fe-Ga bond. However, all the first

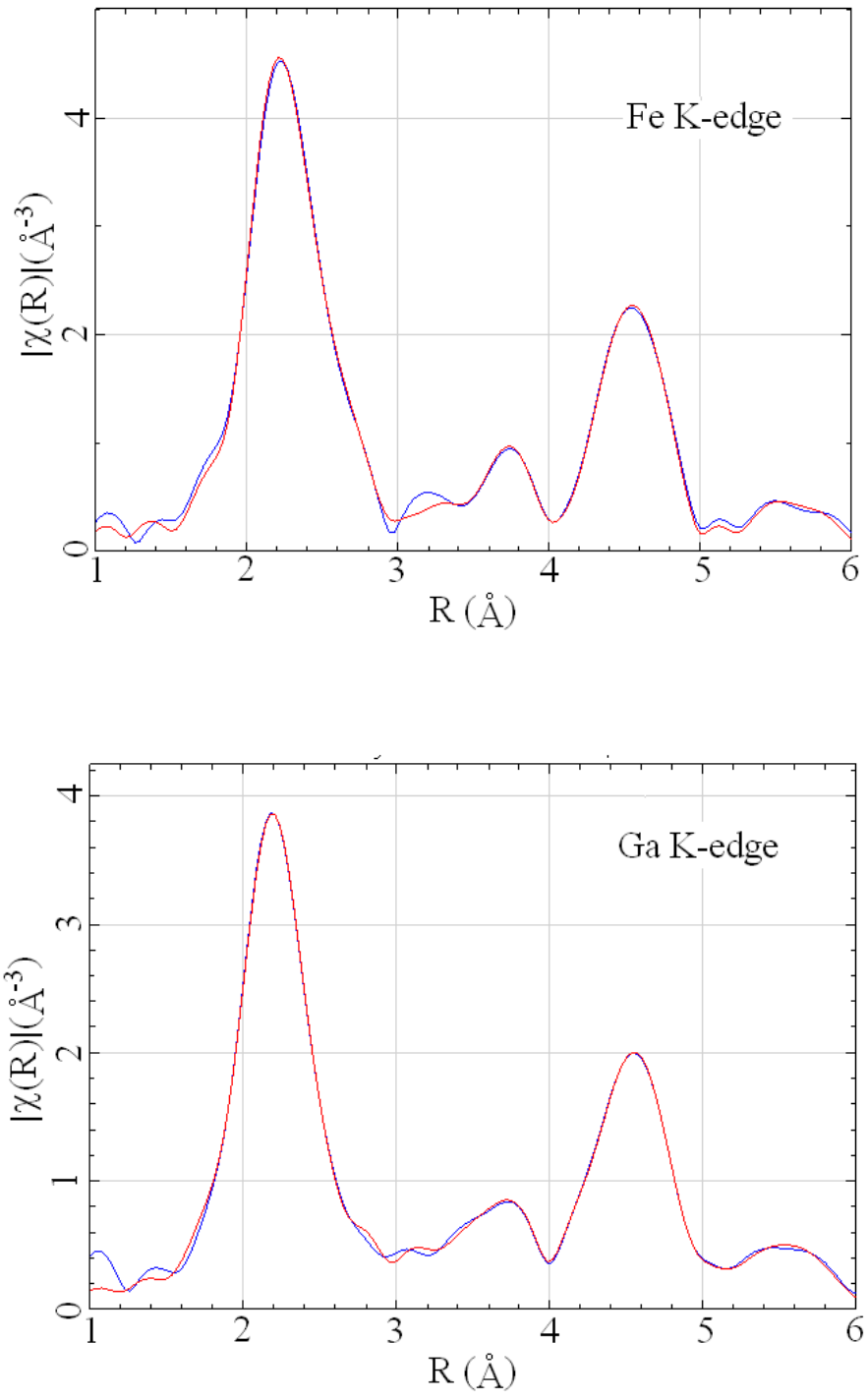

Figure 5.43 Plots of χ for Fe K-edge and Ga K-edge scans of Fe-20 at.% Ga as-grown (DG) single crystal first nearest neighbor analysis in R space. (Blue: Experimental Data; Red: Fit Data)

Table 5.13 First nearest neighbor analysis results of Fe-20 at.% Ga single crystal as-grown (DG) sample Fe K-edge and Ga K-edge scan.

Fe K-edge	
Fe-Fe Path 1st Nearest Neighbor Distance(Å)	2.5093 ± 0.0088
N Value of Fe-Fe Path 1st Nearest Neighbor	0.6946 ± 0.2614
Enot Value of Fe-Fe Path (eV)	7.4475
Fe-Ga Path 1st Nearest Neighbor Distance(Å)	2.5013 ± 0.0115
N Value of Fe-Ga Path1st Nearest Neighbor	0.3054 ± 0.2614
Enot Value of Fe-Ga Path (eV)	6.0075
Ga K-edge	
Ga-Ga Path 1st Nearest Neighbor Distance(Å)	2.5252 ± 0.0370
N Value of Ga-Ga Path 1st Nearest Neighbor	0.3866 ± 0.1665
Enot Value of Ga-Ga Path (eV)	6.2269
Ga-Fe Path 1st Nearest Neighbor Distance(Å)	2.5013 ± 0.0115
N Value of Ga-Fe Path1st Nearest Neighbor	0.6134 ± 0.1665
Enot Value of Ga-Fe Path (eV)	4.5789
R-factor for the Fit	0.000166
amp for the Fit	1.1467

nearest neighbor distances obtained from modeling are not very different from the average value obtained from x-ray diffraction analysis.

Using the same variables, fits were run on the Fe-20 at.% Ga single crystal long-term annealed (LTA) sample data. The k-weights of 1 and 2 were used for both Fe K-edge and Ga K-edge scan data and all the scattering paths were included in the FEFF calculations. A plot of the experimental data and the model fit in R space for the Fe-20 at.% Ga LTA sample is shown in Figure 5.44 and the results of the fit are shown in Table 5.14.

Results from the analysis of EXAFS data of Fe-20 at.% Ga alloy single crystals are similar to the results from the Fe-27.5 at.% Ga alloy single crystal. In all the conditions, the first nearest neighbor Ga-Ga bond distances always show a close or larger value than the average distance calculated from the XRD data which is 2.5253Å for the DG sample and 2.5175Å for the LTA sample. This Ga-Ga bond distance is also larger than the other Fe-Fe, Fe-Ga and Ga-Fe bond distances in the same condition. After long-term annealing, the Ga-Ga bond distance increases about 2.3% from 2.5252Å for DG data to 2.5828 Å for LTA data and all the other Fe-Fe, Fe-Ga and Ga-Fe bond distances have about a 1% drop.

5.4.3.3 Artemis Results of Fe-15 at.% Ga Single Crystals

EXAFS analysis with the same variables and scattering paths were also carried out for the Fe-15 at.% Ga single crystal in the as-grown and annealed conditions. For the best fit obtained for the Fe-15 at.% Ga alloy single crystal in the as-grown (DG) condition, k-weight of 2 was used for both Fe K-edge and Ga K-edge scan data and the third scattering paths were excluded from all of the FEFF calculations. The fit results are

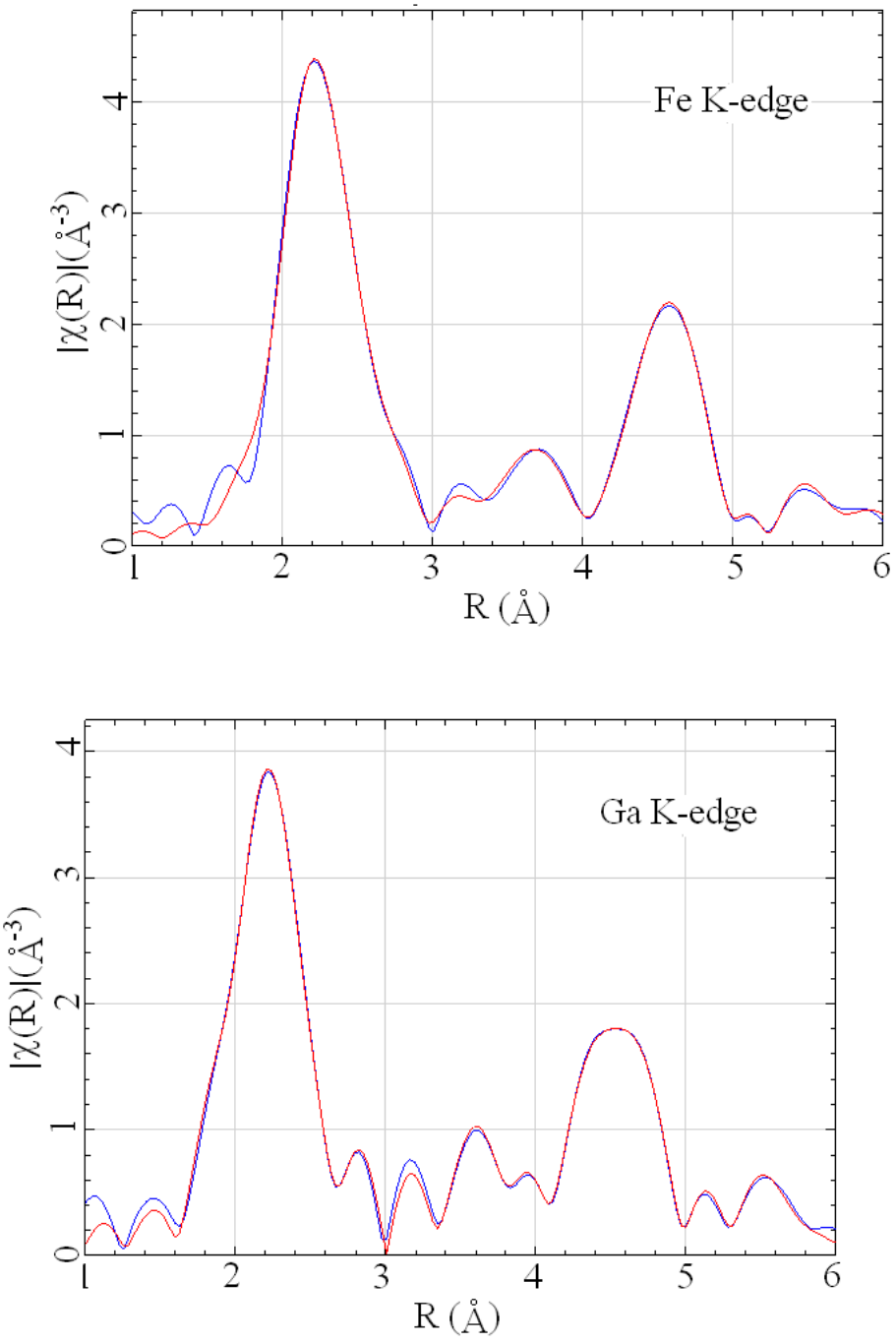

Figure 5.44 Plots of χ for Fe K-edge and Ga K-edge scans of Fe-20 at.% Ga long-term annealed (LTA) single crystal first nearest neighbor analysis in R space. (Blue: Experimental Data; Red: Fit Data)

Table 5.14 First nearest neighbor analysis results of Fe-20 at.% Ga single crystal long-term annealed (LTA) sample Fe K-edge and Ga K-edge scan.

Fe K-edge	
Fe-Fe Path 1st Nearest Neighbor Distance (Å)	2.4823 ± 0.0263
N Value of Fe-Fe Path 1st Nearest Neighbor	0.7726 ± 0.2021
Enot Value of Fe-Fe Path (eV)	4.1551
Fe-Ga Path 1st Nearest Neighbor Distance (Å)	2.4954 ± 0.0213
N Value of Fe-Ga Path1st Nearest Neighbor	0.2274 ± 0.2021
Enot Value of Fe-Ga Path (eV)	0.4816
Ga K-edge	
Ga-Ga Path 1st Nearest Neighbor Distance (Å)	2.5828 ± 0.0192
N Value of Ga-Ga Path 1st Nearest Neighbor	0.2215 ± 0.1225
Enot Value of Ga-Ga Path (eV)	4.5813
Ga-Fe Path 1st Nearest Neighbor Distance (Å)	2.4954 ± 0.0213
N Value of Ga-Fe Path1st Nearest Neighbor	0.7785 ± 0.1225
Enot Value of Ga-Fe Path (eV)	5.3413
R-factor for the Fit	0.0023
amp for the Fit	0.9708

shown in Figure 5.45 and the detailed information derived from the fit is shown in Table 5.15.

The best fit of the Fe-15 at.% Ga single crystal in the long-term annealed (LTA) condition was run with a k-weight of 2 for Fe K-edge and Ga K-edge scan data and all of the scattering paths included in the FEFF calculation. Fit results for this LTA sample are shown in Figure 5.46 with Fe K-edge and Ga K-edge scans plotted in R space, and the related variable values are shown in Table 5.16.

For the Fe-15 at.% Ga alloy single crystal sample, the first nearest neighbor Ga-Ga bond distance increase from 2.5031Å in the DG condition which is almost the same as the average value 2.5106Å to 2.5478 Å in the LTA condition which is about 1.5% larger than the average value 2.5097 Å. The Fe -Fe bond distance shows a 0.4% drop and the Fe-Ga bond distance has a 1.5% increase.

5.4.3.4 Analysis of the First Nearest Neighbor Atomic Environment for α-Fe-Ga Alloys

Comparing the results of the Fe-Ga single crystals with three different Ga contents, there is a general tendency of increase in the Ga-Ga first nearest neighbor distance and a decrease in the Fe-Fe first nearest neighbor distance after long-term annealing treatment. As discussed in the Fe-27.5 at.% Ga alloy single crystal section, this increase of Ga-Ga bond distance will introduce a distortion in the crystal lattice along the [111] direction in the region around the Ga-Ga atom pairs. It has been suggested that the strain placed by these Ga-Ga pairs with large atomic spacing could be one of the reasons for the increase of λ_{100} magnetostriction coefficient value after the long time annealing treatment.

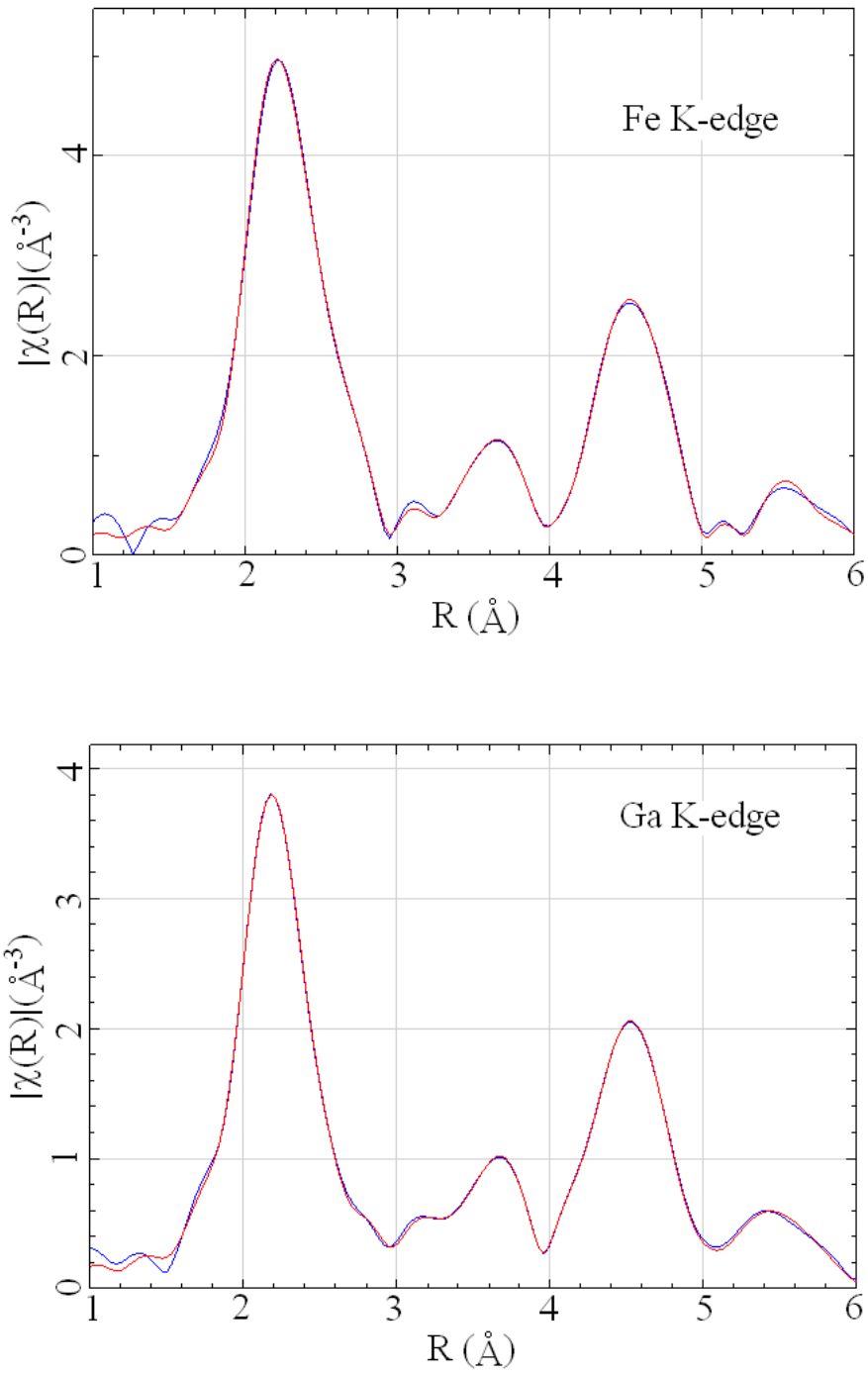

Figure 5.45 Plots of χ for Fe K-edge and Ga K-edge scans of Fe-15 at.% Ga as-grown (DG) single crystal first nearest neighbor analysis in R space. (Blue: Experimental Data; Red: Fit Data)

Table 5.15 First nearest neighbor analysis results of Fe-15 at.% Ga single crystal as-grown (DG) sample Fe K-edge and Ga K-edge scan.

Fe K-edge	
Fe-Fe Path 1st Nearest Neighbor Distance (Å)	2.4961 ± 0.0055
N Value of Fe-Fe Path 1st Nearest Neighbor	0.6758 ± 0.1379
Enot Value of Fe-Fe Path (eV)	6.4266
Fe-Ga Path 1st Nearest Neighbor Distance (Å)	2.4625 ± 0.0445
N Value of Fe-Ga Path1st Nearest Neighbor	0.3242 ± 0.1379
Enot Value of Fe-Ga Path (eV)	6.0074
Ga K-edge	
Ga-Ga Path 1st Nearest Neighbor Distance (Å)	2.5031 ± 0.0048
N Value of Ga-Ga Path 1st Nearest Neighbor	0.6139 ± 0.1281
Enot Value of Ga-Ga Path (eV)	4.6975
Ga-Fe Path 1st Nearest Neighbor Distance (Å)	2.4625 ± 0.0445
N Value of Ga-Fe Path1st Nearest Neighbor	0.3861 ± 0.1281
Enot Value of Ga-Fe Path (eV)	-0.8661
R-factor for the Fit	0.000079
amp for the Fit	1.2166

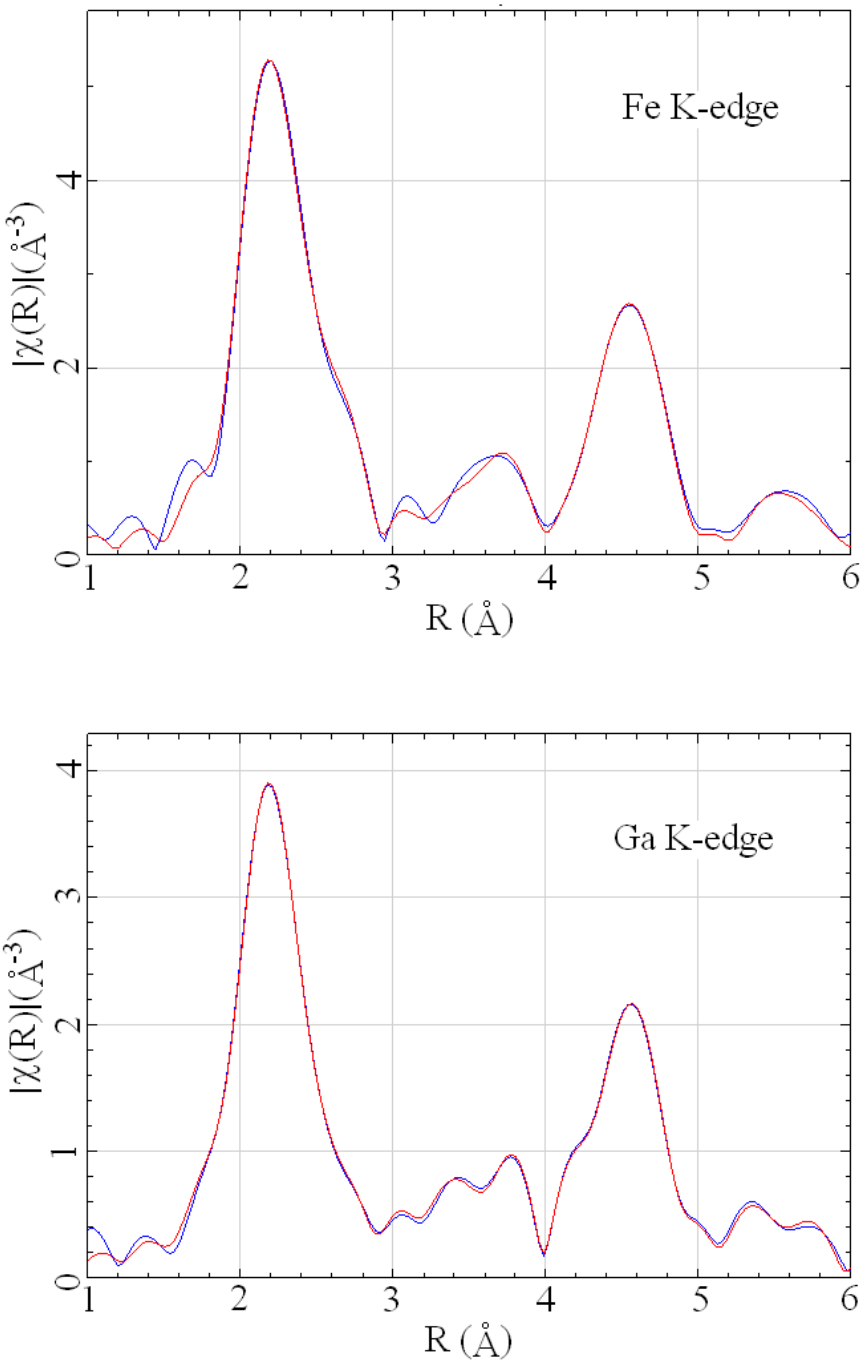

Figure 5.46 Plots of χ for Fe K-edge and Ga K-edge scans of Fe-15 at.% Ga long-term annealed (LTA) single crystal first nearest neighbor analysis in R space. (Blue: Experimental Data; Red: Fit Data)

Table 5.16 First nearest neighbor analysis results of Fe-15 at.% Ga single crystal long-term annealed (LTA) sample Fe K-edge and Ga K-edge scan.

Fe K-edge	
Fe-Fe Path 1st Nearest Neighbor Distance (Å)	2.4852 ± 0.0073
N Value of Fe-Fe Path 1st Nearest Neighbor	0.7501 ± 0.2217
Enot Value of Fe-Fe Path (eV)	5.2798
Fe-Ga Path 1st Nearest Neighbor Distance (Å)	2.5010 ± 0.0228
N Value of Fe-Ga Path1st Nearest Neighbor	0.2499 ± 0.2217
Enot Value of Fe-Ga Path (eV)	4.3386
Ga K-edge	
Ga-Ga Path 1st Nearest Neighbor Distance (Å)	2.5478 ± 0.0306
N Value of Ga-Ga Path 1st Nearest Neighbor	0.3032 ± 0.2250
Enot Value of Ga-Ga Path (eV)	9.3596
Ga-Fe Path 1st Nearest Neighbor Distance (Å)	2.5010 ± 0.0228
N Value of Ga-Fe Path1st Nearest Neighbor	0.6968 ± 0.2250
Enot Value of Ga-Fe Path (eV)	4.0131
R-factor for the Fit	0.00021
amp for the Fit	0.9839

This conclusion can be extended to other α-Fe-Ga alloys by comparing the change of the local lattice distortion introduced by the Ga-Ga pairs and the change of magnetostriction properties before and after long-term annealing. In this case, the lattice strains were calculated based on the Ga-Ga pair atomic distance obtained from the EXAFS model and the average first nearest neighbor atomic distance from XRD data. The change of distortion was quantified by the differences of lattice strain in DG and LTA conditions. The λ_{100} magnetostriction coefficient values were acquired in earlier research [11]. Results are shown in Table 5.17.

Because of the low Ga content in the Fe-15 at.% Ga and Fe- 20 at.% Ga alloys, the strain increase in the Ga-Ga bond is relatively small which is about a 1.8% increase for Fe-15 at.% Ga and 2.6% increase for Fe-20 at.% Ga. As the Ga content increases to a large value as Fe-27.5 at.% Ga which is close to the solid solubility limit of the Fe-Ga alloy, the local strain introduced by the Ga-Ga first nearest neighbor bond also increases to 12.0%, at least 4 times larger than that observed in the other alloys, and makes this bond distance close to the theoretical value for Ga-Ga metallic bond. The change of λ_{100} magnetostriction coefficient value before and after long time annealing treatment also shows a similar tendency as the change of local strain. There is only a relatively small effect of long time annealing to magnetostrictive behavior on Fe-20 at.% Ga and Fe- 15 at.% Ga. However, a significant change occurs as the Ga content increases from 20 at.% to 27.5 at.%. The change of λ_{100} magnetostriction coefficient value before and after long time annealing treatment increases almost two times, from 82×10^{-6} for Fe-20 at.% Ga to 147×10^{-6} for Fe-27.5 at.% Ga. The relationship between the change of lattice strain and change of magnetostriction value is not linear. One of the possible reasons is that a large

Table 5.17 Change of lattice strain of Ga-Ga first nearest neighbor bond and λ_{100} magnetostriction coefficient value before and after long time annealing of Fe-Ga single crystals.

Alloy Composition	Change of Lattice Strain for Ga-Ga Bond DG/LTA	λ_{100} Magnetostriction Coefficient Value DG (x 10^{-6})	λ_{100} Magnetostriction Coefficient Value LTA (x 10^{-6})	Change of λ_{100} Magnetostriction Coefficient Value DG/LTA (x 10^{-6})
Fe-27.5 at.% Ga	+12.195%	193	340	+147
Fe-20 at.% Ga	+2.598%	297	379	+82
Fe-15 at.% Ga	+1.818%	196	258	+62

amount of second phase regions will start forming as the Ga content in the Fe-Ga alloy increases to more than 20 at.%. This second phase has different crystal structure and density from the disordered α- Fe matrix and causes a large drop of the alloy's magnetostriction. As a result, part of the increase of magnetostriction value contributed from lattice strain will be cancelled out because of the effect of these second phase regions. The correlation of the local lattice strain data and the magnetostriction coefficient data is consistent with the hypothesis that the increase in local strain in the crystal lattice caused by the Ga-Ga first nearest neighbor bond contributes to the increase of magnetostriction of Fe-Ga alloys.

5.4.4 Results of Fe-Ga Alloy Second Nearest Neighbor Analysis

5.4.4.1 Artemis Results of Fe-27.5 at.% Ga Single Crystal

The best fit results for the Fe-27.5 at.% Ga single crystal DG sample from second nearest neighbor modeling was obtained by fitting the data with k-weight of 1 for both Fe and Ga k-edge scans. All the scattering paths were included in the fit. The model fit for Fe and Ga K-edge scan data of the Fe-27.5 at.% Ga DG sample using the second nearest neighbor model in the R space are shown in Figure 5.47.

As shown in Figure 5.46, the modeling result fits nicely to the experimental spectra and no large discrepancy is seen. The only small mismatch is at about 3.1Å in R space is well beyond the second nearest neighbor. The R-factor of this fit is 0.0025, which is much smaller than the maximum acceptable limit 0.02. The mean values and uncertainties about atomic spacing, energy shift, amplitude and coordination of this fit are shown in Table 5.18. Except for the Fe-Fe-Ga path 1st nearest neighbor distance which

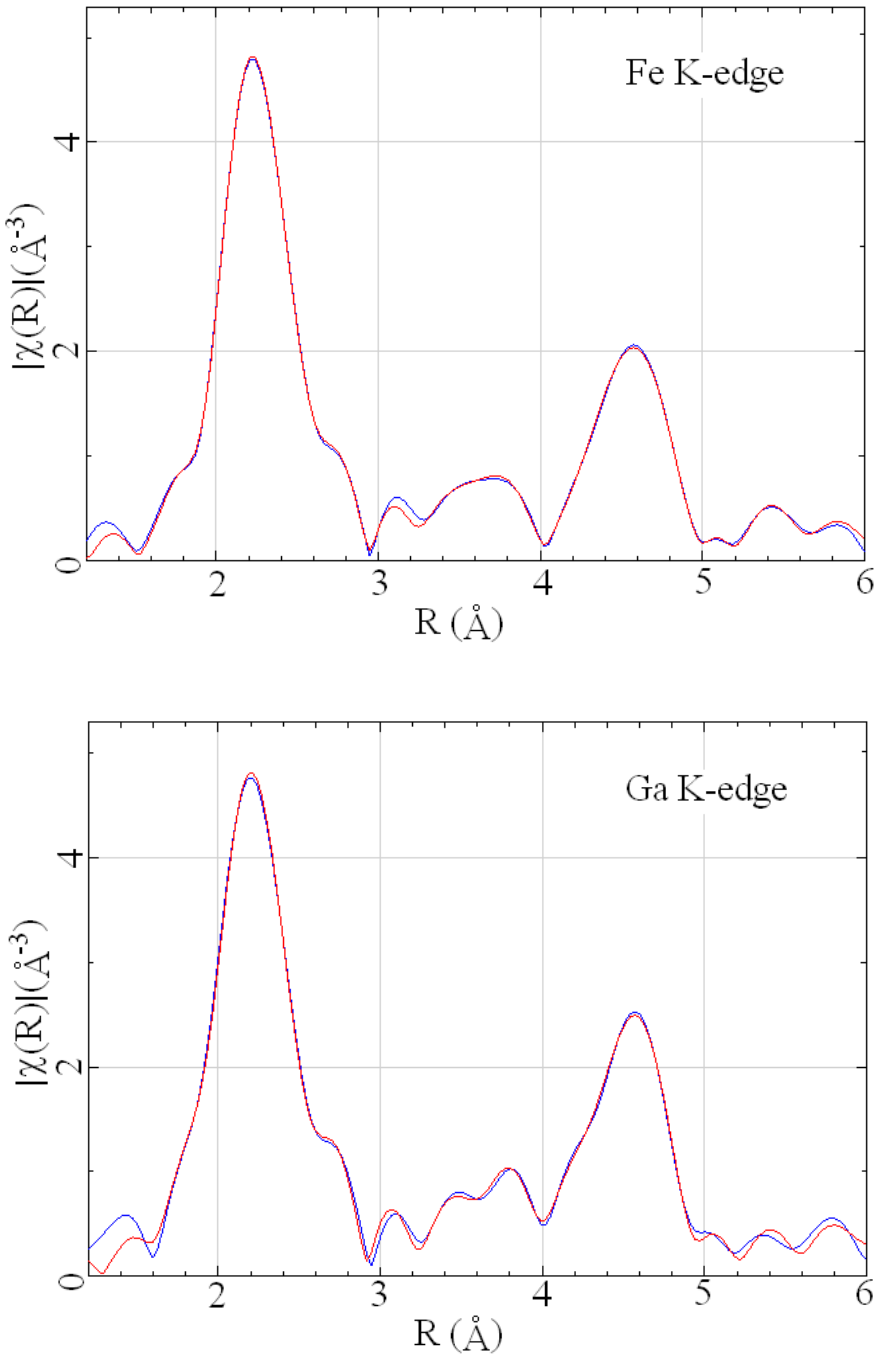

Figure 5.47 Plots of χ for Fe K-edge and Ga K-edge scans of Fe-27.5 at.% Ga as-grown (DG) single crystal second nearest neighbor analysis result in R space. (Blue: Experimental Data; Red: Fit Data)

Table 5.18 Results of Fe-27.5 at.% Ga as-grown (DG) single crystal second nearest neighbor analysis

Fe K-edge	
Fe-Fe-Fe Path 1st Nearest Neighbor Distance (Å)	2.4746 ± 0.0378
Fe-Fe-Fe Path 2nd Nearest Neighbor Distance (Å)	2.8516 ± 0.0362
Fe-Fe-Ga Path 1st Nearest Neighbor Distance (Å)	2.2050 ± 0.2469
Fe-Fe-Ga Path 2nd Nearest Neighbor Distance (Å)	2.9305 ± 0.0583
Fe-Ga-Fe Path 1st Nearest Neighbor Distance (Å)	2.4970 ± 0.0528
Fe-Ga-Fe Path 2nd Nearest Neighbor Distance (Å)	3.0780 ± 0.0522
Fe-Ga-Ga Path 1st Nearest Neighbor Distance (Å)	2.5842 ± 0.0458
Fe-Ga-Ga Path 2nd Nearest Neighbor Distance (Å)	2.6970 ± 0.0686
N_{Fe} at 1st Nearest Neighbor	5.45 ± 1.21
N_{Fe} at 2nd Nearest Neighbor	4.70 ± 0.91
N_{Ga} at 1st Nearest Neighbor	2.55 ± 1.21
N_{Ga} at 2nd Nearest Neighbor	1.30 ± 0.91
Enot (eV)	4.9265

Table 5.18 Continued

Ga K-edge	
Ga-Fe-Fe Path 1st Nearest Neighbor Distance (Å)	2.4981 ± 0.0183
Ga-Fe-Fe Path 2nd Nearest Neighbor Distance (Å)	2.8309 ± 0.0526
Ga-Fe-Ga Path 1st Nearest Neighbor Distance (Å)	2.5194 ± 0.13
Ga-Fe-Ga Path 2nd Nearest Neighbor Distance (Å)	3.0205 ± 0.029
Ga-Ga-Fe Path 1st Nearest Neighbor Distance (Å)	2.4536 ± 0.0205
Ga-Ga-Fe Path 2nd Nearest Neighbor Distance (Å)	2.9462 ± 0.0284
Ga-Ga-Ga Path 1st Nearest Neighbor Distance (Å)	2.5787 ± 0.0234
Ga-Ga-Ga Path 2nd Nearest Neighbor Distance (Å)	2.7755 ± 0.0419
N_{Fe} at 1st Nearest Neighbor	6.71 ± 1.14
N_{Fe} at 2nd Nearest Neighbor	3.44 ± 0.85
N_{Ga} at 1st Nearest Neighbor	1.29 ± 1.14
N_{Ga} at 2nd Nearest Neighbor	2.56 ± 0.85
Enot (eV)	4.5087
R-factor for the Fit	0.0025
amp for the Fit	1.19

shows a low value and very large standard deviation, other values are reasonable and have small standard deviation.

If all the Ga atoms are randomly distributed inside the the crystal lattice of the α-phase, for the Fe-27.5 at.% Ga alloy, there should be 2.20 Ga atoms and 5.80 Fe atoms in the first nearest neighbor positions and about 1.65 Ga atoms and 4.35 Fe atoms in the second nearest neighbor positions. By comparing this average value to the N values obtained from the analysis results, the preference for a specific type of atomic bond formation can be determined. For the Fe-27.5 at.% Ga DG sample, the Ga-Fe or Fe-Ga type of first nearest neighbor bond is more preferred than the average value. There is less preference for forming Ga-Ga first nearest neighbor bonds than an ideal random solid solution.

Artemis® projects with the same atomic arrangement, scattering paths and defined variables were programmed and fits were run on scan data for Fe-27.5 at.% Ga long-term annealed (LTA) and ordered (ORD) samples. The best fit of the Fe-27.5 at.% Ga long-term annealed (LTA) sample was obtained by using a k-weight of 1 and excluding the third scattering path with large scattering angles from the FEFF calculations. Figure 5.48 shows the fit results of the Fe-27.5 at.% Ga LTA sample with Fe K-edge and Ga K-edge scan plotted in R space. As discussed in the DG sample, there is no significant mismatch between the experimental spectra and the modeling results. The R-factor of this fit is 0.0014 which is much better than the acceptable limit. The detailed results obtained from this fit are shown in Table 5.19. Fe-Fe-Ga and Ga-Fe-Ga path first nearest neighbor distances are low value compared to other first nearest neighbor distances.

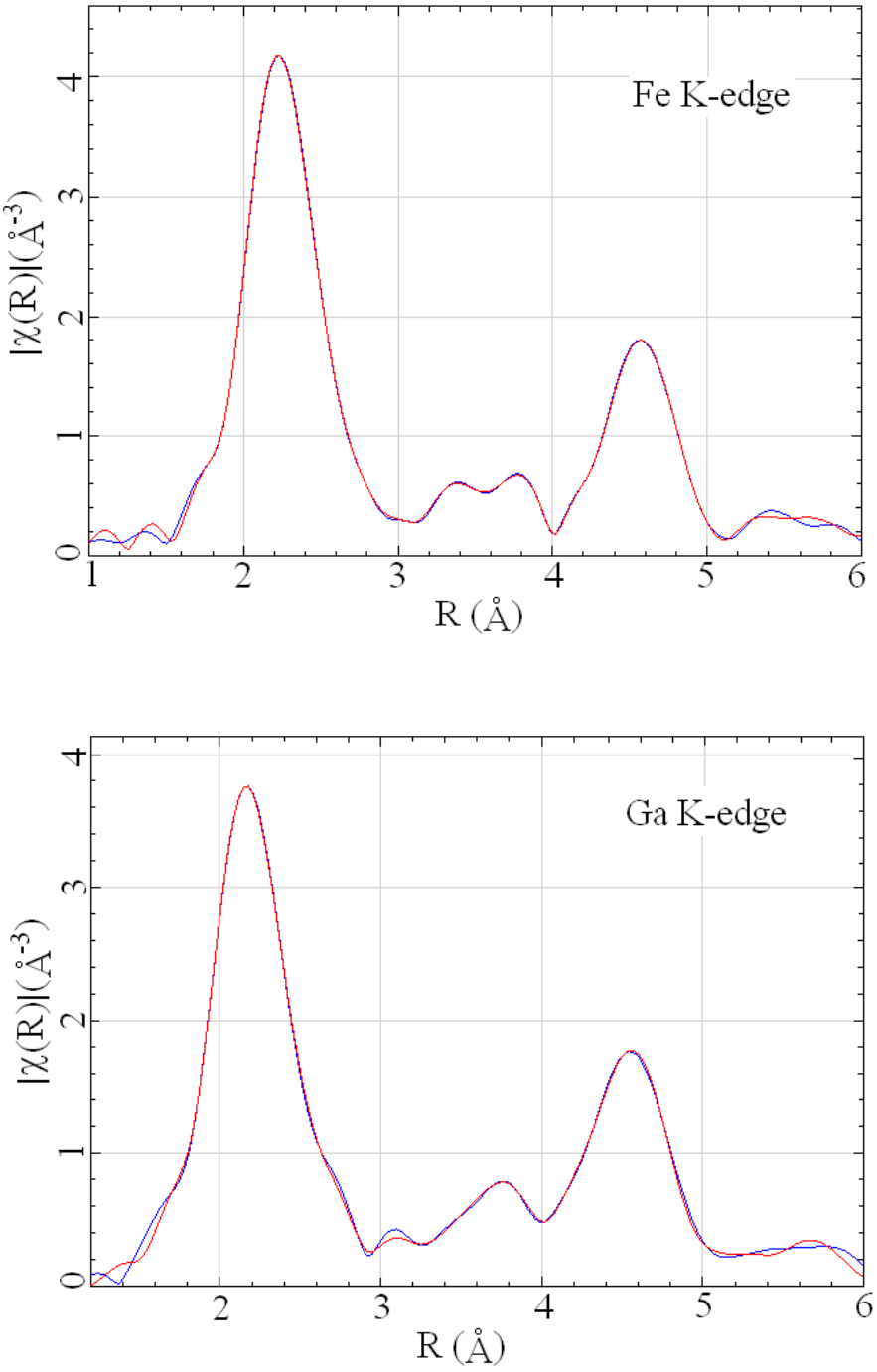

Figure 5.48 Plots of χ for Fe K-edge and Ga K-edge scans of Fe-27.5 at.% Ga long-term annealed (LTA) single crystal second nearest neighbor analysis result in R space. (Blue: Experimental Data; Red: Fit Data)

Table 5.19 Results of Fe-27.5 at.% Ga long-term annealed (LTA) single crystal second nearest neighbor analysis

Fe K-edge	
Fe-Fe-Fe Path 1st Nearest Neighbor Distance (Å)	2.5281 ± 0.0427
Fe-Fe-Fe Path 2nd Nearest Neighbor Distance (Å)	2.877 ± 0.0503
Fe-Fe-Ga Path 1st Nearest Neighbor Distance (Å)	2.4942 ± 0.123
Fe-Fe-Ga Path 2nd Nearest Neighbor Distance (Å)	3.2983 ± 0.0689
Fe-Ga-Fe Path 1st Nearest Neighbor Distance (Å)	2.2623 ± 0.0914
Fe-Ga-Fe Path 2nd Nearest Neighbor Distance (Å)	3.0868 ± 0.0458
Fe-Ga-Ga Path 1st Nearest Neighbor Distance (Å)	2.3362 ± 0.066
Fe-Ga-Ga Path 2nd Nearest Neighbor Distance (Å)	2.8780 ± 0.1066
N_{Fe} at 1st Nearest Neighbor	4.56 ± 0.79
N_{Fe} at 2nd Nearest Neighbor	5.59 ± 0.59
N_{Ga} at 1st Nearest Neighbor	3.44 ± 0.79
N_{Ga} at 2nd Nearest Neighbor	0.41 ± 0.59
Enot (eV)	7.3051

Table 5.19 Continued

Ga K-edge	
Ga-Fe-Fe Path 1st Nearest Neighbor Distance (Å)	2.4760 ± 0.0127
Ga-Fe-Fe Path 2nd Nearest Neighbor Distance (Å)	2.8163 ± 0.0291
Ga-Fe-Ga Path 1st Nearest Neighbor Distance (Å)	2.3199 ± 0.1054
Ga-Fe-Ga Path 2nd Nearest Neighbor Distance (Å)	2.9003 ± 0.0264
Ga-Ga-Fe Path 1st Nearest Neighbor Distance (Å)	2.5455 ± 0.0938
Ga-Ga-Fe Path 2nd Nearest Neighbor Distance (Å)	3.0531 ± 0.0152
Ga-Ga-Ga Path 1st Nearest Neighbor Distance (Å)	2.5384 ± 0.0286
Ga-Ga-Ga Path 2nd Nearest Neighbor Distance (Å)	3.2889 ± 0.0935
N_{Fe} at 1st Nearest Neighbor	5.31 ± 0.76
N_{Fe} at 2nd Nearest Neighbor	4.84 ± 0.57
N_{Ga} at 1st Nearest Neighbor	2.69 ± 0.76
N_{Ga} at 2nd Nearest Neighbor	1.16 ± 0.57
Enot (eV)	1.4973
R-factor for the Fit	0.0014
amp for the Fit	1.1864

After long-term annealing, the N value of the Ga-Ga first nearest neighbor bond increases from 1.29 to 2.69 which indicates an increase in the tendency to form a Ga-Ga pair inside the crystal lattice. The N value of Fe-Ga and Ga-Fe first nearest neighbor bonds does not have a significant change. The number of Fe-Fe type first neighbor bonds decreases slightly as a result of forming more Fe-Ga bonds in Fe centered atomic arrangement after long-term annealing.

The best fit of the Fe-27.5 at.% Ga ordered (ORD) sample was run using k-weights of 1 and 2 for both Fe K-edge and Ga K-edge scans and excluding the third scattering path from the FEFF calculations to minimize the data noise. The results of fit for the Fe-27.5 at.% Ga ORD sample are shown in Figure 5.49 with Fe and Ga K-edge scans plotted in R space. The parameter values obtained in these results are shown in Table 5.20. Fe-Ga-Ga second nearest neighbor distance is very large (3.5176) relative to the average value. The other values are in reasonable range. The fit results show a nice match to the experimental spectra and the R factor is as small as 0.0012. Compared to the LTA data set, the N value for Ga-Ga first nearest neighbor bonds decrease slightly and the N value for Fe-Fe first nearest neighbor bonds increases about 1.18. As a result of decrease in the number of Fe-Ga first nearest neighbor bonds in the Fe centered atomic arrangement, the total number of Fe-Ga and Ga-Fe bonds dropped about 0.72.

EXAFS analyses results from three Fe-27.5 at.% Ga single crystals with different thermal histories show a tendency of increase in the number of Ga-Ga type first nearest bonds after long-term annealing heat treatment from N equal to 1.29 to N equal to 2.69. This value drops to N equal to 2.23 after ordering heat treatment. The N value of Fe-Fe type first nearest neighbor bonds changes in the opposite way to that of N values of Ga-

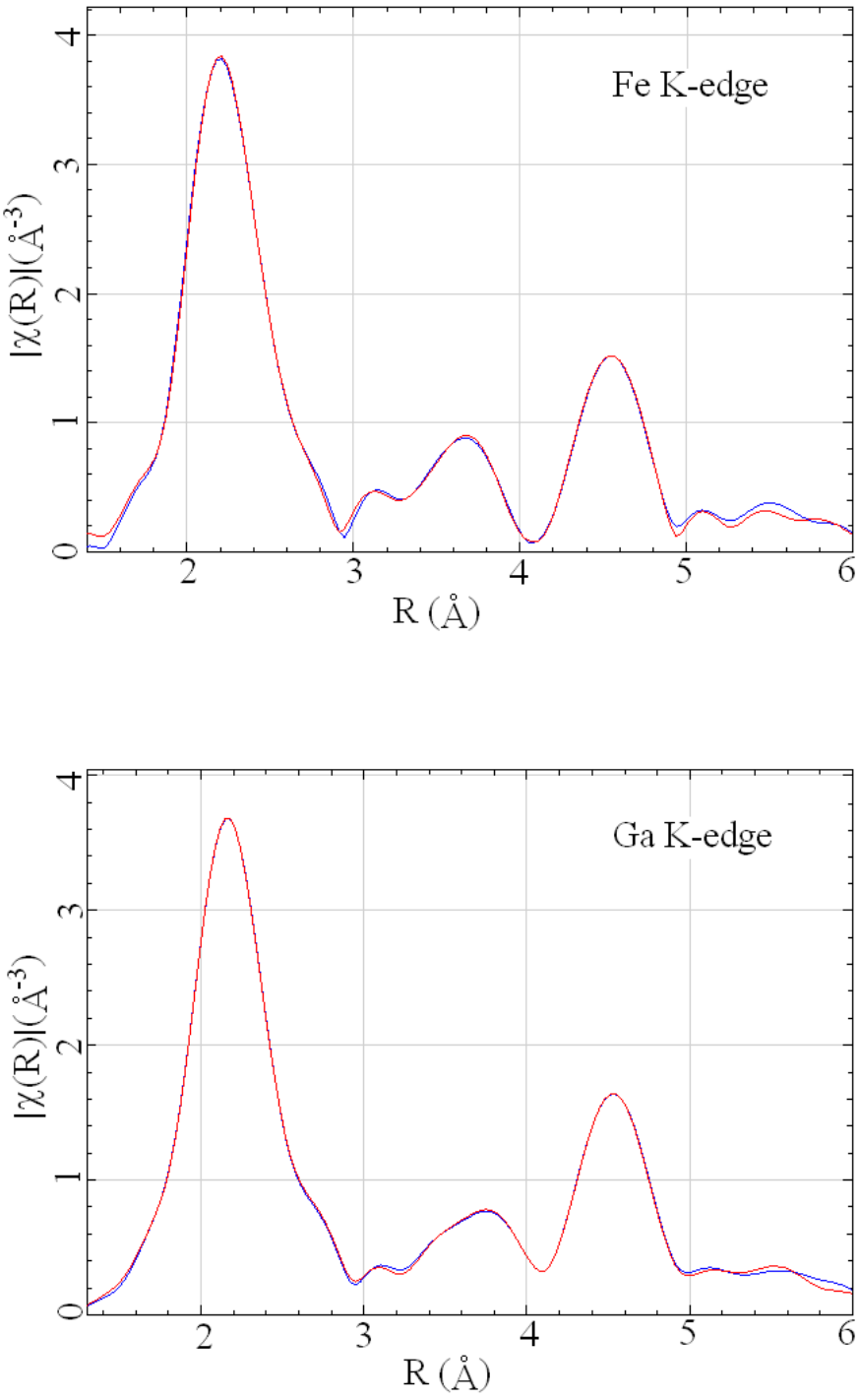

Figure 5.49 Plots of χ for Fe K-edge and Ga K-edge scans of Fe-27.5 at.% Ga ordered (ORD) single crystal second nearest neighbor analysis result in R space. (Blue: Experimental Data; Red: Fit Data)

Table 5.20 Results of Fe-27.5 at.% Ga ordered (ORD) single crystal second nearest neighbor analysis

Fe K-edge	
Fe-Fe-Fe Path 1st Nearest Neighbor Distance (Å)	2.4899 ± 0.0402
Fe-Fe-Fe Path 2nd Nearest Neighbor Distance (Å)	2.8405 ± 0.0768
Fe-Fe-Ga Path 1st Nearest Neighbor Distance (Å)	2.5081 ± 0.2682
Fe-Fe-Ga Path 2nd Nearest Neighbor Distance (Å)	2.9176 ± 0.0573
Fe-Ga-Fe Path 1st Nearest Neighbor Distance (Å)	2.5574 ± 0.0981
Fe-Ga-Fe Path 2nd Nearest Neighbor Distance (Å)	3.0574 ± 0.0411
Fe-Ga-Ga Path 1st Nearest Neighbor Distance (Å)	2.6048 ± 0.1577
Fe-Ga-Ga Path 2nd Nearest Neighbor Distance (Å)	3.5176 ± 0.0718
N_{Fe} at 1st Nearest Neighbor	5.74 ± 2.28
N_{Fe} at 2nd Nearest Neighbor	4.41 ± 1.71
N_{Ga} at 1st Nearest Neighbor	2.26 ± 2.28
N_{Ga} at 2nd Nearest Neighbor	1.59 ± 1.71
Enot (eV)	4.1125

Table 5.20 Continued

Ga K-edge	
Ga-Fe-Fe Path 1st Nearest Neighbor Distance (Å)	2.4979 ± 0.0161
Ga-Fe-Fe Path 2nd Nearest Neighbor Distance (Å)	2.7779 ± 0.0223
Ga-Fe-Ga Path 1st Nearest Neighbor Distance (Å)	2.3973 ± 0.0466
Ga-Fe-Ga Path 2nd Nearest Neighbor Distance (Å)	2.9020 ± 0.0185
Ga-Ga-Fe Path 1st Nearest Neighbor Distance (Å)	2.6044 ± 0.0789
Ga-Ga-Fe Path 2nd Nearest Neighbor Distance (Å)	3.0898 ± 0.0195
Ga-Ga-Ga Path 1st Nearest Neighbor Distance (Å)	2.5617 ± 0.0194
Ga-Ga-Ga Path 2nd Nearest Neighbor Distance (Å)	3.0166 ± 0.024
N_{Fe} at 1st Nearest Neighbor	5.77 ± 0.28
N_{Fe} at 2nd Nearest Neighbor	4.38 ± 0.21
N_{Ga} at 1st Nearest Neighbor	2.23 ± 0.28
N_{Ga} at 2nd Nearest Neighbor	1.62 ± 0.21
Enot (eV)	3.196
R-factor for the Fit	0.0012
amp for the Fit	0.8768

Ga bonds. It first decreases from 5.45 to 4.56 after LTA heat treatment and increases to 5.74 after ordering heat treatment. For the total N value of Fe-Ga and Ga-Fe bonds, there is no significant difference between DG and LTA conditions, but the N value dropped slightly compared to that in the ORD condition. As discussed in the EXAFS first nearest neighbor modeling section, the formation of Ga-Ga first nearest neighbor bonds introduces large local distortions to the lattice. Based on the results of first and second nearest neighbor analysis, the reason for larger magnetostriction value of the Fe-27.5 at.% Ga alloy after long-term annealing may be attributed to both the increase in average Ga-Ga first nearest neighbor bond distance and the increase in the number of this type of bond in the alloy.

In order to extend this study to other Fe-Ga alloys, EXAFS second nearest neighbor analyses were also done for Fe-20 at.% Ga and Fe-15 at.% Ga single crystals in the as-grown and long-term annealed conditions. The related results will be presented in the following sections.

5.4.4.2 Artemis Results of Fe-20 at.% Ga Single Crystal

The best fit for the Fe-20 at.% Ga alloy single crystal in the as-grown (DG) condition was obtained using a k-weight of 1 for both Fe and Ga K-edge scans and excluding the third scattering path from FEFF calculations. The fit results for this Fe-20 at.% Ga DG sample are shown in Figure 5.50 with Fe and Ga K-edge scans plotted in R space. The detailed data results are shown in Table 5.21. Fe-Ga-Fe path first nearest neighbor distance and Fe-Ga-Ga path second nearest neighbor distance are low compared to the average first and second nearest neighbor distances.

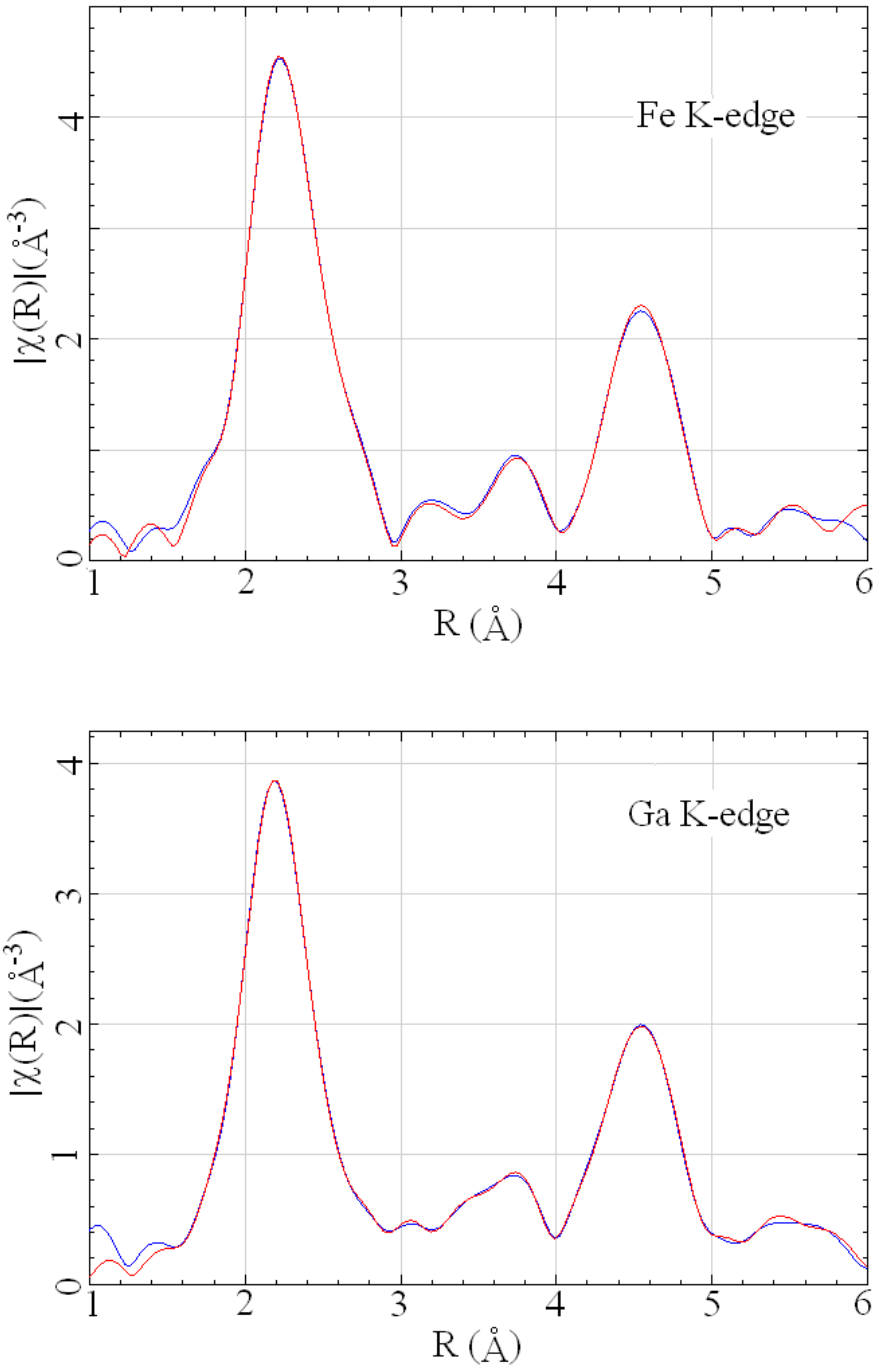

Figure 5.50 Plots of χ for Fe K-edge and Ga K-edge scans of Fe-20 at.% Ga as-grown (DG) single crystal second nearest neighbor analysis result in R space. (Blue: Experimental Data; Red: Fit Data)

Table 5.21 Results of Fe-20 at.% Ga as-grown (DG) single crystal second nearest neighbor analysis

Fe K-edge	
Fe-Fe-Fe Path 1st Nearest Neighbor Distance (Å)	2.4921 ± 0.0152
Fe-Fe-Fe Path 2nd Nearest Neighbor Distance (Å)	2.9419 ± 0.0259
Fe-Fe-Ga Path 1st Nearest Neighbor Distance (Å)	2.6379 ± 0.029
Fe-Fe-Ga Path 2nd Nearest Neighbor Distance (Å)	3.0623 ± 0.0138
Fe-Ga-Fe Path 1st Nearest Neighbor Distance (Å)	2.3546 ± 0.0346
Fe-Ga-Fe Path 2nd Nearest Neighbor Distance (Å)	2.8940 ± 0.0134
Fe-Ga-Ga Path 1st Nearest Neighbor Distance (Å)	2.4426 ± 0.0184
Fe-Ga-Ga Path 2nd Nearest Neighbor Distance (Å)	2.7484 ± 0.0128
N_{Fe} at 1st Nearest Neighbor	7.50 ± 0.38
N_{Fe} at 2nd Nearest Neighbor	3.70 ± 0.29
N_{Ga} at 1st Nearest Neighbor	0.50 ± 0.38
N_{Ga} at 2nd Nearest Neighbor	2.30 ± 0.29
Enot (eV)	8.3122

Table 5.21 Continued

Ga K-edge	
Ga-Fe-Fe Path 1st Nearest Neighbor Distance (Å)	2.4906 ± 0.0191
Ga-Fe-Fe Path 2nd Nearest Neighbor Distance (Å)	2.7901 ± 0.0196
Ga-Fe-Ga Path 1st Nearest Neighbor Distance (Å)	2.6111 ± 0.0414
Ga-Fe-Ga Path 2nd Nearest Neighbor Distance (Å)	3.4586 ± 0.0342
Ga-Ga-Fe Path 1st Nearest Neighbor Distance (Å)	2.5038 ± 0.0397
Ga-Ga-Fe Path 2nd Nearest Neighbor Distance (Å)	2.9798 ± 0.0234
Ga-Ga-Ga Path 1st Nearest Neighbor Distance (Å)	2.6955 ± 0.0293
Ga-Ga-Ga Path 2nd Nearest Neighbor Distance (Å)	2.5857 ± 0.0291
N_{Fe} at 1st Nearest Neighbor	5.55 ± 0.31
N_{Fe} at 2nd Nearest Neighbor	5.65 ± 0.23
N_{Ga} at 1st Nearest Neighbor	2.45 ± 0.31
N_{Ga} at 2nd Nearest Neighbor	0.35 ± 0.23
Enot (eV)	4.7096
R-factor for the Fit	0.0029
amp for the Fit	0.9557

No significant discrepancy was observed between the modeling results and the experimental spectra for this Fe-20 at.% Ga DG sample. The R factor is 0.0029 which is smaller than the acceptable limit value 0.02. In the completely random solid solution condition of this alloy, there should be about 1.6 Ga atoms and 6.4 Fe atoms in the first nearest neighbor positions and 1.2 Ga atoms and 4.8 Fe atoms in the second nearest neighbor positions. Based on the N values in the as-grown condition, there is a slightly higher possibility to form a Ga-Ga first nearest neighbor pair for this sample than the random solid solution condition. There is also a higher N value for Fe-Fe pairs and lower N value for Fe-Ga or Ga-Fe type of bonds in the first nearest neighbor position.

The Artemis® project with the same atomic arrangements, scattering paths and defined variables was programmed for the Fe-20 at.% Ga alloy single crystal in the long-term annealed (LTA) condition; the fit was run with a k-weight of 1 and third scattering path excluded from FEFF calculations. Figure 5.51 shows the results of model fit to the experimental spectra, and Table 5.22 shows the data of fit results. Fe-Fe-Ga and Ga-Ga-Ga path second nearest neighbor distances are large compared to the average second nearest neighbor distances.

For the Fe-20 at.% Ga single crystal sample after long-term annealing, the N values of different types of bonds do not show as much change as in Fe-27.5 at.% Ga. There is no significant change in the N value of Ga-Ga first nearest neighbor bonds, and the N value of the Fe-Fe type first nearest bond decreases slightly from 7.5 to 7.1. The number of Fe-Ga type of first nearest bonds increases from 0.5 to 0.93, but the total number of Fe-Ga and Ga-Fe bonds is nearly constant.

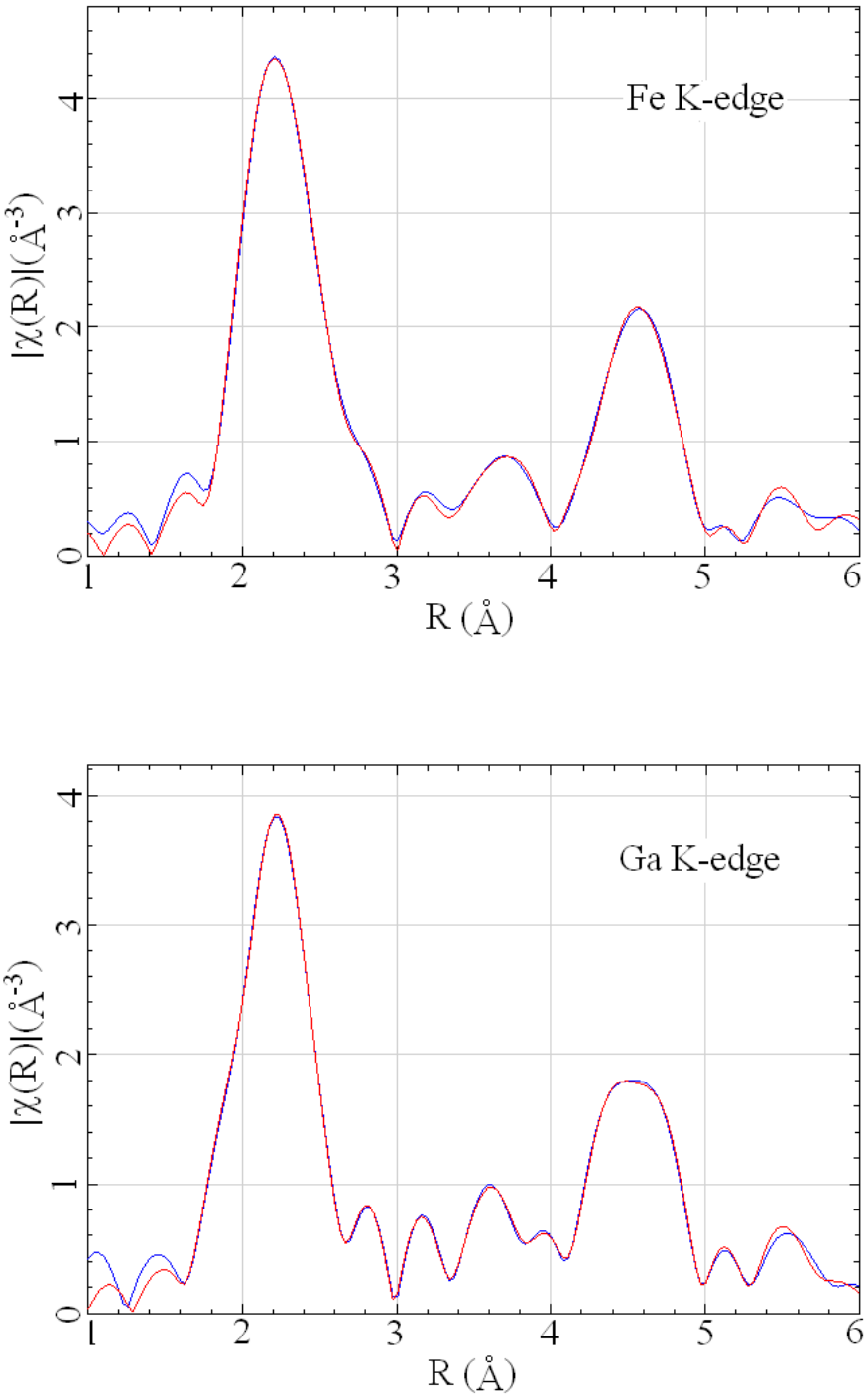

Figure 5.51 Plots of χ for Fe K-edge and Ga K-edge scans of Fe-20 at.% Ga long-term annealed (LTA) single crystal second nearest neighbor analysis result in R space. (Blue: Experimental Data; Red: Fit Data)

Table 5.22 Results of Fe-20 at.% Ga long-term annealed (LTA) single crystal second nearest neighbor analysis

Fe K-edge	
Fe-Fe-Fe Path 1st Nearest Neighbor Distance (Å)	2.4862 ± 0.0137
Fe-Fe-Fe Path 2nd Nearest Neighbor Distance (Å)	2.9511 ± 0.0244
Fe-Fe-Ga Path 1st Nearest Neighbor Distance (Å)	2.6175 ± 0.0529
Fe-Fe-Ga Path 2nd Nearest Neighbor Distance (Å)	3.2404 ± 0.128
Fe-Ga-Fe Path 1st Nearest Neighbor Distance (Å)	2.4447 ± 0.0186
Fe-Ga-Fe Path 2nd Nearest Neighbor Distance (Å)	2.8354 ± 0.0162
Fe-Ga-Ga Path 1st Nearest Neighbor Distance (Å)	2.5637 ± 0.2076
Fe-Ga-Ga Path 2nd Nearest Neighbor Distance (Å)	2.9796 ± 0.1332
N_{Fe} at 1st Nearest Neighbor	7.10 ± 0.7
N_{Fe} at 2nd Nearest Neighbor	4.10 ± 0.52
N_{Ga} at 1st Nearest Neighbor	0.93 ± 0.7
N_{Ga} at 2nd Nearest Neighbor	1.87 ± 0.52
Enot (eV)	6.8162

Table 5.22 Continued

Ga K-edge	
Ga-Fe-Fe Path 1st Nearest Neighbor Distance (Å)	2.4829 ± 0.0263
Ga-Fe-Fe Path 2nd Nearest Neighbor Distance (Å)	2.8670 ± 0.0569
Ga-Fe-Ga Path 1st Nearest Neighbor Distance (Å)	2.6446 ± 0.0678
Ga-Fe-Ga Path 2nd Nearest Neighbor Distance (Å)	3.0022 ± 0.0792
Ga-Ga-Fe Path 1st Nearest Neighbor Distance (Å)	2.5517 ± 0.0719
Ga-Ga-Fe Path 2nd Nearest Neighbor Distance (Å)	2.7690 ± 0.0241
Ga-Ga-Ga Path 1st Nearest Neighbor Distance (Å)	2.6297 ± 0.5017
Ga-Ga-Ga Path 2nd Nearest Neighbor Distance (Å)	3.4537 ± 0.0442
N_{Fe} at 1st Nearest Neighbor	5.50 ± 0.57
N_{Fe} at 2nd Nearest Neighbor	5.70 ± 0.43
N_{Ga} at 1st Nearest Neighbor	2.50 ± 0.57
N_{Ga} at 2nd Nearest Neighbor	0.30 ± 0.43
Enot (eV)	4.9654
R-factor for the Fit	0.0036
amp for the Fit	0.8588

5.4.4.3 Artemis Results of Fe-15 at.% Ga Single Crystal

Artemis® analysis was also done for the Fe-15 at.% Ga single crystal samples. For the best fit of data for the Fe-15 at.% Ga sample in the as-grown condition, k-weights of 1 and 2 were used for fitting both Fe and Ga K-edge scans and the third scattering path was excluded from the FEFF calculations. Figure 5.52 shows the spectra of the fit and experimental data in R space and Table 5.23 shows the detailed data values of this fit. Fe-Ga-Ga path second nearest neighbor distances are low value compared to the other second nearest neighbor distances.

The best fit of data for the Fe-15 at.% Ga single crystal in the long-term annealed (LTA) condition was obtained with a k-weight of 1 for Fe and Ga Kedge scans. All the scattering paths were included in the FEFF calculations. Results of this Fe-15 at.% Ga single crystal LTA sample fit are shown in Figure 5.53 for both Fe and Ga K-edge spectra and the values of all the parameters are given in Table 5.24. Ga-Ga-Fe and Ga-Ga-Ga second nearest neighbor distances are very large relative to the average value.

For the Fe-15 at.% Ga alloy in random solid solution condition, there should be about 1.2 Ga atoms and 6.8 Fe atoms in the first nearest neighbor positions and about 0.9 Ga atom and 5.1 Fe atoms in the second nearest neighbor positions. Based on the DG and LTA analysis results discussed above, after long-term annealing, there is a slight increase in the N value of Ga-Ga first nearest neighbor bonds from 1.46 to 1.74. The N value of Fe-Fe first nearest neighbor bonds increases from 6.02 to 7.78. As a result of the increase in Ga-Ga and Fe-Fe bonds, the total N value of Fe-Ga and Ga-Fe type first nearest bonds decreases from 8.52 for the DG condition to 6.48 for the LTA condition.

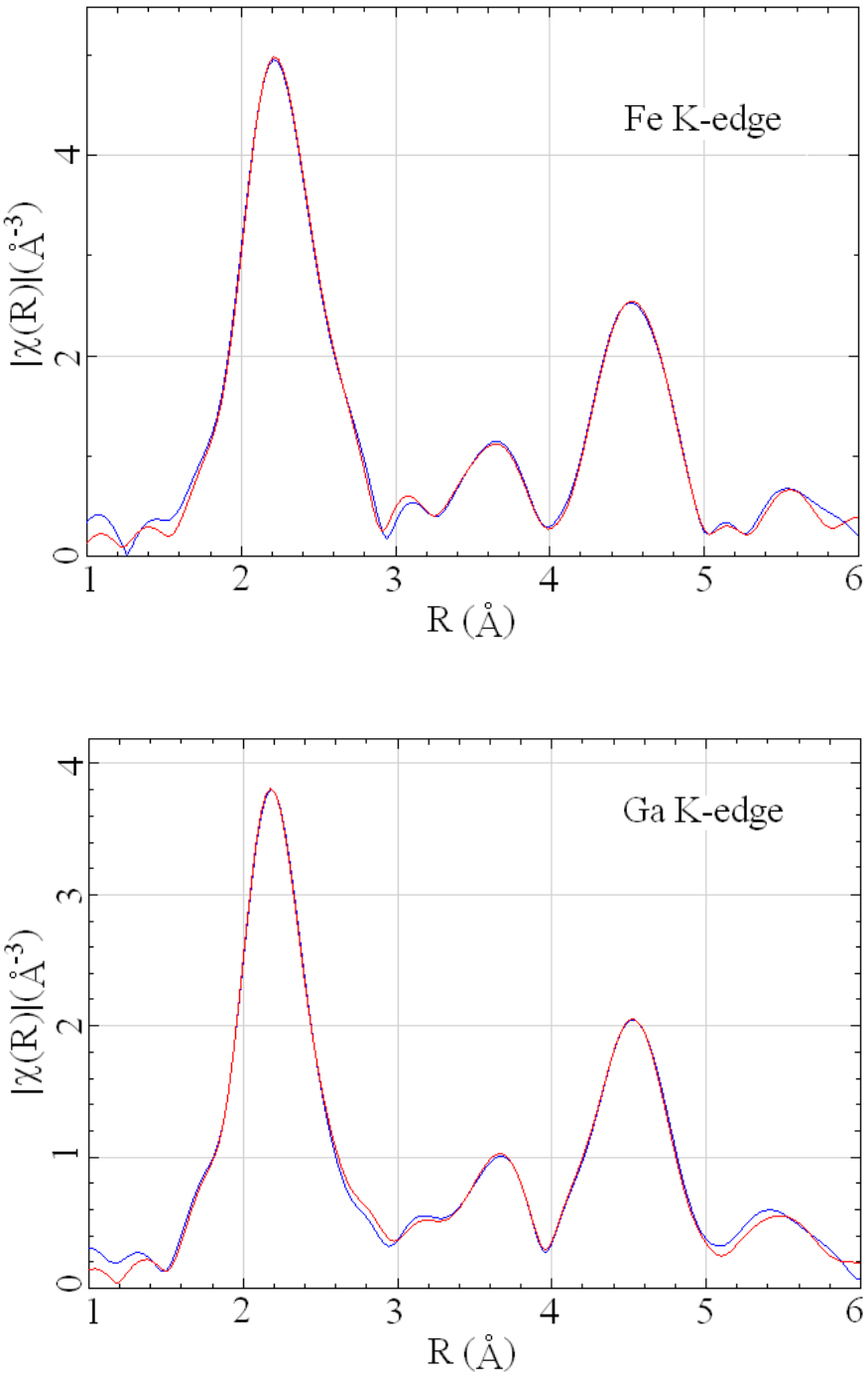

Figure 5.52 Plots of χ for Fe K-edge and Ga K-edge scans of Fe-15 at.% Ga as-grown (DG) single crystal second nearest neighbor analysis result in R space. (Blue: Experimental Data; Red: Fit Data)

Table 5.23 Results of Fe-15 at.% Ga as-grown (DG) single crystal second nearest neighbor analysis

Fe K-edge	
Fe-Fe-Fe Path 1st Nearest Neighbor Distance (Å)	2.4938 ± 0.0129
Fe-Fe-Fe Path 2nd Nearest Neighbor Distance (Å)	2.8621 ± 0.0124
Fe-Fe-Ga Path 1st Nearest Neighbor Distance (Å)	2.2889 ± 0.0171
Fe-Fe-Ga Path 2nd Nearest Neighbor Distance (Å)	2.9844 ± 0.0195
Fe-Ga-Fe Path 1st Nearest Neighbor Distance (Å)	2.3985 ± 0.1098
Fe-Ga-Fe Path 2nd Nearest Neighbor Distance (Å)	3.0696 ± 0.0219
Fe-Ga-Ga Path 1st Nearest Neighbor Distance (Å)	2.5573 ± 0.0213
Fe-Ga-Ga Path 2nd Nearest Neighbor Distance (Å)	2.6662 ± 0.0206
N_{Fe} at 1st Nearest Neighbor	6.02 ± 0.14
N_{Fe} at 2nd Nearest Neighbor	6.23 ± 0.11
N_{Ga} at 1st Nearest Neighbor	1.98 ± 0.14
N_{Ga} at 2nd Nearest Neighbor	0.17 ± 0.11
Enot (eV)	6.604

Table 5.23 Continued

Ga K-edge	
Ga-Fe-Fe Path 1st Nearest Neighbor Distance (Å)	2.4918 ± 0.0096
Ga-Fe-Fe Path 2nd Nearest Neighbor Distance (Å)	2.8536 ± 0.0134
Ga-Fe-Ga Path 1st Nearest Neighbor Distance (Å)	2.7019 ± 0.0312
Ga-Fe-Ga Path 2nd Nearest Neighbor Distance (Å)	3.0674 ± 0.0132
Ga-Ga-Fe Path 1st Nearest Neighbor Distance (Å)	2.5630 ± 0.0182
Ga-Ga-Fe Path 2nd Nearest Neighbor Distance (Å)	2.6111 ± 0.0531
Ga-Ga-Ga Path 1st Nearest Neighbor Distance (Å)	2.4352 ± 0.0677
Ga-Ga-Ga Path 2nd Nearest Neighbor Distance (Å)	2.9652 ± 0.0212
N_{Fe} at 1st Nearest Neighbor	6.54 ± 0.47
N_{Fe} at 2nd Nearest Neighbor	5.36 ± 0.35
N_{Ga} at 1st Nearest Neighbor	1.46 ± 0.47
N_{Ga} at 2nd Nearest Neighbor	0.64 ± 0.35
Enot (eV)	5.2323
R-factor for the Fit	0.0023
amp for the Fit	0.7993

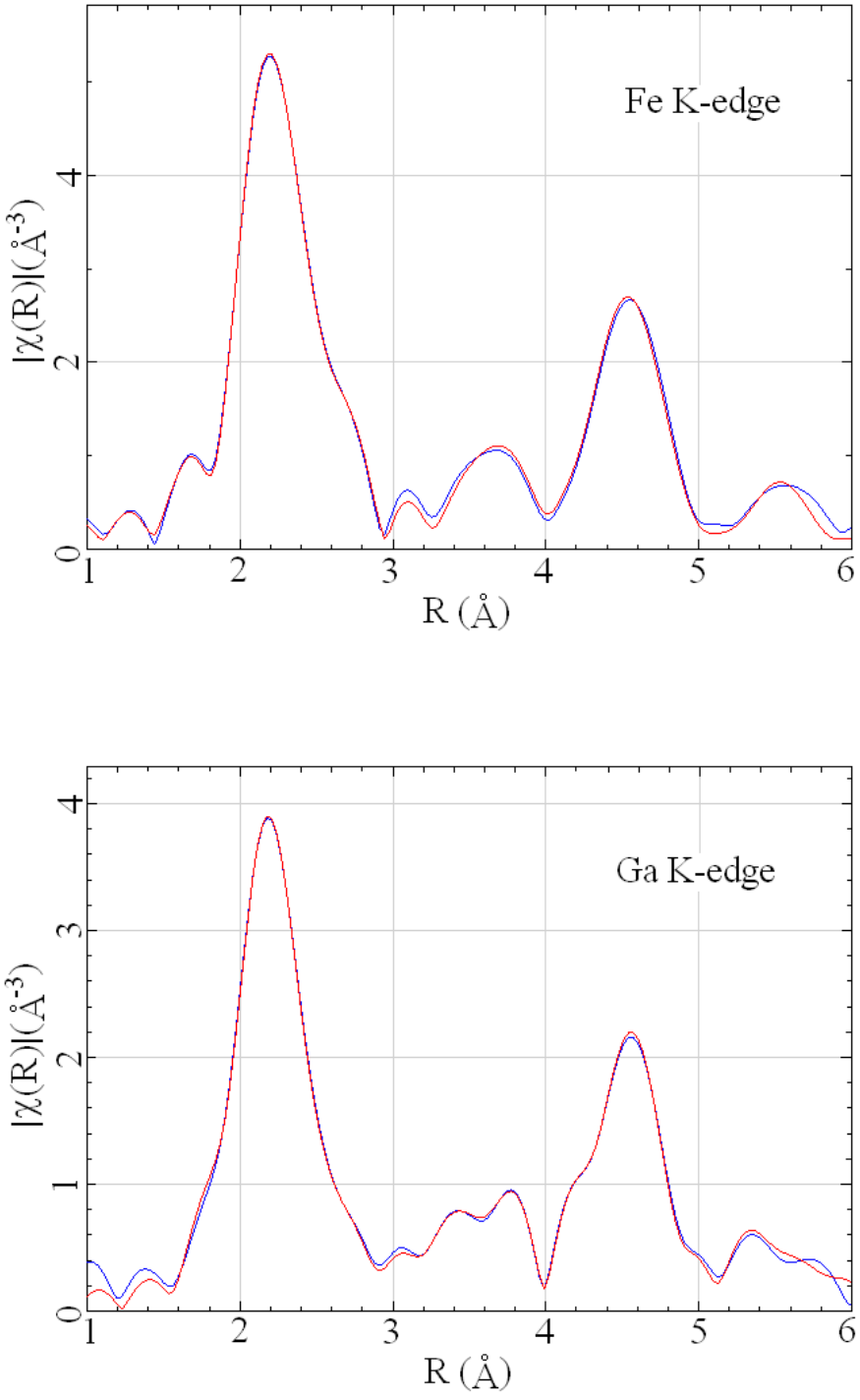

Figure 5.53 Plots of χ for Fe K-edge and Ga K-edge scans of Fe-15 at.% Ga long-term annealed (LTA) single crystal second nearest neighbor analysis result in R space. (Blue: Experimental Data; Red: Fit Data)

Table 5.24 Results of Fe-15 at.% Ga long-term annealed (LTA) single crystal second nearest neighbor analysis

Fe K-edge	
Fe-Fe-Fe Path 1st Nearest Neighbor Distance (Å)	2.4253 ± 0.0156
Fe-Fe-Fe Path 2nd Nearest Neighbor Distance (Å)	2.8604 ± 0.04
Fe-Fe-Ga Path 1st Nearest Neighbor Distance (Å)	2.5837 ± 0.0509
Fe-Fe-Ga Path 2nd Nearest Neighbor Distance (Å)	2.9906 ± 0.0404
Fe-Ga-Fe Path 1st Nearest Neighbor Distance (Å)	2.4100 ± 0.0175
Fe-Ga-Fe Path 2nd Nearest Neighbor Distance (Å)	2.9242 ± 0.0333
Fe-Ga-Ga Path 1st Nearest Neighbor Distance (Å)	2.5142 ± 0.0127
Fe-Ga-Ga Path 2nd Nearest Neighbor Distance (Å)	2.8653 ± 0.032
N_{Fe} at 1st Nearest Neighbor	7.78 ± 0.25
N_{Fe} at 2nd Nearest Neighbor	4.12 ± 0.19
N_{Ga} at 1st Nearest Neighbor	0.22 ± 0.25
N_{Ga} at 2nd Nearest Neighbor	1.88 ± 0.19
Enot (eV)	6.2166

Table 5.24 Continued

Ga K-edge	
Ga-Fe-Fe Path 1st Nearest Neighbor Distance (Å)	2.4782 ± 0.0101
Ga-Fe-Fe Path 2nd Nearest Neighbor Distance (Å)	2.8039 ± 0.0238
Ga-Fe-Ga Path 1st Nearest Neighbor Distance (Å)	2.5532 ± 0.033
Ga-Fe-Ga Path 2nd Nearest Neighbor Distance (Å)	2.9695 ± 0.0292
Ga-Ga-Fe Path 1st Nearest Neighbor Distance (Å)	2.5501 ± 0.0628
Ga-Ga-Fe Path 2nd Nearest Neighbor Distance (Å)	3.5986 ± 0.0614
Ga-Ga-Ga Path 1st Nearest Neighbor Distance (Å)	2.6200 ± 0.0286
Ga-Ga-Ga Path 2nd Nearest Neighbor Distance (Å)	3.3696 ± 0.0557
N_{Fe} at 1st Nearest Neighbor	6.26 ± 0.88
N_{Fe} at 2nd Nearest Neighbor	5.64 ± 0.66
N_{Ga} at 1st Nearest Neighbor	1.74 ± 0.88
N_{Ga} at 2nd Nearest Neighbor	0.36 ± 0.66
Enot (eV)	4.371
R-factor for the Fit	0.0051
amp for the Fit	0.6328

5.4.4.4 Data Analysis of Second Nearest Neighbor Atomic Environment for Fe-Ga Alloy System

Comparing the results of the three Fe-Ga alloy single crystals with different thermal histories, there is a general tendency of increase in the N value of Ga-Ga first nearest neighbor bonds after long-term annealing heat treatment which indicates that more Ga-Ga first nearest neighbor pairs were formed during the long-term annealing. Based on the first nearest neighbor analyses, the long-term annealing heat treatment usually results in an increase in the alloy's magnetostriction. As discussed in the first nearest neighbor analysis, this Ga-Ga pair introduces a large local distortion in the crystal lattice along the [111] crystallographic direction. The strain introduced by the large atomic size Ga-Ga pairs could be one of the reasons for the increase in magnetostriction after long-term annealing. Therefore, the increase in the number of Ga-Ga pairs will also contribute to the formation of local lattice distortion and leads to an increase of magnetostriction.

Large deviations of interatomic distance were observed in all of the Fe-x at.%Ga second nearest neighbor analyses which indicates further improvement of modeling is required to obtain accurate coordination numbers for the Fe-Ga alloy system. However, based on the results, a general tendency can be observed that the N values of Ga-Ga pairs increase as the Ga content increases from Fe-15 at.% Ga to Fe-27.5 at.% Ga. Fe-Ga single crystal's $(3/2)\lambda_{100}$ magnetostriction coefficient value also increases from 258×10^{-6} to 379×10^{-6} as Ga content increase from 15 at.% to 20 at.%. Further increase in the alloy composition from 20 at.% Ga to 27.5 at.% Ga results in a decrease in magnetostriction value from 379×10^{-6} to 340×10^{-6}. As discussed in the earlier section, a

large amount of second phases will start forming as the Ga content increases to more than 20 at.% which causes a decrease in Fe-Ga alloy's magnetostriction. In this high Ga content condition, the contribution of increase in magnetostriction from local lattice strain by Ga-Ga pairs will be cancelled out because of the effect of second phases. Based on the discussion in the EXAFS first and second nearest neighbor analysis, it can be hypothesized that the increase of Fe-Ga alloy's magnetostriction after modifying alloy composition or heat treatment could be partly contributed from the combined effect of both the increase in local strain in the crystal lattice caused by the Ga-Ga first nearest neighbor bond and also the increase of this Ga-Ga bond formation.

CHAPTER 6

CONCLUSIONS

Magnetostriction measurements on [001]-oriented Fe-12.5 at.% Ga-2.5 at.% W, Fe-15 at.% Ga-2.5 at.% W and Fe-17.5 at.% Ga-2.5 at.% W single crystals show that the $(3/2)\lambda_{100}$ magnetostriction coefficient value for Fe-x at.% Ga -2.5at.% W alloys increase by about 67% as the Ga content increases from 12.5 at.% to 15 at.%, and then drops by about 48% as the Ga content increased from 15 at.% to 17.5 at.%. Substitution of W for Ga in Fe-Ga alloys at a level of 2.5 at.% causes a 7% or higher drop in the magnetostriction. These decreases in magnetostriction are likely caused by an increase in the propensity to form second phase regions in the α-Fe matrix of these alloys. Magnetization measurements show that the saturation magnetization of Fe-Ga-W alloy decreases as the solute content increases, and a steep drop occurs after the total solute content increases beyond that of the Fe-15 at.% Ga-2.5 at.% W alloy due to the start of the formation of intermetallic second phases in the α-Fe phase matrix.

Magnetostriction measurements on the [220]-oriented Fe-12.5 at.% Ga-2.5 at.% W alloy single crystal show that the $(3/2)\lambda_{111}$ magnetostriction coefficient of this alloy is about -47×10^{-6} in the annealed condition. Magnetostriction measurements on [220] or [211]-oriented Fe-3 at.% W, Fe-6 at.% W and Fe-7.5 at.% W alloy single crystals show that annealing in α-Fe region and rapid water quenching results in a 30 to 40% increase in the Fe-W alloy's $(3/2)\lambda_{111}$ magnetostriction coefficient value. As the W content

increases from Fe-3 at.% W to Fe-7.5 at.% W, the $(3/2)\lambda_{111}$ magnetostriction coefficient value increased by about 13%. The saturation magnetostriction λ_{si} for any crystallographic direction for this and the other alloys examined can be calculated based on this $(3/2)\lambda_{111}$ and $(3/2)\lambda_{100}$ magnetostriction coefficients that were measured.

The study of B2 and DO_3 ordered second phase regions in the α-Fe phase Fe-27.5 at.% Ga single crystal after annealing and rapid water quenching shows the presence of both B2 and DO_3 ordered domains in the A2 phase matrix. Examination of x-ray diffraction patterns of the [111]-oriented crystal face showed that the relative amounts of B2 phase domains increased with increasing depth up to about 100 μm depth. Beyond the 100 μm depth, the volume ratio of B2 and DO_3 domains showed little variation. This is the first report on any such quantitative measurements.

EXAFS studies of the local atomic environment in Fe-27.5 at.% Ga, Fe-20 at.% Ga and Fe-15 at.% Ga single crystals show a large positive increase in the Ga-Ga first nearest neighbor bond distance after long-term annealing. The value of this positive strain increases as the Ga content increases. Except for the case of the Fe-15 at.% Ga alloy the Fe-Fe, Fe-Ga and Ga-Fe bond distances show a small negative or nearly zero change. The variations of nearest neighbor distances indicate the variation of local lattice distortions. As the changes of magnetostriction values with changes in Ga content and thermal history follow the same tendency, there appears to be a correlation of local lattice strain with the material's magnetostrictive behavior.

APPENDIX A

X-RAY DIFFRACTION PATTERNS OF IRON-BASED ALLOYS

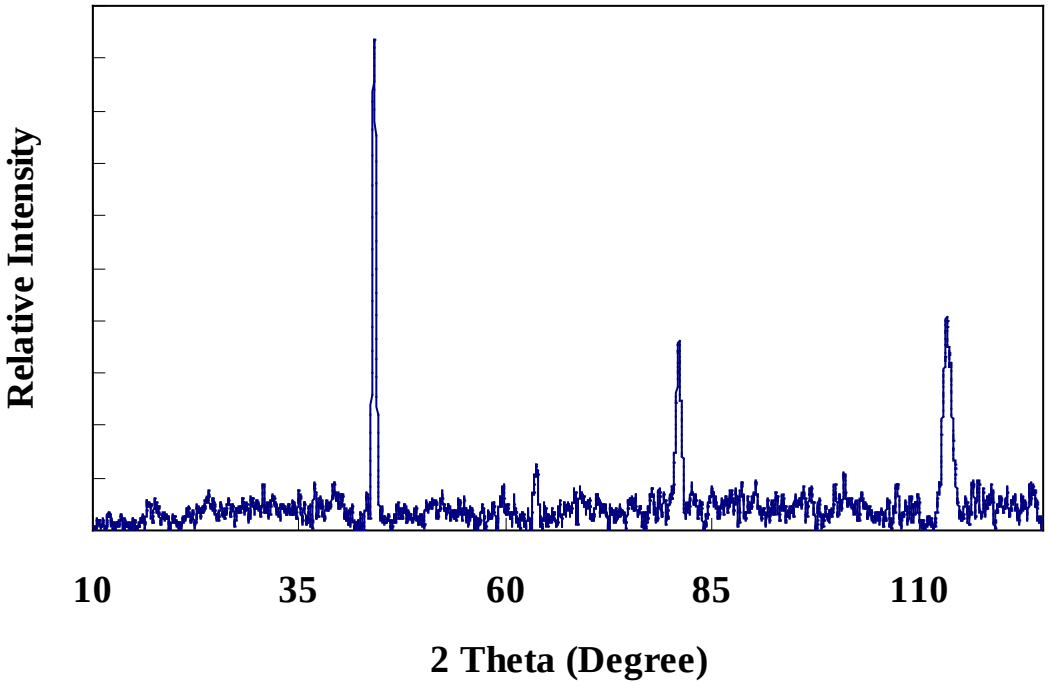

Figure A.1 Theta-2 theta x-ray diffraction scan on the first cut face of DG rod of the Fe-15 at.% Ga-2.5 at.% W single crystal.

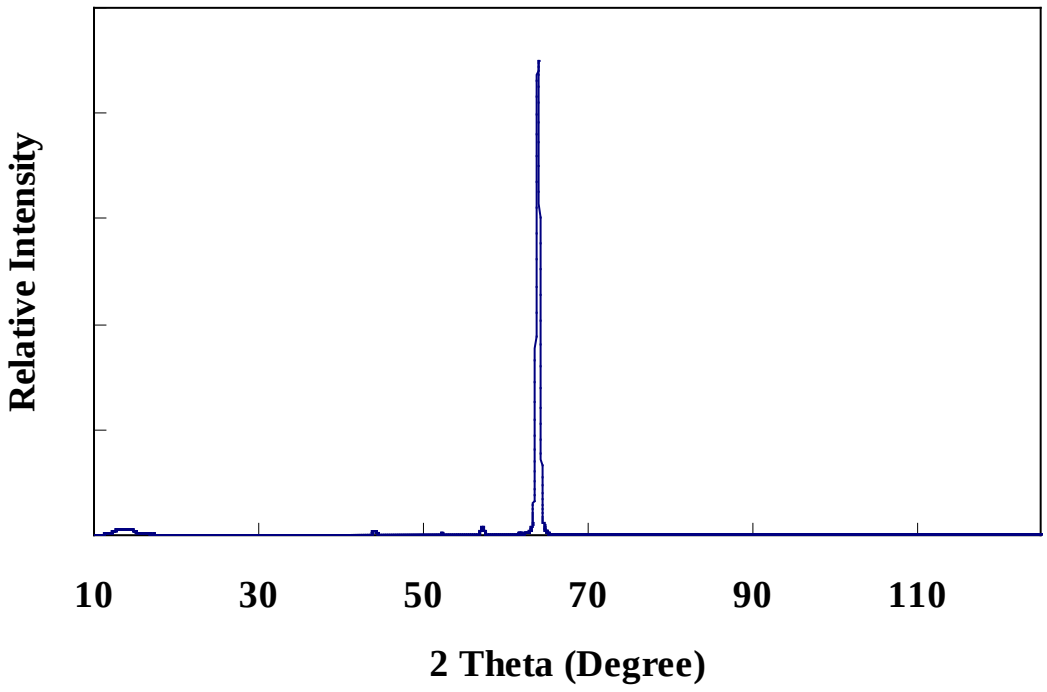

Figure A.2 Theta-2 theta x -ray diffraction scan on the (200) face of the [001]-oriented Fe-15 at.% Ga-2.5 at.% W single crystal.

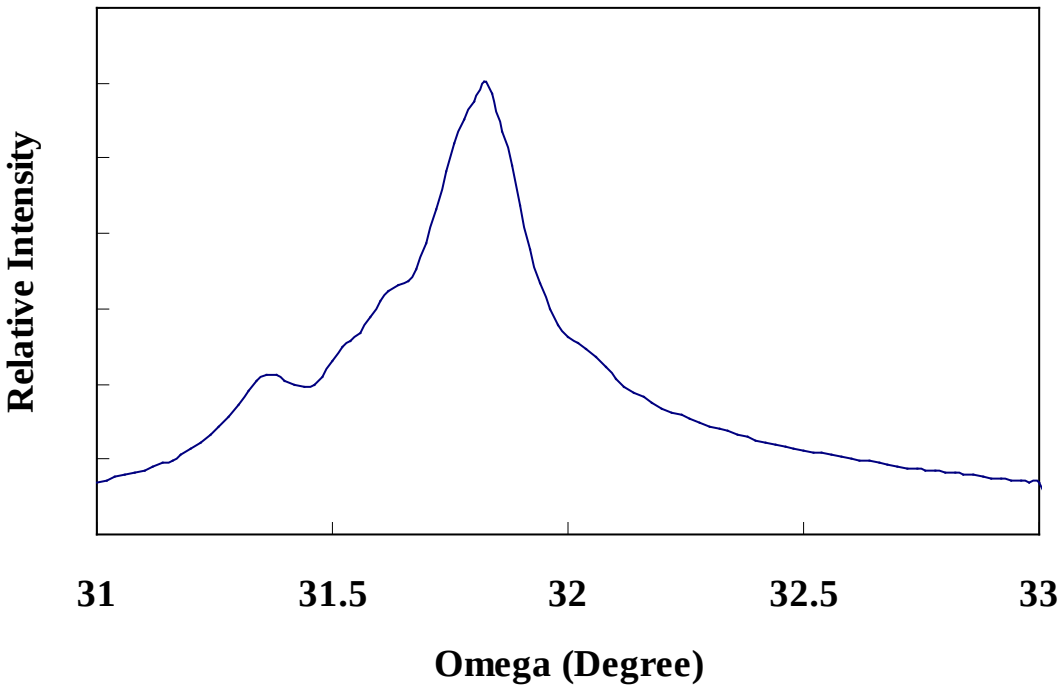

Figure A.3 Rocking curve x-ray diffraction scan on the (200) face of the [001]-oriented Fe-15 at.% Ga-2.5 at.% W single crystal.

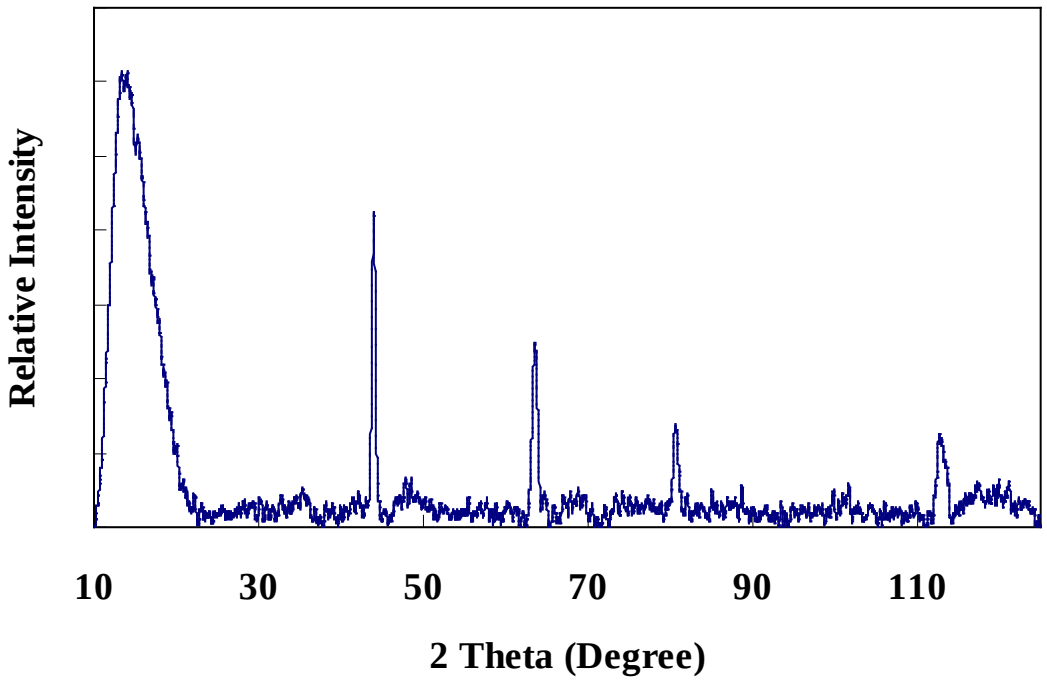

Figure A.4 Theta-2 theta x -ray diffraction scan on the first cut face of DG rod of the Fe-17.5 at.% Ga-2.5 at.% W single crystal.

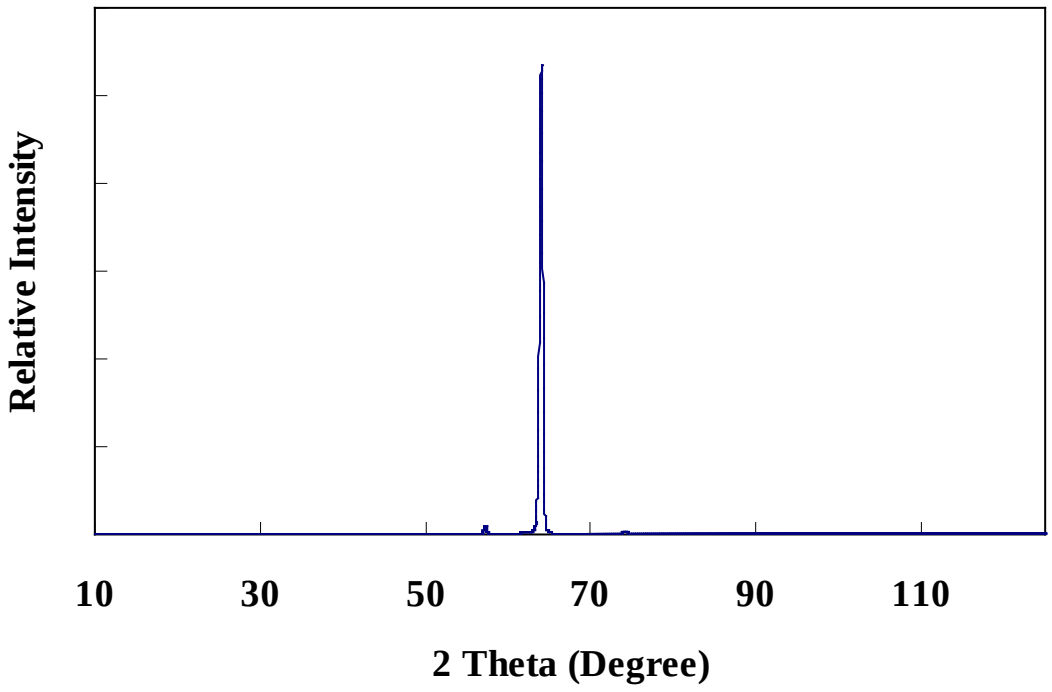

Figure A.5 Theta-2 theta x -ray diffraction scan on the (200) face of the [001]-oriented Fe-17.5 at.% Ga-2.5 at.% W single crystal.

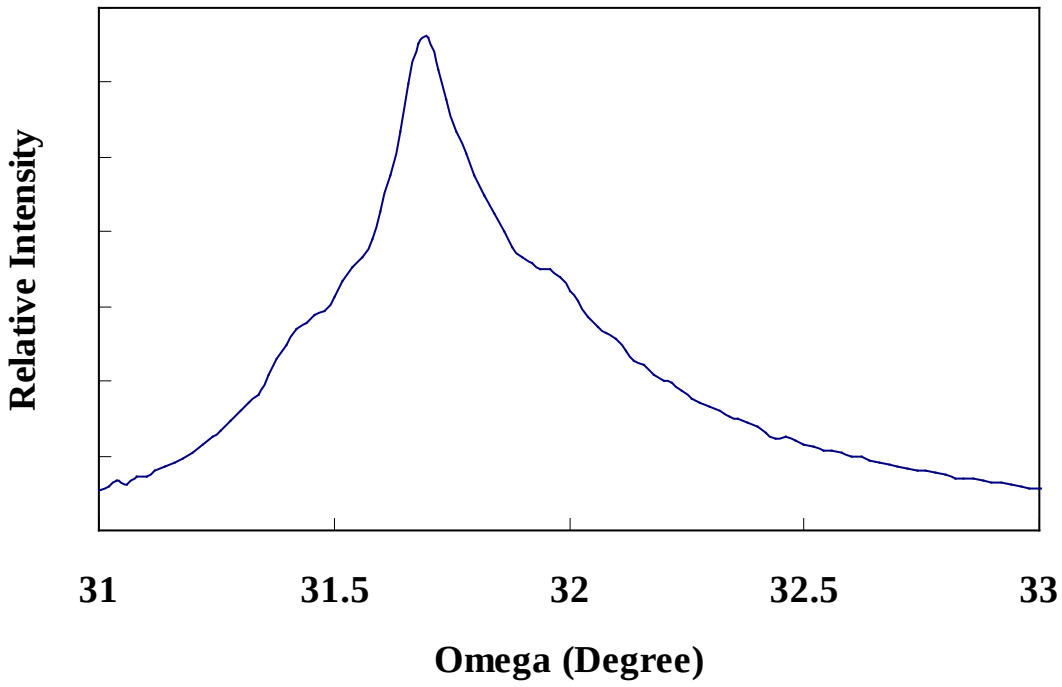

Figure A.6 Rocking curve x-ray diffraction scan on the (200) face of the [001]-oriented Fe-15 at.% Ga-2.5 at.% W single crystal.

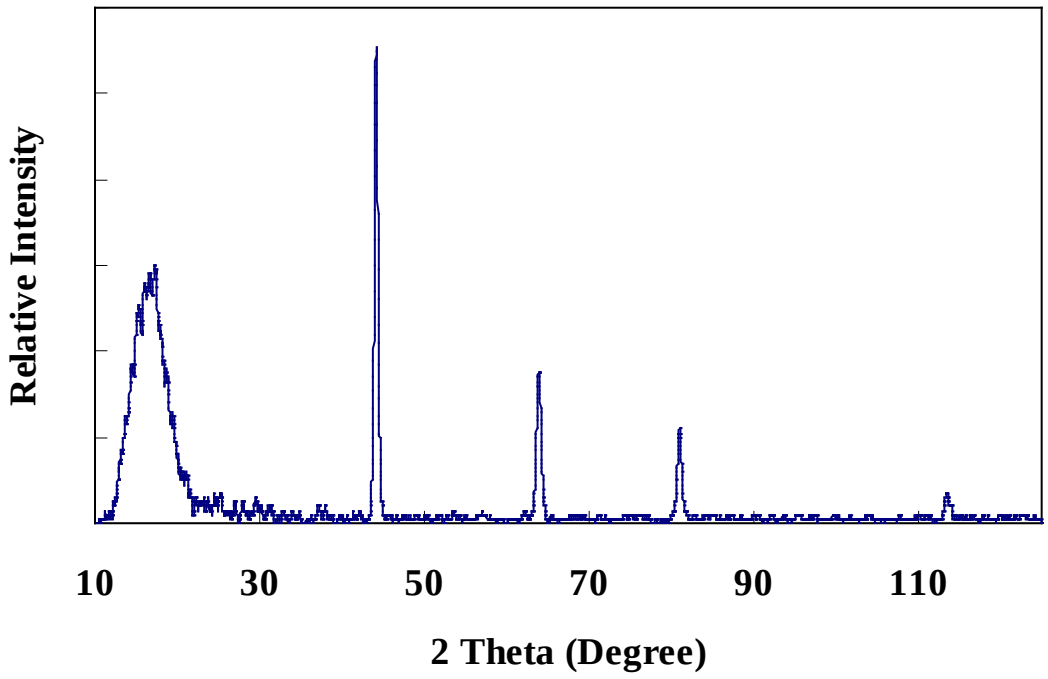

Figure A.7 Theta-2 theta x -ray diffraction scan on the first cut face of DG rod of the Fe-12.5 at.% Ga-2.5 at.% W single crystal.

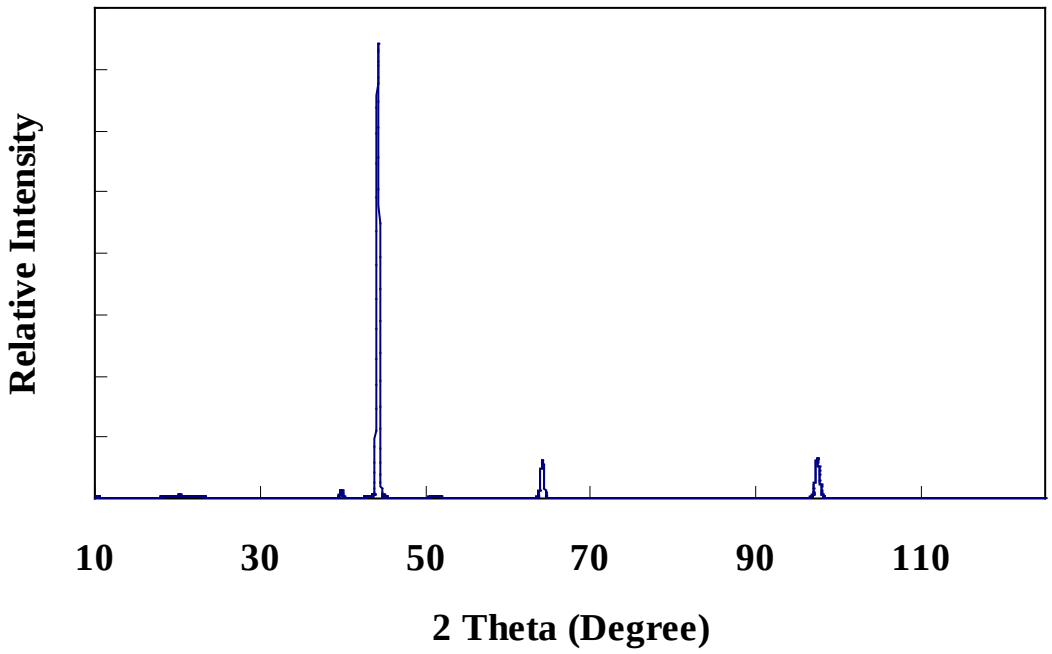

Figure A.8 Theta-2 theta x -ray diffraction scan on the (220) face of the [220]-oriented Fe-12.5 at.% Ga-2.5 at.% W single crystal.

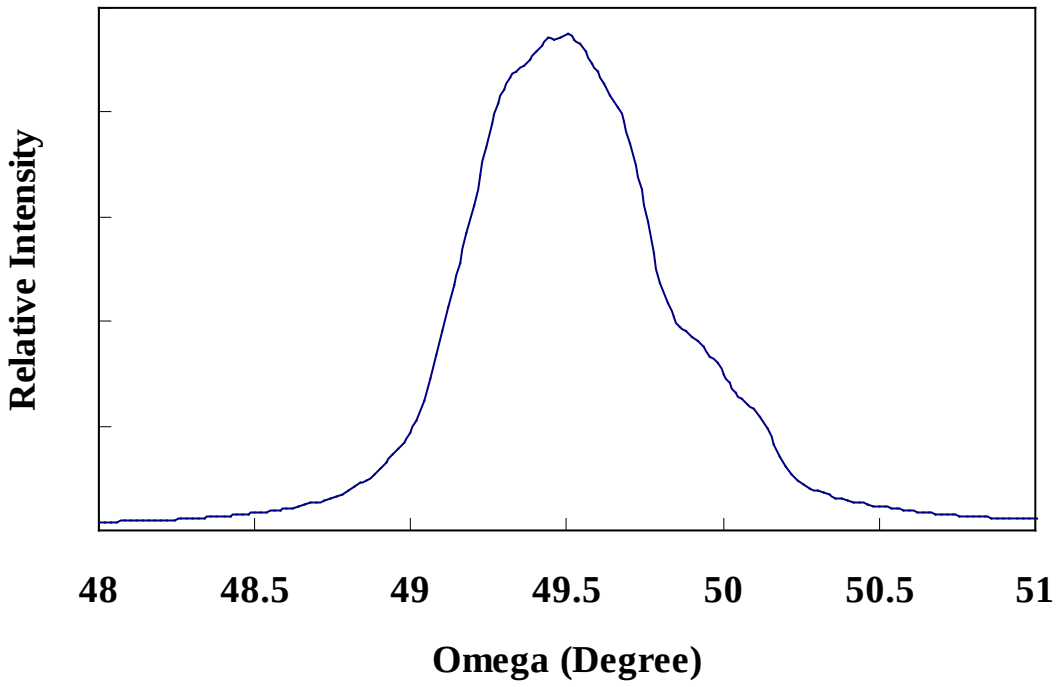

Figure A.9 Rocking curve x-ray diffraction scan on the (220) face of the [220]-oriented Fe-12.5 at.% Ga-2.5 at.% W single crystal.

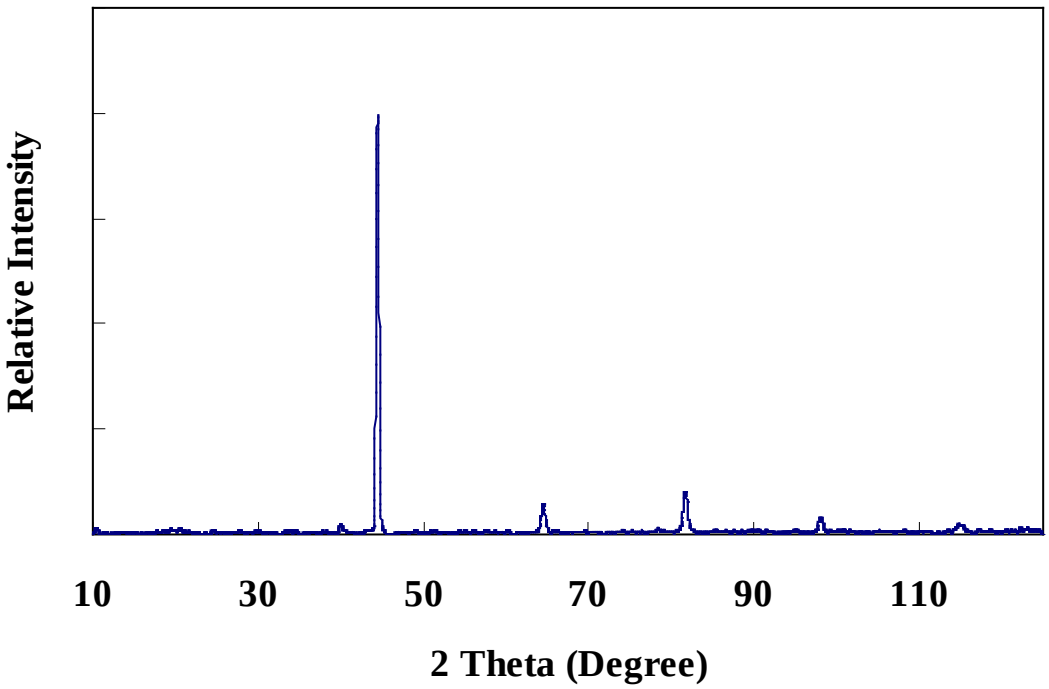

Figure A.10 Theta-2 theta x -ray diffraction scan on the first cut face of DG rod of the Fe-6 at.% W single crystal.

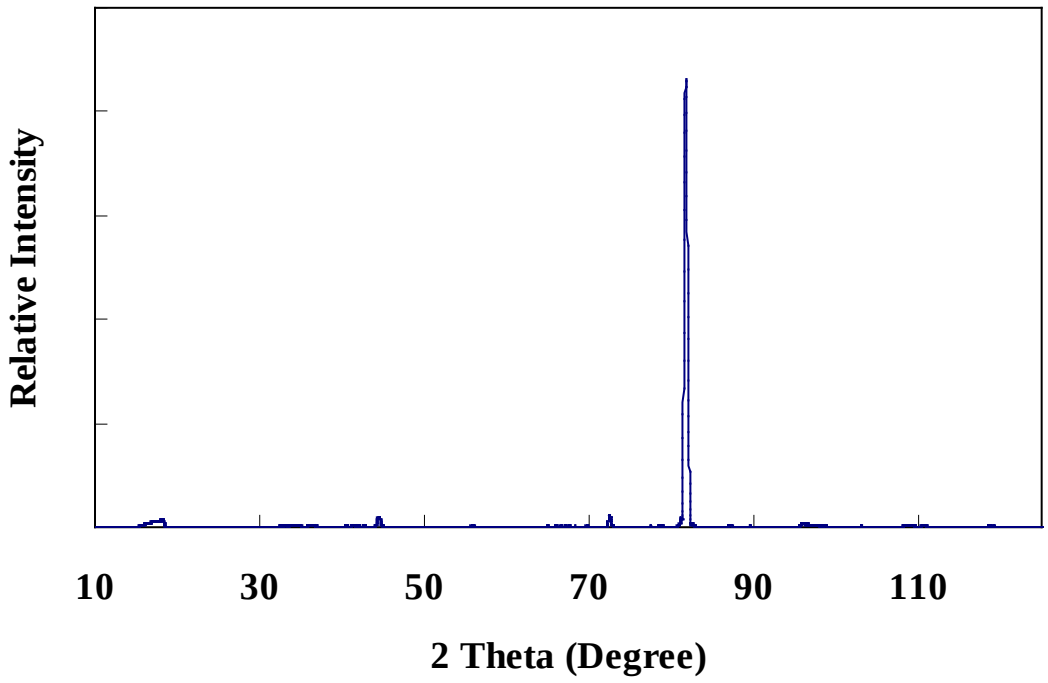

Figure A.11 Theta-2 theta x -ray diffraction scan on the (211) face of the [211]-oriented Fe-6 at.% W single crystal.

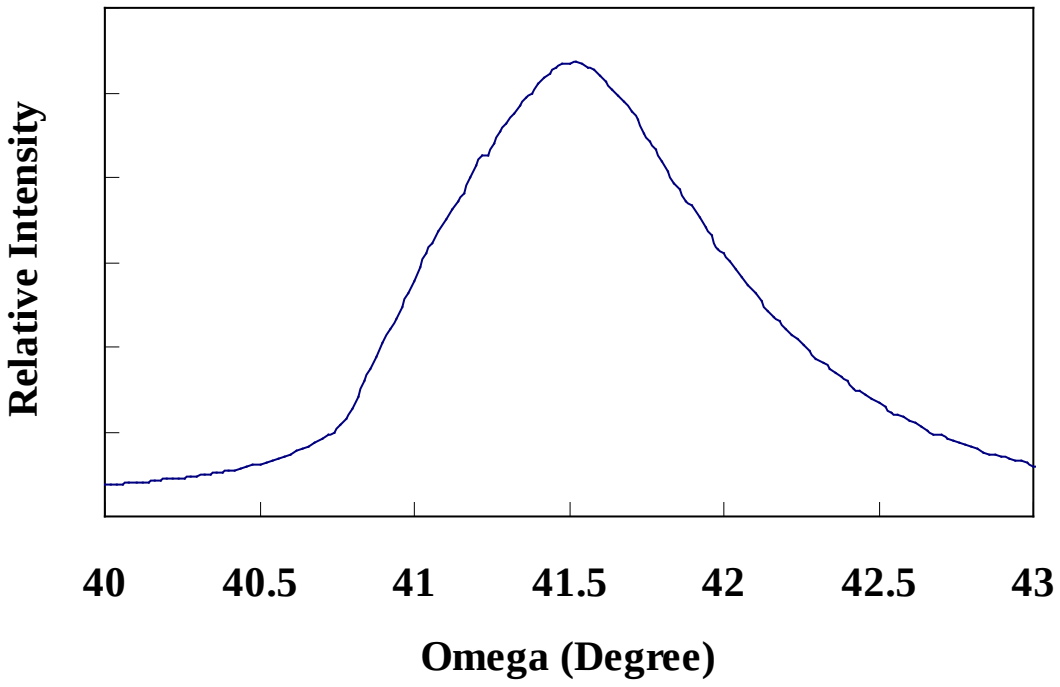

Figure A.12 Rocking curve x-ray diffraction scan on the (211) face of the [211]-oriented Fe-6 at.% W single crystal.

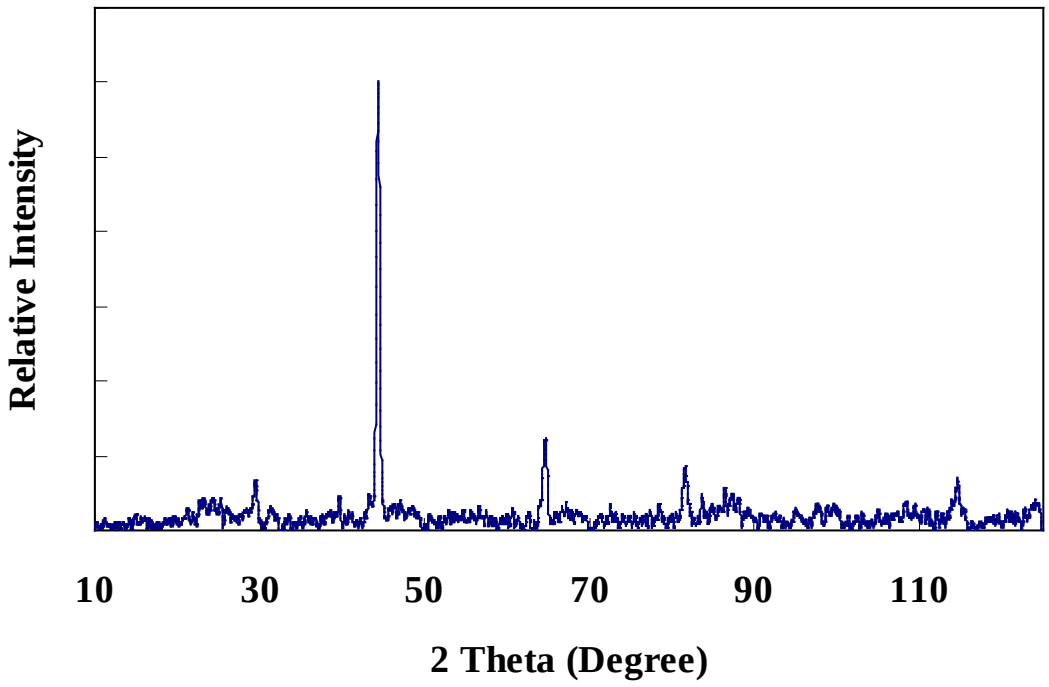

Figure A.13 Theta-2 theta x -ray diffraction scan on the first cut face of DG rod of the Fe-7.5 at.% W single crystal.

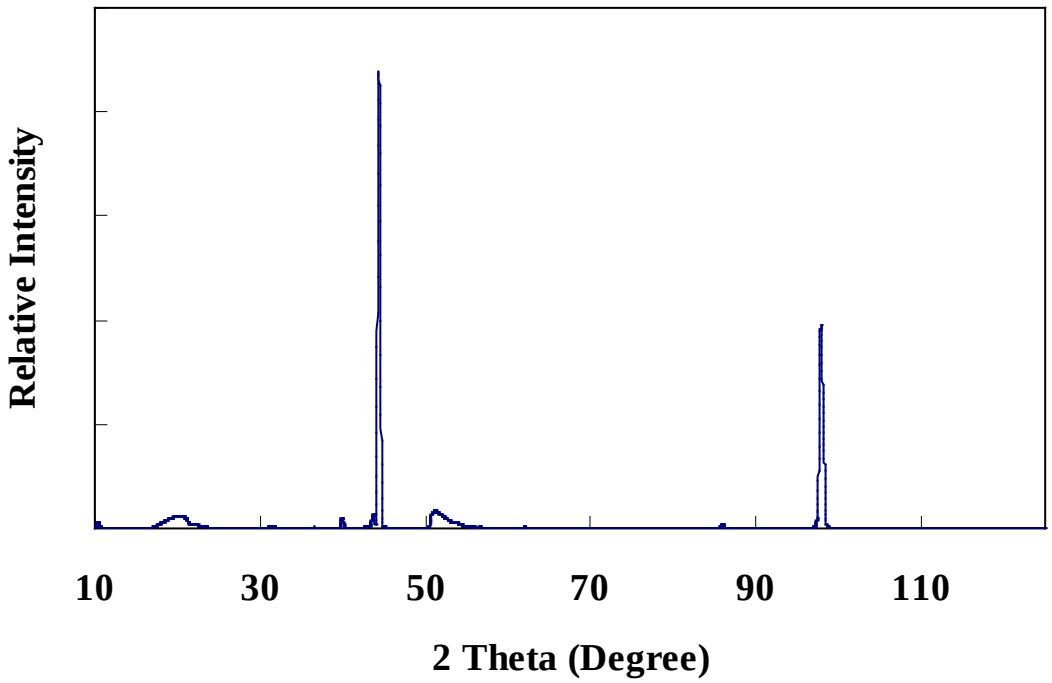

Figure A.14 Theta-2 theta x -ray diffraction scan on the (220) face of the [220]-oriented Fe-7.5 at.% W single crystal.

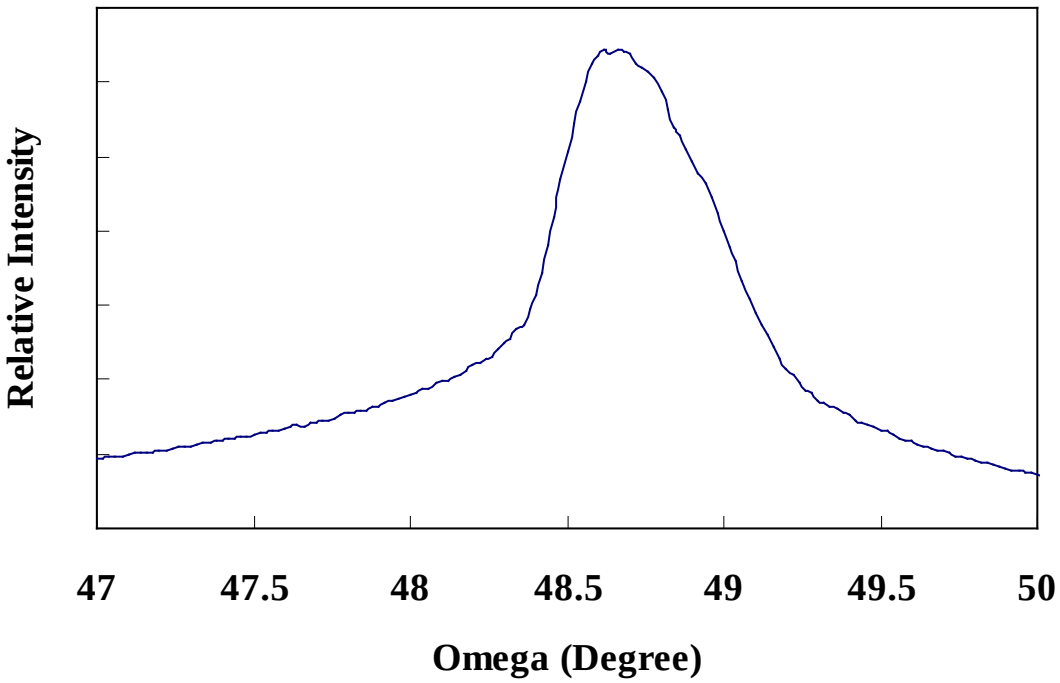

Figure A.15 Rocking curve x-ray diffraction scan on the (220) face of the [220]-oriented Fe-7.5 at.% W single crystal.

APPENDIX B

HYSTERESIS CURVES OF IRON-GALLIUM-TUGSTEN ALLOYS

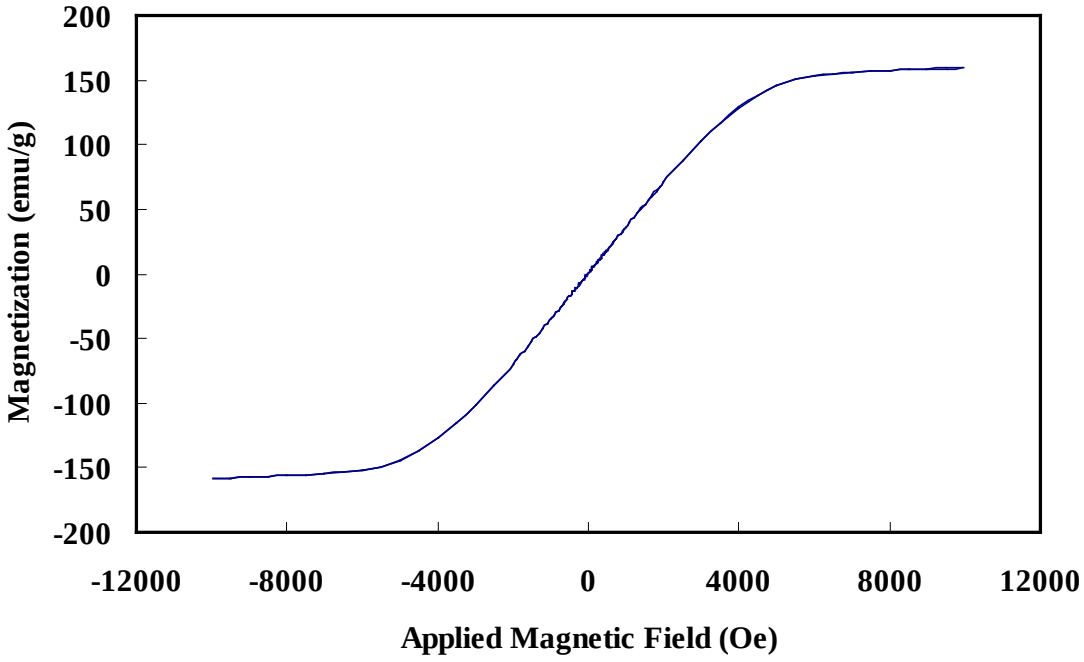

Figure B.1 Hysteresis curve of Fe-15 at.% Ga-2.5 at.% W alloy as directional cast sample.

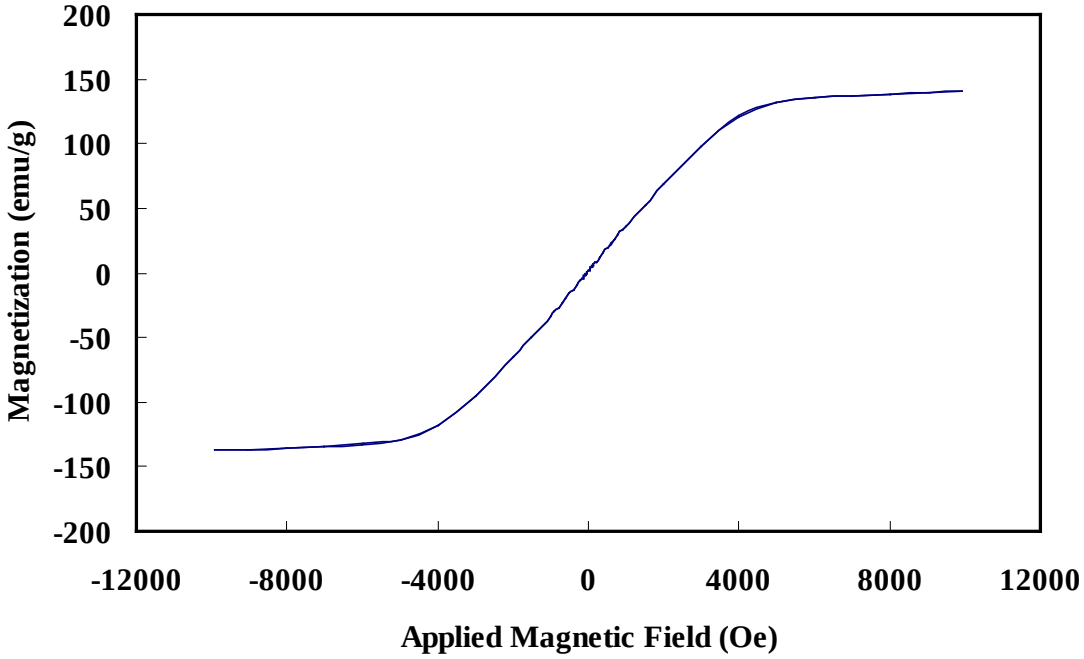

Figure B.2 Hysteresis curve of Fe-17.5 at.% Ga-2.5 at.% W alloy as directional cast sample.

REFERENCES

[1] B. D. Cullity and C. D. Graham, *Introduction to Magnetic Materials*, 2nd ed. Hoboken, NJ: John Wiley & Sons, Inc., 2009.

[2] P. de V. du Plessis, "Magnetoelastic behavior of a terbium single crystal I. anisotropic single-ion properties," *Phil. Mag.*, vol. 18, pp. 581-582, 1968.

[3] A. M. H. Hwang, P. Westwood, Y. J. Bi, and J. S. Abell, "Effect of heat treatment on the magnetostriction and microstructure of terfenol-d," *J. Alloy. Compd.*, vol. 207-8, pp. 390-392, 1994.

[4] R. C. Hall, "Magnetostriction of aluminum-iron single crystals in the region of 6 to 30 atomic percent aluminum," *J. Appl. Phys.*, vol. 28, no. 6, pp. 707-713, 1957.

[5] R. C. Hall, "Single crystal anisotropy and magnetization constants of several ferromagnetic materials including alloys of FeNi, SiFe, AlFe, CoNi, and CoFe," *J. Appl. Phys.*, vol. 30, no. 6, pp. 816-819, 1959.

[6] Z. N. Bolycheva, M. M. Borodkina, and V. L. Sandomirskaya, "Texture and magnetic properties of Fe-Al magnetostriction alloys," *Fiz. Metal. Metalloved*, vol. 19, no. 1, pp. 147-150, 1965.

[7] R. S. Cline and H. Hu, "Formation of annealing textures in rolled aluminum-iron single crystals," *Trans. Metal. Soc. AME*, vol. 233, pp. 57-64, 1965.

[8] S. Guruswamy, N. Srisukhumbowornchai, A. E. Clark, J. B. Restorff, and M. Wun-Fogle, "Strong, ductile, and low-field-magnetostrictive alloys based on Fe-Ga," *Scripta Mater.*, vol. 43, no. 3, pp. 239-244, 2000.

[9] N. Srisukhumbowornchai and S. Guruswamy, "Large magnetostriction in DS FeGa and FeGaAl alloys," *J. Appl. Phys.* vol. 90, pp. 5680-5688, 2001.

[10] N. Srisukhumbowornchai and S. Guruswamy, "Influence of ordering on the magnetostriction of Fe-27.5 at.% Ga alloys," *J. Appl. Phys.* vol. 92, pp. 5371-5379, 2002.

[11] S. Guruswamy, T. V. Jayaraman, R. P. Corson, G. Garside, and S. Thuanboon, "Short range ordering and magnetostriction in α-FeGa alloys," *J. Appl. Phys.* vol. 104, pp. 113919, 2008.

[12] J. R. Cullen, A. E. Clark, M. Wun Fogle, J. B. Restorff, and T. A. Lagrasso "Magnetoelasticity of Fe-Ga and Fe-Al alloys," *J. Magn. Magn. Mater.*, vol. 226-230, pp. 948-949, 2001.

[13] A. E. Clark, M. Wun Folge, J. B. Restroff, T. A. Lagrasso, and J. R. Cullen, "Effect of quenching on the magnetostriction of $Fe_{1-x}Ga_x$ (0.13,x,0.21)," *IEEE T. Magn.*, vol. 37, no. 4, pp. 2678-2680, 2001.

[14] T. A. Lograsso, A. R. Ross, D. L. Schlagel, A. E. Clark, and M. Wun Folge, "Structural transformations in quenched Fe-Ga alloys," *J. Alloy Compd*, vol. 350, pp. 95-101, 2003.

[15] R. Chandler, P. Mungsantisuk, and S. Guruswamy, "Influence of ordering on the magnetostriction of (Fe-(27.5-y) at.% Ga-y at.% Al alloys," in *TMS annual Meeting, 2004, Proceeding of Symposium on Advanced Materials for Energy Conversion II*, 2004, pp. 301-308.

[16] P. Mungsantisuk, "Magnetostriction and texture development in binary and ternary Fe-Ga based alloys," PhD Dissertation, University of Utah, Salt Lake City, UT, 2005.

[17] S. Thuanboon, G. Garside, and S. Guruswamy, "Large low-field magnetostriction in Fe-W and Fe-Mo alloy single crystals," *J. Appl. Phys.*, vol. 104, p. 013912, 2008.

[18] S. Thuanboon, "Magnetic, magnetostrictive and elastic behaviors of Fe-binary alloys," PhD Dissertation, University of Utah, Salt Lake City, UT, 2008.

[19] G. Bunker, *Introduction to XAFS*, Cambridge, UK: Cambridge University Press, 2010.

[20] R. F. Pettifer, O. Mathon, S. Pascarell, M. D. Cooke, and M. R. J. Gibbs, "Measurement of femtometre-scale atomic displacements by x-ray absorption spectroscopy," *Nature (London)*, vol. 435, pp. 78-81, 2005.

[21] V. G. Harris, K. M. Kemmer, B. N. Das, N. C. Koon, A. E. Ehrlich, J. P. Kirkland, J. C. Woicik, P. Crespo, A. Hernando, and A. Garcia-Escorial, "Near-neighbor mixing and bond dilation in mechanically alloyed Cu-Fe," *Phys. Rev. B* vol. 54, no. 10, pp. 6929-6940, 1996.

[22] G. J. Garside, "Probing of local atomic structure using EXAFS and study of magnetostriction in iron-alloy single crystals," PhD Dissertation, University of Utah, Salt Lake City, UT, 2010.

[23] N. S. Akulov, "Zur atomtheorie des ferromagnetismus (atomic theory of ferromagnetism)," *Zeitschrift für Physik*, vol. 54, iss. 7, pp. 582 -587, 1929.

[24] N. S. Akulov, “Ueber den kritischen anisotropiepunkt ferromagnetischer kristalle (critical anisotropy point of ferromagnetic crystals),” *Institute of Metals -- Journal*, vol. 97, no. 4, p. 198, 1931.

[25] J. Crangle, *Solid State Magnetism*, New York, NY: Van Nostrand Reinhold, 1991.

[26] W. D. Callister and D. G. Rethwisch, *Fundamentals of Materials Science and Engineering: An Integrated Approach*, New York, NY: John Wiley & Sons, Inc., 2008.

[27] D. Gignous and M. Schlenker, *Magnetism I- Fundamentals*, Norwell, Mass: Kluwer Academic Publisher, 2002.

[28] E. E. Sechler, *Elasticity in Engineering*, New York, NY: John Wiley & Sons, Inc., 1952.

[29] A. E. Clark, B. F. DeSavage, and E. R. Callen, “Magnetostriction of single crystal dysprosium, gadolinium iron garnet and dysprosium iron garnet,” *J. Appl. Phys.*, vol. 35, no. 3, pp. 1028-1029, 1964.

[30] A. E. Clark and K. B. Hathaway, “Physics of giant magnetostriction,” in *Handbook of Giant Magnetostrictive Materials*, San Diego, CA: Academic Press, 2000.

[31] K. B. Hathaway and A. E. Clark, “Magnetostrictive materials,” *MRS Bull.*, Vol. 18, pp. 34-41, 1993.

[32] U. R. Kattner and B. P. Burton, “Al-Fe (aluminum-iron),” in *Phase Diagrams of Binary Iron Alloys, Monograph Series on Alloy Phase Diagrams No.9*, H. Okamoto, Ed. Materials Park, OH: ASM International, 1993.

[33] R. G. Davies, “An x-ray and dilatometric study of order and the “k-state” in iron-aluminum alloys,” *J. Phys. Chem. Solids*, vol. 24, pp. 985-992, 1963.

[34] J. E. Epperson and J. E. Spruiell, “An x-ray single crystal investigation of iron-rich alloys of iron and aluminum-I. phase relations in alloys containing between 14 and 23 at.% aluminum,” *J. Phys. Chem. Solids*, vol. 30, pp. 1721-1732, 1969.

[35] J. E. Epperson and J. E. Spruiell, “An x-ray single crystal investigation of iron-rich alloys of iron and aluminum-I. diffuse scattering measurements of short-range order in alloys containing 14.0 and 18.3 at.% aluminum,” *J. Phys. Chem. Solids*, vol. 30, pp. 1733-1744, 1969.

[36] J. M. Cook and A. S. Pavlovic, “Magnetostriction and thermal expansion of ordered Fe3Al,” *J. Appl. Phys.*, vol. 50, no. 11, pp. 7710-7712, 1979.

[37] J. M. Cook and A. S. Pavlovic, “Magnetostriction and thermal expansion of single crystal and polycrystalline alloys of iron and aluminum in the vicinity of Fe3Al,” *J. Appl. Phys.*, vol. 55, no. 2, pp. 499-502, 1984.

[38] H. Okamoto, “Fe-Ga,” in *ASM Handbook Vol. 3 Alloy Phase Diagrams*, H. Okamoto, Ed. Materials Park, OH: ASM International, 1993.

[39] Q. Xing, Y. Du, R. J. McQueenery and T. A. Lograsso, “Structural investigations of Fe-Ga alloys: Phase relations and magnetostrictive behavior,” *Acta Mater.*, vol. 56, pp. 4536-4546, 2008.

[40] M. Huang and T. A. Lograsso, “Short range ordering in Fe-Ge and Fe-Ga single crystals,” *Appl. Phys. Lett.*, vol. 95, p. 171907, 2009.

[41] Q. Xing and T. A. Lograsso, “Phase identification of quenched Fe-25at.% Ga,” *Scripta Mater.*, vol. 60, no. 6, pp. 373-376, 2009.

[42] P. Mungsantisuk, R. P. Corson, and S. Guruswamy, “Rare-earth free magnetostrictive Fe-Ga-X alloys for actuators and sensors,” *Advanced Materials for Energy Conversion II in TMS Annual Meeting*, 2004, pp. 275-282.

[43] P. Mungsantisuk, R. P. Corson, and S. Guruswamy, “Influence of Be and Al on the magnetostrictive behavior of FeGa alloys,” *J. Appl. Phys.*, vol. 98, pp. 123907, 2002.

[44] J. B. Restorff, M. Wun-Fogle, A. E. Clark, T. A. Lograsso, A. R. Ross, and D. L. Schlagel, “Magnetostriction of ternary Fe-Ga-X alloys (X = Ni, Mo, Sn, Al),” *J. Appl. Phys.* vol. 91, no. 10, pp. 8225, 2002.

[45] J. Atulasimha and A. Flatau, “Experimental actuation and sensing behavior of single-crystal iron-gallium alloys,” *J. Intell. Mater. Syst. Struct.*, vol. 19, pp. 1371-1381, 2008.

[46] A. E. Clark, J. H. Yoo, J. R. Cullen, M. Wun-Fogle, G. Petculescu, and A. Flatau, “Stress dependent magnetostriction in highly magnetostrictive $Fe_{100-x}Ga_x$, $20<x<30$,” *J. Appl. Phys.*, vol. 105, pp. 07A913, 2009.

[47] S. V. Nagender Naidu, A. M. Sriramamurthy, and P. Rama Rao, “Fe-W (iron-tungsten),” in *Phase Diagrams of Binary Iron Alloys, Monograph Series on Alloy Phase Diagrams No.9*, H.Okamoto, Ed. Materials Park, OH: ASM International, 1993.

[48] F. W. Lytle, “The EXAFS family tree: A personal history of the development of extended x-ray absorption fine structure,” *J. Synchrotron*, vol. 6, pp. 123-134, 1999.

[49] H. Fricke, “The k-characteristic absorption frequencies for the chemical elements magnesium to chromium,” *Phys. Rev.*, vol. 16, no. 3, pp. 202-215, 1920.

[50] G. Hertz, “über die absorptionsgrenzen in der l-serie,” *Z. Phys.*, vol. 3, no. 1, pp. 19-25, 1920.

[51] J. D. Hanawalt, “The dependence of x-ray absorption spectra up on chemical and physical state,” *Phys. Rev.*, vol. 37, no. 6, pp. 715-726, 1931.

[52] R. de L. Kronig, “Zur theorie der feinstruktur in den röntgenabsorptionsspektren,” *Z. Phys.*, vol. 70, no. 5-6, pp. 317-323, 1931.

[53] R. de L. Kronig, “Zur theorie der feinstruktur in den röntgenabsorptionsspektren. III,” *Z. Phys.*, vol. 75, no. 7-8, pp. 468-475, 1932.

[54] F. W. Lytle, “X-ray absorption fine structure in crystalline and non-crystalline materials,” *Physics of Non-Crystalline Solids, Proc. International Conf.*, 1964, pp. 12.

[55] F. W. Lytle, “Determination of interatomic distances from x-ray absorption fine structure,” *Adv. X-ray Anal.*, vol. 9, pp. 398-409, 1966.

[56] D. E. Sayers, E. A. Stern, and F. W. Lytle, “New technique for investigating noncrystalline structures: Fourier analysis of the extended x-ray absorption fine structure,” *Phys. Rev. Lett.*, vol. 27, no. 18, pp. 1204-1207, 1971.

[57] D. E. Sayers, F. W. Lytle, and E. A. Stern, “Structure determination of amorphous Ge, GeO2 and GeSe by fourier analysis of extended x-ray absorption fine structure (EXAFS),” *J. Non Cryst. Solids*, vol. 8-10, iss. C, pp. 401-407, 1972.

[58] P. J. Duke, *Synchrotron Radiations: Productions and Properties*, Oxford, England: Oxford University Press, 2000.

[59] D. C. Koningsberger and R. Prins, *X-Ray Absorption*, New York: John Wiley & Sons, Inc., 1988.

[60] E. A. Stern, “Theory of the extended x-ray absorption fine structure,” *Phys. Rev. B*, vol. 10, no. 8, pp. 3027-3037, 1974.

[61] M. Newville, “X-ray absorption fine-structure spectroscopy,” Lecture Note of APS XAFS Summer School, 2008.

[62] S. Pascarelli, M. P. Ruffoni, R. Sato Turtelli, F. Kubel, and R. Grossinger, “Local structure in magnetostrictive melt-spun $Fe_{80}Ga_{20}$ alloys,” *Phys. Rev. B* vol. 77, pp. 184406, 2008.

[63] R. S. Turtelli, S. Pascarelli, M. Ruffoni, R. Grossinger, and C. Eisenmenger-Sittner, “Extended x-ray absorption fine structure (EXAFS) and x-ray absorption near-edge structure (XANES) study of melt-spun $Fe_{85}Ga_{15}$ ribbons,” *J. Magn. Magn. Mater.*, vol. 320, pp. e578-e582, 2008.

[64] J. Gao, A. Yang, Y. Chen, J. P. Kirkland, J. Lou, N. X. Sun, C. Vittoria, and V. G. Harris, "The effect of boron addition on the atomic structure and microwave magnetic properties of FeGaB thin films," *J. Appl. Phys*. vol. 105, pp. 07A323, 2009.

[65] B. Ravel, M. Newville, "Athena, Artemis, Hephaestus: Data analysis for x-ray absorption spectroscopy using IFEFFIT," *J. Synchrotron Rad.*, vol. 12, pp. 537-541, 2005.

[66] M. Newville, "EXAFS analysis using FEFF and FEFFIT," *J. Synchrotron Rad.*, vol. 8, pp. 96-100, 2001.